Study of the correlation between thermophysical properties and structural evolution of molten oxides by aerodynamic levitation

Zheng Zhang

To cite this version:

Zheng Zhang. Study of the correlation between thermophysical properties and structural evolution of molten oxides by aerodynamic levitation. Material chemistry. Université d'Orléans, 2023. English. NNT : 2023ORLE1004 . tel-04235700

HAL Id: tel-04235700
https://theses.hal.science/tel-04235700
Submitted on 10 Oct 2023

UNIVERSITÉ D'ORLÉANS

ÉCOLE DOCTORALE
ÉNERGIE, MATÉRIAUX, SCIENCES DE LA TERRE ET DE L'UNIVERS
LABORATOIRE CEMHTI
(Conditions Extrêmes et Matériaux : Haute Température et Irradiation)

THÈSE présentée par :

Zheng ZHANG

soutenue le : **08 février 2023**

pour obtenir le grade de : **Docteur de l'Université d'Orléans**
Discipline/ Spécialité : Physique. Sciences des Matériaux

Study of the Correlation between Thermophysical Properties and Structural Evolution of Molten Oxides by Aerodynamic Levitation

THÈSE dirigée par :

Emmanuel de BILBAO	Professeur, CEMHTI, Université d'Orléans

RAPPORTEURS :

Alexander PISCH	Chargé de recherche CNRS, SIMaP Grenoble
Pascal PILUSO	Directeur de recherche, CEA Cadarache

JURY :

Fabrice GAILLARD	Directeur de recherche CNRS, ISTO Orléans, Président du jury
Alexander PISCH	Chargé de recherche CNRS, SIMaP Grenoble
Pascal PILUSO	Directeur de recherche, CEA Cadarache
Philippe Le MASSON	Professeur, IRDL Université Bretagne Sud
Louis HENNET	Ingénieur de recherche CNRS, ICMN Orléans
Emmanuel de BILBAO	Professeur, CEMHTI, Université d'Orléans

Acknowledgments

Time flies and the three-year PhD career is nearing its end. My mood at this moment is complicated and unspeakable, with some nervousness mixed with excitement, and a little uneasiness in delight. Looking back on these three years, there are too many unforgettable and precious moments, experiences, and insights. The greatness of human nature consists in knowing how to be grateful.

First of all, I would like to thank Université d'Orléans for having financed this thesis project. At the same time, I would also like to thank the CEMHTI director: Mme. ***Catherine Bessada****, for allowing me to start and develop doctoral research work under excellent conditions.*

Of course, I would like to express my sincere gratitude to Professor ***Emmanuel de Bilbao*** *for the trust he has placed in me to carry out this project. It has been my good fortune and honor to be his student and to work with him. During these three years, his vast knowledge, his experience, his guidance, his patience, his humor, and his support kept me on the right path until the end. His attitude towards scientific research and students has benefited me for the rest of my life. I also learned the great meaning of teaching and educating. He has made me who I am now. Every discussion with him is something to remember, and it is the most precious memory of my PhD career. I thank him for developing my interest in research, opening me up to new perspectives, and broadening my horizons.*

I would also like to sincerely thank Mr. ***Louis Hennet*** *for instructing me in the aerodynamic levitation device, teaching me to operate the experimental test, sharing the data of neutron diffraction, and reviewing my paper. I have benefited a lot from his extensive experience and expertise in aerodynamic levitation, which greatly promotes the early stage of my experiments.*

My sincere thanks to Mr. ***Alexander Pisch*** *and Mr.* ***Pascal Piluso*** *for agreeing to be the rapporteurs of this thesis and for all the constructive comments that resulted from it. I thank them for their interest in my research work, which certainly added more value to this thesis manuscript. Thanks also to the jury members, Mr.* ***Fabrice Gaillard*** *and Mr.* ***Philippe le Masson****, for agreeing to judge this research work.*

I would like to express my gratitude to the people with whom I have had the good fortune to work. I am thinking mainly of ***Caroline Denier****, who has helped me a lot with data processing. We had a very*

good collaboration in optimizing the experimental tests. Thank ***Séverine Brassamin*** *for her support and help in the maintenance of aerodynamic levitation. Thank* ***Tingwei Sun*** *for sharing her experience and knowledge in molecular dynamics simulations. Also, I would like to thank* ***Audrey Tixier*** *and* ***Vinciane Reynaud*** *for helping me with the daily work.*

Finally, I am grateful to my parents and my wife. They are my strong backing and their love is my driving force to keep going in the face of challenges.

Table of Contents

Lists of figures

Lists of tables

Résumé général

Les oxydes fondus ont une large application dans les industries à haute température, notamment dans les procédés métallurgiques et la corrosion des scories sur les réfractaires. Les propriétés thermophysiques in situ à haute température (densité, tension superficielle, viscosité) des oxydes fondus jouent un rôle important dans ces applications. Des propriétés thermophysiques précises sont utiles pour comprendre en profondeur les phénomènes interfaciaux entre le laitier en fusion et l'acier en fusion et le mécanisme de corrosion du laitier sur le réfractaire.

Cependant, la mesure de données fiables sur les propriétés thermophysiques reste un sérieux défi scientifique. La nucléation hétérogène au niveau de la paroi du récipient dans les méthodes conventionnelles et les limites de température sont inévitables, ce qui entraîne l'incapacité d'obtenir une densité, une tension superficielle et une viscosité précises et limite également la plage de mesure. Pour surmonter les défis mentionnés, la lévitation aérodynamique combinée aux méthodes d'oscillation des gouttelettes a été considérée et développée comme une approche prometteuse. Cependant, cet appareil de lévitation aérodynamique combiné présente encore des problèmes non résolus, tels que l'incertitude des mesures et les outils de post-traitement des données.

Cependant, la mesure de données fiables sur les propriétés thermophysiques reste un sérieux défi scientifique. Dans les méthodes conventionnelles, la nucléation hétérogène à la paroi du récipient et les limites de température sont inévitables, ce qui entraîne l'incapacité d'obtenir une densité, une tension superficielle et une viscosité précises et limite également la plage de mesure. Pour surmonter les défis mentionnés, la lévitation aérodynamique combinée aux méthodes d'oscillation des gouttelettes a été considérée et développée comme une approche prometteuse. Cependant, cet appareil de lévitation aérodynamique combiné présente encore des problèmes non résolus, tels que l'incertitude des mesures et les outils de post-traitement des données.

De plus, il est généralement reconnu que les propriétés thermophysiques des fondus sont étroitement corrélées à l'évolution structurelle des oxydes fondus. Bien que l'évolution structurelle des fondus de $(CaO)_x(Al_2O_3)_{1-x}$ et du système CaO-Al_2O_3-SiO_2 ait été étudiée avec persistance dans notre laboratoire depuis les années 1990, il est toujours difficile de clarifier la corrélation entre les propriétés thermophysiques et la structure des oxydes fondus en raison de l'incommensurabilité de ces propriétés et de la particularité de l'évolution de la structure à haute température. Par conséquent, cette recherche importante reste à promouvoir.

Par conséquent, le travail présenté dans la thèse concerne deux parties. L'une concerne l'optimisation des mesures, incluant les développements d'outils de post-traitement des données et le calcul de l'incertitude des mesures. L'autre partie consiste à éclairer les corrélations entre les propriétés thermophysiques et l'évolution structurelle des fondus de $(CaO)_x(Al_2O_3)_{1-x}$ et des fondus de CaO-Al_2O_3-SiO_2, à l'aide de la dynamique moléculaire classique et des mesures de structure précédentes.

i. Le manuscrit de la thèse est divisé en 6 chapitres:
ii. Le premier chapitre est consacré au contexte de cette recherche et à l'état actuel de la recherche.
iii. Le chapitre 2 décrit les optimisations des mesures de l'appareil de lévitation aérodynamique et la théorie des simulations de dynamique moléculaire.
iv. Le troisième chapitre est consacré aux mesures des propriétés thermophysiques (densité, tension superficielle et viscosité), à l'évolution structurale et à leurs corrélations des fondus de $(CaO)_x(Al_2O_3)_{1-x}$.
v. Le quatrième chapitre, basé sur le système CaO-Al_2O_3, est consacré à la mesure et à la simulation des fusions CaO-Al_2O_3-SiO_2, ce qui valide davantage l'applicabilité de la corrélation théorique entre les propriétés thermophysiques et l'évolution structurelle.
vi. Le chapitre 5 énumère les modèles de viscosité actuellement courants pour les comparer aux valeurs de viscosité expérimentales, ce qui prépare le terrain pour le développement d'un modèle de viscosité plus précis.

Dans le dernier chapitre, les principales conclusions de ce travail sont rappelées et des perspectives d'études futures sont proposées.

General abstract

Molten oxides have a wide application in high-temperature industries, particularly in metallurgical processes and slag corrosion on refractory. High-temperature in situ thermophysical properties (density, surface tension, viscosity) of molten oxides play a significant role in these applications. Accurate thermophysical properties are beneficial to deeply understanding the interfacial phenomena between molten slag and molten steel and the slag corrosion mechanism on refractory.

However, measuring reliable thermophysical properties data is still a serious scientific challenge. In conventional methods, heterogeneous nucleation at the container wall and temperature limitations are unavoidable, which results in the inability to obtain accurate density, surface tension, and viscosity and also limits measurement range. To overcome the mentioned challenges, aerodynamic levitation combined with the droplet oscillation methods has been considered and developed as a promising approach. However, this combined aerodynamic levitation apparatus still presents unsolved problems, such as measurement uncertainty and data post-treatment tools.

Furthermore, it is generally recognized that the thermophysical properties of melts are closely correlated to the structural evolution of molten oxides. Although the structural evolution of $(CaO)_x(Al_2O_3)_{1-x}$ melts and the CaO-Al_2O_3-SiO_2 system had been persistently studied in our laboratory since the 1990s, it is still challenging to clarify the correlation between thermophysical

properties and the structure of molten oxides due to the immeasurability of these properties and the particularity of the structure evolution at high temperatures. As a result, this significant research remains to be promoted.

Therefore, the work presented in the thesis concerns two parts. The one is optimizing measurements, including the development of data post-processing tools and calculation of measurement uncertainty. The other part is illuminations of the correlations between thermophysical properties and structural evolution of the $(CaO)_x(Al_2O_3)_{1-x}$ melts and the $CaO-Al_2O_3-SiO_2$ melts, with the assistance of classical molecular dynamics and previous structure measurements.

The thesis manuscript is divided into 6 chapters:

i. The first chapter is devoted to the context of this research and the current research status.
ii. Chapter 2 describes the optimizations in measurements of aerodynamic levitation apparatus and the theory of molecular dynamic simulations.
iii. The third chapter is dedicated to the thermophysical properties (density, surface tension, and viscosity) measurements, the structural evolution, and their correlations of the $(CaO)_x(Al_2O_3)_{1-x}$ melts.
iv. The fourth chapter, based on the $CaO-Al_2O_3$ system, is devoted to the measurement and simulation of the $CaO-Al_2O_3-SiO_2$ melts, which further validates the applicability of the theoretical correlation between thermophysical properties and structural evolution.
v. Chapter 5 lists currently common viscosity models for comparison with experimental viscosity values, which sets the stage for the development of a more precise viscosity model.
vi. In the last chapter, the main conclusions of this work are recalled and future study perspectives are proposed.

Chapter 1

Chapter 1. Context and current research status

Résumé du Chapitre 1

Ce chapitre est de fournir au lecteur une compréhension générale des applications des fondus de CaO-Al_2O_3 et CaO-Al_2O_3-SiO_2. Le fondu à base de CaO-Al_2O_3 et le fondu à base de CaO-Al_2O_3-SiO_2 sont des laitiers industriels de base communs qui sont largement appliqués dans la métallurgie. Les propriétés thermophysiques (densité, tension superficielle et viscosité) de ces masses fondues jouent un rôle indispensable dans la fabrication de l'acier et la corrosion des scories sur les réfractaires. La génération de données fiables sur la densité, la tension superficielle et la viscosité des fondus à haute température est importante pour optimiser le processus de fusion, explorer le mécanisme de transfert entre le laitier fondu et l'acier liquide, et révéler le mécanisme de corrosion du laitier fondu sur les réfractaires.

Cependant, dans les méthodes conventionnelles, telles que la méthode d'Archimède à double corps, la méthode de la goutte sessile, le viscosimètre à sphère contrebalancée et le viscosimètre à bobine rotative, la nucléation hétérogène sur la paroi du récipient, les limites de température et la contamination de l'échantillon sont inévitables, ce qui entraîne l'incapacité d'obtenir une densité, une tension superficielle et une viscosité précises et limite également la plage de mesure.

Pour surmonter le défi mentionné, les techniques sans récipient ont été considérées et développées comme une approche prometteuse au cours des dernières décennies. La lévitation électromagnétique et la lévitation électrostatique ne sont pas adaptées à la mesure des propriétés thermophysiques des oxydes fondus, car la plupart des oxydes fondus n'ont pas de conductivité électrique. Enfin, la lévitation aérodynamique combinée à la méthode d'oscillation des gouttes, au chauffage laser, à un système d'excitation acoustique, à une source de rétroéclairage et à une caméra à haute vitesse a été construite et choisie comme dispositif de mesure dans la présente thèse.

Cependant, cet appareil de lévitation aérodynamique combiné présente encore des problèmes non résolus :

- Les mesures complètes impliquent divers paramètres, le traitement et l'ajustement des images, et des calculs, ce qui conduit à la difficulté d'estimer l'incertitude des mesures.
- Le principe de la tension superficielle mesurée par l'appareil de lévitation aérodynamique est la théorie de Rayleigh. Par conséquent, la mesure de la tension superficielle est extrêmement sensible à la fréquence de Rayleigh sur la source acoustique, ce qui entraîne l'imprécision des mesures.

De plus, la dynamique moléculaire classique, combinée aux résultats des caractérisations précédentes (diffraction des neutrons, NMR) des systèmes CaO-Al_2O_3 et CaO-Al_2O_3-SiO_2, a été utilisée pour explorer l'évolution structurelle à différentes températures et compositions.

La description ci-dessus conduit aux objectifs de l'étude à la fin de ce chapitre: i) optimisation des mesures, ii) mesure de la densité, de la tension superficielle et de la viscosité des systèmes CaO-Al_2O_3 et CaO-Al_2O_3-SiO_2, iii) exploration de l'évolution structurelle des systèmes CaO-Al_2O_3 et CaO-Al_2O_3-SiO_2, iv) révélation des corrélations entre la densité, la tension superficielle et la viscosité.

Abstract of Chapter 1

This chapter is to provide the reader with a general understanding of the applications of CaO-Al_2O_3 and CaO-Al_2O_3-SiO_2 melts, where the CaO-Al_2O_3-based melt and CaO-Al_2O_3-SiO_2-based melt are common basic industrial slag which is widely applied in metallurgy. The thermophysical properties (density, surface tension, and viscosity) of these melts play an indispensable role in steelmaking and slag corrosion on refractories. The generation of reliable density, surface tension, and viscosity data of melts at high temperatures is important for optimizing the smelting process, exploring the transfer mechanism between molten slag and liquid steel, and revealing the corrosion mechanism of molten slag on refractories.

However, in conventional methods, such as the double bod Archimedean method, the sessile drop method, the counterbalanced sphere viscometer, and the rotating bob viscometer, heterogeneous nucleation at the container wall, temperature limitations, and sample contamination are unavoidable, which results in the inability to obtain accurate density, surface tension, and viscosity and also limits measurement range.

To overcome the mentioned challenge, container-less techniques have been considered and developed as a promising approach in recent decades. Electromagnetic levitation and electrostatic levitation are not suitable for measuring the thermophysical properties of oxide melts, due to most oxide melts without electrical conductivity. Finally, aerodynamic levitation combined with the droplet oscillation method, laser heating, an acoustic excitation system, a backlight source, and a high-speed camera was built and chosen as the measurement device in the present thesis.

However, this combined aerodynamic levitation apparatus still presents unsolved problems:

- Complete measurements involve various parameters, image-processing and -fitting, and calculations, which leads to the difficulty in estimating the uncertainty of the measurements.
- The principle of surface tension measured by the aerodynamic levitation apparatus is the Rayleigh theory. As a result, the measurement of surface tension is extremely sensitive to the Rayleigh frequency on the acoustic source, which causes the inaccuracy of measurements.

In addition, classic molecular dynamics, combined with previous characterization results (neutron diffraction, NMR) of the CaO-Al_2O_3 and CaO-Al_2O_3-SiO_2 systems, was used to explore the structural evolution at different temperatures and compositions.

The above description leads to the study objectives at the end of this chapter: i) optimization in measurements, ii) measuring density, surface tension, and viscosity of the CaO-Al_2O_3 and CaO-

Al_2O_3-SiO_2 systems, iii) exploring structural evolution of the CaO-Al_2O_3 and CaO-Al_2O_3-SiO_2 systems, iv) revealing the correlations between density, surface tension, and viscosity.

1.1 Current status of molten oxide systems

Oxide systems play a significant role in many fields, such as refractories, metallurgy, solar cells, and optical glass, which could be divided into unary, binary, ternary, and multivariate systems, according to their composition, such as CaO-Al_2O_3, CaO-Al_2O_3-SiO_2, CaO-Fe_2O_3-SiO_2, and Li_2O-Al_2O_3-ZrO_2-SiO_2. Molten oxide systems are of technological and scientific interest, which are derived from their well-behaved refractory nature, and optical and mechanical properties, making them attractive for a wide range of industrial applications. In the various melts, CaO-Al_2O_3 and CaO-Al_2O_3-SiO_2 are emphatically presented as the objects of study, which are overviewed as follows:

Calcium aluminates is a special glass-forming system because Al_2O_3 does not resemble SiO_2 as a typical network former, which leads to complex internal structures and specific glass-forming processes. Molten calcium aluminates have long been considered a valuable and promising melt system, due to their numerous applications. Calcium aluminate cement has high resistance to acid attack and particularly biogenic corrosion and abrasion resistance in hydraulic structures [Scrivener et al., 1999]. Crystalline calcium aluminate is an important setting agent in cement production [Liu et al., 2020]. Liu et al studied the dynamic mechanism of phase transitions, density, and viscosity from liquid calcium aluminate, through the supercooled stage to crystalline phases, during cement clinker production. The calcium aluminate family of glasses was predicted as potential ultra-low-loss optical materials because these glasses exhibit intrinsic optical losses at 1.55 μm confirmed by scattering measurements [Lines et al., 1989]. And also, calcium aluminate glasses introduced with rare earth elements have exhibited good conversion in the process from infrared light to visible light [Chung et al., 2005]. Calcium aluminate porous ceramics which have shown nice cell attachment and stable cell growth behavior were proposed as a potential bone graft in biomaterials as well [Kalita et al., 2002]. It is noteworthy that 12CaO•7Al_2O_3 (C12A7) as the lowest eutectic of the Al_2O_3-CaO system has a unique network structure, which has been successfully prepared to solvate electrons apply in the chemistry and engineering of cement [Edwards, 2011]. It means that the system Al_2O_3-CaO has much potential in combining the quantum physics of excess electrons, associated electrons, and vitrification transitions [Miyakawa et al., 2007; Kim et al., 2012]. Molten calcium aluminates are also a common binary metallurgical slag that is used to quantify the corrosion kinetic of high-alumina refractory [De Bilbao et al., 2018], putting forward reaction models based on the dissolution-precipitation-diffusion mechanisms.

Calcium aluminate glasses are considered based on the above description. However, these glasses have a high-liquidus temperature and a tendency to devitrify easily [Cormier et al., 2000], which may be overcome by introducing a small amount of SiO_2, forming the CaO-Al_2O_3-SiO_2 system. The CaO-

Al_2O_3-SiO_2 melts is a relatively common but complex chemical system that has a wide range of industrial applications such as metallurgy, nuclear and industrial waste storage, glass, materials corrosion, and geology [Jakse et al., 2012; Zhang et al., 2021a]. Among the various applications, the CaO-Al_2O_3-SiO_2-based melt is common basic industrial slag as well. Yehorov et al. [Yehorov et al., 2021] investigated the interaction between MgO–C refractory bricks and less basic industrial slag (CaO-Al_2O_3-SiO_2-MgO-Fe_2O_3-MnO) with CaO/Al_2O_3 ratios equal to 1 and varying SiO_2 content. It provided insight into the influence of slag properties on its infiltration, as well as the possible formation of a protective spinel layer. Xu et al. [Xu et al., 2021] used a ladle refining slag of CaO-Al_2O_3-SiO_2-based to examine the corrosion resistance of bauxite-corundum refractory castables, hoping to find out an excellent method to improve the performance of high alumina refractory castable. The slag (CaO-Al_2O_3-SiO_2-based) reaction behaviors of lightweight materials were reported by Fu et al. [Fu et al., 2019], discussing the role of nano-sized intracrystalline pores and material compositions on the slag corrosion and penetration of materials. We have a general understanding of the applications of the CaO-Al_2O_3 and CaO-Al_2O_3-SiO_2 systems, based on the above overview.

1.2 The application of thermophysical properties of melts.

The thermophysical properties of a melt such as its heat capacity, density, surface tension, viscosity, thermal conductivity, etc, are directly related to the structure of the melt and the dynamics of the atoms inside the melt. Thermophysical properties of glass are key properties for melting, fining, processing optimization, glass formation, and annealing process [Cheng et al., 2013]. In cement studies, the thermophysical properties of principal molten phases can help understand their eventual crystalline structures [Liu et al., 2020]. Related simulations of metallurgical processes also require reliable and accurate thermophysical properties (density, surface tension, and viscosity), which help a deep understanding of interactions between molten slag and molten steel to improve steelmaking processes [Siafakas et al., 2018]. Meanwhile, the thermophysical properties of molten slag are essential for studying slag corrosion and penetration of materials in corrosion science [De Bilbao et al., 2015; Blond et al., 2020]. Reliable thermophysical properties contribute to revealing the corrosion mechanism.

1.2.1 The influence of thermophysical properties of molten melts on steel making

The most important function of the molten slags in steel making is concentrating the ash of gangue and fuel in ore and separating the smelting products under high temperatures. Furthermore, the molten slags have other functions as follows: (i) As reaction medium. In some melting processes, the extraction reaction of metals takes place in the molten slags; (ii) Control the contents of impurities in the melting products. The molten slags can react with some components of the molten metal, which can reduce the inclusions in the molten metal such as steel; (iii) As a protection layer to isolate oxygen from the molten metals and prevent their oxidation. Therefore, investigating the thermal properties of molten slags plays a significant role in optimizing the melting process.

First of all, the melting temperature of slags determines the reduction temperature of the furnaces, the fluidity of molten slags, and the separation of molten slags and molten metals. On the one hand, when the melting temperature of the molten slags is high, their melting is more difficult, which would cause a decrease in their fluidity and make the separation of slags and molten metals more difficult. On the other hand, however, when the melting temperature of the molten slags is low, the heat in the furnaces is insufficient, which increases the difficulty in controlling the furnace temperature and reduces the recovery rate of the products in the smelting process. Therefore, the measurement and adjustment of the molten slag melting temperature are of vital importance.

Additionally, the surface tension is one of the most important properties of molten slags and has a critical influence on metallurgical processes (especially the emulsification and separation process between melting steel and molten slag as well as the removal of inclusions and foaming operations), which is defined as the excess free energy per unit area of surface, determined by the energetic interactions between ions in the surface layer. On one hand, when the surface tension is greater, the adhesion work between the melting steel and molten slag is reduced, which makes it more difficult for the slag to mix with melting steel in the form of inclusions, thereby improving the quality of the steel. On the other hand, when the surface tension is smaller, the foaming process of molten slag is more easily, due to the lower energy consumption for generating bubbles. What’s more important, smaller surface tension can increase the life of bubbles and maintain the foaming ability of molten slag. Based on the analysis above, proper surface tension is a significant prerequisite for ensuring the quality of liquid steel and smooth smelting [Wegener et al., 2015; Yan et al., 2018; Zhang et al., 2021b].

Furthermore, the density of molten slags determines the settling velocity of small alloy droplets, the successful separation of molten slag and melting metal, and the foaming of molten slags in the smelting process [Zhang et al., 2010; Shu et al., 2013; Yan et al., 2018]. A higher density of molten slags decreases the setting velocity, which will influence the efficiency of the smelting process and the separation of molten slag and melting metal. However, the experimental data of molten slags are scarce, because of their high reactivity and the technical difficulty of taking precise measurements at elevated temperatures [Zhang et al., 2010].

Besides, viscosity is the ratio of the shearing stress to the velocity gradient [Zhang et al., 2015], which is used to describe the fluid resistance to flow. The viscosity of molten slags affects the reaction kinetics and smelting reaction rate, which is inversely proportional to the transfer rate in the smelting process. Molten slags with lower viscosity increase their transfer rate, which accelerates the smelting reactions and reduces the content of oxides in molten metals. On the contrary, if the viscosity is high, the reaction rate will decrease. Therefore, keeping a proper viscosity of molten slags is of vital importance in the smelting process [Zhang et al., 2015; T. Wu et al., 2016; Kondo et al., 2019].

According to the analysis above, the thermodynamic properties of slags have a great impact on the smelting process. Therefore, the measurement and adjustment of the thermodynamic properties of the slags are important for guaranteeing reasonable and efficient operation of the smelting process.

1.2.2 The influence of thermophysical properties on slag corrosion on refractories

Besides affecting the melting process, the thermodynamic properties (including the melting temperature, viscosity, surface tension, and density) also have important effects on the refractories, which could be considered from two aspects:

(i) The dissolution of refractories into molten slags at high temperatures.

During this process, besides the difference of composition contents in the slags and in the refractories as well as the temperature, the viscosity and the melting temperature of molten slags play a significant role. The dissolution rate V_s of refractories in a molten slag could be calculated by the following Eq. (1-1):

$$V_s=\frac{\rho_s}{\rho_r}\beta(C_s\text{-}C_o) \qquad \text{Eq. (1-1)}$$

wherein β represents the mass transfer coefficient; ρ_s and ρ_r are the densities of slags and refractories; C_s and C_o represent the supersaturated concentration and the concentration of refractories in the molten slags, respectively [Fu et al., 2017, 2019]. β can be obtained by the following Eq. (1-2):

$$\beta=0.558\frac{\rho_s^{\frac{1}{6}}\cdot D^{\frac{2}{3}}\cdot(r\sigma cos\theta)^{\frac{1}{4}}}{\mu^{\frac{5}{12}}\cdot t^{\frac{1}{4}}\cdot l^{\frac{1}{2}}} \qquad \text{Eq. (1-2)}$$

D, r, σ, θ, μ, t, and l represent the effective dissolution coefficient, the radius of the pore, the surface tension of molten slags, the wetting angle between molten slags and refractories, the dynamic viscosity of molten slags, the time, and the mean pore diameter of refractories, respectively [Fu et al., 2019].

From Eq. (1-2), we can see that the thermodynamic properties (such as viscosity, density, and surface tension) of molten slags all affect the dissolution rate of refractories. When the density and surface tension of molten decreases, the mass transfer coefficient β decreases, which reduces the dissolution rate of refractories V_s, because V_s is positively related to the mass transfer coefficient β. Furthermore, a higher viscosity can reduce the mass transfer coefficient β, and then decrease the dissolution rate of refractories V_s [Luz et al., 2011; Fu et al., 2017].

(ii) The penetration of molten slags into refractories at high temperatures.

During the melting procedure, the penetration of molten slags into refractories by open pores and cracks is not ignorable, which could be described by a model of liquid permeating a capillary tube. The penetration depth L and penetration velocity v are calculated by the following Eq. (1-3) and Eq. (1-4):

$$L=\left(\frac{rt\sigma\cos\theta}{2\mu}\right)^{\frac{1}{2}} \quad \text{Eq. (1-3)}$$

$$v=\frac{r\sigma\cos\theta}{4\mu L} \quad \text{Eq. (1-4)}$$

From Eq. (1-3) and Eq. (1-4), it can be obtained that besides the pore size of refractories and the wetting angle between molten slags and refractories, the surface tension and dynamic viscosity of molten slags play a significant role in the penetration of slags into refractories. The penetration velocity of slags into refractories is positively related to the surface tension of the molten slag: with an increase in the surface tension, the penetration velocity of molten slags increases. On the contrary, the penetration velocity of molten slags into refractories is negatively correlated with the dynamic viscosity of molten slags: with an increase in the dynamic viscosity, the penetration velocity of molten slags decreases.

Based on the analysis above, measuring the thermodynamic properties of molten slags accurately is significant in researching the dissolution of refractories into slags and the penetration of molten slags into refractories at high temperatures.

1.3 Measurement methods

There are many methods for measuring the thermophysical properties of high-temperature melts. The measurement methods of melt density, surface tension, and viscosity have been studied for many years, which are artificially divided into conventional contact measurements and novel levitation methods.

1.3.1 Conventional methods

Conventional methods, such as the Archimedean double bob method, the sessile drop method, and the maximum bubble pressure, have been usually performed to measure the density and surface tension of melts at high temperatures.

1.3.1.1 Double bob Archimedean method

The principle of the double bob Archimedean method is to measure the buoyancies of two Pt bobs with different volumes (V1 and V2) [Sasaki et al., 1994; Arman et al., 2019]. The buoyancy (*W*) against the volume (*V*) of the bob immersed in a glass melt is determined by the following Eq. (1-5) and) [Sasaki et al., 1994;]. The schematic apparatus for density measurement is shown in Figure 1-1.

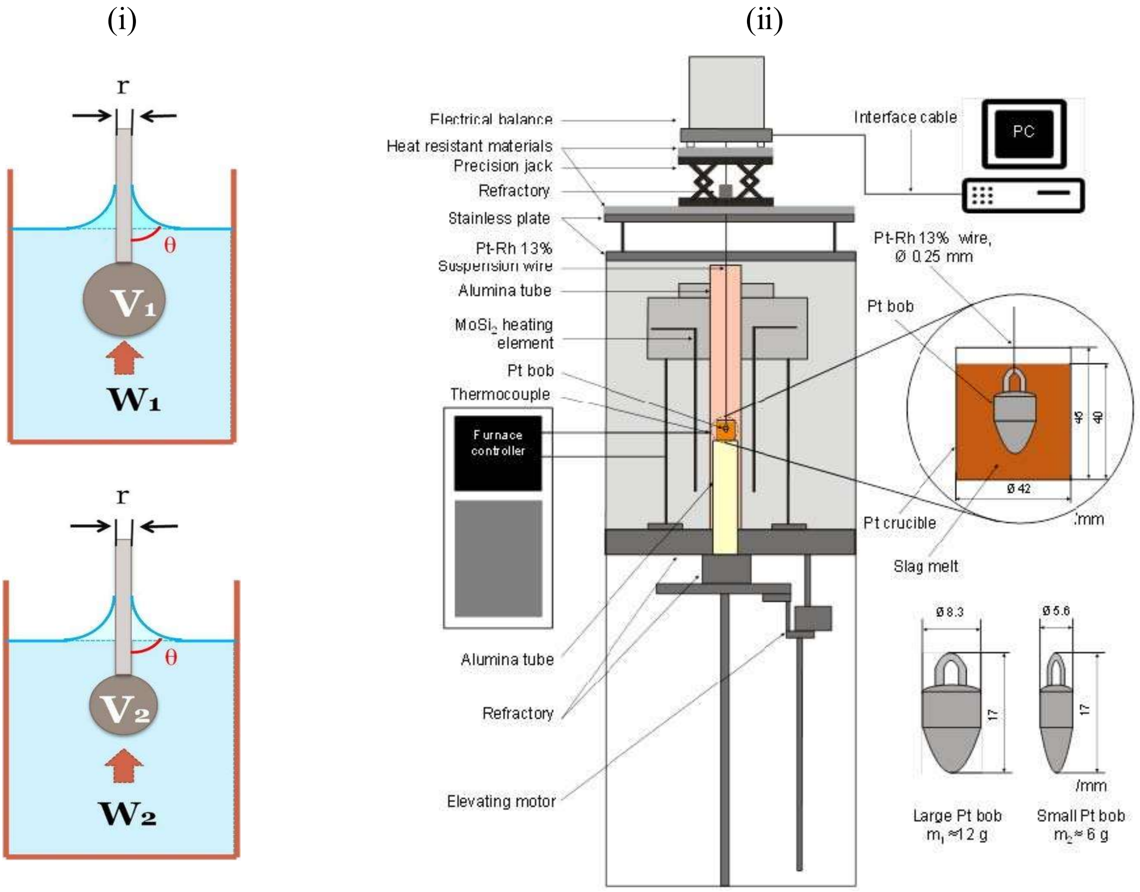

Figure 1-1 Schematic apparatus for density measurements of glass melts: (i) the double bob Archimedean method; (ii) the image of the double bob Archimedean device [Arman et al., 2019].

$$W_1 = V_1\rho - 2\pi r\gamma\cos\theta + A \qquad \text{Eq. (1-5)}$$

$$W_2 = V_2\rho - 2\pi r\gamma\cos\theta + A \qquad \text{Eq. (1-6)}$$

where *W* is the buoyancy of the bob immersed in the melt;

V is the volume of the bob immersed;

ρ is the density of the melt;

r is the radius of the suspending wire;

γ is the surface tension of the melt;

θ is the contact angle between the suspending wire and the melt;

A is the constant that is related to the adhesion and convection of air.

The density of the glass melt is described by the following equation:

$$\rho=\frac{(W_1-W_2)}{(V_1-V_2)} \quad \text{Eq. (1-7)}$$

The density of oxide melts, such as Na_2O-SiO_2 melts [Arman et al., 2019], CaO-SiO_2-Al_2O_3-R_2O (CaO/SiO_2=0.67, Al_2O_3=20 mass%, R_2O=10.8 %, R= Li, Na, K) melts [Fujino et al., 2004], and PbO-B_2O_3-SiO_2 system [Sukenaga et al., 2011] was measured by the double bob Archimedean approach during the temperature range of 1623-1773 K.

1.3.1.2 Sessile drop method

The sessile drop method as another often used technique [Bachmann et al., 2000; Susana et al., 2012; Duchesne et al., 2017] is to project the contour naturally formed by the melt on the Al_2O_3 or Si_3N_4 horizontal board to an imaging system via a backlight source. The volume of the droplet is calculated by taking its cross-section photo and analyzing the geometric shape of the photo. The schematic of the sessile drop apparatus is shown in Figure 1-2 [Duchesne et al., 2017]. The mass of the droplet after solidification was measured and the melt density was calculated. Meanwhile, the surface tension can be synchronously measured by this method. The principle of measurements of surface tension is based on the description of the Young-Laplace equation on the relationship (shown as Eq. (1-8)) between droplet surface pressure and surface tension.

$$\Delta p=\gamma\bullet\left(\frac{1}{R_1}+\frac{1}{R_2}\right) \quad \text{Eq. (1-8)}$$

where γ is surface tension; R_1 and R_2 represent the radius of curvature of the droplet; Δp is the surface pressure difference of the droplet.

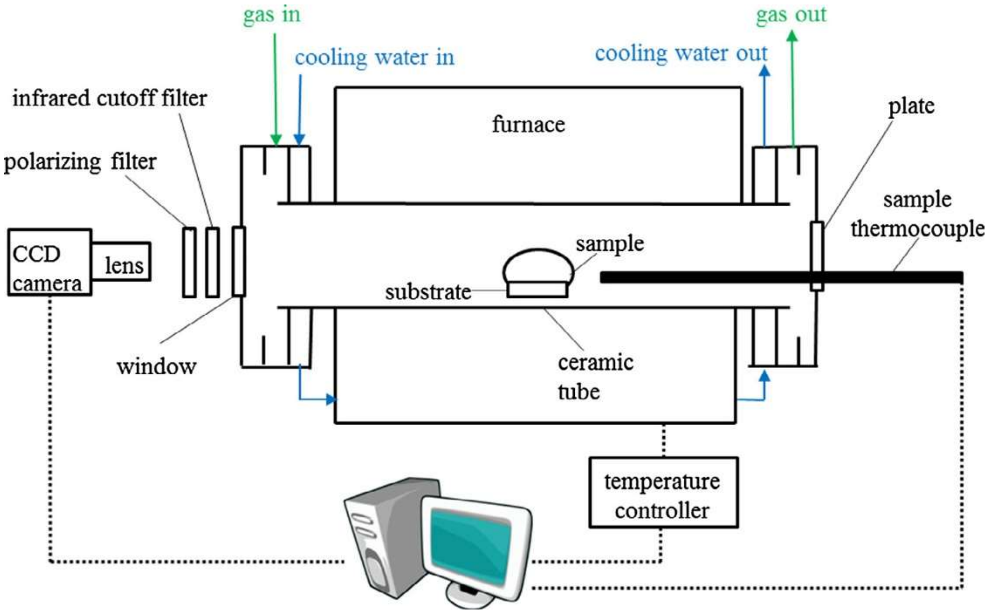

Figure 1-2. Schematic of the sessile drop method [Duchesne et al., 2017].

The accuracy of the sessile drop method mainly depends on the image processing technique, calculation of the volume, and contact angles on substrates. It is worth mentioning that the sessile drop technique can measure both the density and surface tension of melts. The density and surface tension of synthetic coal slags were measured by the sessile drop technique during the temperature range 1473-1873 K [Duchesne et al., 2017].

The viscosity of melts is an important property applied in metallurgy and glass production and some measuring methods have been developed in recent years, such as capillary, oscillating vessel, rotational bob, oscillating plate, and draining vessel [Iida et al., 1993; Brooks et al., 2005].

1.3.1.3 Capillary rheometer

The capillary rheometer is considered to be a simple and effective method for the measurements of the viscosity of melts, as shown in Figure 1-3. The principle of the capillary rheometer is the time for a finite volume of melts to flow through a narrow bore tube under a given pressure [Brooks et al., 2005]. The Hagen-Poiseuille equation describes the correlation between viscosity and efflux time, as follows:

$$\eta=\frac{\pi r^4\rho g h t}{8V(l+nr)}-\frac{m\rho V}{8\pi(l+nr)t} \qquad \text{Eq. (1-9)}$$

where r is the radius of the capillary;

l is the length of the capillary;

h is the effective height of the column of liquid;

ρ is the melt density;

V is the volume discharged in time *t*;

m and *n* are constants that can be determined experimentally.

ρgh is the pressure difference along the capillary.

nr is called end correction and corrects for the surface tension effect when the fluid is drained from the capillary.

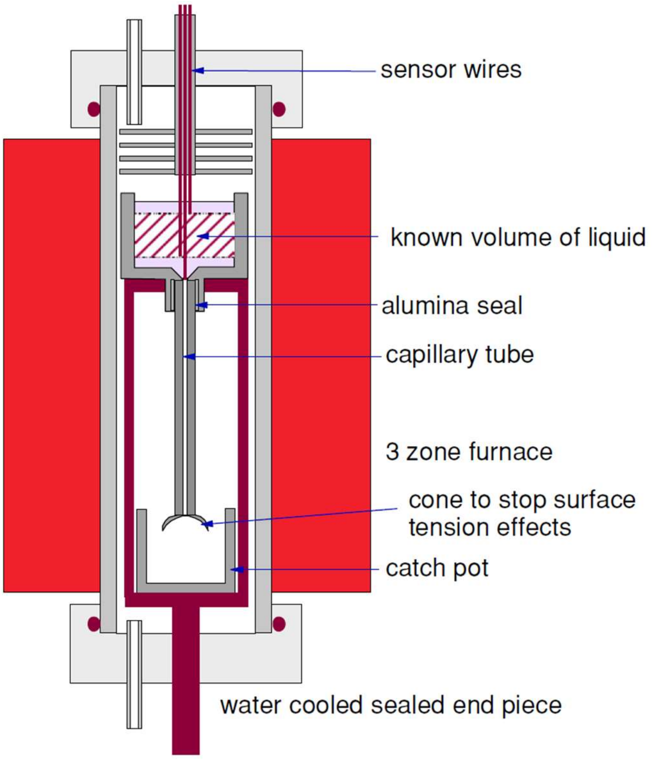

Figure 1-3. Schematic of the capillary viscometer [Brooks et al., 2005].

However, during measuring the viscosity of melts by the capillary method, high viscosity melt or solid granular melt may block the capillary and make it impossible to measure the viscosity, due to the fine capillary.

1.3.1.4 Counterbalanced sphere viscometer

The measured process of the counterbalanced sphere viscometer [Riebling, 1963; Brooks et al., 2005] is either the drop of the platinum sphere because of gravity or dragged upwards into the melt. The schematic of the counterbalanced sphere viscometer is shown in Figure 1-4. According to Stokes' law, the relationship between the viscosity of melt and descent or ascent speed is shown in the following Eq. (1-10).

$$\eta = \frac{2gr^2(\rho_{pt} - \rho_{melt})}{9S} \qquad \text{Eq. (1-10)}$$

where g is the gravitational acceleration; r is the radius of the platinum sphere; ρ_{pt} and ρ_{melt} are the density of the platinum sphere and the melt, respectively; S is the velocity of descent or ascent of the sphere. The correction for the expansion of the platinum sphere is necessary for this apparatus. Oxide melts with low viscosity (especially Reynolds number Re < 0.1) can not be measured by the counterbalanced sphere viscometer because Stoke's law does not hold and a modified equation must be used [Brooks et al., 2005]. For melts with Re > 0.1, the following Oseen's equation is given to express the relationship between the Reynolds number and viscosity [Hara et al., 1997],

$$f_1 = 3\pi\eta DV(1 + 3/16\,Re) \qquad \text{Eq. (1-11)}$$

where f_1 is viscous resistance when a sphere of its diameter D (cm) moves at the velocity V (cm/sec) in the melt of its viscosity η.

Hara et al [Hara et al., 1997] used the counterbalance sphere viscometer to measure the viscosity of the CaO-SiO_2-Al_2O_3-Fe_2O_3 melts at the temperature range of 1600-1900 K.

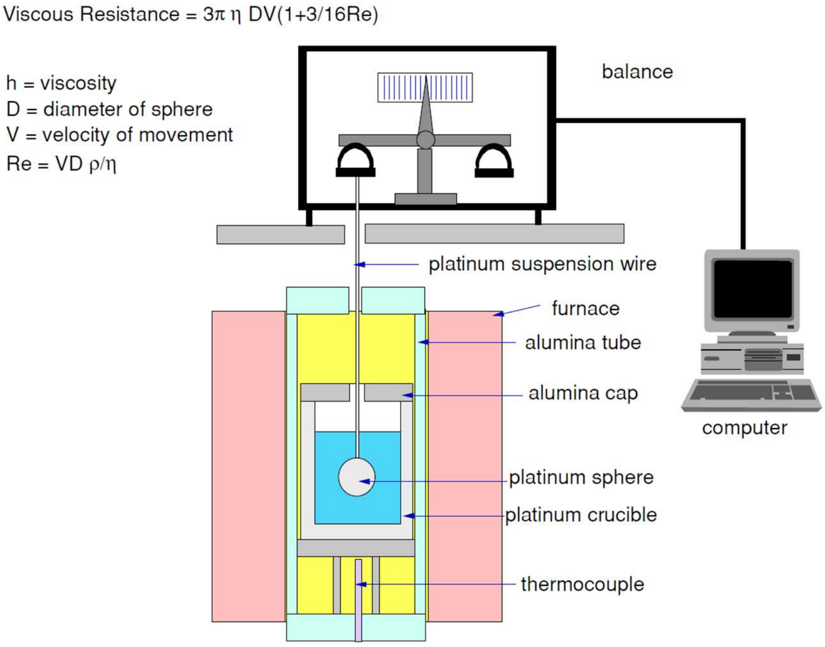

Figure 1-4. Schema of a counterbalanced sphere viscometer [Brooks et al., 2005].

1.3.1.5 Rotating bob viscometer

For the rotating bob viscometer (shown in Figure 1-5), the torque on the cylinder rotated in a melt is related to the viscosity of a liquid. The viscosity is determined by measuring the torque developed on the rotor arm of the rotating cylinder. The viscosity of a melt can be calculated from the following Eq. (1-12) under the rotating cylinder at a constant speed.

$$\eta=\left(\frac{1}{r_1^2}-\frac{1}{r_0^2}\right)\frac{M}{8\pi^4 nh} \qquad \text{Eq. (1-12)}$$

where M is the torque; n is the number of revolutions per second; r_1 is the radius of bob, r_0 is the radius of a crucible; h is the height of the bob.

This device to measure a wide range of viscosity from 10^{12} to 10^{1} Pa•s has been successfully demonstrated with various glasses to a temperature of 1473 K.

However, any instability regarding rotation speed or alignment would improve the measured viscosity value of the melt. When a melt with lower viscosity is measured by the rotating bob viscometer, it is difficult to keep the clearance between the stationary and rotating parts extremely small and maintain the system coaxially.

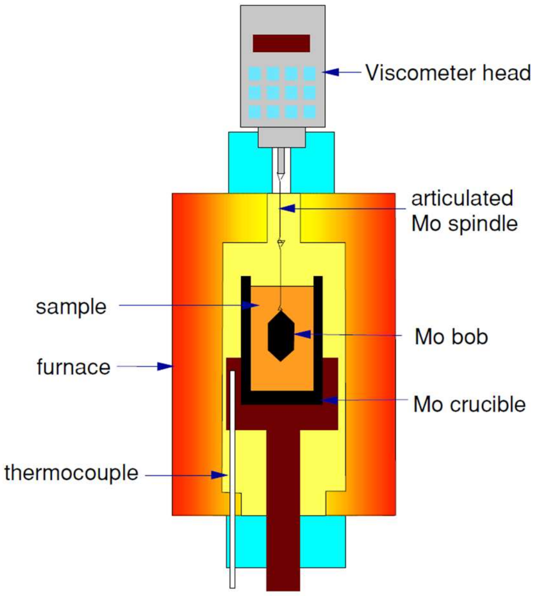

Figure 1-5. Schema of a rotating bob viscometer [Brooks et al., 2005].

Except for own shortcomings of each approach, all the conventional approaches to measure thermophysical properties mentioned above have an inevitable defect. By observing these device schematics, the melt is in contact with the container or substrate during the whole measuring process. High temperatures tend to induce the risk of interactions between a melt and the container/substrate, which result in contamination of the melt, heterogeneous nucleation under supercooled conditions, as well as large measured error. Temperature limitations are unavoidable, which also limits the measurement range of density, surface tension at high temperatures, and viscosity. Conventional container methods cannot meet the requirements of ultra-high temperature testing. Therefore, for the thermophysical properties of molten oxide systems, how to accurately measure them in situ at high temperatures is still a scientific challenge.

1.3.2 Containerless levitation methods

In contrast to conventional approaches, levitation technology can perfectly eliminate the problems of the contact between a melt and the container to avoid contaminations, which is the ideal method for studying the structure and dynamics properties of ultra-high temperature melts [Hennet et al., 2007]. An additional advantage of the levitation approach is that it can precisely explore the crystallization and properties of supercool hot melts below their equilibrium freezing point. Different levitation techniques have been developed and the principal approaches are introduced as follows.

1.3.2.1 Electromagnetic levitation

Electromagnetic levitation [Jacobs et al., 1996; Brillo et al., 2011; Watanabe et al., 2018; Su et al., 2020; Perepezko et al., 2021] is one of the primary techniques used for contactless measurements, as shown in Figure 1-6. For this technique, a levitated coil generates a radio-frequency electromagnetic field and the Foucault current is induced into a sample. The accompanying electromagnetic induction generates heat to melt the sample. In the meantime, the formation of interaction between the magnetic field of the coil and the Foucault currents can counteract the gravity to levitate the sample. The levitated coil is located in the sample chamber with extremely high-purity gas (He). The temperature of the sample is controlled by changing the gas flow to the sample through a ceramic tube. The viscosity of liquid zirconium was investigated by electromagnetic levitation with the oscillation drop method [Su et al., 2020]. The density, spectral emissivity, heat capacity, and thermal conductivity of liquid Co were measured by the electromagnetic levitation technique in a static magnetic field [Watanabe et al., 2018]. However, the sample was limited to materials with electrical conductivity (metals, alloys, and semiconductors), using this method.

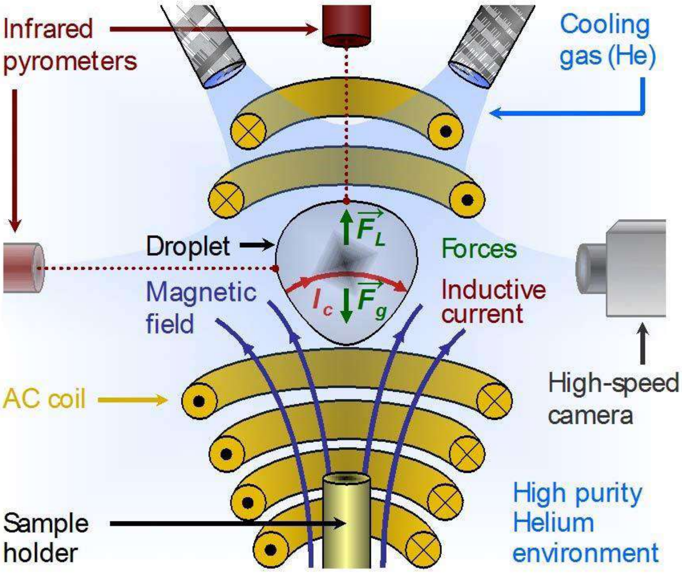

Figure 1-6. Schematics of electromagnetic levitation [Perepezko et al., 2021]

1.3.2.2 Electrostatic levitation

Electrostatic levitation [Rhim et al., 1999] is also a commonly useful tool for measuring the thermophysical properties of metals or alloys and its schematic image is shown in Figure 1-7 [Yoo et al., 2015]. With this technique, a sample is electrically charged and levitated in a vertical electrostatic field between two electrodes. There are two pairs of smaller electrodes on two sides which are performed to control the horizontal position of the sample. Lasers were carried out to heat the levitated sample in a high vacuum. The density, volume expansion coefficient, and ratio of specific heat to emissivity were successfully tested by electrostatic levitation [Du et al., 2018]. The Ni self-diffusion, density, and viscosity of $Zr_{64}Ni_{36}$ were measured by the technique of electrostatic levitation [Brillo et al., 2011]. Although some oxides without electrical conductivity can be measured by electrostatic levitation, most of the samples are metals or alloys.

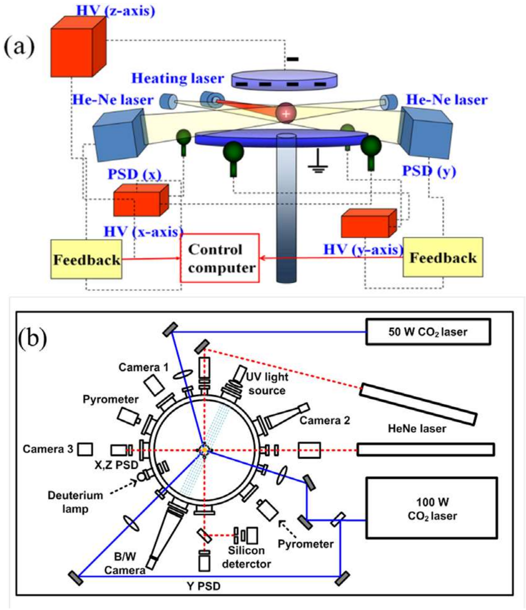

Figure 1-7. Schematic diagram of electrostatic levitation [Yoo et al., 2015]

1.3.2.3 Aerodynamic levitation

To overcome the challenge of oxide melts without electrical conductivity, aerodynamic levitation has been considered and developed as a promising approach in recent decades [Winborne et al., 1976; Weber et al., 1995; Hennet et al., 2017]. In aerodynamic levitation, a convergent-divergent nozzle in the levitation system channels a regulated gas flow upwards to counteract the gravity of a droplet [Hennet et al., 2011]. The droplet is levitated by adjusting the gas. The principle formula was shown in Eq. (1-13) [Benmore et al., 2017]:

$$Mg=C_d\int(\rho u^2+p)dA \qquad \text{Eq. (1-13)}$$

where C_d is the drag coefficient, ρ is the gas density, u is the gas flow velocity, p is the pressure drop, and A is the area of a sample.

Laser heating and sample levitation were successfully applied inside the Nuclear magnetic resonance to obtain NMR spectra of Al_2O_3-CaO liquids [Poe et al., 1994]. Moreover, Hennet et al. [Hennet et al., 2011] presented detailedly applications of aerodynamic levitation and laser heating at synchrotron and neutron sources, which perfectly solved sample contamination and temperature limitation. Furthermore, the droplet oscillation technique is based on Rayleigh theory [Rayleigh, 1879]. It describes oscillations of a spherical liquid droplet driven by its surface tension. It is widely applied in electromagnetic levitation to measure the surface tension and viscosity of liquid metals [Egry et al., 2005], which aroused the dawn of thermophysical properties measurements of oxide melts. Aerodynamic levitation combined with the droplet oscillation method and laser heating became a possible and valuable approach for measuring surface tension and viscosity of oxide melts. Finally, aerodynamic levitation combined with the droplet oscillation method, laser heating, an acoustic excitation system, a backlight source, and a high-speed camera was built [Langstaff et al., 2013; Kargl et al., 2015], as shown in Figure 1-8, where the acoustic excitation system was used to control the oscillation mode [Cummings et al., 1991; Ozawa et al., 2009; Langstaff et al., 2013] and the backlight source was to improve the contrast of the image recorded by the high-speed camera [Langstaff et al., 2013].

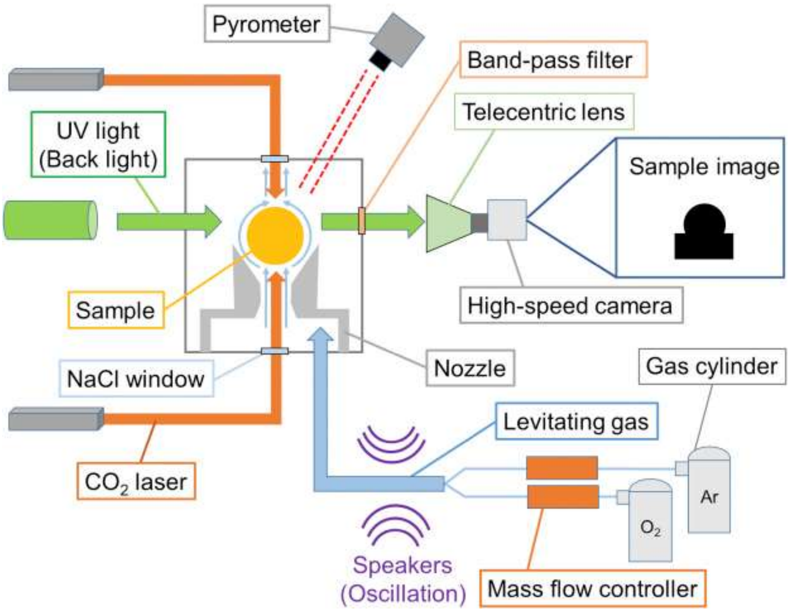

Figure 1-8. Schematic diagram of the laser aerodynamic levitator [Kondo et al., 2019].

The aerodynamic levitation apparatus is currently a better choice for measuring oxide melts without electrical conductivity since it does not limit the type of materials tested. Meanwhile, compared with electromagnetic levitation, the heating in the aerodynamic levitation apparatus is independent of the levitation system, which can decrease more or less experimental errors. And compared with electrostatic levitation, the measurement of the aerodynamic levitation apparatus is not vulnerable to interactions between a charged surface and an electrostatic field [Langstaff et al., 2013]. Recently, the viscosity or density of some oxide systems such as SiO_2-CaO-Al_2O_3 slags [Siafakas et al., 2018], liquid ZrO_2 [Kondo et al., 2019], and Al_2O_3-ZrO_2 molten materials [Ohishi et al., 2017], have been successfully measured during a wide temperature range by the aerodynamic levitation apparatus.

Although the aerodynamic levitation apparatus has been successfully built and applied in measurements of thermophysical properties of oxide melts, this apparatus still presents three unsolved problems. (i) It is difficult for pyrometers to determine the real temperature of oxide melts under high temperatures because their emissivity is generally unknown. That makes it extremely difficult to get an accurate correspondence between thermophysical properties and real temperature. (ii) Complete measurements involve different parameters, image-processing and -fitting, and calculations, which leads to the difficulty in estimating the uncertainty of the measurements. (iii) The principle of surface tension measured by the aerodynamic levitation apparatus is the Rayleigh theory [Rayleigh, 1879]. As a result, the measurement of surface tension is extremely sensitive to the Rayleigh frequency on the acoustic source, which causes the inaccuracy of measurements. That is why few papers have reported the surface tension of oxide melts measured by aerodynamic levitation with the droplet oscillation method during a wide temperature range.

1.4 Objectives of this study

The overall goal of the thesis is to contribute to

- improving measurements of the thermophysical properties of oxide melts, such as density, surface tension, and viscosity, using aerodynamic levitation;
- exploring the structural evolution of the CaO-Al_2O_3 system and the CaO-Al_2O_3-SiO_2 system on the atomic scale;
- describing the correlation between structural evolution and thermophysical properties.

Before performing the thermophysical properties, the levitation device was improved as well as the image and data processing to improve the thermophysical properties assessment accuracy.

The thermophysical properties were then measured on two groups of melts: the first group was based on the binary CaO-Al_2O_3 with molar compositions corresponding to 3CaO•Al_2O_3 (C3A), 12CaO•7Al_2O_3 (C12A7), CaO•Al_2O_3 (CA), and CA2 (CaO•2Al_2O_3), with C=CaO and A= Al_2O_3. The second group was based on the ternary CaO-Al_2O_3-SiO_2 with CaO/Al_2O_3=1 and SiO_2 weight content ranging from 0 to 25 wt.%.

Molecular dynamics calculations were carried out with LAMMPS software to determine the structure of each melt and extract some structural descriptors and relate the measured property trends to these descriptors.

1.5 Contents of the thesis

The outline of this thesis is as follows:

Chapter 2 is to describe the improvements in the measurements of the aerodynamic levitation apparatus, basic knowledge of classical molecular dynamics (MD), and calculation details of structural parameters. In Chapter 3, the results of the thermophysical properties of the CaO-Al_2O_3 system are listed. With the help of the previously reported structure measurements, the MD simulation with combined hybrid potential is verified to be appropriate for the CaO-Al_2O_3 system. We deeply demonstrate by MD simulations how temperature and R=CaO/Al_2O_3 variations affect the structural transformations of the CaO-Al_2O_3 system. Meanwhile, a preliminary attempt is to explain the correlation between structural evolution and thermophysical properties, based on structural parameters from MD simulations. The aim of Chapter 4 is to expand the binary oxide system to a ternary system (CaO-Al_2O_3-SiO_2) to further confirm the theoretical methods in Chapter 3, in particular, rationality and application of MD simulation with combined hybrid potential and the correlation between structural evolution and thermophysical properties in the CaO-Al_2O_3-SiO_2 system. In Chapter 5, the numerical models (Urbain model, FactSage®, MD) of viscosity are described and the viscosity data comparison between experimental measurements and simulations is shown, which provides a reference for experimental measurement and study on viscosity. The content of Chapter 6 is the conclusions for this thesis, unsolved problems, and perspectives of future research.

Chapter 2

Chapter 2. Method and Theory

Résumé du Chapitre 2

Dans ce chapitre, l'objectif principal est d'offrir aux lecteurs une compréhension claire des mesures de la lévitation aérodynamique. Pour ce faire, les principes et les processus de mesure de la densité, de la tension superficielle et de la viscosité ont été décrits en détail.

Par conséquent, le fond de la gouttelette lévitée est inévitablement protégé par la tuyère conique convergente-divergente lors des mesures. Reconstituer le bord de l'échantillon fondu et mesurer le diamètre horizontal et le diamètre vertical sont la condition préalable au calcul de la densité, de la tension superficielle et de la viscosité.

En outre, nous avons expliqué le mode d'oscillation lié aux mesures de la tension superficielle et de la viscosité, les corrélations entre la fréquence d'oscillation de la force, la fréquence d'oscillation de l'amortissement et les mesures de la tension superficielle et de la viscosité. On peut noter que lorsque la fréquence d'excitation n'est pas éloignée de la fréquence de résonance, le système atteint cette dernière presque instantanément. Ainsi, la comparaison de la fréquence forcée de l'oscillation harmonique et de la fréquence de résonance de l'oscillation d'amortissement, qui doivent être proches, peut être utilisée comme une indication de la validité de la mesure.

Pour optimiser les mesures et obtenir des données précises, il est nécessaire de traiter les images testées en vrac, d'estimer l'incertitude des mesures de la densité, de la tension de surface et de la viscosité, d'optimiser l'ajustement de la courbe pour obtenir des paramètres précis et de calculer la densité, la tension de surface et la viscosité.

Pour résoudre les problèmes ci-dessus, l'outil de post-traitement des données (une série de scripts Python) a été créé, basé sur l'algorithme de détection des bords de Canny, la méthode de Monte Carlo et les transformées de Fourier. L'outil de post-traitement des données a été utilisé pour:

- reconstituer le bord de l'ombre de l'échantillon de gouttelettes ;
- traiter les images de la caméra haute vitesse ;
- tracer et ajuster la courbe d'oscillation ;
- estimer l'incertitude des mesures de densité, de tension superficielle et de viscosité ;
- déterminer les fréquences des oscillations harmoniques et d'amortissement ;
- calculer la densité, la tension superficielle et la viscosité.

Parallèlement, les principes et concepts de base de la dynamique moléculaire classique ont été introduits, le choix de fonctions potentielles appropriées étant la clé des résultats corrects de la simulation MD. Le potentiel total associé au système du verre comprend des forces électrostatiques à longue portée (force coulombienne) et des forces à courte portée (contenant la force répulsive et la force attractive de Van der Waals). Les verres d'oxyde et d'halogénure présentant des caractéristiques de liaison ionique et covalente et leur physique à l'état solide ont pu être abordés via le modèle de Born. Le modèle de Born a été optimisé au cours des dernières décennies, où une répulsion de loi de puissance n-ième a été remplacée par une expression exponentielle. Les expressions combinées représentant à la fois la répulsion exponentielle et l'attraction dispersive sont connues sous le nom de potentiels de Born-Mayer-Huggins (BMH) ou de Buckingham. Cependant, seules les paires cation-anion se voyaient attribuer les interactions à courte portée dans le potentiel de Buckingham, alors qu'aucune interaction à courte portée n'était supposée entre les cations et les cations en raison de la longue distance de séparation entre eux. En fait, il existe une force de répulsion maximale qui sert de limite à une faible séparation atomique. Le potentiel BMH qui est homologue au potentiel de Buckingham a été appliqué pour résoudre la suppression de l'interaction à courte portée entre les cations et les cations dans Buckingham, en utilisant la forme de potentiels hybrides de LAMMPS. Dans ce travail, les potentiels hybrides combinés composés du potentiel de Buckingham et du potentiel BMH ont d'abord été appliqués aux interactions interatomiques.

Dans l'analyse de la simulation MD, la méthode de calcul de certains paramètres structurels, tels que les distributions d'angles de liaison, les facteurs de structure et les fonctions de distribution radiale, sont répertoriée. En même temps, l'outil de visualisation OVITO pro et l'outil de post-traitement des données (script Python) ont été utilisés pour calculer et analyser davantage la trajectoire atomique à partir des simulations MD.

Abstract of Chapter 2

In this chapter, the main goal is to offer readers a clear understanding on the measurements of aerodynamic levitation. For this goal, the principles and processes in measurements of density, surface tension, and viscosity were described in detail.

As a result, the bottom of the levitated droplet is inevitably shielded by the convergent-divergent conical nozzle in measurement. Reconstituting the edge of the molten sample and measuring the horizontal diameter and vertical diameter are the prerequisite for calculating the density, surface tension, and viscosity.

In addition, we explained the oscillation mode related to measurements of surface tension and viscosity, the correlations between force oscillation frequency, damping oscillation frequency, and measurements of surface tension and viscosity. It can be noted that when the excitation frequency is not far from the resonance frequency, the system will reach the latter almost instantaneously. Thus, comparing the forced frequency in the harmonic oscillation and the resonant frequency of the damping oscillation which should be close, can be used as an indication of the measurement validity. To optimize the measurements and obtain accurate data, it is necessary to process the tested images in bulk, estimate measurements uncertainty of density, surface tension, and viscosity, optimize the fitting of the curve to obtain precise parameters, and calculate density, surface tension, and viscosity.

To solve the above problems, the data post-treatment tool (a series of Python scripts) was created, based on the Canny edge detection algorithm, Monte Carlo method, and Fourier transforms. The data post-treatment tool was used to

- reconstitute the shadow edge of the droplet sample;
- process the images from the high-speed camera;
- plot and fit the oscillation curve;
- estimate the uncertainty of density, surface tension, and viscosity measurements;
- determine frequencies of harmonic and damping oscillations;
- calculate density, surface tension, and viscosity.

Meanwhile, basic principles and concepts of classical molecular dynamics were introduced, where choosing appropriate potential functions is the key to the correct results of MD simulation. The total potential associated with the glass system includes long-range electrostatic forces (Coulombic force) and short-range forces (containing repulsive force and Van der Waals attractive force). Oxide and halide glasses with ionic and covalent bonding characteristics and their solid-state physics could be approached via the Born model. The Born model was optimized over the past few decades, where an n-th power law repulsion was replaced by an exponential expression. Combined expressions representing both the exponential repulsion and the dispersive attraction were known as Born-Mayer-Huggins (BMH) or Buckingham potentials. However, only cation-anion pairs were given the short-range interactions in the Buckingham potential, whereas no short-range interaction was assumed between cations and cations due to the long separation distance between them. In fact, there is a maximum repulsive force that serves as the limit at low atomic separation. The BMH potential that is homologous with Buckingham potential was applied to solve the deletion in the short-range interaction between cations and cations in Buckingham, through utilizing the hybrid potentials form of LAMMPS. In this work, the combined hybrid potentials composed of Buckingham potential and BMH potential were first applied in interatomic interactions.

In the analysis of MD simulation, the calculated method of some structural parameters, such as bond angle distributions, structure factors, and radial distribution functions, are listed. At the same time, the OVITO pro visualization tool and data post-treatment tool (Python script) were used to further calculate and analyze atomic trajectory from MD simulations.

2.1 Aerodynamic levitation with the drop oscillation method

Laser aerodynamic levitation combined with the drop oscillating technique (ADL) is a novel device for measuring the thermophysical properties of melts, which integrates a levitation system, a laser heating system, a temperature monitor system, an acoustic oscillator system, and an image recording system [Hennet et al., 2007; Langstaff et al., 2013]. The schematic image of ADL used in this work was shown in Figure 2-1.

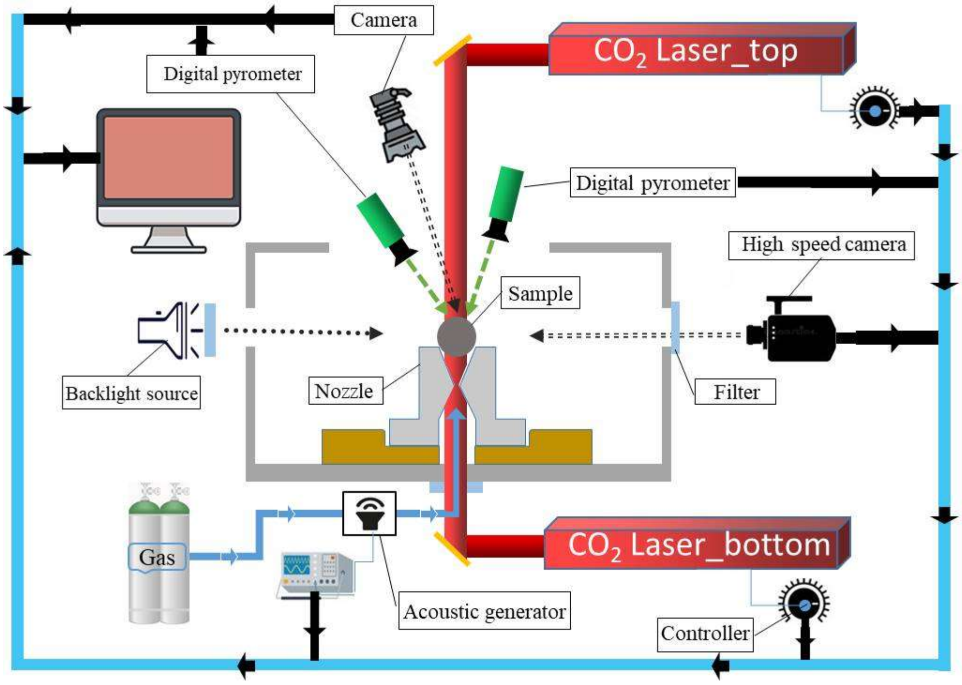

Figure 2-1. Schematic diagram of laser aerodynamic levitation.

The sample placed in a convergent-divergent conical nozzle was levitated by a mixture gas flow (20% O_2 and 80% Ar). The flow rate of the mixture gas is controlled by using a smart mass flow controller (Brooks Instrument, USA). The laser heating system consists of two CO_2 lasers with different powers (Synrad Evolution 240 W and 125 W) which are focused at the top and bottom of the sample, respectively, to prevent temperature gradient across the sample. The temperature of the sample is measured by using two digital pyrometers (Impac IN 140/5-H, $\lambda_1 = 5.14$ μm and IS 140-TV, $\lambda_2 = 0.9$ μm). The molten sample was excited with a conventional sine wave obtained by coupling the gas flow system with two speakers monitored by a function generator (GBF GF467AF). The excitation frequency was set to the resonant frequency of the sample and the molten sample was thus forced to harmonic oscillation. A calibrated high-speed camera (CamRecord-CR Series, Optronics) with a 2X telecentric lens allows the recording of the shadow of the sample with a resolution (pixel size) of about 4 μm×4 μm. For this study, backlighting with a cold light source was employed as this proved to be the most effective way to detect the edge of the small ball sample [Langstaff et al., 2013].

2.1.1 Temperature correction

The temperature of the sample is measured by using two digital pyrometers ($\lambda_1 = 5.14$ μm and $\lambda_2 = 0.9$ μm). In order to perform temperature correction, one should know the emissivity of the sample and correct the pyrometer accordingly. However, the emissivity of samples at high temperatures is generally unknown. Here, a common method of temperature correction is to observe a crystallization peak as the investigated substance solidifies. If the eutectic temperature is known and calculated for each sample by thermodynamic calculations, it is possible to correct the temperature assuming that the emissivity does not change over the temperature range during the cooling. The eutectic temperature ($T_{L,P}$), the pyrometer (T_P), and Wien's law [Krishnan et al., 1990] are used to correct temperature, where the formulas are as follows [Hennet et al., 2011; Ohishi et al., 2017]

$$\frac{1}{T}-\frac{1}{T_p}=\frac{1}{T_L}-\frac{1}{T_{L,p}} \qquad \text{Eq. (2-1)}$$

$$\frac{1}{T}-\frac{1}{T_p}=\frac{\lambda}{C_2}ln(\varepsilon_\lambda) \qquad \text{Eq. (2-2)}$$

where T_L is the melting point, T is the temperature correction, λ is the wavelength of the pyrometer, C_2 is Planck's second radiation constant, and ε_λ is the emissivity. Here the T_L was calculated by FactSage® 8.1 [Bale et al., 2016]. $T_{L,P}$ (eutectic temperature) is obtained from the free-cooling curve of the sample.

Taking CA2 as an example, Figure 2-2 shows the time-dependent temperature of CA2 measured by the pyrometer (λ_2 = 0.9 μm). The temperatures are kept constant before the heating lasers are off. The sample is cooled down rapidly by the levitated gas flow after the heating lasers are shut down. The emissivity of CA2 is calculated by Eq. (2-1) and Eq. (2-2), based on three free-cooling processes at different temperatures. The results show that the emissivity calculated in this way does not depend on the different initial temperatures and the slight changes in the flow rate.

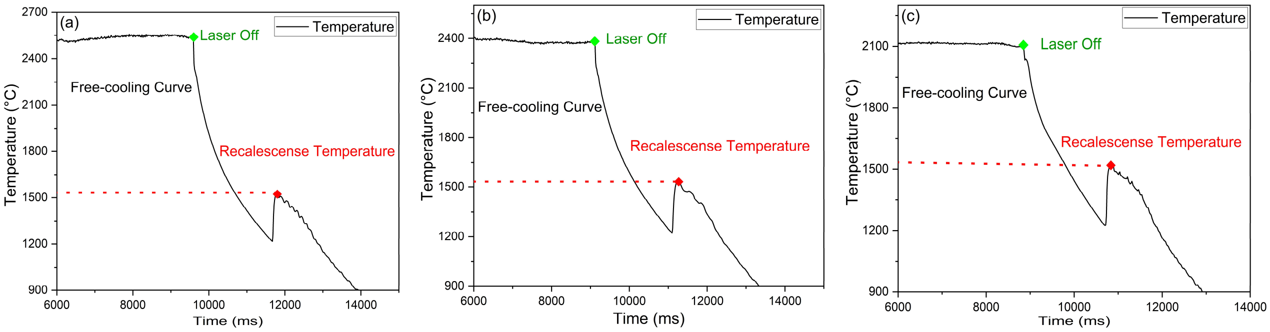

Figure 2-2. Cooling curves of the CA2 recorded by the pyrometers.

However, such crystallization peak is not observed during the cooling (the studied compositions form glasses at room temperature) and thus, the temperature could not be corrected. In this case, the measurement temperature was chosen as the apparent temperature of the pyrometer (λ_2 = 0.9 μm), since the glass samples were transparent and the emissivity of the tested samples was unknown. Furthermore, the wavelength range which is typically applied for temperature measurements of molten glass lies between 0.78-1.15 μm. In this range, whatever the emissivity, its temperature dependence may be assumed to be low. As a result, the pyrometer with 0.9 μm was assumed to be well applicable to measure the temperature of the tested glass samples. Meanwhile, the apparent temperature with the pyrometer is directly applied in data, which facilitates temperature correction in the future when the emissivity will be known.

2.1.2 The principles of measurements and calculations

The measuring principles and methods of the thermophysical properties are divided into two categories. The first category is to measure the surface tension and the viscosity at a constant temperature, where the principle and method of surface tension and viscosity are related. The second one is performed to measure the density along with the free cooling.

2.1.2.1 The measurement of surface tension and viscosity

The measurement of surface tension and viscosity of melts is based on the droplet oscillation technique [Egry et al., 2005]. For a spherical free-force droplet, the relationship between surface tension γ and oscillation frequencies f is expressed in Eq. (2-3), namely Rayleigh theory [Rayleigh, 1879; Egry et al., 2005],

$$f_l^2 = l(l-1)(l+2)\frac{1}{3\pi}\frac{\gamma}{M} \qquad \text{Eq. (2-3)}$$

where l is the mode of asphericity and rotational motion, and M is the droplet mass. This formula provides the basis of the droplet oscillation technique. The levitated droplet is acted to both the gravity and the levitated force of equal size but in opposite directions. These two forces cancel each other out only when integrated over the volume of the droplet. However, there are still residual forces present along the droplet surface, causing the droplet deformation to invalidate the sphere assumption [Egry et al., 2005]. So in measurements of surface tension and viscosity, the stable droplet is assumed to be spherical.

Determining oscillation frequency and the mode of asphericity rotational motion is a precondition to calculating surface tension γ. The droplet shows axisymmetric oscillations [Rhim et al., 1999] when $l = 2$, corresponding to Rayleigh frequency. The frequency of $l = 2$ modes could be split into three corresponding to $m = 0, \pm1, \pm2$ oscillations which are shown in Figure 2-3 [Cummings et al., 1991; Ozawa et al., 2009]. By sweeping through a range of frequencies with high-speed camera imaging, a resonance spectrum can be obtained from which ($l = 2$, $m = 0, \pm1, \pm2$)-mode frequencies can be determined [Langstaff et al., 2013]. When the droplet is excited by the primary resonant frequency, the oscillation mode is $l = 2$, $m = 0$. Its oscillation characteristic is most easily observed by the eyes, where horizontal and vertical motions of the droplet exhibit a 90° phase shift, as shown in Figure 2-4(a).

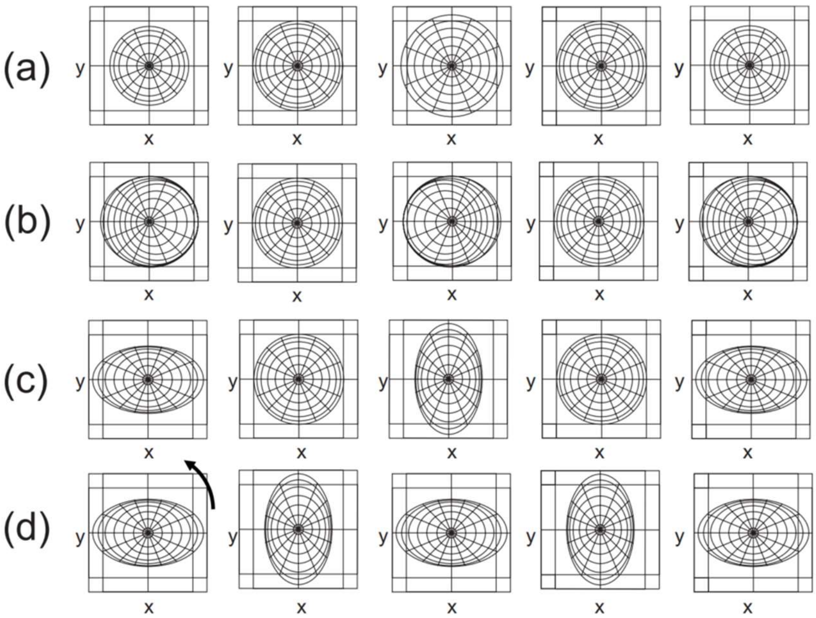

Figure 2-3. Images of $l = 2$, ($m = 0, \pm1, \pm2$) oscillations and rotation from the top view. (a) $m = 0$, (b) $m = \pm1$, (c) $m = \pm2$, and (d) rotation [Ozawa et al., 2009].

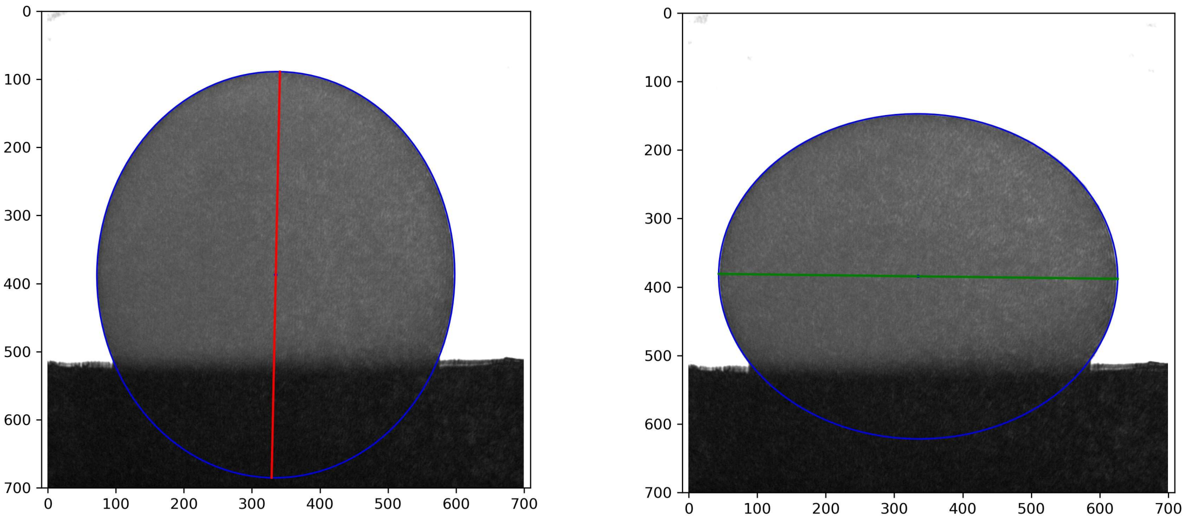

(a) (b)

Figure 2-4. Images of oscillation from the front view.

When $l = 2$, Eq. (2-3) can be simplified into Eq. (2-4), as shown below:

$$\gamma = \frac{3}{8}\pi f_R^2 M \qquad \text{Eq. (2-4)}$$

where f_R is the resonance frequency.

In the droplet oscillation theory, there is a relationship between viscosity η of the spherical droplet and the damping constant Γ of the resonant surface oscillation ($l = 2$, $m = 0$) [Lamb, 1881; Langstaff et al., 2013], as follows:

$$\eta = \frac{3M\Gamma}{4\pi r_0(l-1)(2l+1)} = \frac{3M\Gamma}{20\pi r_0} \qquad \text{Eq. (2-5)}$$

where r_0 is the radius of the oscillated sphere in rest states, M is the droplet mass, and ρ is density. In order to determine the damping constant Γ, the droplet is excited by primary resonant frequency f_R for several seconds, and then the acoustic excitation was shut down. Correspondingly, the droplet resonant oscillation transforms into the decay oscillation. The high-speed camera was set to 2000 fps to the transient whole process of the droplet sample, taking a series of pictures, like Figure 2-4. Pictures of the droplet states are then analyzed for horizontal and vertical diameters, r_h and r_v, respectively. Here, the time-dependent amplitude of horizontal diameter is taken as an example to explain how some calculated parameters are obtained, as shown in Figure 2-5. It displays that the liquid sample was excited by the acoustic source to do harmonic oscillation until around 0.18s.

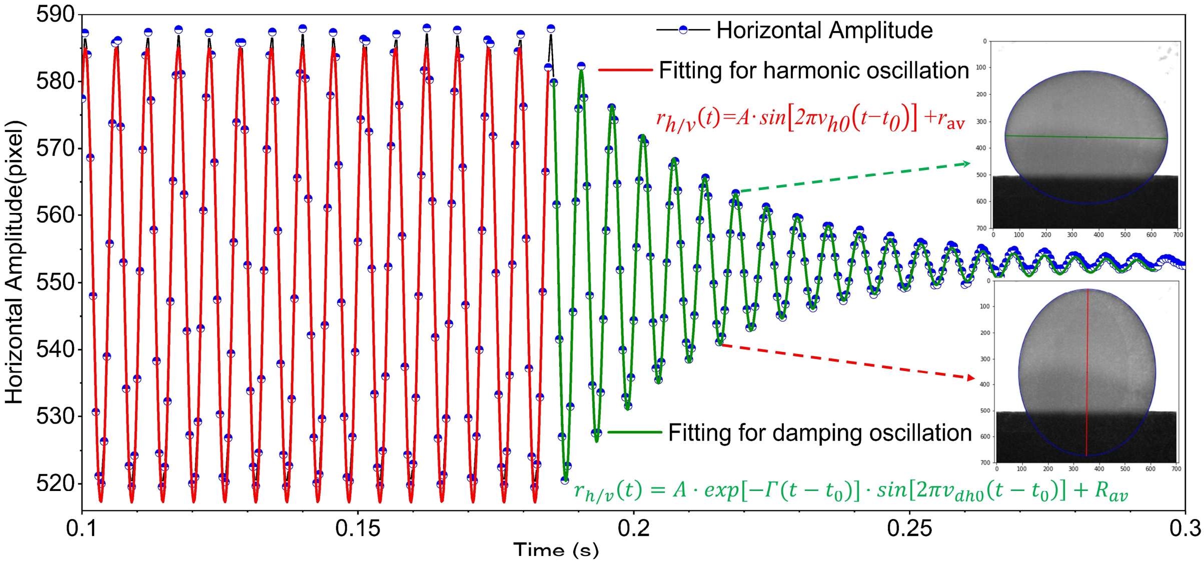

Figure 2-5. Time-dependent horizontal amplitude of the droplet in the oscillation and the damping decay. The red and green curves show the fitted results of resonant oscillation and damping oscillation, respectively.

The harmonic oscillation was represented by Eq. (2-6) [Langstaff et al., 2013], where A is the amplitude, v_{h0} is the excitation frequency, r_{av} is the mean sample radius, and t_0 is an offset.

$$r_{h/v}(t)=A\cdot sin\,[2\pi v_{h0}(t-t_0)]+r_{av} \qquad \text{Eq. (2-6)}$$

Here the resonant frequency of the droplet can be determined by the oscillation of the sample droplet. As soon as the acoustic excitation is turned off, the liquid sample is immediately subjected to damped oscillation. Eq. (2-7) expresses the damped decay, where Γ is the damping constant of the resonant oscillations, A is the same constant as in Eq. (2-6), v_{dh0} is the resonant frequency for the droplet sample, R_{av} is the radius of the droplet sample in rest, t_1 is the start time for damping decay [Langstaff et al., 2013].

$$r_{h/v}(t)=A\cdot exp[-\Gamma(t-t_1)]\cdot sin\,[2\pi v_{dh0}(t-t_0)]+R_{av} \qquad \text{Eq. (2-7)}$$

It can be noted that when the excitation frequency is not far from the resonance frequency, the system will reach the latter almost instantaneously. Thus, comparing the forced frequency (f_n) in the harmonic oscillation and the resonant frequency of the damping oscillation which should be close, can be used as an indication of the measurement validity. Utilizing fittings of Eq. (2-6) and Eq. (2-7) on the curve, obtained the primary resonant frequency v_{dh0} and the damping constant Γ can be used in Eq. (2-4) and Eq. (2-5), respectively, to calculate the corresponding the surface tension γ and viscosity η.

2.1.2.2 Density measurement

Time-dependent density (ρ) was measured by shutting down the lasers and letting the molten droplet cool freely. The frame rate of the high-speed camera was set at 500 fps and the temperature of the molten droplet was recorded simultaneously. The mass of each sample was tested before and after the measurement to check the mass loss. It was assumed that the droplet was an ellipsoid with the vertical axis being the revolution axis and alternatively, the horizontal and vertical axis corresponding to oblate and prolate spheroid, respectively, as shown in Figure 2-4(b).

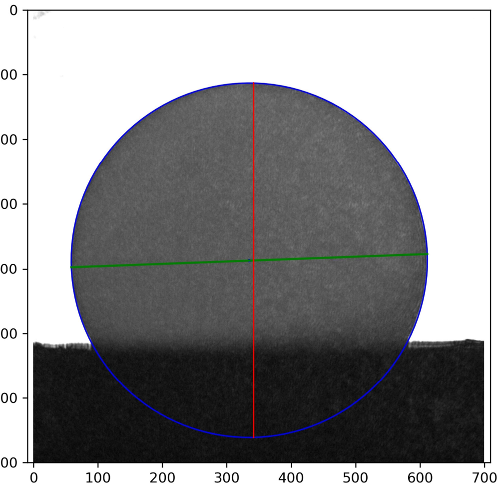

Figure 2-6. One of the images recorded by the high-speed camera and post-processed. The droplet is assumed to be an oblate or prolate spheroid (green axis) with its revolution axis vertical (red axis).

The density was calculated from the mass (M) and volume (V) of each sample. The equation of ρ is described as Eq. (2-8).

$$\rho = \frac{3M}{4\pi r_{\mathrm{h}}^{2} r_{\mathrm{v}}} \qquad \text{Eq. (2-8)}$$

where r_h and r_v are the horizontal radius and vertical radius, respectively.

2.1.3 Optimization of data-processing

Due to the shape of the convergent-divergent conical nozzle, the bottom of the levitated droplet is inevitably shielded by the nozzle. Reconstituting the edge of the molten sample and measuring horizontal diameter (d_h) and vertical diameter (d_v) is the prerequisite for calculating the density, surface tension, and viscosity. The Canny edge detection with a multi-stage algorithm is widely used in computer vision to locate intense gradient magnitude changes and to obtain object edges in images [Canny, 1986; Ding et al., 2001; McIlhagga, 2011], which is selected as the detector using for reconstituting and obtaining the horizontal and vertical diameters of the droplet. In addition, whether the forced frequency equals resonant frequency is a critical condition for the success of measurements for surface tension and viscosity, based on analyzing the principles of the droplet method. However, the resonant frequency of material is influenced by many factors, such as temperature, size, composition, and mass. Labview® as the previous method of data processing does not include the detection of oscillation frequencies and calculations. Relying on the characteristics of the oscillation (l = 2, m = 0) judges the forced frequency used, which causes the greater experimental error. In consideration of the relation between the forced frequency of the harmonic oscillation and the frequency of the damped oscillation and its influence on measurements, developing a method for extracting and calculating the two frequencies from the harmonic oscillation and the damped oscillation was necessary. To solve the above problems, Python scripts were developed for detecting the edge of the droplet and the determination of resonant frequency, based on the Canny edge detector with a multi-stage algorithm [Canny, 1986], Fourier transform [Strang, 1993], and Lorentz function [Carothers et al., 1993].

Figure 2-7 shows the forced frequency of harmonic oscillation, the frequency of the damping part, and the comparison of frequencies determined by the Python scripts. With the help of Figure 2-7, the experimental result of each sample can be optimized to the maximum extent, which ensures the accuracy of measurements and reduces the experimental error.

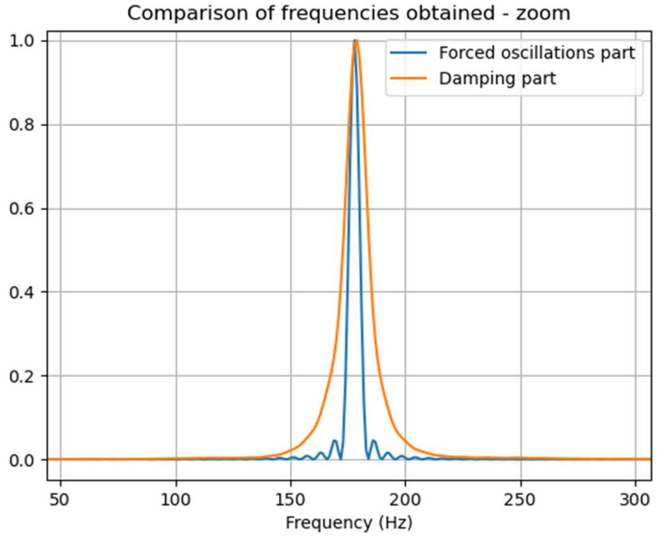

Figure 2-7. The comparison between forced frequency and damping frequency of the droplet.

Meanwhile, the scripts can call the functions of droplet contour detection and curve fitting. The schematic diagram of the droplet contour detection and the principle of data processing are shown in Figure 2-4 and Figure 2-5, respectively, where the blue circle is used for predicting the outline of the droplet, and the red and green lines are utilized for detecting the horizontal and vertical diameters, respectively. Here, taking the data post-treatment of C12A7 ($12CaO•7Al_2O_3$) as an example, the final schematic diagram of fitting horizontal amplitude at the harmonic oscillation and at the damping decay is shown in Figure 2-8, which can verify the application and precision of the scripts.

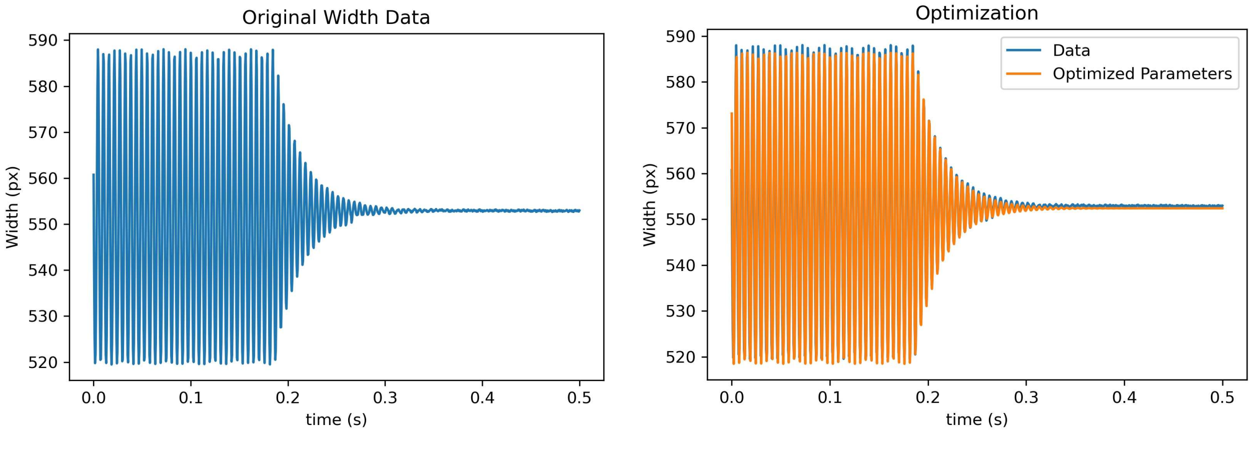

(a) (b)

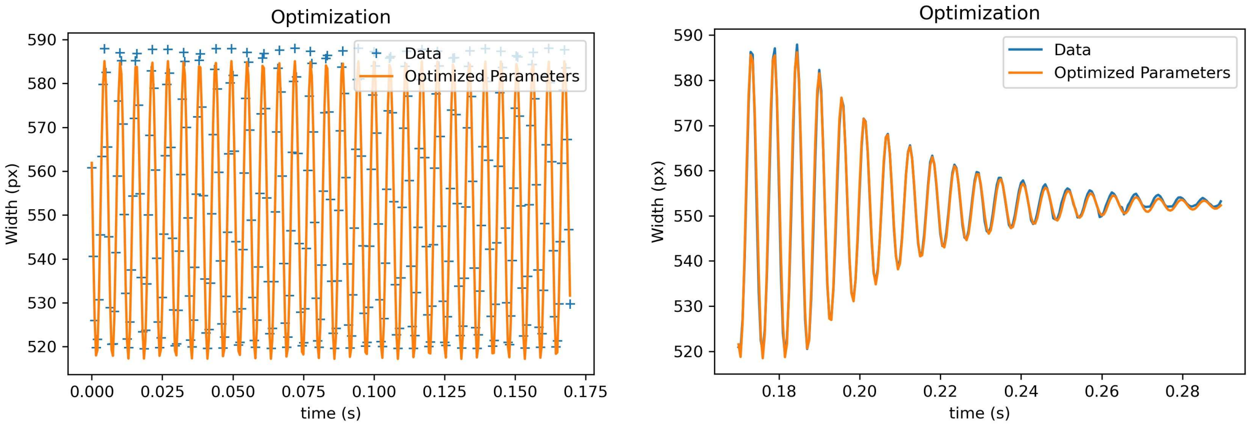

(c) (d)

Figure 2-8. Fittings of the droplet horizontal amplitude: (a) original data, (b) the whole fitting, (c) the fitting of harmonic oscillation, and (d) the fitting of damping oscillation.

2.1.4 Uncertainty on the measurements of density, surface tension, and viscosity.

2.1.4.1 Uncertainty of calibration factor

The high-speed camera is responsible to record the state of the sample droplet in real-time. The calibration of the high-speed camera which is utilized for determining the diameter of the sample droplet is an urgent problem to be solved.

At first, three standard steel balls (diameters: 1.8, 2.0, and 2.5 mm) and a nozzle with an angle of 60° (N60) are used in the calibration of the high-speed camera. Table 2-1 detailedly records the gas flow used in calibration and the diameters of the balls in pixels measured.

There is a linear equation between the real diameter (d_{real}: mm) and the measured diameter (d_{mea}: pixel), as shown in Eq. (2-9) and named as calibration function,

$$d_{real}=k\bullet d_{mea} \qquad \text{Eq. (2-9)}$$

where k is the calibration factor.

Table 2-1. Real diameters of the steel beads and measured diameters in pixels with standard deviation for the calibration of horizontal and vertical diameters.

Nozzle	Standard ball (mm)	Gas flow (%)	Horizontal diameter (d_h, pixel)	Standard deviation on d_h (σ_h, pixel)	Vertical diameter (d_v, pixel)	Standard deviation on d_v (σ_v, pixel)
N60	1.8	75	439	1.0	431	3.2
		85	440	1.3	436	4.0
	2	25	488	2.1	482	7.0
		30	489	2.5	483	9.3
		40	488	1.7	482	5.4
		50	489	1.7	483	6.0
	2.5	0	612	0.1	609	0.5
		20	613	1.2	607	7.2
		25	613	0.6	608	3.7
		30	613	0.4	610	1.9
		50	613	0.4	610	1.9

Figure 2-9 shows the relationship between the measured (in pixel) and real (in mm) diameters, where the calibrated result is a resolution (pixel size) of about 4.09 µm×4.12 µm.

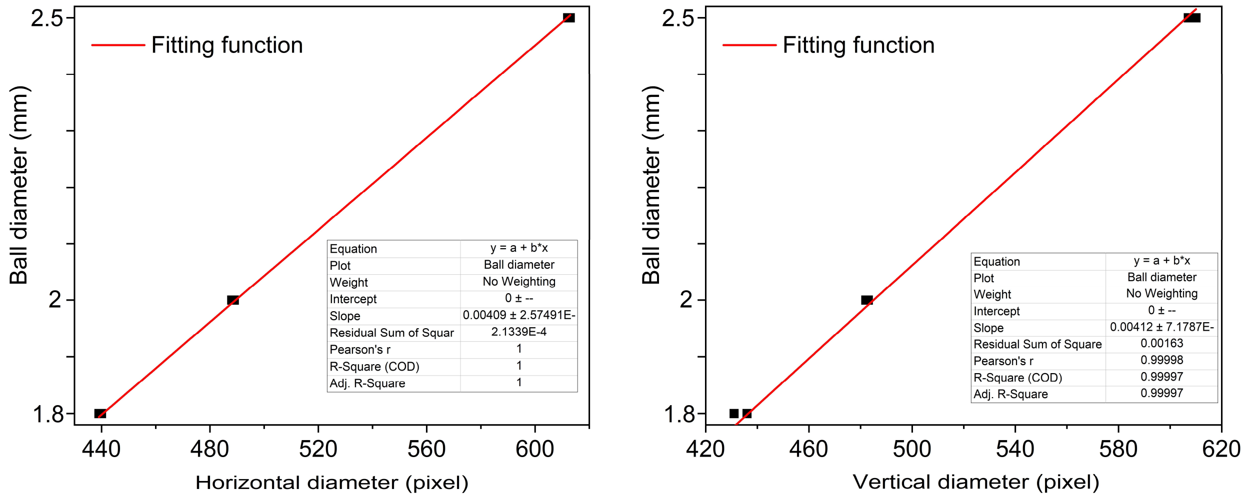

Figure 2-9. Relationship between the measured (in pixel) and real (in mm) diameters of the standard balls.

Furthermore, the standard deviation of *k* can be expressed as:

$$\sigma_k = \frac{\sigma_{d_{mea}}}{\sqrt{\sum n_i d_i^2}} \qquad \text{Eq. (2-10)}$$

where σ_{dmea} is the standard deviation of the measured diameter, n_i is the number of calibrations for the steel balls, and d_i is the real diameter of the steel balls. The slope of the calibration function can be expressed as $k \pm \sigma_k$. The uncertainty for the calibration factor is given as

$$u_k = \frac{1}{2}\left(\left|k - \frac{1}{k+\sigma_k}\right| + \left|k - \frac{1}{k-\sigma_k}\right|\right) \qquad \text{Eq. (2-11)}$$

Therefore, based on the uncertainty of the calibration factor u_k, corresponding to the uncertainties of the horizontal diameter and the vertical diameter are estimated into $u(h)$=0.19 % and $u(v)$=0.52 %, respectively.

2.1.4.2 Uncertainty of density

Estimating the uncertainties of measurements of density, surface tension, and viscosity is the ultimate objective after solving the uncertainty of the calibration factor. Following the guide to the expression of uncertainty in measurement (GUM method) [BIPM, 2008], the uncertainty of density can be derived from Eq. (2-8), which is estimated from uncertainties on the horizontal radius, the vertical radius, and mass of the sample droplet. Here the uncertainty of the density $u^2(\rho)$ is expressed as:

$$u^2(\rho) = \left(\frac{\partial \rho}{\partial M}\right)^2 u^2(M) + \left(\frac{\partial \rho}{\partial r_h}\right)^2 u^2(r_h) + \left(\frac{\partial \rho}{\partial r_v}\right)^2 u^2(r_v) \qquad \text{Eq. (2-12)}$$

$$\left(\frac{u(\rho)}{\rho}\right)^2 = \left(\frac{u(M)}{M}\right)^2 + \left(\frac{2u(r_h)}{r_h}\right)^2 + \left(\frac{u(r_v)}{r_v}\right)^2 \qquad \text{Eq. (2-13)}$$

where $u(M)$ is the uncertainty of the sample weight and is derived from the balance characteristics. $u(r_h)$ and $u(r_v)$ are the uncertainty of the vertical and horizontal radii of the sample droplet, respectively. They are derived from the image processing including the edge detection and the image dimension (pixel) to real dimension (mm) conversion with the calibration factor.
The uncertainty of the radii is evaluated as follows:

$$r_i = k_i p_i \qquad \text{Eq. (2-14)}$$

where i is h or v; r_i is the radius in real dimension; p_i is the radius of the image dimension (pixel).

$$\left(\frac{u(r_i)}{r_i}\right)^2 = \left(\frac{u(k_i)}{k_i}\right)^2 + \left(\frac{u(p_i)}{p_i}\right)^2 \qquad \text{Eq. (2-15)}$$

where $u(k_i)$ is the uncertainty of the calibration factor and has been evaluated above and $u(p_i)$ is the uncertainty of the radius in image dimension and results from the edge detection.

The uncertainties on the detection of the horizontal and vertical radii in the image dimension of the droplet are estimated by the Python script based on the Monte Carlo method [Metropolis et al., 1949] and the Canny edge detector with a multi-stage algorithm. The results show that the relative standard uncertainties are far less than the relative standard uncertainties of the calibration factors:

$$\left(\frac{u(p_i)}{p_i}\right)^2 \ll \left(\frac{u(k_i)}{k_i}\right)^2 \qquad \text{Eq. (2-16)}$$

Finally, the uncertainty of density is expressed as:

$$\left(\frac{u(\rho)}{\rho}\right)^2 = \left(\frac{u(M)}{M}\right)^2 + \left(\frac{2u(k_h)}{k_h}\right)^2 + \left(\frac{u(k_v)}{k_v}\right)^2 \qquad \text{Eq. (2-17)}$$

Table 2-2 summarizes the elementary calculations to determine the density measurement uncertainty. The nominal values chosen for the calculation correspond to typical values measured in our experiments. The coverage factor has been chosen to $k = 2$ for the relation between the extended and the standard uncertainties to get a confidence interval of about 95%: $U(X)=ku(X)$.

Table 2-2. Uncertainty budget for the calculation of the density measurement uncertainty

	Value	U(X)	u(X)	$(\frac{u(X)}{X})^2$	$\frac{u(X)}{X}$
M (mg)	20	0.1	0.05	6.25E-6	0.25%
k_h (µm/pixel)	4			3.71E-6	0.19 %
kv (µm/pixel)	4			2.70E-5	0.52 %
ρ (g/cm^3)				4.81E-5	0.69 %

2.1.4.3 Uncertainty of surface tension

Based on Eq. (2-4), the uncertainty of surface tension involves the uncertainties of the mass $u(M)$ and forced frequency $u(f_n)$ of the sample droplet, as expressed:

$$\left(\frac{u(\gamma)}{\gamma}\right)^2=\left(\frac{u(M)}{M}\right)^2+\left(\frac{2u(f_n)}{f_n}\right)^2 \qquad \text{Eq. (2-18)}$$

It is worth noting that the surface tension and its measurement uncertainty do not depend on the sample size. The uncertainty of frequency is assumed to be equal to the resolution of the function generator (1 Hz), and the uncertainty of the mass has been estimated previously.

Table 2-3 summarizes the elementary calculations to determine the surface tension measurement uncertainty. Here again, the nominal values chosen for the calculation correspond to typical values measured in our experiments and the coverage factor has been chosen to $k = 2$ for the relation between the extended and the standard uncertainties to get a confidence interval of about 95%: $U(X)=ku(X)$.

Table 2-3. Uncertainty budget for the calculation of the surface tension measurement uncertainty

	Value	U(X)	u(X)	$(\frac{u(X)}{X})^2$	$\frac{u(X)}{X}$
M (mg)	20	0.1	0.05	6.25E-6	0.25 %
f_n (Hz)	200	1	0.5	6.25E-6	0.25 %
γ (N/m)				1.25E-5	0.35 %

2.1.4.4 Uncertainty of viscosity

The same reasoning can be applied to the viscosity measurement, where the uncertainty of viscosity is expressed by:

$$\left(\frac{u(\eta)}{\eta}\right)^2=\left(\frac{u(M)}{M}\right)^2+\left(\frac{u(\Gamma)}{\Gamma}\right)^2+\left(\frac{u(r_0)}{r_0}\right)^2 \qquad \text{Eq. (2-19)}$$

The uncertainty of viscosity depends on the uncertainties of mass $u(M)$, the damping constant $u(\Gamma)$, and the average radius of the spherical droplet $u(r_0)$. The calculation of r_0 is given as

$$r_0=\frac{r_h+r_v}{2} \qquad \text{Eq. (2-20)}$$

As it has been observed the uncertainties of r_h and r_v are very close (Uncertainty of density), the uncertainty of r_0 may be assumed equal to them.

However, there is currently no proper solution for the uncertainty of Γ. This value $(\frac{u(\Gamma)}{\Gamma})^2$ is temporarily ignored before the problem is solved.

Similarly, Table 2-4 summarizes the elementary calculations to estimate the viscosity measurement uncertainty.

Table 2-4. Uncertainty budget for the calculation of the viscosity measurement uncertainty

	Value	U(X)	u(X)	$(\frac{u(X)}{X})^2$	$\frac{u(X)}{X}$
M (mg)	20	0.1	0.05	6.25E-6	0.25 %
r_0 (mm)				3.71E-6	0.19 %
η (Pa•s)				9.96E-6	0.31 %

So far, a series of scripts for optimizing data processing that integrated precise image processing, the estimation of uncertainties, the comparison of frequencies, curve fitting, and calculations of density, surface tension, and viscosity were created.

2.2 Molecular dynamic simulation

2.2.1 Introduction of classical molecular dynamics

Classical molecular dynamic (MD) is a computer simulation method that is used to study the physical motion of atoms and the evolution of the atomic configuration of a complicated system. The velocities, positions, and trajectories of atoms and molecules are determined by numerically integrating Newton's second law of motion [Leach, 1996].

$$F(t)=ma(t)=m\frac{d^2r(t)}{dt^2} \qquad \text{Eq. (2-21)}$$

Boltzmann's formulations of statistical mechanics relate the trajectories of atoms to equilibrium thermodynamic properties. Linear response theory can extract time-dependent properties such as transport properties. The Hamiltonian of a system is its total energy which equals the sum of kinetic energy and potential energy. It is derived from the potentials or force fields which include all the electronic, ionic, and electron-ion interactions and depends on the positions of atoms. In MD simulations, a system can be researched at an atomic resolution on short time- (femtosecond, picosecond, microsecond) and length- (angstrom) scales and the processes and mechanisms in the system do not need to be assumed. The most noteworthy is that thermodynamic properties of the system depicting the driving force for atomic interactions are obtained by MD simulations, which can express the energetic relationships between different possible states of the system. MD simulations based on experimental conditions, correct parameters, and reasonable settings, may lead to the discovery of new physical mechanisms [Goodman, 2015]. So the classical MD simulation is a bridge between theory and experiments, occupying an important position in biology, chemistry, and materials science. It is also widely applied in the study of glass structure [Pedone, 2009].

2.2.2 The Algorithm of molecular dynamics

It is extremely difficult for the Newton equation of a multi-particle system to be solved analytically, so one needs to find a solution with the help of the numerical integration method. In this case, the finite difference method can be performed to solve the equation of motion.

To solve Eq. (2-21), forces on each particle are specified in a form of the potential energy functions, as shown below:

$$F(r(t)) = -\nabla U(r(t)) \qquad \text{Eq. (2-22)}$$

Eq. (2-21) is integrated by the Velocity Verlet algorithm [Swope et al., 1982] which uses the Taylor series expansion to define positions, velocities, and forces at time t ± δt as shown in Eq. (2-23) and Eq. (2-24) below:

$$r(t+\delta t)=r(t)+\delta v(t)+\frac{1}{2m}F(t)\delta t^2 \qquad \text{Eq. (2-23)}$$

$$v(t+\delta t)=v(t)+\frac{1}{2m}[F(t+\delta t)+F(t)]\delta t^2 \qquad \text{Eq. (2-24)}$$

The Velocity Verlet algorithm needs to store the coordinates, velocities, and forces of each time step. The time step of this algorithm involves two time steps which are necessary to calculate the force after a coordinate update and before a velocity update. Compared with the Verlet algorithm and the Leap-frog algorithm, the Velocity Verlet algorithm is the best in accuracy and stability, which is the one preferred by many MD packages, such as LAMMPS, DL_POLY, and GROMACS.

2.2.3 Boundary condition

MD simulations are generally applied in small systems with an appropriate number of particles, due to the limitation of the computing power. This results in the so-called “size effect” in which the simulated system has fewer particles than the real one. To reduce the impact of the size-effect problem, MD simulations usually use periodic boundary conditions which divide into one, two, and three dimensions. For molecular dynamics simulation, the selection of appropriate boundary conditions requires considering two aspects. First, in order to decrease the amount of computation, the simulated cell should be as small as possible, and the simulated cell should be large enough to exclude any possible dynamic disturbance that may affect the results. In addition, the simulated cell must be large enough to satisfy the reliability requirements of statistical processing. Secondly, physical coupling problems such as volume change, strain compatibility, and systemic stress balance should be considered.

For most of the simulations discussed in this thesis, the MD simulations of glass melt focus on structural evolution and the calculations of thermophysical properties. Meanwhile, the simulation objects are macromolecular liquids. The periodic boundary condition was therefore optimum for MD simulations in this work.

2.2.4 Ensemble theory

MD is at heart a statistical mechanics technique: the MD trajectory is an effort to sample the ensemble microstates, that is the different atomic configurations [Du et al., 2022]. Molecular dynamics includes equilibrium and non-equilibrium simulation, which must be carried out under a certain ensemble. According to the characteristics of the research object, the ensemble commonly used includes the microcanonical NVE ensemble, the canonical NVT ensemble, and the isothermal-isobaric NPT ensemble.

The microcanonical NVE ensemble is a statistical ensemble that is isolated and has no exchange of energy between the particles and the environment. In this ensemble, the number of particles N, the systemic volume V, and the total energy of the system are constant. Although microcanonical integration provides a very convenient framework for studying the evolution of systems, this ensemble is not commonly used to derive system properties, because of the difficulty to obtain experimentally an isolated system.

The canonical NVT ensemble shows possible microstates of a closed system that are in thermal equilibrium with a surrounding heat bath of fixed temperature [Du et al., 2022]. In the NVT ensemble, the number of particles N, the systemic volume V, and temperature T are constant. and the total energy of the system is zero. The closed system can exchange heat either with the environment or with other systems that are described by any ensemble at the same temperature and it can describe real systems more accurately than the microcanonical NVE ensemble.

The isothermal-isobaric NPT ensemble as a common ensemble is used in MD simulations of homogenous liquids, where the number of particles N, the systemic pressure P, and the systemic temperature T remain constant, allowing the volume and the total energy to change., The pressure value can be adjusted by the volume of the scaling system since the pressure P of the system is conjugate with its volume V. At present, many methods of regulating pressure are based on this principle.

For various simulation purposes, different ensembles can be generally used in combination for simulations. The NVT ensemble and the NVE ensemble were applied in different relaxation stages for studying the structure of Strontium Aluminosilicat glass [Charpentier et al., 2018]. Hu et al [Hu et al, 2020] predicted the densities and elastic moduli of SiO_2-based glasses by MD simulations. And NVT, NPT, and NVE ensembles all were employed in his simulated process. In this thesis, NVT and NPT ensembles were employed in the simulated process, considering the real experimental condition and calculations of thermophysical properties.

2.2.5 A new-form hybrid potential applied in MD simulations

2.2.5.1 Born model

In the classical non-quantum simulations, the nature of bonds between atoms in solids is the key to understand the interatomic forces at work in materials. For oxide and halide glasses, the bonding is a mixture of ionic and covalent characters, and their solid-state physics can be approached via the Born model [Born et al., 1955; Born et al., 1988; Du et al., 2022].

Inorganic glass-forming materials generally may exhibit ionic and covalent bondings. For instance, the common Si-O bond is quite rigorously shown in the electron-sharing nature of covalent bonds, and the [SiO_4] tetrahedral structure is a demonstration of predominantly covalent bonding. Meanwhile, the sharing of electrons between Si and O atoms is not complete. The atoms in silicates tend to have a residual net charge, which is the reason for glass-forming materials with ionic-covalent bonding [Du et al., 2022]. Moreover, alkali and alkaline earth modifiers are stronger cationic, which exhibit ionic bonding in glasses. The mixed ionic-covalent nature of bonding in inorganic solids atomistic simulations forms the basis of the Born model of solids [Du et al., 2022].

In the Born model, atoms are defined as point charges where short-range forces and Coulombic forces are acting between atoms. The total energy of the structure is generally named the lattice energy which can be represented as below:

$$E_{lattice} = \sum \frac{q_i q_j}{r_{ij}} + \sum V(r_{ij}) + \sum U(\theta_{ijk}) + \sum W(\delta_{ijkl}) + \cdots \qquad \text{Eq. (2-25)}$$

where the first term expresses Coulombic interactions; the second term is pair interactions of atoms, which is the largest contribution to the overall lattice energy; the third and fourth terms represent bond-bending and torsional bond energy contributions.

The atoms are charged in the Born model, which is its key feature, compared with the models of rare gas or fluids. That would need to calculate a large number of electrostatic interactions. In addition, the parameter $1/r$ associated with the long-range coverage is mathematically slow to converge. The calculation of Coulombic forces is likely the most time-consuming process in evaluating the lattice. In this thesis, the Ewald summation [Ewald, 1921; Ziman, 1972] which takes advantage of the periodic lattice structure to rearrange the expression for the total energy into a readily evaluated form was utilized to solve the mathematical problem of the slow converging sum $\sum q/r$.

2.2.5.2 Potential

In classic MD simulations, the total potential associated with the glass system includes long-range electrostatic forces and short-range forces. As noted above, Coulombic force is the long-range interaction between charged atoms. For efficient MD simulations, the cutoff for long-range interactions is restricted to 12 Å.

The short-range interactions contain repulsive force and Van der Waals attractive force. The generation of the repulsive force is derived from the overlap of electron clouds (Pauli Exclusion Principle). Induced dipole moments cause Van der Waals interaction. The short-range interactions are generally specified by empirical potential energy functions. So appropriate interatomic potentials are crucial to successful MD simulations of glasses.

The Born model was optimized over the past few decades, where an n-th power law repulsion was replaced by an exponential expression. Combined expressions representing both the exponential repulsion and the dispersive attraction were known as Born-Mayer-Huggins (BMH) [Born et al., 1932; Huggins et al., 1933] or Buckingham [Buckingham, 1937] potentials. The BMH and the Buckingham potentials were widely used in MD simulations of oxide systems, such as the CaO-Al_2O_3-TiO_2 system [Jakse et al., 2021], the CaO-Al_2O_3-SiO_2 system [Bouhadja et al., 2013], the SrO -Al_2O_3-SiO_2 system [Charpentier et al., 2018], etc.

The Buckingham potential and BMH potential are shown in Eq. (2-26) [Charpentier et al., 2018] and Eq. (2-27) [Jabraoui et al., 2017], respectively.

$$U_{ij}(r) = A_{ij}\, exp\left(-\frac{r_{ij}}{\rho_{ij}}\right) - \frac{C_{ij}}{r_{ij}^{6}} \qquad \text{Eq. (2-26)}$$

$$U_{ij}(r) = f_0\left(b_i+b_j\right) exp\left(\frac{r_{ij}\left(a_i+a_j\right)}{\left(b_i+b_j\right)}\right) - \frac{C_{ij}}{r_{ij}^{6}} + \frac{D_{ij}}{r_{ij}^{8}} = A_{ij}\, exp\left(-\frac{r_{ij}\sigma_{ij}}{\rho_{ij}}\right) - \frac{C_{ij}}{r_{ij}^{6}} + \frac{D_{ij}}{r_{ij}^{8}} \qquad \text{Eq. (2-27)}$$

It must be highlighted that only cation-anion pairs were given the short-range interactions in the Buckingham potential [Kieu et al., 2011; J. Du et al., 2022], whereas no short-range interaction was assumed between cations and cations due to the long separation distance between them [Fa et al., 2005]. But this does not mean there is no short-range interaction at all. In fact, there is a maximum repulsive force that serves as the limit at low atomic separation [Morris et al., 2020], and Morris et al used a standard ZBL potential for small atomic separations in MD simulation. In addition, as we mentioned above, the BMH potential is homologous with Buckingham potential. Note that, apart from the r^{-8} term, the BMH potential after simple recasting and Buckingham expressions both contain the same number of variable parameters and are effectively mathematically equivalent [Du et al., 2022]. BMH potential does have a unique advantage that is the parameters for individual atoms can be defined in principle [Xu et al., 2010], rather than for atom pairs as in Buckingham form. Combining with the BMH potential can fix the deletion of no short-range interaction between cations and cations in Buckingham by utilizing the hybrid potentials form of LAMMPS. Therefore, in this study, the hybrid potentials composed of Buckingham potential and BMH potential are first combined to be applied in interatomic interactions. The final results demonstrate that the hybrid potential is more appropriate and precise in the CaO-Al_2O_3 system and the CaO-Al_2O_3-SiO_2 system (details in Section 3.3.2.1 and Section 4.3.2.1).

2.2.6 Simulator and analysis tools

LAMMPS which focuses on materials modeling is a popular classical molecular dynamics code and an acronym for Large-scale Atomic/Molecular Massively Parallel Simulator. LAMMPS has been widely used to simulate liquid, solid, or gaseous particle systems. Further, it can simulate the structure evolution and thermodynamic properties of organic polymer, biomacromolecule, metal alloy, and glass by defining atomic number, interatomic potential, boundary condition, etc.

LAMMPS runs on single processors or in parallel using message-passing techniques and spatial decomposition of the simulation domain, which brings up to be easy to modify or extend with new functionality [Plimpton, 1995]. However, LAMMPS is not perfect in every way. The disadvantage is that there are no graphical interfaces and data processing imperfections. So we need a software-OVITO pro visualization tool [Stukowski, 2010] and self-created scripts based on Python to process simulated data.

2.3 Structure parameters

Considering the various applications of molten oxide systems, the main challenge confronting researchers working in melts science is to determine the correlations among composition, structure, and eventual properties. For this purpose, molecular dynamic simulations which can predict the structure and thermophysical properties are gradually becoming an extremely tool for molten glass studies. In this section, we will introduce the characteristics of melt structures and the statistical distribution of parameters for analyzing structure.

2.3.1 Radial distribution function

The radial distribution function (RDF) is necessary for describing the structure of glass [Du et al., 2022], which counts the number of atoms in a shell of thickness at a range of interatomic distance from a reference atom. Radial distribution functions (RDF) are utilized to determine the short-range order and long-range disorder of molten systems and to establish a correlation between the local atomic structure and macroscopic properties. RDF can be derived from MD simulations and experimental measurements (neutron or X-ray diffraction). The comparison of RDFs from MD simulation and neutron diffraction can be a condition to verify the rationality of MD simulations. The

RDF $g_{ij}(r)$ gives the normalized probability of finding an atom of type j in a shell of thickness dr at a distance r from a reference i atom. The RDF $g_{ij}(r)$ can be written as [Li et al., 2017; Du et al., 2022]:

$$g_{ij}(r)=\frac{Nc_{\mathrm{i}}}{4\pi r^2 V}\frac{dn_{ij}(r)}{dr} \qquad \text{Eq. (2-28)}$$

where N and V represent the total number of atoms and volume of the simulation box, respectively;

c_i is the concentration of i atomic species;

$dn(r)$ denotes the number of atoms located at distances lying between r and $r + dr$.

2.3.2 Coordination number

The coordination number (CN) of one atom type to the other one provides insight into the arrangement of atoms, which can be described as the number of nearest neighbors of atom type i surrounding atom type j. For instance, Al atoms in the CaO-Al_2O_3 system can have 4-, 5-, and 6-coordinate with oxygen atoms, as shown in Figure 2-10.

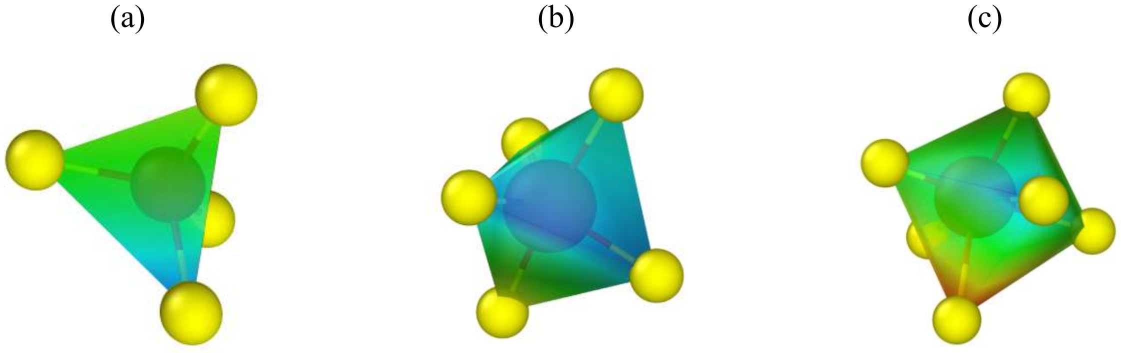

Figure 2-10. Visual representations of (a) 4-coordinated Al, (b) 5-coordinated Al, and 6-coordinated Al.

The mean CN is calculated by integrating the corresponding RDF [Li et al., 2017], providing the mean number of the neighbor atoms j present within the coordination sphere with the radius r of the central atom i:

$$CN_{ij}(r)=\frac{4\pi N_j}{V}\int_0^r g_{ij}(r)r^2dr \qquad \text{Eq. (2-29)}$$

The value of r is named the cutoff value, obtained from the first minimum after the first strong peak on RDF.

2.3.3 Structure factors

The structure factors can represent scattered waves from all atoms in the unit cell, reflecting the specific distribution of atoms and the internal structure of the crystal/melt, which is often measured by neutron diffraction. The difference between experimental and model total scattering structure factors is used as the acceptable level for simulations. Therefore, to study the structure on intermediate-length scales and verify MD simulations, the structure factors are computed to be compared with the structure factors from neutron diffraction. The partial structure factor has a relation with the corresponding partial pair RDF, as illustrated in Eq. (2-30) [Hennet et al., 2016a; Li et al., 2017],

$$S_{ij}(Q)=1+4\pi\rho\int_{0}^{R}\frac{sin\,(Qr)}{Qr}r^{2}(g_{ij}(r)-1)dr \qquad \text{Eq. (2-30)}$$

where Q is the scattering vector, ρ is the average atom number density, and R is the maximum value of the integration in real space. The total structure factor($S_N(Q)$) can be expressed [Li et al., 2017]:

$$S_N(Q)=\left(\sum_{i,j=1}^{n}c_ic_jb_ib_j\right)^{-1}\sum_{i,j=1}^{n}c_ic_j\,b_ib_jS_{ij}(Q)\pi r^2 \qquad \text{Eq. (2-31)}$$

where c_i is the fraction of atom i and b_i is the neutron scattering length of the species.

2.3.4 Bond angle distribution and bond length distribution

Bond angle distribution (BAD) is an important characteristic parameter of the intermediate range to study the distribution of the angle $a_{ikj}(\theta)$ formed by an atom k with two adjacent atoms i and j. BAD can be calculated by OVITO visualization tool, where the cutoff value for calculating BAD is the same as the cutoff value used to calculate CN as discussed earlier.

The bond length between a central atom k and its nearest neighbors can be estimated from the position of the first peak in the RDF $g(r)$ [Sukhomlinov et al., 2017]. The bond length distribution in the time-averaged distributions was evaluated by using the software OVITO pro visualization tool [Stukowski, 2010].

2.4 Conclusions

The Python scripts used for data processing have optimized the measurements and improved the accuracy of density, surface tension, and viscosity well. In classical MD simulation, the hybrid potential is created to define the interaction between atoms in the CaO-Al_2O_3 and the CaO-Al_2O_3-

SiO_2 systems, based on Buckingham, BMH, and Coulombic potentials. Furthermore, structure factors, radial distribution functions, and coordination numbers were utilized for analyzing the basic information of network structure, which lays the foundation for in-depth analysis of the structural parameters of the melts. The specific conclusions are as follows:

i. The script, based on the Canny edge detection algorithm, can detect the edge of the droplet and reconstitute the outline of the droplet. The horizontal and vertical radius can be determined well, which is greatly beneficial for improving the data accuracy.

ii. The Fourier transform-based script allows for the calculation and extraction of frequencies of harmonic oscillation and damped oscillation. Based on this calculation, the deviation between the excitation frequency and the resonant frequency can be determined, which can be used to check the reasonability of the measurement of surface tension and viscosity.

iii. The script integrated with Monte Carlo methods can successfully estimate the uncertainty of the measurements, where the relative standard uncertainty of density, surface tension, and viscosity are 0.69 %, 0.35 %, and 0.31 %, respectively.

iv. In the hybrid potential, the Buckingham potential is used to define the short-range interaction between cations and anions; the short-range interaction between cations is defined by the BMH potential; the Coulombic potential is responsible for the long-range interaction between ions.

Chapter 3

Chapter 3. The correlation between thermophysical properties and structural evolution of molten calcium aluminates investigated by aerodynamic levitation and molecular dynamics simulation

Résumé du Chapitre 3

Peu d'études ont été rapportées sur les propriétés thermophysiques (densité, tension superficielle et viscosité) des masses fondues de $(CaO)_x(Al_2O_3)_{1-x}$ depuis les points de fusion jusqu'aux ultra-hautes températures et sur la corrélation entre les propriétés thermophysiques et l'évolution structurelle. Dans ce chapitre, des mesures systématiques in situ de la densité, de la tension superficielle et de la viscosité des masses fondues de $(CaO)_x(Al_2O_3)_{1-x}$ sont effectuées par lévitation aérodynamique avec la méthode d'oscillation des gouttelettes sur une large gamme de températures.

En même temps, des simulations de dynamique moléculaire combinées aux résultats de caractérisation rapportés précédemment ont permis d'explorer la structure des produits fondus $(CaO)_x(Al_2O_3)_{1-x}$. Les facteurs de structure S(Q) des produits fondus de $(CaO)_x(Al_2O_3)_{1-x}$ ont été calculés à partir de simulations MD en utilisant différents potentiels (le potentiel hybride combiné, le potentiel de Buckingham et le potentiel BMH), qui ont été comparés à S(Q) de la diffraction neutronique expérimentale. La comparaison montre que les résultats calculés de S(Q) des fondus de $(CaO)_x(Al_2O_3)_{1-x}$, basés sur le potentiel hybride combiné, sont en bon accord général avec les mesures expérimentales. En outre, les fonctions de distribution de paires totales (PDF) et les nombres de coordination des fondus de $(CaO)_x(Al_2O_3)_{1-x}$ ont été calculés, sur la base du potentiel hybride combiné, ce qui était également en bon accord avec les résultats précédents de RMN. Les résultats ci-dessus vérifient la pertinence des simulations MD et fournissent un support précis pour l'analyse suivante sur la structure des produits fondus $(CaO)_x(Al_2O_3)_{1-x}$.

Des simulations MD des masses fondues $(CaO)_x(Al_2O_3)_{1-x}$ ont été effectuées pour chaque composition et pour quatre températures (1800, 2200, 2600, et 3000 K). Nous calculons les distributions de longueur de liaison (BLD), les distributions de longueur de liaison (BAD), les espèces d'oxygène, la compensation de charge et les liaisons d'oxygène insatisfaites et nous révélons le double rôle des cations Ca^{2+} pour prédire le degré de polymérisation du réseau dans les fusions de $(CaO)_x(Al_2O_3)_{1-x}$ à différentes températures et R (le rapport molaire de CaO à Al_2O_3).

L'augmentation de la température entraîne une diminution de l'oxygène de pontage et du degré de compensation de charge, tandis qu'une tendance opposée est observée pour l'oxygène non de pontage et l'oxygène tri-cluster. L'augmentation de R conduit à une augmentation de l'oxygène non pontant et à une diminution de l'oxygène tri-cluster, alors que l'oxygène pontant montre d'abord une augmentation puis une diminution spectaculaire. Le double rôle des cations Ca^{2+} dépend du rapport CaO/Al_2O_3: (i) R < 1, les cations Ca^{2+} agissent de préférence comme compensateurs de charge, ce qui augmente le degré de polymérisation ; (ii) R > 1, les cations Ca^{2+} deviennent progressivement dominants en tant que modificateurs de réseau, ce qui entraîne une diminution de l'oxygène de pontage et de l'oxygène tri-cluster et une forte augmentation de l'oxygène non pontant, réduisant ainsi le degré de polymérisation.

Sur la base des paramètres structurels, la corrélation entre les propriétés thermophysiques et l'évolution de la structure dans les fusions de $(CaO)_x(Al_2O_3)_{1-x}$ est révélée à différentes températures et R, dont les principales conclusions sont les suivantes :

i. L'amélioration de la température et de R entraîne un changement de la distribution des longueurs de liaison, et une diminution de l'intensité de la BAD Al-O-Al et du degré de polymérisation, ce qui diminue la connectivité des $[AlO_n]$ entre eux pour augmenter le volume et réduire la densité des masses fondues $(CaO)_x(Al_2O_3)_{1-x}$. L'influence de $\rho(Al_2O_3) > \rho(CaO)$ sur la densité des masses fondues $(CaO)_x(Al_2O_3)_{1-x}$ est également non-négligeable.

ii. Avec la diminution de R, le contenu des liaisons oxygénées modifiées non satisfaites causées par la compensation de charge augmente, ce qui compense l'influence de la diminution de Al-O-n[Ca] et fait augmenter la tension superficielle. Avec l'augmentation des températures, les contenus totaux de 2Al-O-n[Ca], 3Al-O-n[Ca], et 2Al-O-[Al] ne montrent qu'une légère diminution et le changement de Al-O-n[Ca] peut être négligeable, ce qui entraîne une légère diminution de la tension de surface.

La viscosité η des masses fondues de $(CaO)_x(Al_2O_3)_{1-x}$ grimpe puis diminue de CA2 à C3A, car l'un des rôles des cations Ca^{2+} est de compenser la charge à faible teneur en CaO, ce qui entraîne une augmentation incessante du degré de polymérisation (CA2-CA). Au contraire, l'autre rôle des cations Ca^{2+} est de modifier le réseau pour réduire le degré de polymérisation en augmentant davantage R (CA-C3A). L'augmentation de la température peut diminuer la teneur en oxygène de pontage et le degré de compensation de charge, ce qui réduit le degré de polymérisation et entraîne une baisse de la viscosité des fusions de $(CaO)_x(Al_2O_3)_{1-x}$.

Abstract of Chapter 3

Few studies have been reported on the thermophysical properties (density, surface tension, and viscosity) of $(CaO)_x(Al_2O_3)_{1-x}$ melts from melting points to ultra-high temperatures and the correlation between thermophysical properties and structural evolution. In this chapter, systematic in-situ measurements of density, surface tension, and viscosity of $(CaO)_x(Al_2O_3)_{1-x}$ melts are performed by aerodynamic levitation with the droplet oscillation method over a wide temperature range.

Meanwhile, molecular dynamic simulations combined with the previously reported characterization results explored the structure of the $(CaO)_x(Al_2O_3)_{1-x}$ melts. Structure factors S(Q) of the

$(CaO)_x(Al_2O_3)_{1-x}$ melts were calculated from MD simulations by using different potentials (the combined hybrid potential, Buckingham potential, and BMH potential), which compared to S(Q) from experimental neutron diffraction. The comparison shows that the S(Q) calculated results of $(CaO)_x(Al_2O_3)_{1-x}$ melts, based on the combined hybrid potential, are in good overall agreement with the experimental measurements. Furthermore, total pair distribution functions (PDF) and coordination numbers of the $(CaO)_x(Al_2O_3)_{1-x}$ melts were calculated, based on the combined hybrid potential, which was also in good agreement with previous NMR results. The above results verify the relevance of the MD simulations and provide accurate support for the following analysis on the structure of $(CaO)_x(Al_2O_3)_{1-x}$ melts.

MD simulations of the $(CaO)_x(Al_2O_3)_{1-x}$ melts were carried out for each composition and for four temperatures (1800, 2200, 2600, and 3000 K). We calculate bond length distributions (BLD), bond length distributions (BAD), oxygen species, charge compensation, and unsatisfied oxygen bonds and reveal the dual role of Ca^{2+} cations in predicting the degree of network polymerization in $(CaO)_x(Al_2O_3)_{1-x}$ melts at different temperatures and R (the mole ratio of CaO to Al_2O_3).

Rising temperature causes a decline in bridging oxygen and the degree of charge compensation, while an opposite trend is observed for non-bridging oxygen and tri-cluster oxygen. Increasing R leads to an increase in non-bridging oxygen and a decrease in tri-cluster oxygen, where bridging oxygen shows an increase first and then a dramatic decrease. The dual role of Ca^{2+} cations depends on the CaO/Al_2O_3: (i) $R < 1$, Ca^{2+} cations preferentially act as charge compensators, which increases the degree of polymerization; (ii) $R > 1$, Ca^{2+} cations as network modifiers gradually become dominant, which causes the decrease in bridging oxygen and tri-cluster oxygen and a great increase in non-bridging oxygen, reducing the degree of polymerization.

Based on the structural parameters, the correlation between thermophysical properties and structure evolution in the $(CaO)_x(Al_2O_3)_{1-x}$ melts is revealed at different temperatures and R.

3.1 Introduction

Calcium aluminates have been considered a valuable and promising glass system, due to their numerous applications such as setting agents of cement, optical glass, corrosion of refractories, and photomemory materials[Hafner et al., 1958; Onoda et al., 1970; Lines et al., 1989; De Bilbao et al., 2014, 2018; Liu et al., 2020]. Accurate knowledge of thermophysical properties (density, surface tension, and viscosity) of the $(CaO)_x(Al_2O_3)_{1-x}$ melts is significant for industrial applications. The influence of structure evolution on the thermophysical properties of calcium aluminates has always been a hot topic of interest. In calcium aluminates, Ca^{2+} cations can be network modifiers or charge compensators and Al^{3+} with various coordination numbers as a non-typical network former cation can form a series of $[AlO_n]$ polyhedrons [Akola et al., 2013], which leads to the complicated and changeable structure and glass-forming process. It is still challenging to clarify the correlation between thermophysical properties and structure, due to the immeasurability of these properties and the particularity of the structure evolution at high temperatures. Therefore, an in-depth understanding of the correlation of structure-thermophysical properties is of particular importance for potential applications of Al_2O_3-CaO-based glasses.

For the $(CaO)_x(Al_2O_3)_{1-x}$ melts, to the best of our knowledge, only the density and viscosity of CaO•Al_2O_3 (CA) melt were measured by Kargl et al. [Kargl et al., 2015]. And Liu et al. [Liu et al., 2020] only reported the viscosity of $(CaO)_x(Al_2O_3)_{1-x}$ melts at high temperatures. Therefore, it is important to optimize measurements and propose complete thermophysical properties values. It will provide a valuable reference for scholars who study the thermophysical properties of melts.

It is generally recognized that the thermophysical properties of glass melts are closely correlated to structural evolution. The density is related to factors, such as the degree of polymerization and the twining degree of structural units, which can affect microvolume. Surface tension which reflects the structural difference between the ionic groups of the surface and bulk at the micro level is extremely sensitive to the melt structure [Zhang et al., 2021b]. Meanwhile, Zhang et al. [Zhang et al., 2021b] proposed unsatisfied oxygen bonds (UOBs) which formed from the oxygen anions locking of fewer adjacent cations to provide stabilizing force at the surface layer. The content of UOBs with higher energy has a great influence on surface tension. Additionally, it is generally believed that viscosity is related to the network modifier and former of a melt, especially the degree of polymerization of the network structure.

Therefore, exploring the structural evolution of $(CaO)_x(Al_2O_3)_{1-x}$ melts is the other key to understanding the correlation after solving the measurements of thermophysical properties. There were considerable research efforts regarding the structural transformations, the chemical shift, and structural units of $(CaO)_x(Al_2O_3)_{1-x}$ melts that have been persistently studied in our laboratory since the 1990s. Poe et al. [Poe et al., 1994] performed ^{27}Al NMR and Raman spectra on $(CaO)_x(Al_2O_3)_{1-x}$ melts and revealed the influence of oxygen exchange between neighboring polyhedral units on viscous flow and the lead role of AlO_n polyhedral units on the vibrational time scale. Luga et al. [Iuga et al., 2005] utilized high-resolution solid-state NMR to study the structural units of the CaO•$2Al_2O_3$ (CA2) crystalline phase, indicating the isotropic chemical shift of Al, the unambiguously different bonding connections between O and Al, and the formation of OAl_3 tri-cluster. Massiot et al. [Massiot et al., 1995] found that the [AlO_4] tetrahedron units could dissociate to generate [AlO_5] and [AlO_6] polyhedrons in liquid CA by the study of high-temperature ^{27}Al NMR. Meanwhile, there were also numerous diffraction researches on the Al_2O_3-CaO system, which have been performed by neutron diffraction, fast X-ray scattering, time-resolved synchrotron x-ray diffraction to determine the structure factors, the coordination number (CN) of Oxygen around Al, the Al-O and Ca-O bond lengths. The above studies have laid foundations for understanding the structure of the $(CaO)_x(Al_2O_3)_{1-x}$ melts from the perspective of experimental tests.

In addition, molecular dynamic (MD) simulation in recent years has been developed to be an effective method on the atomic scale for studying network structure, structural evolution, and structure-properties correlation in glasses [Du, 2015]. Drewitt et al. [Drewitt et al., 2012] studied the structure transformations on vitrification of the fragile glass-forming material CA with the aid of neutron diffraction and MD simulations during the quenching, revealing the evolution of Al-polyhedrons and coordination numbers of Ca. Cristiglio et al. [Cristiglio et al., 2010] analyzed the structures of $3CaO•Al_2O_3$ (C3A), CA, and CA2 melts, based on the structure factors, the total pair correlation functions, and the bond angle distributions of O-Al-O and O-Ca-O, by Neutron diffraction and Ab initio MD simulation. Liu et al. [Liu et al., 2020] utilized MD simulation to reproduce the viscosity and coefficients of thermal expansion of the $(CaO)_x(Al_2O_3)_{1-x}$ melts. Although the above studies demonstrated the function of cations, the formational discipline of polyhedral units, bond angle distribution, and calculation of viscosity and density in $(CaO)_x(Al_2O_3)_{1-x}$ melts, to date, there is still no analysis of the correlation between structure and thermophysical properties.

Herein, surface tension and viscosity of molten C3A, $12CaO•7Al_2O_3$ (C12A7), CA, and CA2 and their density were completely measured by ADL with the droplet oscillation method (DOM) at temperature ranges of 1900-2700 K and 1450-2600 K, respectively, which compared with thermophysical properties of $(CaO)_x(Al_2O_3)_{1-x}$ melts from previous studies in a benchmark approach. Meanwhile, we deeply demonstrate by molecular dynamic (MD) simulations how temperature and $R=CaO/Al_2O_3$ (mole/mole) variations affect the structural transformations of C3A, C12A7, CA, and CA2, combined with the previous measurements and studies on the structure of calcium aluminates. Based on the structural analysis of the atomic scale, the correlation between structural evolution and thermophysical properties of $(CaO)_x(Al_2O_3)_{1-x}$ melts will be explored from the angles of bond length distribution, the bond angle distribution, network modifier, charge compensation, oxygen species, and unsatisfied oxygen bonds at different temperatures and R.

3.2 Experiment and MD simulation

3.2.1 Preparation of the $(CaO)_x(Al_2O_3)_{1-x}$ samples

CaO and Al_2O_3 (ALMATIS, CT3000 SG, 99.8%) were used as raw materials to prepare samples of the $(CaO)_x(Al_2O_3)_{1-x}$ melts. CaO was obtained from full calcination of $CaCO_3$ powder (ALFA AESAR, 99.0%) at 1273 K for 12 h by using the Muffle furnace (Nabertherm, Germany). The pre-calcination can ensure the complete decomposition of $CaCO_3$ powder. The component of C3A, C12A7, CA, and CA2 are shown detailedly in Table 3-1. Two kinds of powder were mixed completely for 0.5 h by using an agate mortar and pressed into pellets under 9.5 MPa. The pellets were placed in a drying oven for 12 h at 373 K. Each pellet was crushed into small pieces after drying. Aerodynamic levitation (ADL) was utilized to premelt the pieces into spherical samples of 16.2 ± 1 mg and a diameter of 2 ± 0.2 mm. Meanwhile, liquidus temperatures of C3A, C12A7, CA, and CA2 were calculated by thermodynamic software FactSage® 8.1 [Bale et al., 2016], shown in Table 3-1, where FTOxid and FactPS databases were chosen.

Table 3-1. Composition of prepared melts (mol.%) and liquidus temperatures (K).

Melts System	Sample No.	CaO (mol.%)	Al_2O_3 (mol.%)	R=CaO/Al_2O_3	Liquidus temp (K)
$CaO\text{-}Al_2O_3$	C3A	75.0	25.0	3.0	2197
	C12A7	63.2	36.8	1.7	1638
	CA	50.0	50.0	1	1877
	CA2	33.0	67.0	0.5	2038

3.2.2 Measurements by aerodynamic levitation

The measurements, principles, and methods of data processing were detailedly described in Section 2.

3.2.3 MD simulations

Well-defined crystal structures from Materials Project [Jain et al., 2013] and AMCSD databases [Re3data.Org, 2014] for C3A, C12A7, CA, and CA2 were utilized as initial configurations of MD simulations, creating 5940, 5664, 5600, and 5760 atomic ensembles, respectively. Detailed information is shown in Figure 3-1, and their lattice parameters are detailedly listed in Table 3-2.

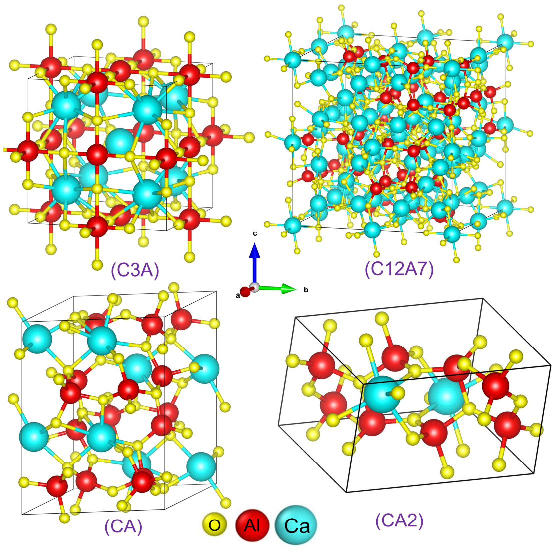

Figure 3-1. Initial configurations of C3A, C12A7, CA, and CA2.

Table 3-2. Lattice parameters and atom number of C3A, C12A7, CA, and CA2.

Materials	Lattice parameters						Number of atoms			Total
	a(Å)	b(Å)	c(Å)	α(°)	β(°)	γ(°)	Ca	Al	O	
C3A	7.668	7.668	7.668	90.000	90.000	90.000	1620	1080	3240	5940
C12A7	12.120	12.120	12.120	90.000	90.000	90.000	1152	1344	3168	5664
CA	8.707	8.040	10.378	84.986	90.000	90.000	800	1600	3200	5600
CA2	7.887	7.887	5.497	76.638	76.638	69.289	480	1920	3360	5760

As mentioned above (Section 2.2.5), choosing appropriate potential functions is the key to the correct results of MD simulation. In MD simulations of the $CaO-Al_2O_3$ system, the combined hybrid potential composed of Buckingham potential and BMH potential was first combined to apply in interatomic interactions of calcium aluminates. The Born-Mayer-Huggins (BMH) which contains the inter-core short-range repulsion and the van der Waals attraction, was applied to describe Ca-Ca, Ca-Al, and Al-Al pair interactions. Buckingham potential was utilized to define the pair interactions of Ca-O, Al-O, and O-O. In addition, all the atomic pairs were overlayed by long-range Coulombic interactions at the same time. All parameters for BMH and Buckingham are given in Table 3-3. The long-range Coulombic interaction was calculated by the Ewald-sum summation method with a precision of 10^{-6}, using 8 Å as a cutoff distance to evaluate repulsive forces with periodic boundary conditions and 12 Å for the long-range Coulombic interactions.

Table 3-3. Parameters of the BMH potential [Bouhadja et al., 2013] and the Buckingham potential [Charpentier et al., 2018; Hu et al., 2020; Liu et al., 2020] for the $CaO-Al_2O_3$ system.

Pair	BMH Potential				
	$A=f_0(b_i+b_j)$ (eV)	$\rho=(b_i+b_j)$ (Å)	$\sigma=(a_i+a_j)$ (Å)	C (eV•Å^6)	D (eV•Å^8)
$Ca^{1.2+}$—$Ca^{1.2+}$	0.0035	0.0800	2.3440	20.9856	0
$Ca^{1.2+}$—$Al^{1.8+}$	0.0032	0.0740	1.9572	17.1710	0
$Al^{1.8+}$—$Al^{1.8+}$	0.0029	0.0680	1.5704	14.0498	0

Pair	Buckingham Potential		
	A (eV)	ρ (Å)	C (eV•Å^6)
$Ca^{1.2+}$—$O^{1.2-}$	7747.0000	0.252600	93.100
$Al^{1.8+}$—$O^{1.2-}$	12 201.4170	0.195628	31.997
$O^{1.2-}$—$O^{1.2-}$	2029.2200	0.343645	192.580

The MD simulation processes used the canonical ensemble (NVT) where the number of particles (N), the system volume (V), and temperature (T) are constant [Bouhadja et al., 2013; Wang et al., 2021]. The time step was set to 1 fs for all the simulations. Each simulated process took 2490 ps, which included relaxation, heating up, cooling down, and heat preservation to reproduce the experimental process, as shown in Figure 3-2. Each simulation was started at 1800K and kept 50 ps for relaxation to mix the system enough and eliminate the effects of the initial distribution. The temperature was heated up to 4000 K (200 ps) and kept 200 ps, then it began to cool down, which experienced successively four temperature points: 3000 K, 2600 K, 2200 K, and 1800 K in sequence. This annealing protocol leads to a nominal quenching rate of 5 K/ps. Each temperature point was kept 400 ps for relaxation to calculate structure and transport information, including structural factors, total pair distribution function (PDF), and coordination number. And the simulation trajectories were analyzed with the visualization software OVITO pro [Stukowski, 2010].

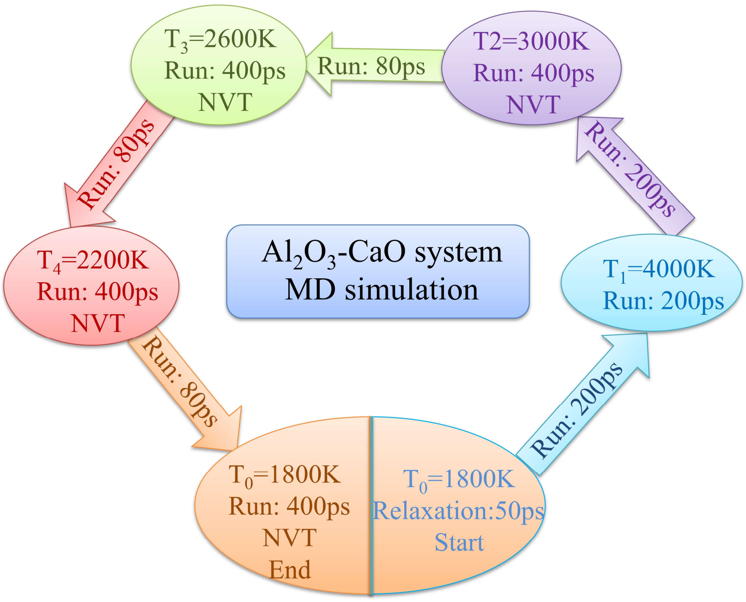

Figure 3-2. The diagrammatic drawing of the MD simulations process

3.2.4 Computational objects

To deeply understand our simulated results of C3A, C12A7, CA, and CA2, it is useful to remind several key definitions should be indicated in advance (Figure 3-3): (i) Al atoms are surrounded by O atoms to form [AlO_n] polyhedrons; (ii) non-bridging oxygens (NBO) are defined as only joining one Al atom and one or more Ca atoms (Al-O-*n*Ca, $n \geq 1$); (iii) free oxygens (FO) are only connected by Ca atoms (O-*n*Ca); (iv) tri-cluster oxygens (TCO) means that an oxygen atom is shared by three [AlO_n] polyhedrons and connected by *n* Ca atoms (3Al-O-*n*Ca); (v) bridging oxygens (BO) is that an oxygen atom as a bridging atom is shared by two [AlO_n] polyhedrons; (vi) the degree of charge compensation in structure was defined with the ratio of total specific oxygen atoms to all oxygen atoms, where the specific oxygen atom is shared by multiple AlO_n polyhedrons and connected by n Ca atoms (mAl-O-nCa, $m \geq 2$, $n \geq 1$).

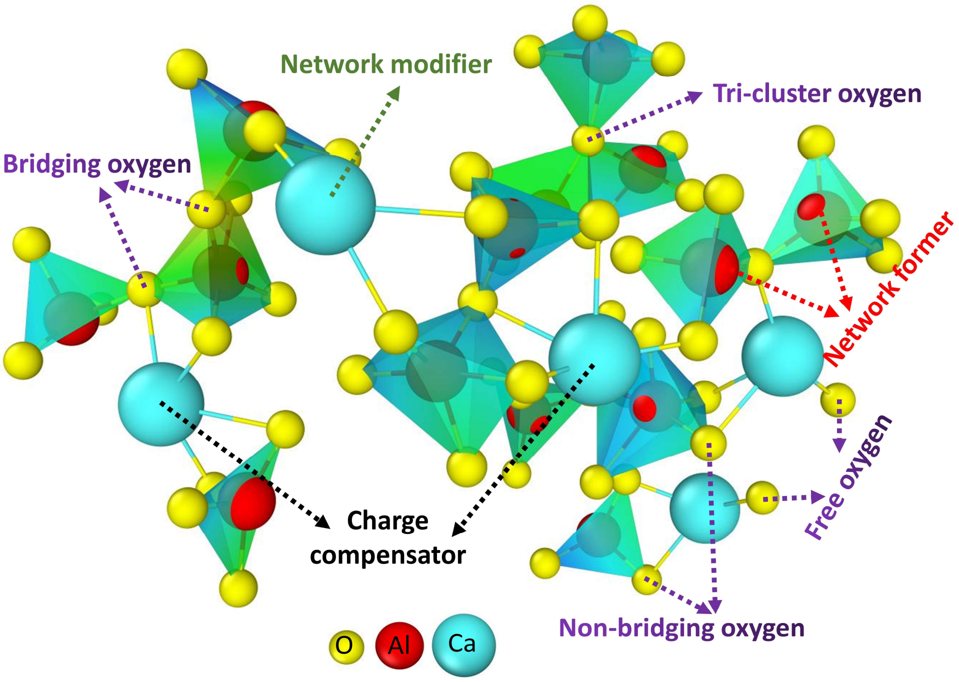

Figure 3-3. The definitions of structure parameters in the network structure of $(CaO)_x(Al_2O_3)_{1-x}$ melts: bridging oxygen (BO), Non-bridging oxygen (NBO), tri-cluster oxygen (TCO), free oxygen (FO), charge compensator, and network modifier.

3.3 Results

3.3.1 Experimental results: density, surface tension, and viscosity of the $(CaO)_x(Al_2O_3)_{1-x}$ melts over a wide temperature range

The density for melts composed of the CaO-Al_2O_3 system in a wide temperature range (from 2600 to 1450 K) is shown in Figure 3-4 (a), with the density of CA (Ar) measured by Kargl et al. [Kargl et al., 2015], chosen as referenced data. It can be noted that the latter were obtained using Argon as levitation gas, whereas the mixture gas (20% O_2 and 80% Ar) was utilized in the present work. As shown in reference [Kargl et al., 2015], the levitation gas influences drastically the temperature dependence of the CA density and the experimental data in this work is lower, compared to the referenced data, which agrees with the description of the influence of levitation gas from Kargl et al. Meanwhile, the density of $(CaO)_x(Al_2O_3)_{1-x}$ melts increases distinctly during the whole free cooling process. And the difference (0.263 g/cm^3) in the density of C3A at 1450 K and 2550 K is the largest among these four compositions. For C12A7 and CA, the density difference from 1450 to 2550 K is 0.181 ± 0.01 g/cm^3. The density of CA2 increases the least during the whole cooling phase, from 2.646 to 2.761 g/cm^3. Moreover, the density increases with decreasing R. The density of the CA2 melt containing the most Al_2O_3 content is highest than that of the other melts. In contrast, the density C3A with the lowest content of Al_2O_3 is the lowest. Generally, it illustrates that the density change of $(CaO)_x(Al_2O_3)_{1-x}$ melts was caused by the synthetical influence of temperature and R.

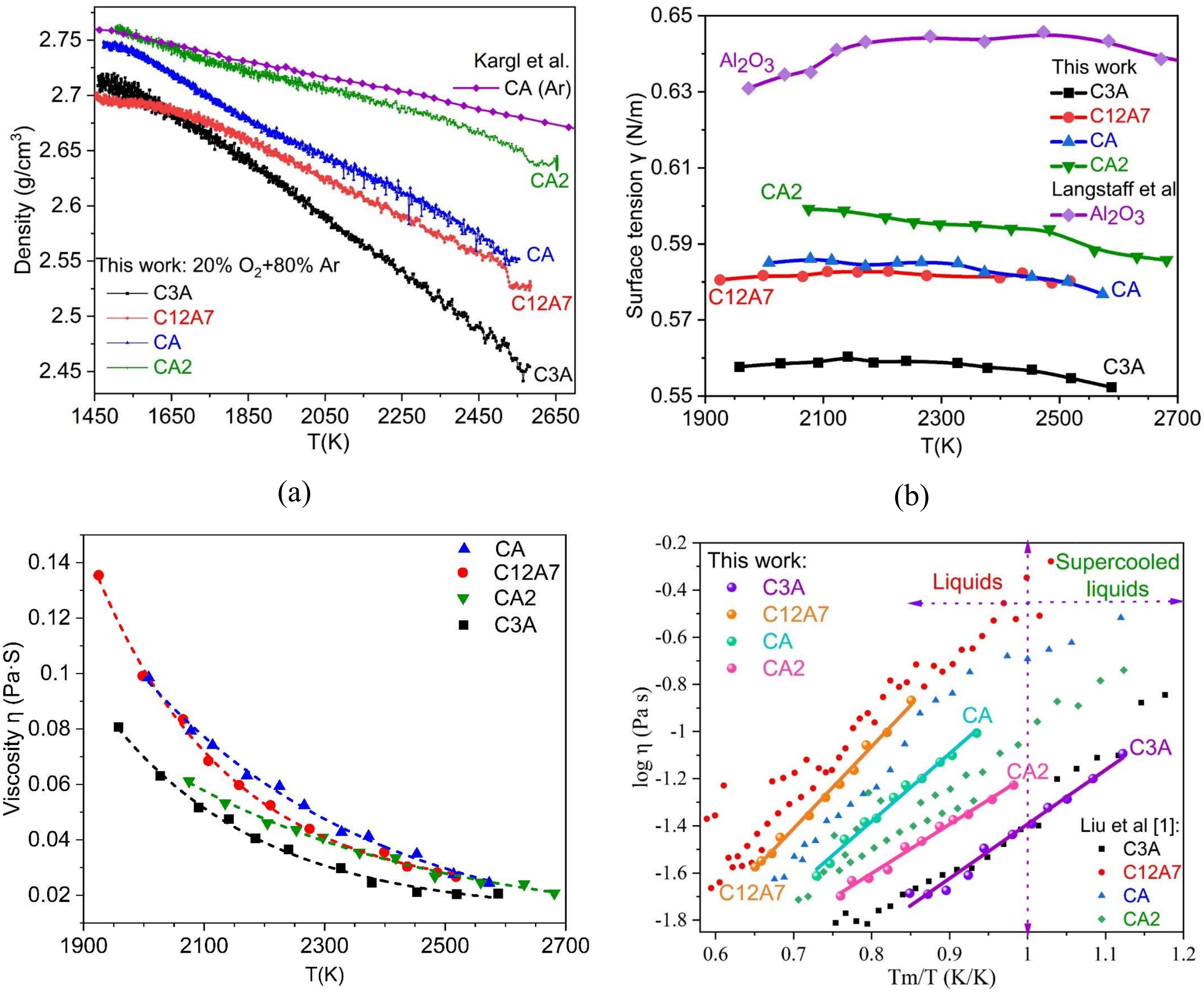

(a) (b)

(c1) (c2)

Figure 3-4 Temperature-dependent density, surface tension, and viscosity of the $(CaO)_x(Al_2O_3)_{1-x}$ melts: (a) the density ρ versus T; (b) surface tension γ versus T; (c1) viscosity η versus T; (c2) $\log(\eta)$ versus Tm/T.

The liquid Al_2O_3 data measured by Langstaff et al. (ADL with DOM) was selected as the reference data since the surface tension of $(CaO)_x(Al_2O_3)_{1-x}$ melts measured by levitation technique is not reported in previous papers. The surface tension of $(CaO)_x(Al_2O_3)_{1-x}$ melts at different temperatures in comparison with the reference liquid Al_2O_3 data are shown in Figure 3-4 (b). The surface tension of C3A, C12A7, CA, and CA2 slightly decreases as the temperature rises from 1950 to 2700 K. However, except for CA2 (0.599-0.5886 N/m), the surface tensions of CA, C12A7 and C3A are 0.585-0.577 N/m (CA), 0.581-0.580 N/m (C12A7), and 0.558-0.553 N/m (C3A), respectively, while the differences are less than 0.01 N/m, which means the temperature has a slight influence on the surface tension. Compared to the effect of temperature, the composition of $(CaO)_x(Al_2O_3)_{1-x}$ melts has a greater influence on surface tension. With decreasing R, the surface tension of melts increases obviously. The surface tension of C3A with the lowest content of Al_2O_3 is the lowest, compared to the other compositions. On the contrary, the surface tension values of CA2 are the highest over the entire interval temperature.

The viscosities of $(CaO)_x(Al_2O_3)_{1-x}$ melts at high temperatures lie in a narrow range (Figure 3-4 (c1)). For the sake of observation and comparison, viscosity versus temperature is expressed in log(η) versus Tm/T, which is compared to viscosity data from ADL with DOM by Liu et al. [Liu et al., 2020], as described in Figure 3-4 (c2). The log(η) versus Tm/T shows a linear relationship, which illustrates the viscosity of melts exponentially decreases as the temperature rises, in agreement with Arrhenius law [Roller, 1986]. This exponential correlation between the viscosity of melts and temperature verifies the description of studies [Duchesne et al., 2013; Wu et al., 2015; Wu et al., 2015]. As expected, the viscosity of melts declines gradually with the increase in temperature. It should be pointed out that the composition of $(CaO)_x(Al_2O_3)_{1-x}$ melts has crucial effects on viscosity. At the $R < 1$, the viscosity η of molten CA2 and CA increases with increasing R. However, as R increases further (from CA to C3A) and CaO is gradually abundant in melts, the viscosity η of melts dramatically declines, especially, from C12A7 to C3A. R affects the ratio of former to modifier in network structure, causing structural evolution. Therefore, it is necessary to explore the influence of R on structural evolution to understand the relationship between viscosity and network structure.

3.3.2 Simulation results

3.3.2.1 Structure factors and Radial distribution functions of $(CaO)_x(Al_2O_3)_{1-x}$ melts.

3.3.2.1.1 Structure factors

Figure 3-5 (A1-A4) shows the comparison of structure factors S(Q) of C3A and CA2 at 2170 K [Drewitt et al., 2011], C12A7 at 1723 K [Hannon et al., 2000; Akola et al., 2013], and CA at 1973 K [Hennet et al., 2016b] from experimental neutron diffraction and S(Q) calculated from MD simulations by using different potentials, expressed by colored circles and colored solid lines, respectively. The conjectures of the combined hybrid potential function are verified by the comparison of structural factors. By observing the comparison of S(Q) in Figure 3-5, there is a relatively larger shift error on the structural factors calculated from a single potential (Buckingham or BMH), compared with that from experimental measurements. The calculated results of S(Q) of $(CaO)_x(Al_2O_3)_{1-x}$ melts, based on the combined hybrid potential, are in good overall agreement with the experimental measurements, except for a little discrepancy at the low-Q zone for S(Q), which systematically validates the correctness and applicability of the combined hybrid potential in MD simulations of the $(CaO)_x(Al_2O_3)_{1-x}$ melts.

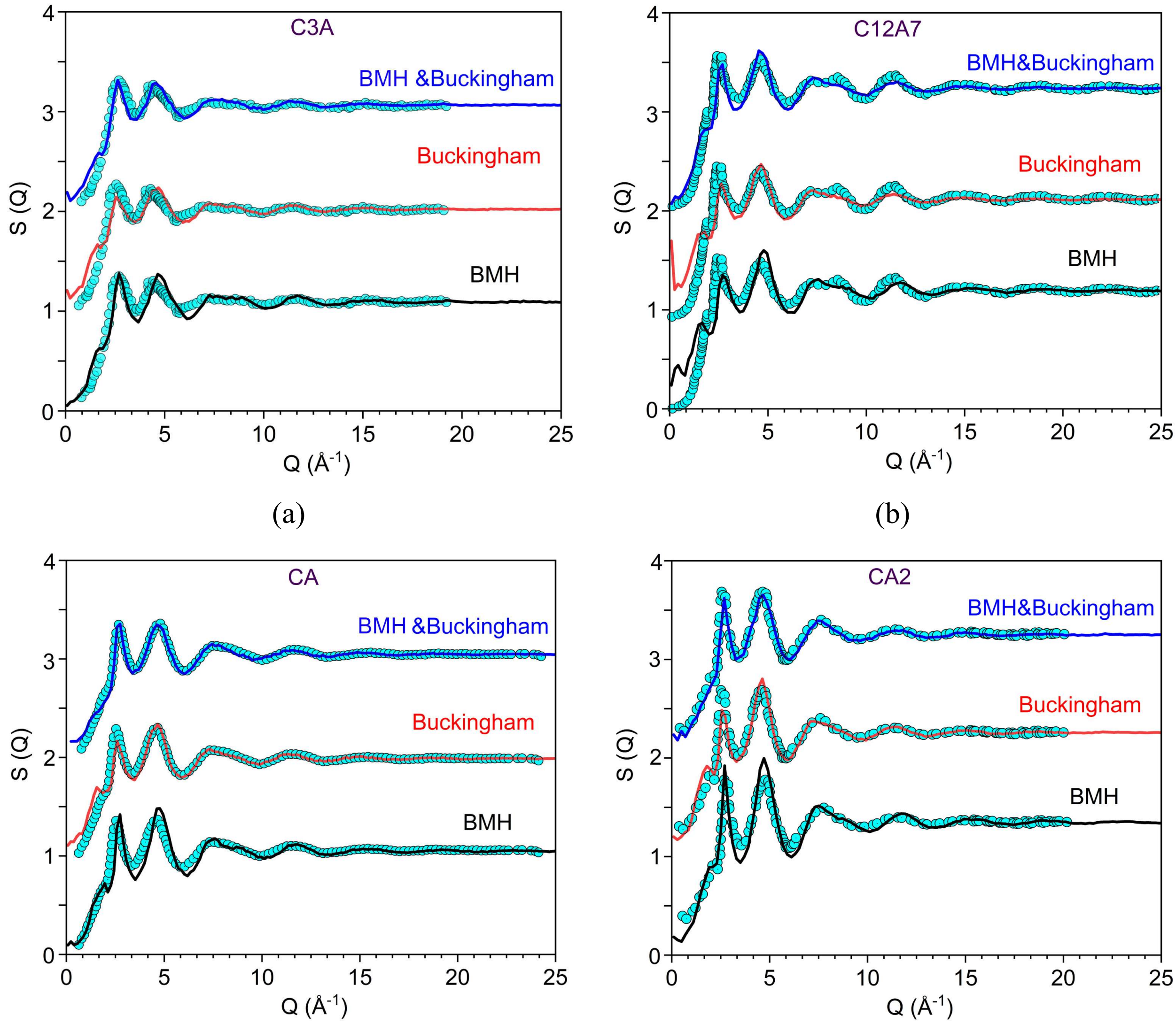

(a) (b)

(c) (d)

Figure 3-5. The comparison between experimental S(Q) (colored circles) [Hannon et al., 2000; Drewitt et al., 2011; Hennet et al., 2016b] and simulated S(Q) (colored solid lines), where simulated structure factors are based on BMH potential, Buckingham potential, and BMH&Buckingham hybrid potential. (a) C3A: S(Q) at 2170 K; (b) C12A7: S(Q) at 1723 K; (c) CA: S(Q) at 1973 K; (d) CA2: S(Q) at 2170 K.

3.3.2.1.2 Radial distribution functions

To further verify the applicability of the combined hybrid potential, the total pair distribution functions of C3A, CA, and CA2 were calculated from MD simulations at 2100 K as well, as shown in Figure 3-6. And the radial distribution functions (RDF) of Al-O and Ca-O in C3A, CA, and CA2 are shown in Figure 3-7. Compared with the neutron diffraction study of molten calcium aluminates (C3A, CA, and CA2) at 2100 K reported by Cristiglio et al [Cristiglio et al., 2010], for all pair correlation functions of $(CaO)_x(Al_2O_3)_{1-x}$ melts from MD simulations, the first peak in Figure 3-6 which is the nearest neighbor Al-O distance is observed at 1.77 ± 0.03 Å, (neutron diffraction: 1.82 ± 0.03 Å), the corresponding results are also in Figure 3-7. It is interesting to note that the second peak was found at 2.33 ± 0.03 Å for the curve of C3A in Figure 3-6. However, the visualization of the second peak gradually becomes less obvious with decreasing CaO content from C3A to CA2. The Ca-O correlations were possibly the main reason for this phenomenon. The third peak, namely the nearest-neighbor O-O distance, was found at 2.92 ± 0.03 Å on the curve C3A in Figure 3-6. Further, the third peak gradually shifts to lower r (2.90 ± 0.03 Å) from C3A to CA2. The peak values are basically in the experimental range from neutron diffraction and the shifts of peak values from C3A to CA2 are also in agreement with experimental measurement. This is one of the accurate supports for the following MD simulation analysis of $(CaO)_x(Al_2O_3)_{1-x}$ melts structure.

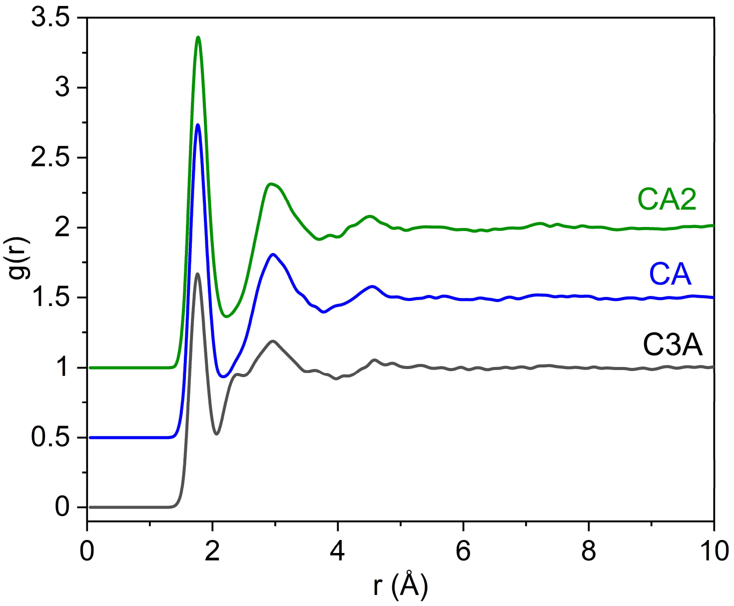

Figure 3-6. Total pair distribution functions for $(CaO)_x(Al_2O_3)_{1-x}$ melts (C3A, CA, and CA2) at 2100 K. The upper curve are shifted up by 0.5 for clarity.

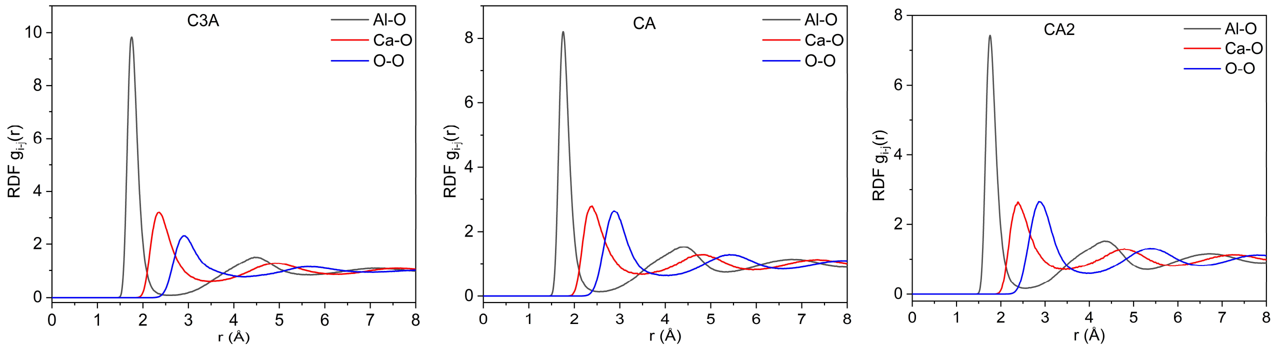

Figure 3-7. Radial distribution functions of Al-O, Ca-O, O-O in (a) C3A, (b) CA, and (c) CA2 at 2100 K.

We also calculated the coordination numbers (CN) of Al-O and Ca-O by corresponding to radial distribution functions, shown in Figure 3-8. As noted above, the first trough value (r = 2.48 ± 0.02 Å) of the Al-O RDF curves in Figure 3-7 is the cutoff radius between Al atoms and O atoms. The same description is suitable for Ca-O (r = 3.35 ± 0.05 Å) and O-O (r = 3.95 ± 0.07 Å). The integral values at the cutoff radii are the ordinates corresponding to the platform CN curves, which are average CN between Al atoms and O atoms. As evident in Figure 3-8, the curves of CN_{Al-O} have a wide and smooth platform, compared with curves of CN_{Ca-O} and CN_{O-O}, which indicates the Al-O coordination in structure is more stable [Li et al., 2017; Wu et al., 2021]. Based on the curves of CN, the average CN of Al-O and Ca-O in C3A, CA, and CA2 can be calculated, where the average CN of Al-O are 4.2 ± 0.1 (C3A), 4.1 ± 0.1 (CA), and 4.1 ± 0.1 (CA2), respectively, and the average CN of Ca-O is about 6.0 ± 0.3 (C3A), 6.0 ± 0.3 (CA), and 6.0 ± 0.3 (CA2). All the parameters of the nearest-neighbor distance and coordination number from measurements and simulations are summarized in Table 3-4. The comparison results are that the pair distribution functions, coordination numbers, and the nearest-neighbor distance of atoms from MD simulations meet an agreement in error range with those parameters of C3A, CA, and CA2 reported by Cristiglio et al [Cristiglio et al., 2010]. The above-mentioned results verify the reasonability of the MD simulations and provide accurate support for the following MD simulation analysis on the structure of $(CaO)_x(Al_2O_3)_{1-x}$ melts.

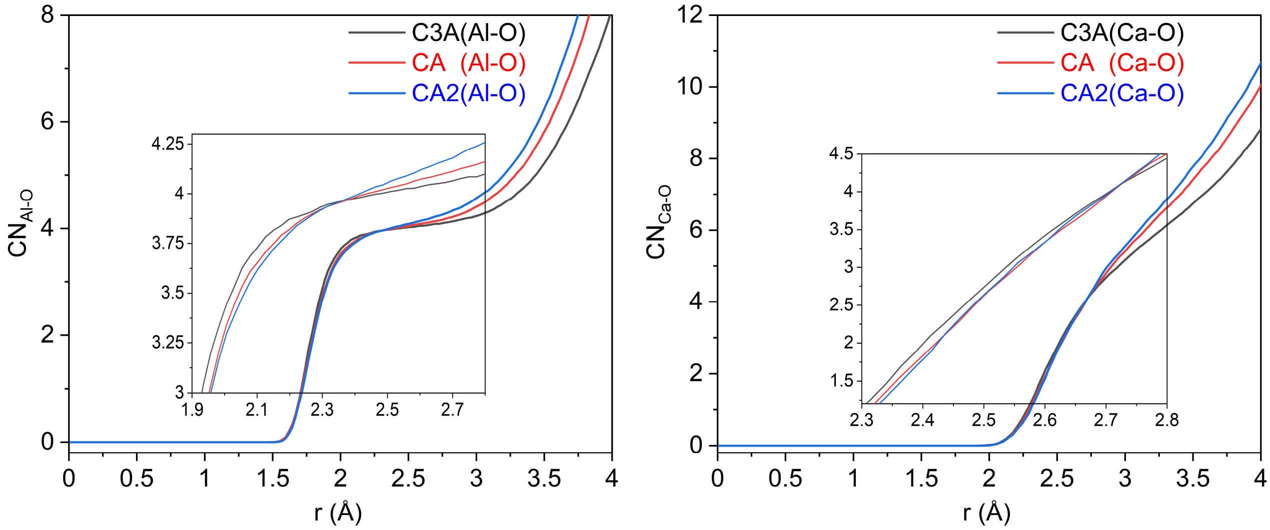

(a)

(b)

Figure 3-8. Coordination numbers of (a) Al-O and (b) Ca-O in C3A, CA, and CA2

Table 3-4. The nearest-neighbor distance and coordination numbers of Al-O and Ca-O from neutron diffraction data [Cristiglio et al., 2010] and MD simulation results.

	MD				Exp			
	$r_{Al\text{-}O}$ (Å) (± 0.03)	$CN_{Al\text{-}O}$ (± 0.1)	$r_{Ca\text{-}O}$ (Å) (± 0.03)	$CN_{Ca\text{-}O}$ (± 0.4)	$r_{Al\text{-}O}$ (Å) (± 0.03)	$CN_{Al\text{-}O}$ (± 0.5)	$r_{Ca\text{-}O}$ (Å) (± 0.05)	$CN_{Ca\text{-}O}$ (± 0.5)
C3A	1.77	4.2	2.33	6.1	1.82	4.5	2.30	5.7
CA	1.77	4.1	2.34	6.0	1.82	4.4	2.32	5.4
CA2	1.76	4.1	2.36	6.0	1.82	4.1	-	-

In order to deeply understand the structures of C3A, C12A7, CA, and CA2, the structural parameters are calculated, strictly in accordance with the partial RDF. The partial RDF is shown as follows.

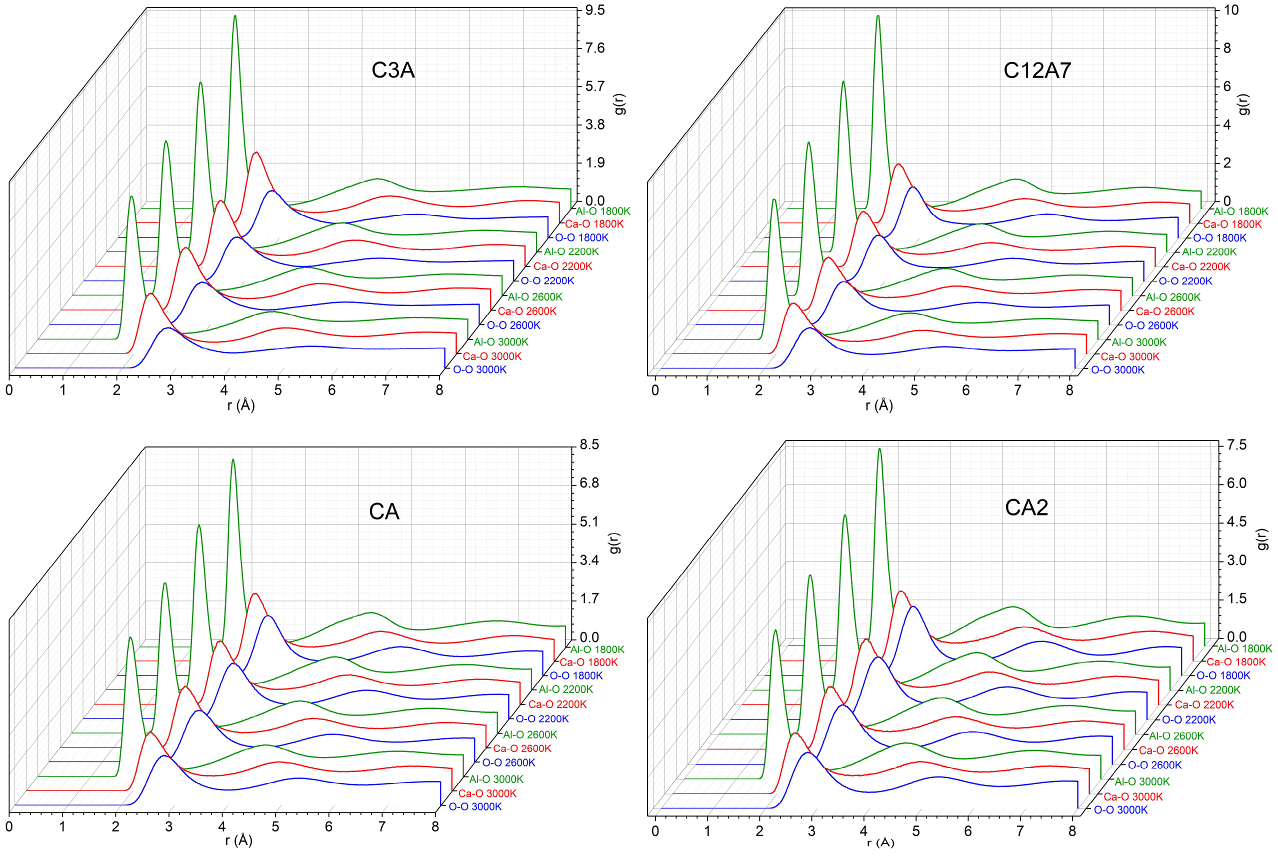

Figure 3-9. Radial distribution functions of Al-O, Ca-O, and O-O of $(CaO)_x(Al_2O_3)_{1-x}$ melts at 1800, 2200, 2600, and 3000 K.

3.3.2.2 Bond length distribution, chemical bond count, and bond angle distribution of $(CaO)_x(Al_2O_3)_{1-x}$ melts at 1800, 2200, 2600, and 3000 K.

MD simulations were carried out for each composition and for four temperatures (1800, 2200, 2600, and 3000 K). If structural parameters have a similar trend, we would choose a composition and a temperature as examples to illustrate this trend.

Bond length distribution (BLD) and bond angle distribution (BAD) show the range of bond length and bond angles, respectively, presenting for a particular atomic triplet. BLD and BAD which are along with radial distribution function and coordination number are important parameters to understand insight into the arrangement of atoms in the structure of a material. Counting the number of chemical bonds is beneficial to directly understanding the changing of bond energy in the melt along with composition and temperature. These structure parameters are listed in detail below.

3.3.2.2.1 Bond length distribution

The bond length distribution of $(CaO)_x(Al_2O_3)_{1-x}$ melts at different temperatures (1800 K, 2200 K, 2600 K, and 3000 K) is shown in Figure 3-10, which are divided into two groups for comparing the difference of BLD along with composition and temperature. Figure 3-10 (a-d) shows the temperature-dependent BLD of C3A, C12A7, CA, and CA2 at different temperatures. The first and second peaks in Figure 3-10(a-c) are the BLD of Al^{3+} bonded to O^{2-} located at 1.76 ± 0.02 Å and the BLD of Ca^{2+} bonded to O^{2-} located at 2.36 ± 0.02 Å, respectively. The BLDs of Al-O and Ca-O end at 2.05 ± 0.02Å and 2.99 ± 0.05 Å, which means the bond length of Al-O $\leq 2.05 \pm 0.02$ Å and Ca-O bond length $\leq 2.92 \pm 0.05$ Å, respectively. The peak of BLD of Ca-O in CA2 is gentle, compare with C3A, C12A7, and CA. That is because there is less content CaO in CA2. This result also corresponds to the total pair distribution function of CA2 in Figure 3-6, where the second peak of the total pair distribution function corresponding to the near-neighbor Ca-O distance is not visible in CA2. In Figure 3-10(d), the first and second peaks are the BLD of Al^{3+} bonded to O^{2-} located at 1.76 ± 0.02 Å and the BLD of Ca^{2+} bonded to O^{2-} located at 2.45 ± 0.03 Å, respectively. The BLDs of Al-O and Ca-O end at 2.15 ± 0.02 Å and 2.83 ± 0.05 Å. Meanwhile, the peak values of BLD corresponding to Al-O are gradually increasing (1800 K, from 1.38 to 2.14) with increasing the content of Al_2O_3 from C3A to CA2. On the contrary, the peak values of BLD corresponding to Ca-O are decreasing (1800 K, from 1.44 to 0.47) along with decreasing CaO. In addition, the areas under the Al-O peak and the Ca-O gradually decrease from 1800 K to 3000 K in Figure 3-10(a-d). It probably expresses that increasing temperature can reduce the count of the Al-O bond and Ca-O bond. It accords that elevated temperature can increase the energy and ionic motion of the system, causing some chemical bonds to break.

Figure 3-10(e-h) shows the composition-dependent BLD. The first and second peaks are mostly located at 1.76 ± 0.02 Å and 2.36 ± 0.05 Å, respectively. The area under the first peak successively becomes small from CA2 to C3A. On the contrary, the area of the second peak successively increases from CA2 to C3A. The content changes of CaO and Al_2O_3 result in this phenomenon. The area difference caused by chemical composition is more obvious, compared with that of the effect of temperature. This result demonstrates that composition has a greater influence on the BLD of the $(CaO)_x(Al_2O_3)_{1-x}$ melts than that of temperature.

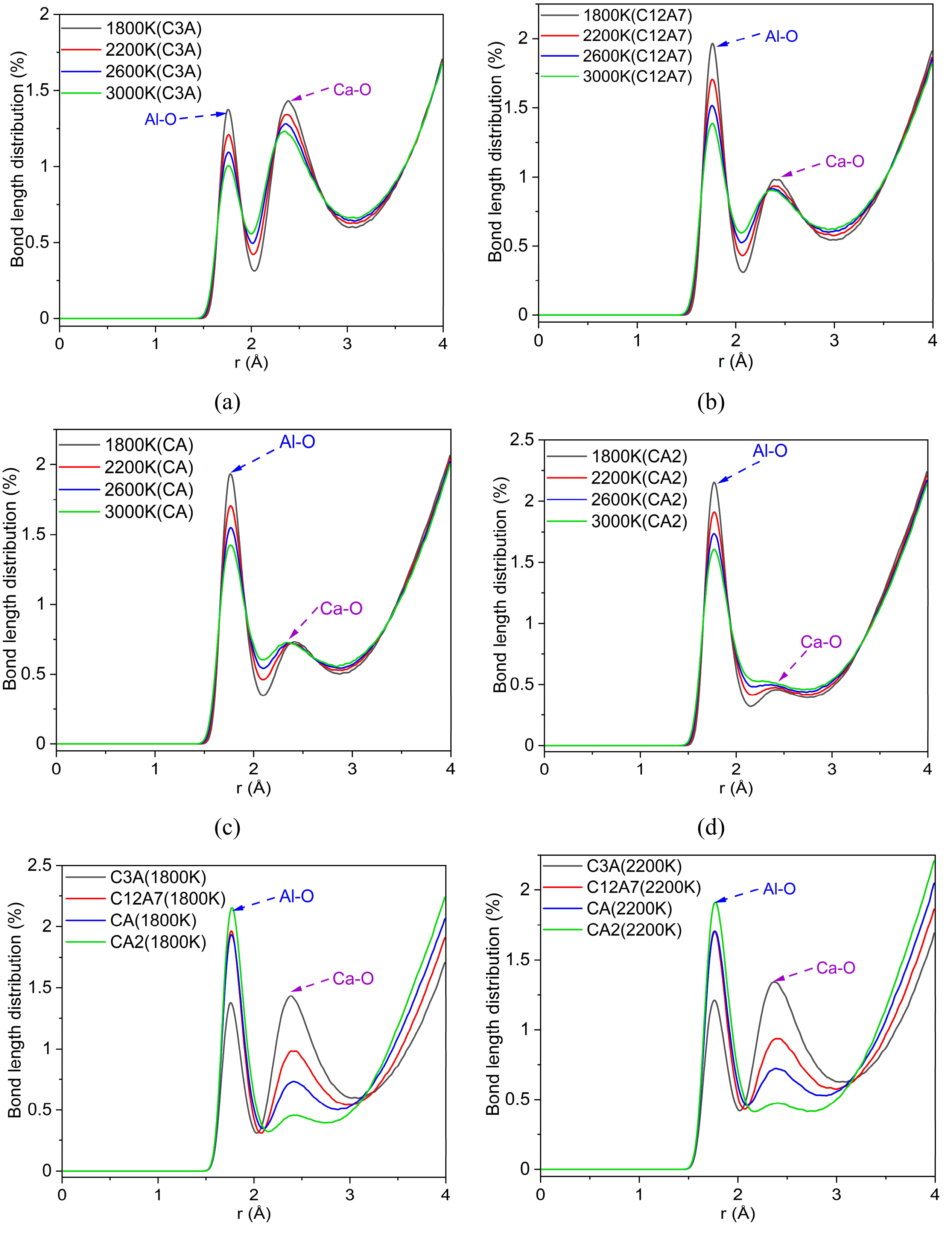
Bond length distribution (%)
r (Å)
1800K(C3A)
2200K(C3A)
2600K(C3A)
3000K(C3A)
Al-O
Ca-O
1800K(C12A7)
2200K(C12A7)
2600K(C12A7)
3000K(C12A7)
Al-O
Ca-O
1800K(CA)
2200K(CA)
2600K(CA)
3000K(CA)
Al-O
Ca-O
1800K(CA2)
2200K(CA2)
2600K(CA2)
3000K(CA2)
Al-O
Ca-O
C3A(1800K)
C12A7(1800K)
CA(1800K)
CA2(1800K)
Al-O
Ca-O
C3A(2200K)
C12A7(2200K)
CA(2200K)
CA2(2200K)
Al-O
Ca-O
0
0.5
1
1.5
2
2.5
0
1
2
3
4

(a) (b)

(c) (d)

(e) (f)

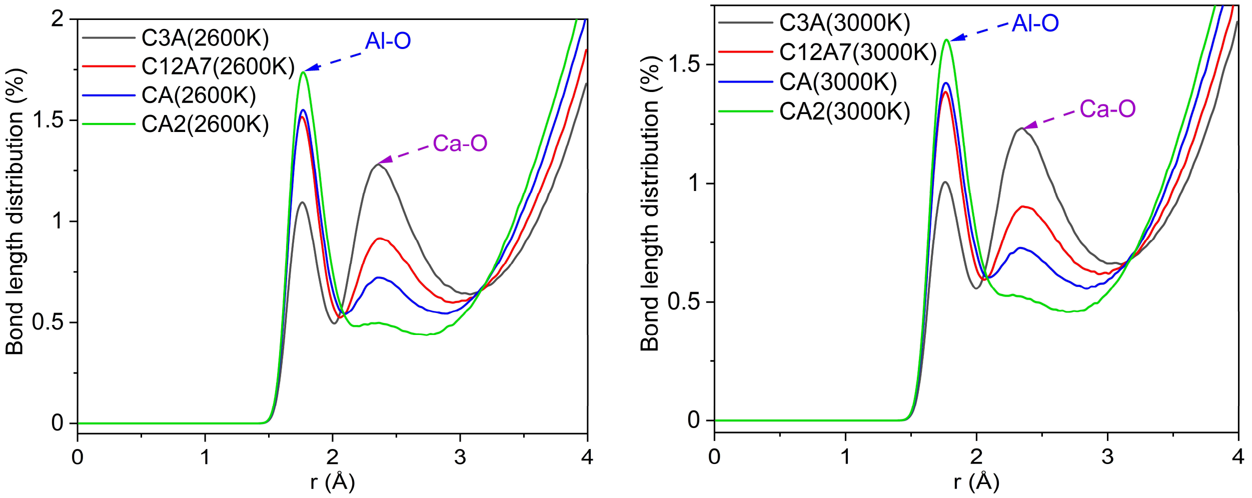

(g) (h)

Figure 3-10. Bond length distribution (BLD) of $(CaO)_x(Al_2O_3)_{1-x}$ melts after normalization along with temperature (cutoff ≤ 4 Å):1. composition (a) C3A, (b) C12A7, (c) CA, (d), CA2; 2. temperature (e) 1800 K, (f) 2200 K, (g) 2200 K, (h) 3000 K.

3.3.2.2.2 Chemical bond count

To verify the effect of composition and temperature on bond energy, Al-O bonds and Ca-O bonds which are ensemble averages taken over all the timesteps in the MD trajectory are counted in simulations of $(CaO)_x(Al_2O_3)_{1-x}$ melts at different temperatures. It is to express the change of bond energy, and the results were plotted in Figure 3-11. As R decreases, the average amount of the Al-O bond increases, while the Ca-O bond number decreases. Taking composition as constant, Ca-O bonds and Al-O bonds slightly decrease with increasing temperature. Taking C12A7 as an example, Al-O and Ca-O bonds in this melt decrease respectively from 5390 to 5272 and from 6849 to 6596 with increasing temperature (1800-3000 K). On the whole, no matter which composition, the amount of Al-O bond and Ca-O bond just slightly decreases with increasing temperature.

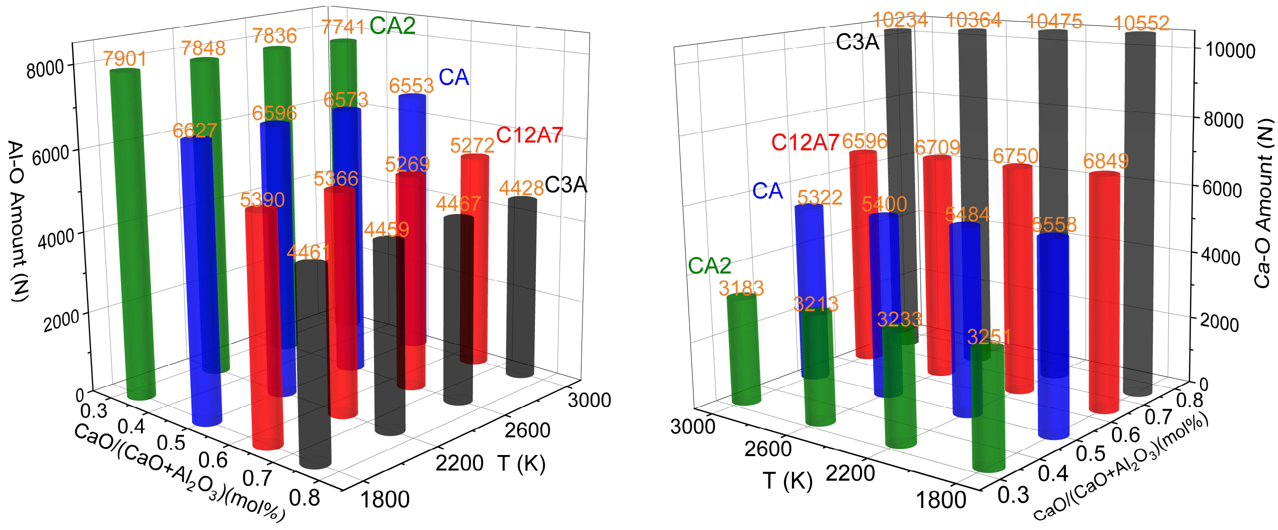

(a) (b)

Figure 3-11. The count of Al^{3+} and Ca^{2+} bonded to O^{2-} of $(CaO)_x(Al_2O_3)_{1-x}$ melts at 1800 K, 2200 K, 2600 K, 3000 K: (a) Al-O bonds; (b) Ca-O bonds.

3.3.2.2.3 Bond angle distribution

In addition, the total bond angle distribution (BAD) of O-Al-O, Al-O-Al, and O-Ca-O in $(CaO)_x(Al_2O_3)_{1-x}$ melts also was studied at different temperatures (1800, 2200, 2600, 3000 K), as shown in Figure 3-12, which are divided into two groups for comparing the difference of total BAD along with composition and temperature. Figure 3-12 (a-d) shows the temperature-dependent BAD of C3A, C12A7, CA, and CA2. And Figure 3-12 (e-h) shows the composition-dependent BAD at 1800, 2200, 2600, 3000 K. Here, we take BAD of O-Al-O, Al-O-Al, and O-Ca-O in C12A7 and at 2200 K as an example to describe relevant explanations.

In Figure 3-12 (b1), with increasing temperature, the intensity of the main peaks of O-Al-O BAD of C12A7 is gradually decreasing and the positions of the main peaks shift from 105.5° to 101.5°. The FWHM of these peaks gradually enlarges. In Figure 3-12 (b2), the intensity of the main peaks of Al-O-Al BAD becomes low and their positions shift to low angles with rising temperature. On the contrary, the shoulders located at 94.5 ± 2° are gradually increasing with an increase in temperature. In Figure 3-12 (b3), the intensity of the main peaks of O-Ca-O BAD are sightly decreasing and their positions shift to high angles with increasing temperature. It is interesting to note that a broad feature centered around 82° exhibits in the O-Ca-O BAD at 1800 K.

In Figure 3-12 (f1), the main peaks of O-Al-O BAD are located at 102.5 ± 1° (C3A, CA, and CA2) and 104.5 ± 1° (C12A7). With decreasing R, the intensity of main peaks and their full width at half maximum (FWHM) are gradually higher and broader, respectively. In Figure 3-12 (f2), the main peaks of Al-O-Al BAD are at 120.5 ± 3° and the shoulders are located at 94.5 ± 2°. With increasing R, the intensity of the main peaks becomes low. The main peaks of O-Ca-O BAD are located at 66.2 ± 1° (C12A7, CA, and CA2) and 72.5 ± 1° (C3A), respectively. The broad features appear at BAD in

Figure 3-12 (f3), where their width and angle location depend on R. With increasing CaO, the intensity of the main peaks of O-Ca-O BAD is increasing. Based on the description of the results, R has a greater influence on the bond angle distribution of $(CaO)_x(Al_2O_3)_{1-x}$ melts than temperature.

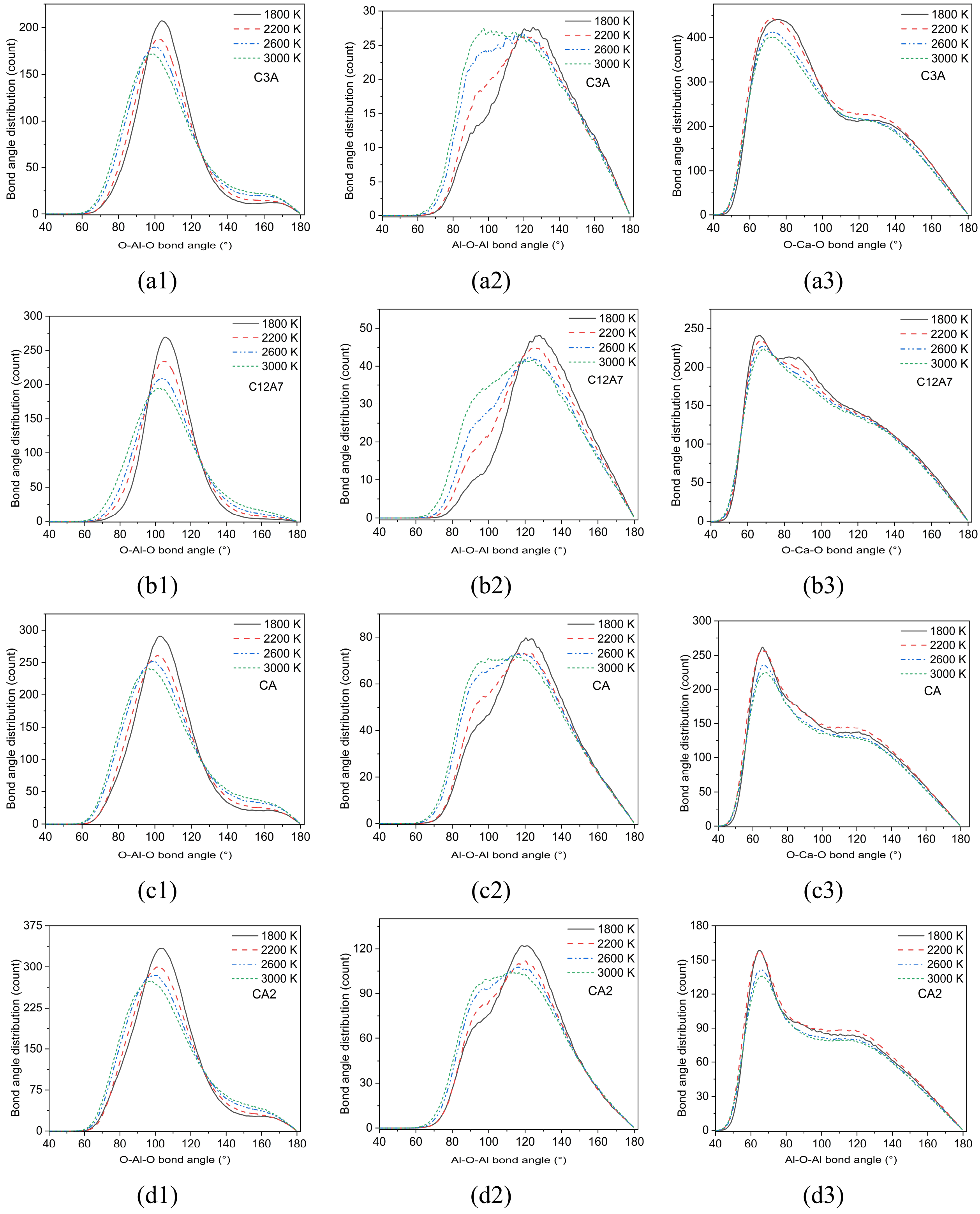

(a1) (a2) (a3)

(b1) (b2) (b3)

(c1) (c2) (c3)

(d1) (d2) (d3)

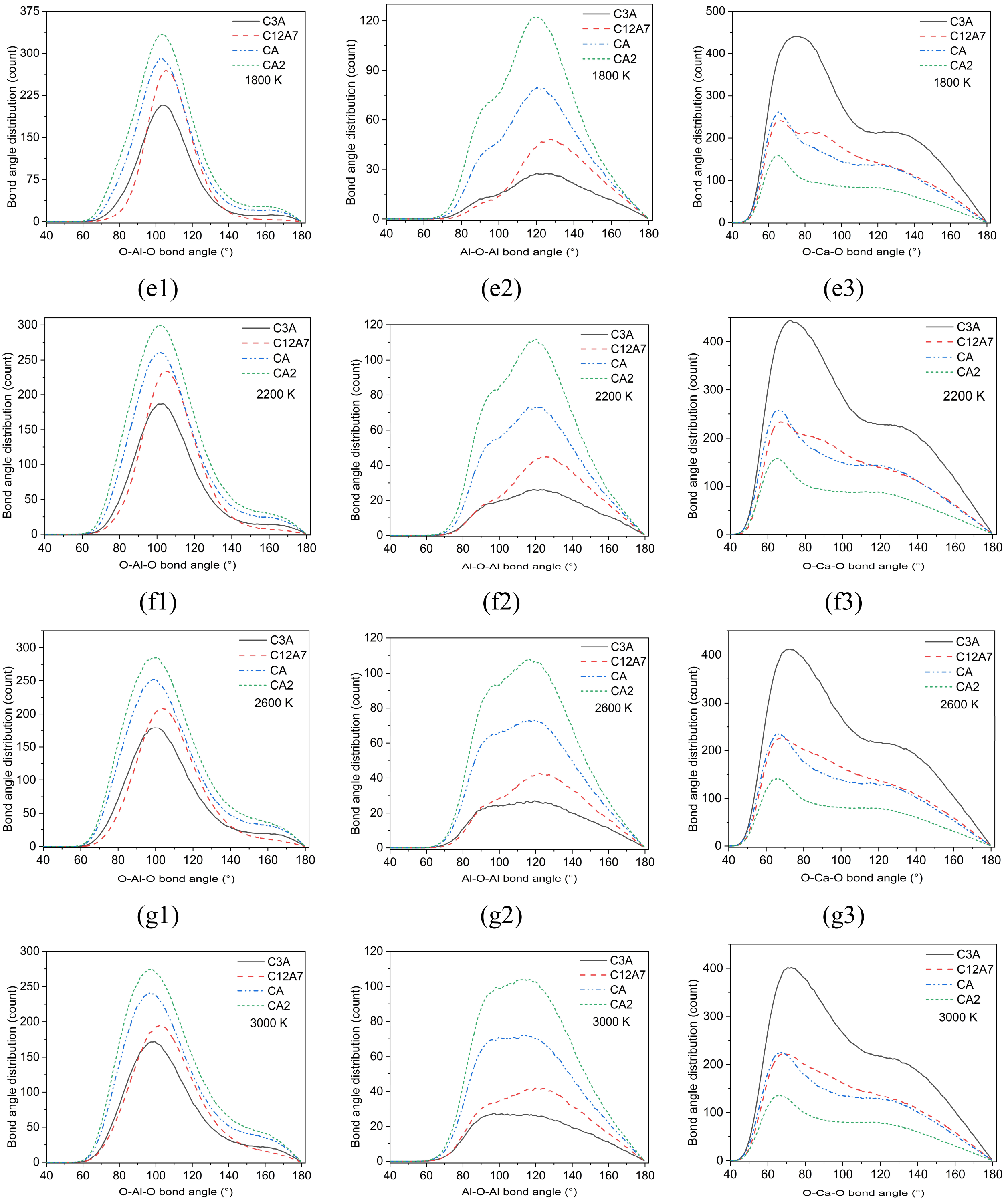

(e1) (e2) (e3)

(f1) (f2) (f3)

(g1) (g2) (g3)

(h1) (h2) (h3)

Figure 3-12. Bond angle distribution (BAD) of O-Al-O, Al-O-Al, and O-Ca-O of the $(CaO)_x(Al_2O_3)_{1-x}$ melts. Composition: (a) C3A, (b) C12A7, (c) CA, (d) CA2; Temperature: (e) 1800 K, (f) 2200 K, (g) 2600 K, (h) 3000K.

The O-Al-O BAD is related to Al coordination numbers, which reflects the bonding of an Al atom and two O atoms in $[AlO_n]$ units. The fraction of $[AlO_n]$ species in the $(CaO)_x(Al_2O_3)_{1-x}$ melts at 2200K and in C12A7 at different temperatures are shown in Figure 3-13 (a1, a2). The O-Ca-O BAD is related to Ca coordination numbers. Here the Ca coordination number in C12A7 is shown in Figure 3-13 (b), to help discuss the evolution of O-Ca-O BAD in C12A7.

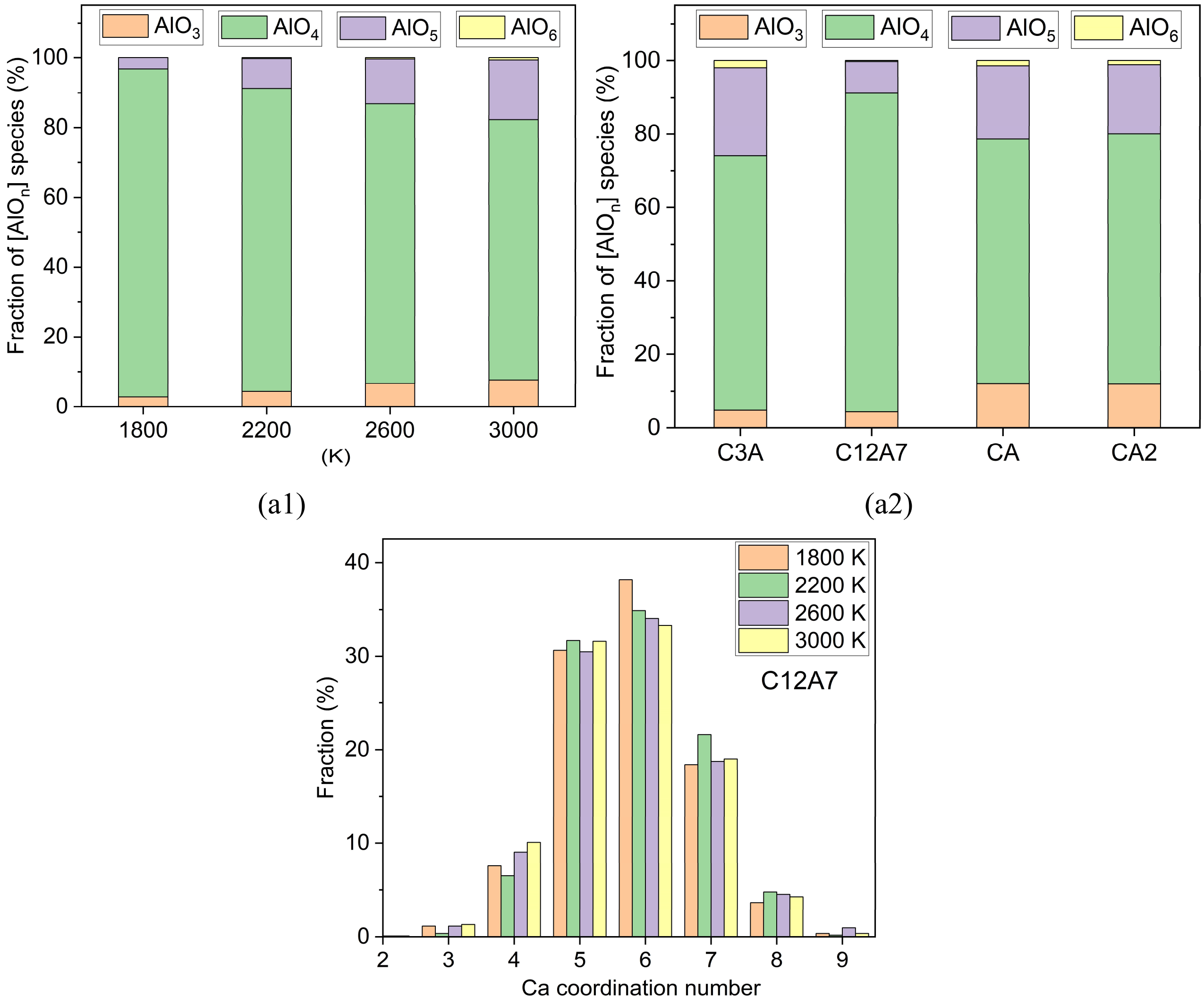

(a1) (a2)

(b)

Figure 3-13. Factions of $[AlO_n]$ species and Ca coordination number: (a1) Factions of $[AlO_n]$ species in C12A7 at different temperatures; (a2) Factions of $[AlO_n]$ species in the $(CaO)_x(Al_2O_3)_{1-x}$ melts at 2200 K; (b) Ca coordination number in C12A7.

A snapshot taken from the MD simulation is shown in Figure 3-14 to visualize and discuss the origin of the main peaks observed in BAD.

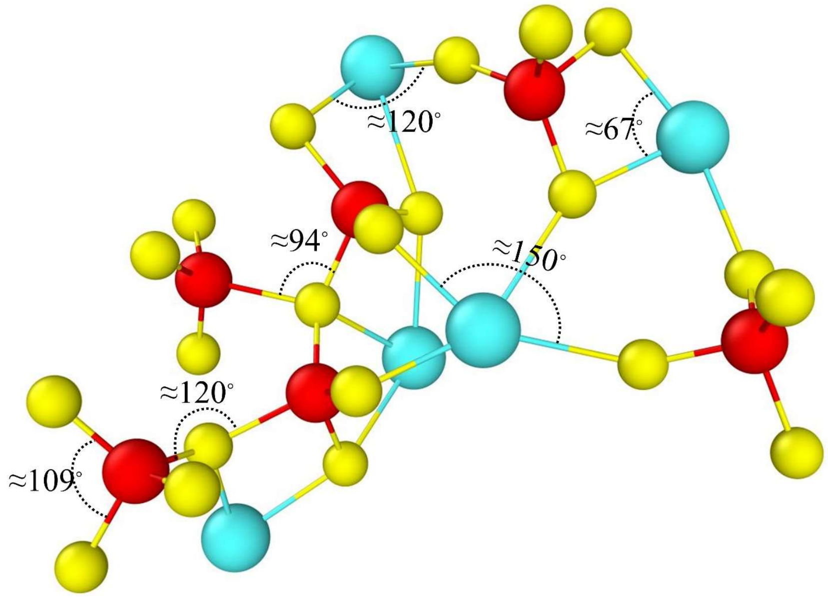

Figure 3-14. A snapshot is taken from the MD simulation of the structure of the C12A7 melt illustrating the origin of the main peaks observed in the bond angle distributions shown in Figure 3-12.

3.3.2.3 Oxygen species, the degree of charge compensation, and unsatisfied oxygen bonds of $(CaO)_x(Al_2O_3)_{1-x}$ melts at 1800, 2200, 2600, and 3000 K.

3.3.2.3.1 Oxygen species

To understand deeply the effect of structure on thermophysical properties, bridging oxygen (BO), non-bridging oxygen (NBO), tri-cluster oxygen (TCO), and free oxygen (FO) were defined (Section 3.3.2.1) and analyzed in each MD simulation for the $(CaO)_x(Al_2O_3)_{1-x}$ melts.

The contents of BO, NBO, TCO, and FO, in C3A, C12A7, CA, and CA2 at 1800, 2200, 2600, and 3000 K are described in Figure 3-15. By analyzing Figure 3-15(a)(b)(c)(d), the content of BO in C12A7, CA, and CA2 gradually increases (C3A: 0.375 to 0.408, C12A7: 0.533 to 0.640, CA: 0.532 to 0.635, and CA2: 0.495 to 0.570) with decreasing temperature. The content of TCO gradually increases (C3A: from 0.023 to 0.064, C12A7: from 0.049 to 0.114, CA: from 0.20 to 0.288, and CA2: 0.357 to 0.410) with increasing temperature (1800-3000 K). The content of NBO in C3A reduces with increasing temperature. For other compositions, the NBO just slightly increases with increasing temperature. The content of FO is seemingly not sensitive to temperature.

Meanwhile, we can find that the trends of BO, NBO, TCO, and FO contents in the $(CaO)_x(Al_2O_3)_{1-x}$ melts at 1800 K, 2200 K, 2600 K, and 3000 K are extremely similar by observing Figure 3-15 (e)(f)(g)(h). So taking the trends of BO, NBO, TCO, and FO in $(CaO)_x(Al_2O_3)_{1-x}$ melts at 2200 K as an example, it describes and explains the evolution of oxygen species. The content of NBO and FO in the $(CaO)_x(Al_2O_3)_{1-x}$ melts gradually increases with an increase of R: NBO dramatically increases (0.079-0.450), and there is an obvious increase (0.021-0.098) for FO from C12A7 to C3A. On the contrary, the content of TCO decreases (0.385-0.055) with increasing R (from CA2 to C3A). It is worth mentioning that the content of BO increases firstly from 0.533 to 0.587 and then decreases to 0.395 with increasing R, C12A7 (BO = 0.587) is an obvious turning point for $(CaO)_x(Al_2O_3)_{1-x}$ melts.

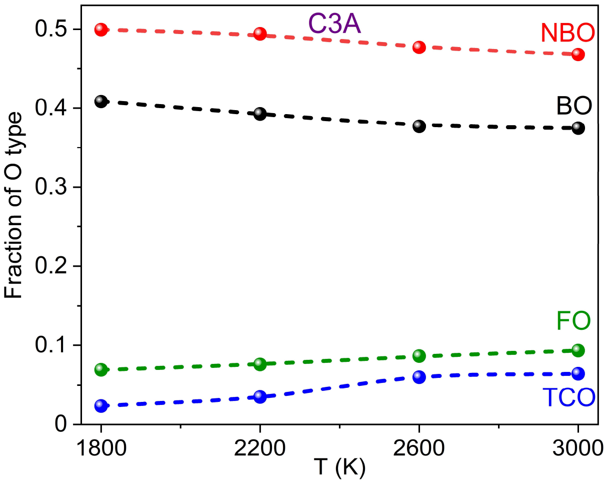

(a)

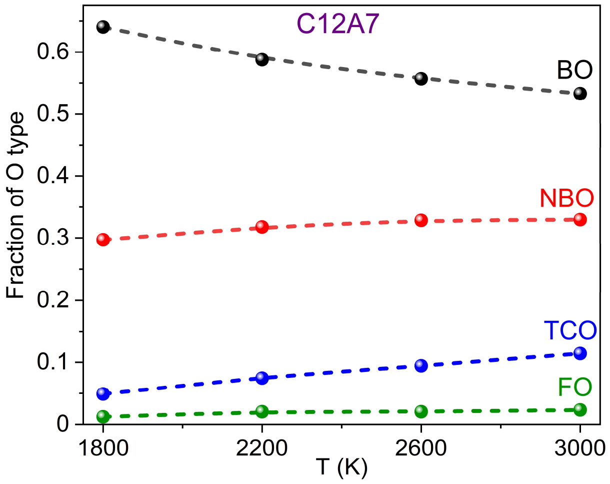

(b)

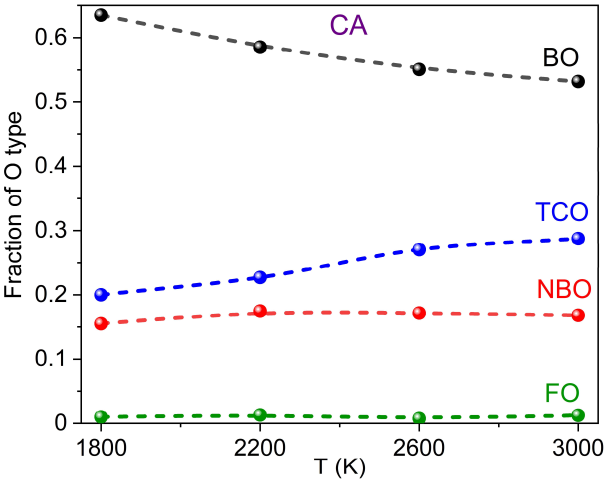

(c)

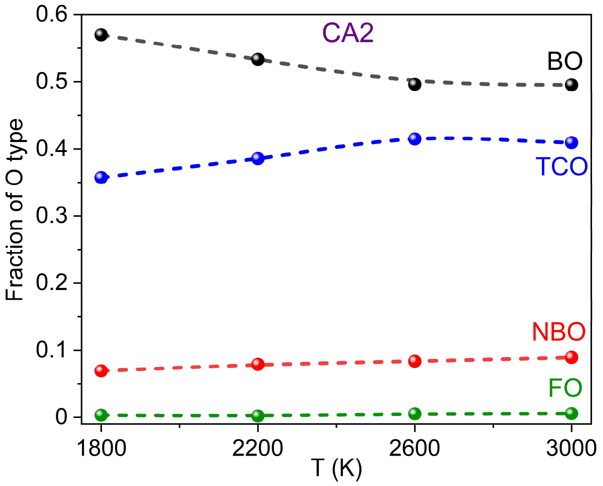

(d)

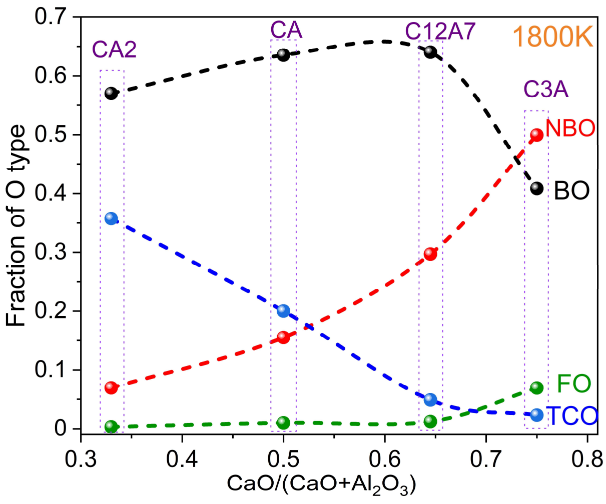

(e)

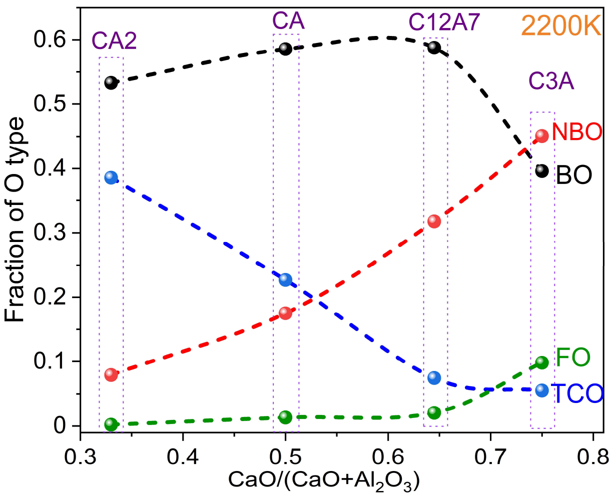

(f)

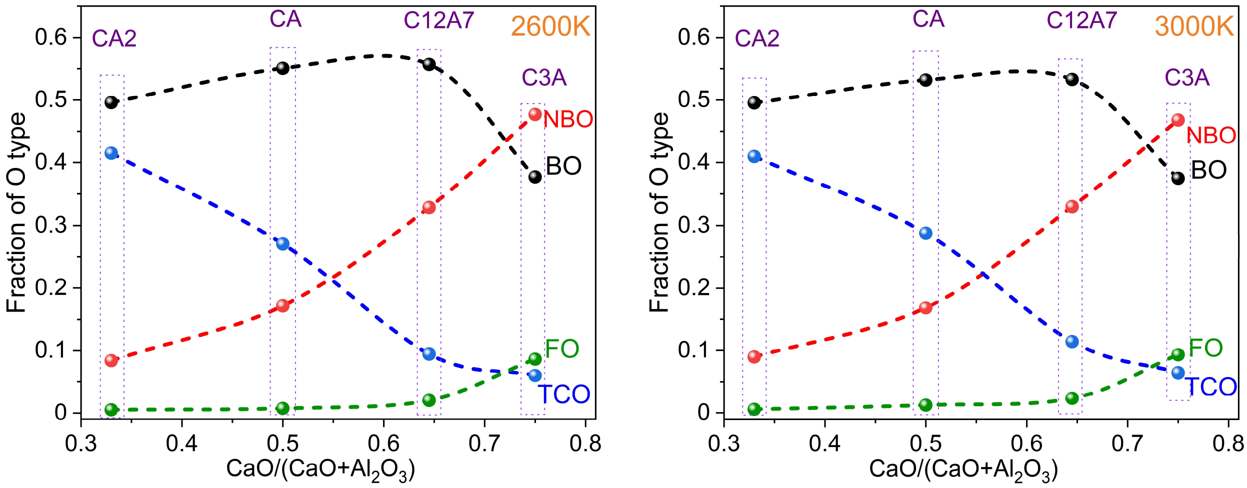

(g) (h)

Figure 3-15. Oxygen speciation BO, NBO, TCO, and FO in $(CaO)_x(Al_2O_3)_{1-x}$ melts. i) temperature-dependent BO, NBO, TCO, and FO in (a) C3A, (b) C12A7, (c) CA, and (d) CA2 at different temperatures; ii) composition-dependent BO, NBO, TCO, and FO in $(CaO)_x(Al_2O_3)_{1-x}$ melts at (e-f) 1800, 2200, 2600, and 3000 K.

Table 3-5. The trends of BO, TCO, NBO and FO with x (x=R/Temperature)

$\frac{\partial(\text{oxygen species})}{\partial x}$	BO	TCO	NBO (C3A)	NBO (others)	FO
x = R	+, -	-	+		**~ 0,+**
x = Temperature	-	+	-	~ +	**~ 0**

"+": increase "-": decrease "~": constant "~ 0": tending to zero

3.3.2.3.2 The degree of charge compensation

Ca^{2+} cations play a dual role in $(CaO)_x(Al_2O_3)_{1-x}$ melts as network modifiers and charge compensators. As charge compensator, the Ca^{2+} cation offers unbalanced charges for specific oxygens which are connected to two or more network-forming [AlO_n] polyhedrons. By counting the ratio of these specific oxygen atoms to all oxygen atoms, the degree of charge compensation was obtained and listed in Figure 3-16. The degree of charge compensation in each composition decreases with increasing temperature while that of C3A is not sensitive to the temperature. Compared with the effect of temperature, the degree of charge compensation in $(CaO)_x(Al_2O_3)_{1-x}$ melts increases firstly and then decreases with increasing R, where CA is the turning point for this process. In addition, based on the comparison and analysis of results, R has a greater influence on the degree of charge compensation than temperature.

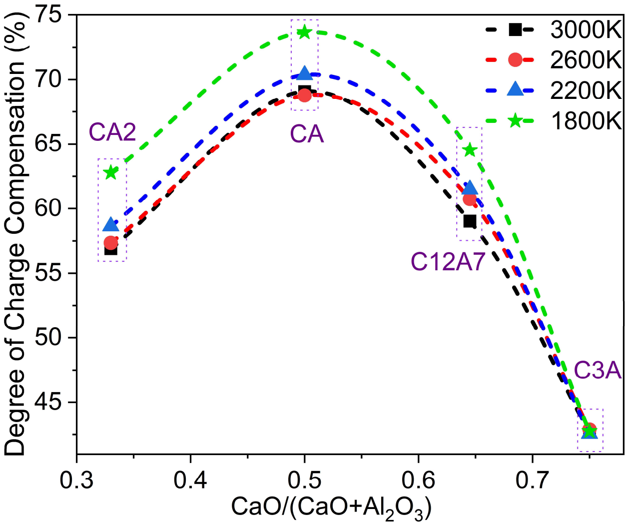

Figure 3-16. The degree of charge compensation of the $(CaO)_x(Al_2O_3)_{1-x}$ melts at different temperatures.

3.3.2.3.3 Unsatisfied oxygen bonds

Surface tension is considered to be related to UOBs at the surface layer of the melt. However, the present MD simulations focus more on the bulk phase and the following interpretation is an initial attempt to explore the relationship between surface tension and UOBs, thus laying the foundation for a more precise study of the surface layer in future studies. In addition, the description of UOBs is still abstract. Further understanding, the definition of modified UOBs is reified as follows: partial oxygen ions forming stable bonds with network-formed cations still need network-modified cations to keep charge balance and partial NBOs are bonding with modifying cations, which forms modified unsatisfied oxygen bonds; Additionally, it is worth noting that in the $(CaO)_x(Al_2O_3)_{1-x}$ melts, charge compensation of $[AlO_4]$ is accomplished by the formation of three coordinated oxygens (as known as TCO) [J. Du et al., 2022].

Specific classifications are

2Al-O-n[Ca] (an oxygen atom bonding with two Al atoms connects $n \geq 1$ Ca atoms),

3Al-O-n[Ca] (an oxygen atom bonding with three Al atoms connects $n \geq 1$ Ca atoms),

2Al-O-[Al] (an oxygen atom bonding with three Al atoms),

Al-O-n[Ca] (an oxygen atom bonding with one Al atom connects $n \geq 1$ Ca atoms),

where [atom] is as a charge compensator. For the CaO-Al_2O_3 system, the O-Ca and pure Al-O-Al are categorized into satisfied oxygen bonds (OBs).

Modified UOBs and OBs in the $(CaO)_x(Al_2O_3)_{1-x}$ melts at different temperatures are shown in Figure 3-17. Figure 3-17 (a-d) expresses temperature-dependent UOBs and OBs in C3A, C12A7, CA, and CA2. with increasing temperatures, the content of 2Al-O-n[Ca] is gradually decreasing and the contents 3Al-O-n[Ca] and 2Al-O-[Al] are increasing. The changes of Al-O-n[Ca] and OBs are slightly increasing, while the Al-O-n[Ca] of C3A decreases. The fraction of OBs is slightly increasing with increasing temperature. However, the total content of the UOBs caused by charge compensation (2Al-O-n[Ca], 3Al-O-n[Ca], and 2Al-O-[Al]) is only slightly decreasing in C12A7, CA, and CA2. From Figure 3-17 (e-f), with decreasing R, the OBs decrease first and then increase, while the total content of modified UOBs has an opposite trend. Further, the content of Al-O-n[Ca] is reducing, while the contents of 3Al-O-n[Ca] and 2Al-O-[Al] are gradually increasing. The content of 2Al-O-n[Ca] climbs up and then declines, which correspondings to the content change of BO. It is worth mentioning that the total content of the modified UOBs caused by charge compensation is gradually increasing.

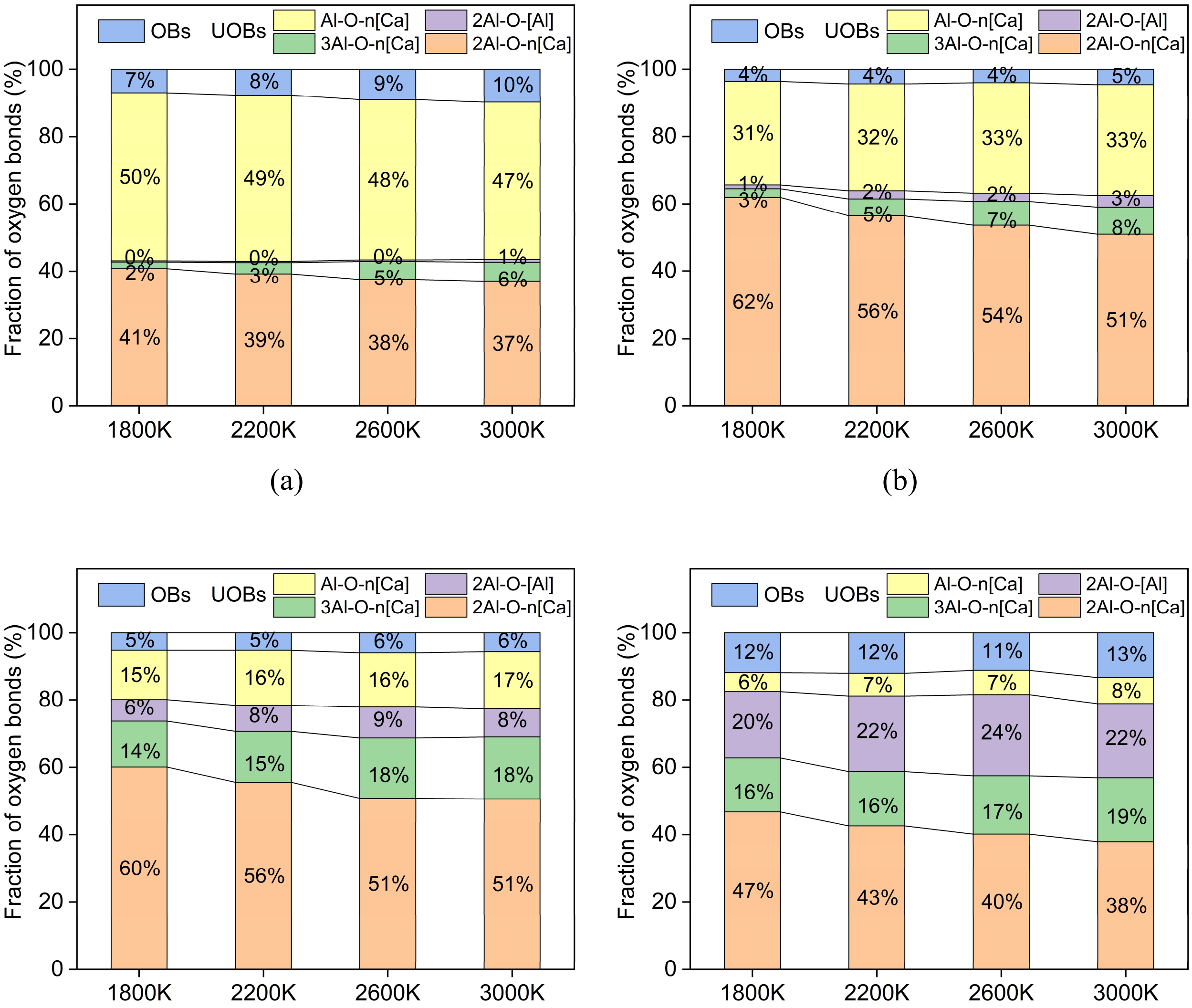

(a) (b)

(c) (d)

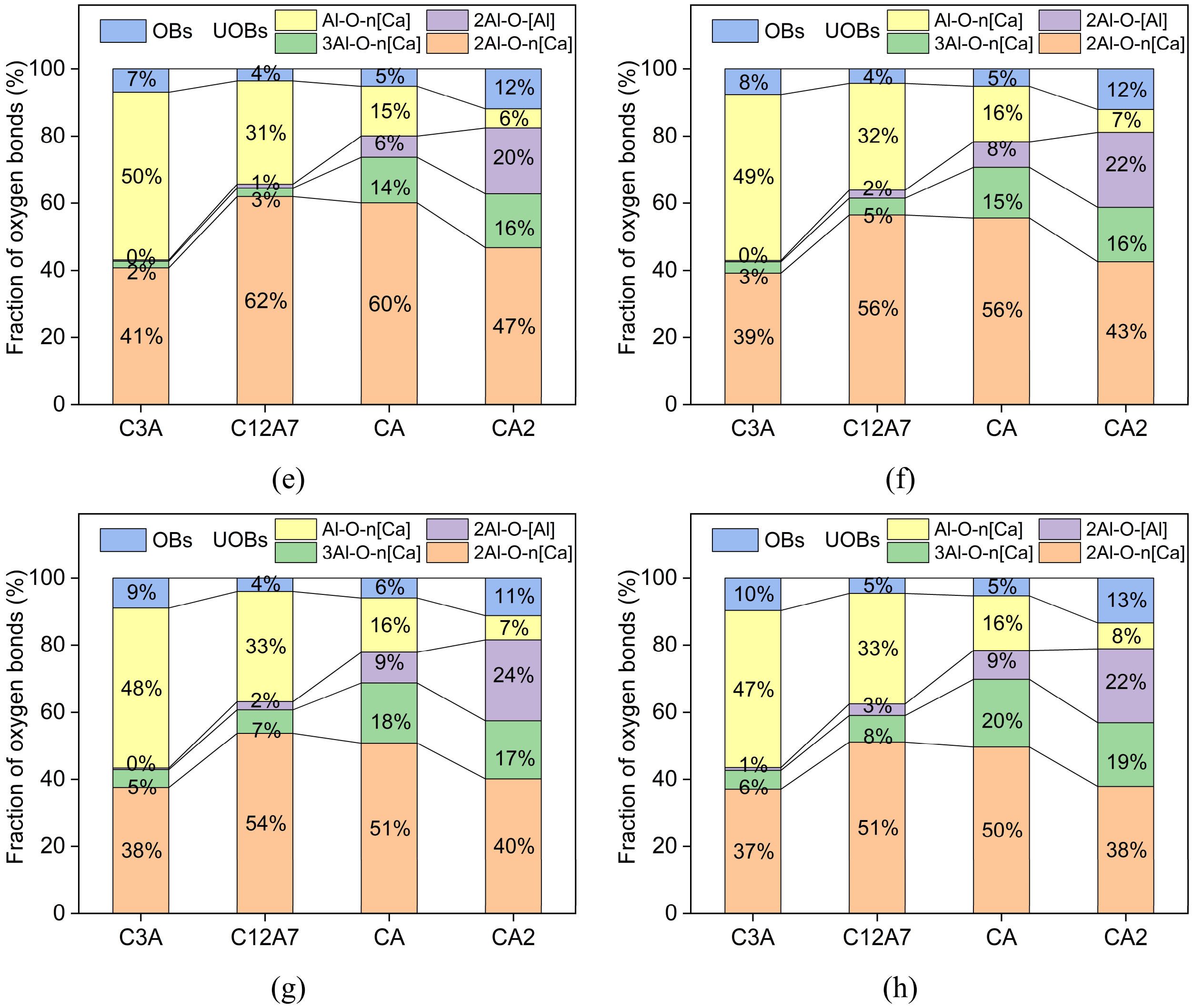

(e) (f)

(g) (h)

Figure 3-17. Fraction of oxygen bonds (normalization) in the $(CaO)_x(Al_2O_3)_{1-x}$ melts. Composition: (a) C3A, (b) C12A7, (c) CA (d) CA2; Temperature: (e) 1800 K, (f) 2200 K, (g) 2600 K, (h) 3000 K.

3.4 Discussions

3.4.1 The influence of temperatures and R=CaO/Al_2O_3 on the structural parameters of $(CaO)_x(Al_2O_3)_{1-x}$ melts

Based on the results of the structural parameters, the effects of temperature and R on the structure of the $(CaO)_x(Al_2O_3)_{1-x}$ melts are observed. Increasing temperature can improve the energy and atomic motion of the system, which causes some bonds to break free from the bondage of the interaction, thereby breaking some bond connections. It results in the peaks of BLD gradually decreasing with an increase in temperature. With increasing R, CaO content and Al_2O_3 content are increasing and decreasing, respectively, corresponding to the changes of BLDs of Al-O and Ca-O.

The O-Al-O BAD is related to the Al coordination number, which is in agreement with the content of [AlO_n] species. The O-Al-O bond angle in a perfect tetrahedron is equal to $\cos^{-1}(-1/3) = 109^\circ$. The existence of threefold, fivefold, and sixfold coordinated Al species makes the peaks of O-Al-O BAD shift away 109°. An obvious decrease of [AlO_5] in the C12A7 melt causes an increase in the weight ratio of [AlO_4], which makes the peak of BAD shift towards 109°, compared to the other three compositions. With decreasing R, the FWHM of the main peak is larger with higher Al_2O_3 concentration reflecting the greater content of [AlO_n] polyhedron. The Al-O-Al BAD reveals insight into how the [AlO_n] are relative to each other [Zhao et al., 2019]. The peak at ≈ 120.5° in the Al-O-Al BAD arises from corner-shared polyhedrons. The peaks at ≈ 94.5° may indicate twofold rings representing $AlO_{(4,5)}$ polyhedrons shared by an edge. Further analysis shows the bridging oxygens are concentrated around 120° and the peaks at ≈ 90° arise from configurations that involve oxygens with three nearest Al neighbors (TCO) [Drewitt et al., 2011]. With increasing R, the intensity of the main peaks and shoulders reduces, where the change of the shoulders is in agreement with the evolutions of TCO in the $(CaO)_x(Al_2O_3)_{1-x}$ melts at 2200 K. It means that the intensity of the Al-O-Al BAD is related to the total content of BO and TCO.

The main peaks of O-Ca-O BAD around 67° originate from Ca bonded to two O atoms of the same [AlO_4] tetrahedron forming distorted triangles. In addition, the broad features in BAD arise from Ca connected to two O atoms of two different [AlO_n] polyhedrons. This kind of O-Ca-O bonding is related to charge compensation, corresponding to a broad angle range.

With increasing temperature, the weight ratio of [AlO_3], [AlO_5], and [AlO_6] are gradually increasing, which makes the intensity of the main peaks of O-Al-O BAD lower and FWHM broader. TCO and BO are respectively increasing and decreasing with rising temperature, corresponding to the intensity of the shoulders at 94° and the main peaks around 125° in Al-O-Al BAD have respectively an increase and a decrease. The O-Ca-O BAD at 1800 K exhibits a broad feature centered around 82° possibly indicative of distorted sixfold octahedra [Drewitt et al., 2011], which is consistent with an increase in sixfold coordinated Ca species (Figure 3-13 (b)). The intensity and FWHM of the peaks are probably related to the influence of temperature on charge compensation.

In the influence of temperature on oxygen species in $(CaO)_x(Al_2O_3)_{1-x}$ melts, a possible explanation for an increase of BO and a decrease of TCO with decreasing temperature is as follows: tri-cluster oxygen which is shared by three Al^{3+} cations belongs to an unstable configuration. The higher temperature can maintain the formation of tri-cluster oxygen configurations. Once the temperature goes down, tri-cluster oxygen configurations could resolve into BO or NBO configurations with lower energy. Furthermore, the explanations for the influence of composition on oxygen species depend on the network former/modifier (Al_2O_3/CaO) ratio. The CA2 melt with the lowest CaO content has the highest TCO content than the other compositions. Whereas TCO as unstable configurations would be cut into BO or NBO by network modifier cations (Ca^{2+}). So at the lower R, it is prior for the high content of TCO to be resolved and transformed into BO or partial NBO with increasing CaO content, which causes an increase in their content. With further increasing R, when the CaO network modifier is abundant and the content of TCO is low, Ca^{2+} would cut more BO in the network to unceasingly generate NBO. It leads to a dramatic decrease in BO and a continuous increase in NBO from C12A7 to C3A. Meanwhile, CaO as network modifiers can reduce the polymerization degree of melts to increase NBO and generate FO as well. The dual effects lead to a bigger increasing range of NBO than that of BO and FO.

Although Ca^{2+} cations are network modifiers for breaking the network in the whole process, they are prior as charge compensators at the lower R, since Ca^{2+} cations are absent and anionic polymer groups need charge balance. With improving R, Ca^{2+} cations become plentiful in melts, while the charge compensation also reaches the upper limit. Further increasing R, Ca^{2+} acts as network modifiers to destroy BO and decrease the polymerization degree of [AlO_n] polyhedrons. These above aspects cause Ca^{2+} cations to wreak havoc on the network of the melt, which corroborates the sharp decline of charge compensation and BO content from C12A7 to C3A.

In order to facilitate a more in-depth analysis, the partial skeleton of the network structure, the dual roles of Ca^{2+}, the evolution of charge compensators, and network modifiers on the structure were singled out from a virtualized system, described in Figure 3-18. In the following discussion section, we will combine our experimental thermophysical properties with the evolution of structural parameters in MD simulations, bringing out the correlations between the structure and thermophysical properties in $(CaO)_x(Al_2O_3)_{1-x}$ melts.

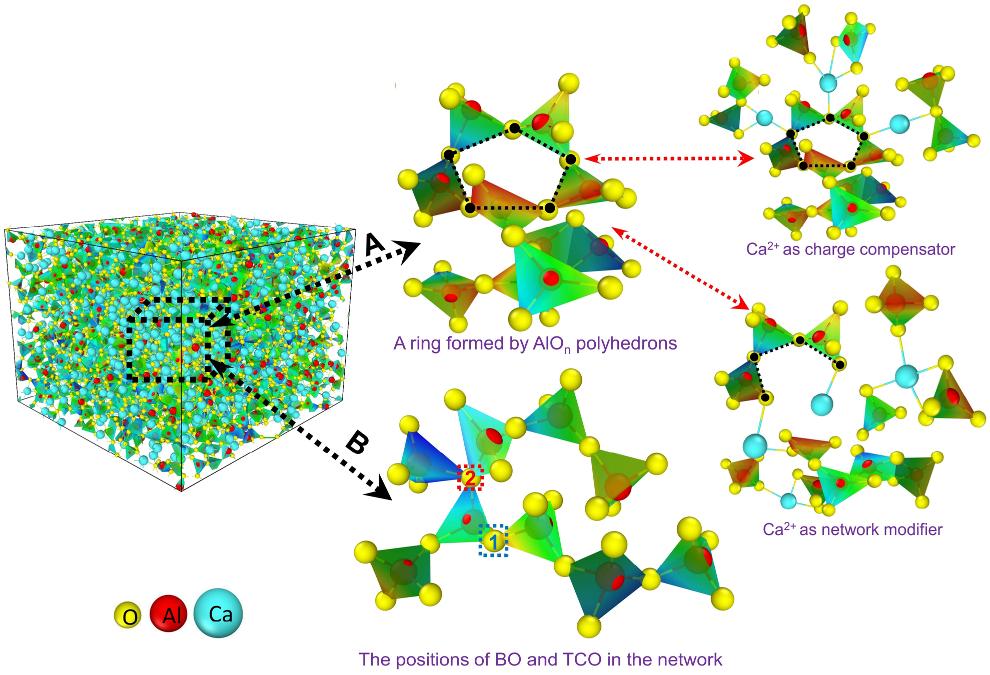

Figure 3-18. Partial skeletons of network structure and evolutions of charge compensators and network modifiers in the structure of $(CaO)_x(Al_2O_3)_{1-x}$ melts: Process A: the black dot line describes a ring formed by AlO_n polyhedrons; Process B: 1 represents a position of BO and 2 for TCO.

3.4.2 The influences of R=CaO/Al_2O_3 and temperatures on the thermophysical properties of $(CaO)_x(Al_2O_3)_{1-x}$ melts

3.4.2.1 Density

From the R point of view, compositional variation in $(CaO)_x(Al_2O_3)_{1-x}$ melts has a significant effect on bond lengths, bond angles, microstructural units, and oxygen network structures. With increasing R, Al-O bonds decrease and Ca-O bonds increase, plus the length of Al-O bonds is shorter than that of Ca-O bonds, which causes the increase of micro-volume in $(CaO)_x(Al_2O_3)_{1-x}$ melts. From CA2 to C3A, the intensity of the Al-O-Al BAD is gradually decreasing, which means a decrease in the connectivity of $[AlO_n]$ each other to possibly reduce the twining degree of $[AlO_n]$. Because there are many rings consisting of $[AlO_n]$ polyhedrons in the melts with low R that are derived from edge-sharing and corner-sharing of $[AlO_n]$ polyhedrons [Akola et al., 2013], as shown in Figure 3-18. The decrease in the connectivity of $[AlO_n]$ would decrease this type of polymerization connectivity. In addition, abundant tri-cluster oxygen (TCO) configurations with a high polymerization degree are also in $(CaO)_x(Al_2O_3)_{1-x}$ melts with low R. Ca^{2+} cations as network modifiers could cut off the ring of $[AlO_n]$ polyhedrons, the TCO configurations, and bridging oxygens (BO), which generates more and more non-bridging oxygen (NBO) and microstructural units to reduce the polymerization degree of network structure. Accordingly, a mass of smaller microstructural units can lead to an increase in volume. Meanwhile, the density of Al_2O_3 (3.97 g/cm^3) is more than CaO (3.34 g/cm^3), which is a non-negligible reason. These could be explanations for why the density decreases successively with increasing R.

As we analyzed earlier, regarding the effect of temperature on the density of $(CaO)_x(Al_2O_3)_{1-x}$ melts, the increasing temperature can cause to break off some Al-O bonds and Ca-O bonds and make some atoms in a free state. In addition, the increasing temperature leads to a decrease in BO content and an increase in TCO. Here, further analysis is necessary for these two opposite influences. In glasses network structure, BO and TCO can be connection points to form a network skeleton, shown in Figure 3-18: process B. However, the formation of TCO and the breaking of BO are different impacts on the polymerization degree of network structure. From Figure 3-18, if position 1 was broken, its destructiveness on the connection of the network skeleton probably is more than the formation of TCO at position 2. So the decrease in BO content can not only counterbalance the influence of the TCO formation but also generate microstructural units and reduced the degree of polymerization. Meanwhile, increasing temperature causes a decrease in the total content of BO and TCO, which means a decrease in the connectivity of $[AlO_n]$ polyhedrons, making some structural units in a dissociated state. Furthermore, Ca^{2+} cations as charge compensators can promote the compactness of $[AlO_n]$ polyhedrons in the network structure. Improving temperature leads to a decrease in the degree of charge compensation. More structural units in a dissociated state would decrease the twining degree of each other to promote volume increase. The above explains why the temperature rise causes the decrease in density of the $(CaO)_x(Al_2O_3)_{1-x}$ melts.

3.4.2.2 Surface tension

It is necessary to mention that 2Al-O and 3Al-O express an O atom shared by two [AlO_n] units and an O atom shared by three [AlO_n] units, respectively. The contents of 2Al-O-n[Ca], 3Al-O-n[Ca], and 2Al-O-[Al] are related to the change of BO and TCO, respectively, where Al-O-n[Ca] is equal to NBO. The oxygen atoms are shared by multi-[AlO_n] units, where the forming groups more require extra compensating charges to maintain the electrical neutrality of the network due to the electronegativity of the anionic units. Thus, 2Al-O-n[Ca], 3Al-O-n[Ca], and 2Al-O-[Al] could have a greater influence on surface tension than Al-O-n[Ca]. With decreasing R, the total content of modified UOBs shows an increase first and then a decrease. Furthermore, decreasing R results in a decrease in the content of Al-O-n[Ca] and an increase in the content of 3Al-O-n[Ca] and 2Al-O-[Al], where the content of 2Al-O-n[Ca] shows the same trend with BO (climb up and then decline). However, the total content of the modified UOBs caused by charge compensation is gradually increasing. In CA2, although the content of modified UOBs is lowest, the total content of the modified UOBs caused by charge compensation is highest, leading to the largest surface tension. Additionally, in C12A7, CA, and CA2, increasing temperature causes an increase in the content of 3Al-O-n[Ca], 2Al-O-[Al], Al-O-n[Ca], and OBs, and a decrease in the content of 2Al-O-n[Ca]. However, the total content of the UOBs caused by charge compensation is slightly decreasing with an increase in temperature. This and an increase of OBs not only counteract the influence of the slight increase in Al-O-n[Ca] but also lead to a slight decrease in surface tension. C3A has a slight difference from other compositions. In C3A, a decrease in the content of Al-O-n[Ca], a slight increase in OBs, and a slight increase in the content of the UOBs caused by charge compensation result in a slight decrease in the surface tension. Based on the above description, the clear influence ratio of different UOBs on surface tension is still a challenging issue for future study.

3.4.2.3 Viscosity

R and temperature have a great influence on the viscosity of $(CaO)_x(Al_2O_3)_{1-x}$ melts as well, as shown in Figure 3-4 (c2). It is generally recognized that viscosity is related to the degree of polymerization of the network structure. So the impact factors on the degree of polymerization, such as BO, NBO, and the charge compensation, are crucial for studying the viscosity of melts.

At the lower R, TCO configurations are numerous in CA2 melts. One role of Ca^{2+} cations as network modifiers can break off unstable TCO configurations into BO or NBO, which causes the increase of BO and NBO, and the decrease of TCO. As we analyzed the influence of the formation of TCO and the breaking of BO on the network skeleton, the effect of breaking TCO configurations on the skeleton of the network structure is rather limited as well. However, at the lower R, Ca^{2+} cations as charge compensators are dominated in melts. The degree of charge compensation gradually increases from CA2 to CA, shown in Figure 3-16. From Figure 3-18, Ca^{2+} cations as charge compensators can make the network structure closer, which increases the degree of polymerization in melts. With unceasingly improving R, the CaO composition is up to high content and $[AlO_n]$ polyhedrons are decreasing. Ca^{2+} cations as network modifiers would dominate the structure of melts after the charge compensation achieves a saturation state. As more rings formed by $[AlO_n]$ polyhedrons are opened by network modifiers, the degree of charge compensation in C3A is less than that in CA2. Ca^{2+} cations which are used as charge compensators may also be transformed into network modifiers. During this process from C12A7 to C3A, the content of BO suddenly reduces and NBO content dramatically increases, which results in a sharp decrease in polymerization degree. It is interesting to note TCO in the process from C12A7 to C3A decreases relatively slowly, which could confirm the above description about the role exchange of network modifiers and charge compensators. Furthermore, the trends of BO and the degree of charge compensation are closely similar to the trend of experimental viscosity, which reveals the consistent correlation of BO and the degree of charge compensation on viscosity. The above analysis explains that the viscosity η of $(CaO)_x(Al_2O_3)_{1-x}$ melts increases firstly and then decreases with increasing R, where CA is the turning point, η_{C12A7} is between η_{CA} and η_{CA2}, and the viscosity η of C3A is less than that of CA2.

Both BO and the degree of charge compensation decrease, and TCO increases, as the temperature rise. In the structural evolution of $(CaO)_x(Al_2O_3)_{1-x}$ melts, increasing temperature could improve the system energy, which is beneficial for BO transforming to TCO. Also increasing temperature would accelerate the atomic motion and break some Ca-O bonds, which causes a decrease in the degree of charge compensation. The reductions of both structural parameters are detrimental to the polymerization degree of the network structure. So improving temperature leads to a decrease in the viscosity of $(CaO)_x(Al_2O_3)_{1-x}$ melts.

3.5 Conclusions

Optimized measurements of the density (1450-2600 K), surface tension, and viscosity (1900-2700 K) were proposed, which would promote the measurements of ADL with DOM and provide a valuable reference for researching thermophysical properties of the $(CaO)_x(Al_2O_3)_{1-x}$ melts.

The structural evolution of the $(CaO)_x(Al_2O_3)_{1-x}$ melts system at different temperatures and R is revealed by the MD simulations with modified potentials in conjunction with previous test characterization (neutron diffraction and NMR). Furthermore, the influences of R and temperature on BLD, BAD, oxygen species, the degree of charge compensation, and UOBs were explored, while the correlation between BAD and coordination number, BO, TCO, and charge compensations was revealed. Valuable conclusions about structural evolution were obtained by changing temperature and R, as follows:

i. The intensity of Al-O-Al BAD corresponds to the total content of BO and TCO, which may be related to the connection of [AlO$_n$] polyhedrons. Increasing temperature or R causes a decrease in the connection of [AlO$_n$] polyhedrons, which may make some structure units in the dissociated state.
ii. Ca^{2+} cations show a dual role in the network structure of the $(CaO)_x(Al_2O_3)_{1-x}$ melts during the process of increasing R, where Ca^{2+} cations as charge compensators dominate from CA2 to CA; Ca^{2+} cations as network modifiers dominate from CA to C3A. In the process of Ca^{2+} cations as charge compensators, Ca^{2+} cations mainly replace the TCO to participate in charge compensation, which is less destructive to the network structure. Ca^{2+} cations, as network modifiers, destroy BO structure and increase the content of NBO. Overall, the charge compensation degree and the polymerization degree of the network structure show an increase and then a decrease from CA2 to C3A.

The correlation between structure and thermophysical properties was deeply analyzed and obtained the following conclusions:

i. Improving temperature and R result in a change in bond length distribution, and a decrease in the intensity of the Al-O-Al BAD and polymerization degree, which decreases the connectivity of [AlO$_n$] each other to increase the volume and to reduce the density of the $(CaO)_x(Al_2O_3)_{1-x}$ melts. The influence of $\rho_{Al2O3} > \rho_{CaO}$ on the density of the $(CaO)_x(Al_2O_3)_{1-x}$ melts is non-negligible as well.
ii. With decreasing R, the contents of modified UOBs caused by charge compensation are increasing, which offsets the influence of the decrease in Al-O-n[Ca] and makes the surface tension increase. With increasing temperatures, the total contents of 2Al-O-n[Ca], 3Al-O-n[Ca], and 2Al-O-[Al] only show a slight decrease and the change of Al-O-n[Ca] can be neglectable, which results in a slight decrease in surface tension.
iii. The viscosity η of the $(CaO)_x(Al_2O_3)_{1-x}$ melts climbs up and then declines from CA2 to C3A, because one of the Ca^{2+} cations roles is as a charge compensator at the low CaO content, leading to an unceasingly rise in the degree of polymerization (CA2-CA). On the contrary, the other role of Ca^{2+} cations is a network modifier to reduce the degree of polymerization by further increasing R (CA-C3A). Rising temperature can decrease BO content and the degree of charge compensation, which reduces the degree of polymerization and causes a decline in the viscosity of $(CaO)_x(Al_2O_3)_{1-x}$ melts.

Chapter 4

Chapter 4. The correlation between thermophysical properties and structural evolution of molten $CaO-Al_2O_3-SiO_2$ system studied by aerodynamic levitation and molecular dynamics simulation

Résumé du Chapitre 4

Dans ce chapitre, des mesures systématiques in situ de la densité, de la tension superficielle et de la viscosité des masses fondues $CaO-Al_2O_3-SiO_2$ (rapport pondéral: $CaO/Al_2O_3=1$, SiO_2: 0-25 % en poids) sont effectuées par lévitation aérodynamique sur une large gamme de températures. Les simulations de dynamique moléculaire, combinées aux résultats de caractérisation rapportés précédemment, permettent de vérifier l'applicabilité du potentiel hybride combiné aux oxydes fondus. Les résultats montrent que le potentiel hybride combiné est approprié dans les simulations MD du système $CaO-Al_2O_3-SiO_2$ en utilisant une méthode de comparaison similaire à celle des facteurs structurels S(Q), des fonctions de distribution totale et des nombres de coordination du Chapitre 3. De même, les paramètres structurels comprenant la distribution de la longueur de liaison (BLD), la distribution de l'angle de liaison (BAD), les espèces d'oxygène (oxygène pontant : BO ; oxygène non pontant : NBO ; oxygène tri-cluster : TCO), le degré de compensation de la charge, la connectivité du réseau (espèces Qi, clusters tétraédriques) et les liaisons oxygène insatisfaites (UOB) sont calculés pour explorer l'évolution structurelle du système $CaO-Al_2O_3-SiO_2$ à différentes températures et teneurs en SiO_2.

i) L'augmentation de la température peut accélérer le mouvement des atomes et rompre la connexion de liaison partielle, ce qui diminue l'intensité du pic de la BLD. L'amélioration de la teneur en SiO_2 peut augmenter la teneur en liaison Si-O, ce qui entraîne l'élargissement progressif de la largeur à mi-hauteur (FWHM) du premier pic de la BLD et le déplacement de l'emplacement du premier pic vers la valeur r basse.

ii) La BAD O-Al-O et la BAD O-Si-O sont liées aux polyèdres [AlOn] (numéro de coordination Al) et aux polyèdres [SiOn] (numéro de coordination Si), respectivement. Et la BAD Al-O-Al et la BAD Al-O-Si sont déterminées par Al-BO-Al et nAl-TCO, Al-BO-Si et nAl-TCO-mSi.

iii) L'augmentation de la température entraîne une augmentation du BAD et une diminution du BO, du degré de compensation des charges et de la connectivité du réseau. Au contraire, l'augmentation de la teneur en SiO_2 entraîne une diminution du NBO et une augmentation du BO, du degré de compensation des charges et de la connectivité du réseau.

La corrélation entre les propriétés thermophysiques et la structure des fondus $CaO-Al_2O_3-SiO_2$ est révélée, ce qui étend également l'applicabilité de la corrélation théorique obtenue au chapitre 3. Les conclusions notables sont présentées comme suit:

i. L'amélioration de la température peut diminuer la teneur en BO et le degré de compensation de charge, ce qui conduit à une diminution du degré de polymérisation. Cela provoquerait une augmentation du micro-volume et une diminution de la densité. Bien que l'augmentation de la teneur en SiO_2 puisse améliorer le degré de polymérisation, la liaison Si-O pourrait étendre considérablement la structure de la chaîne, elle diminue le degré de torsion des polyèdres pour augmenter le micro-volume et diminuer la densité.
ii. L'augmentation de la température entraîne une augmentation du contenu des Al-O-n[Ca], Si-O-n[Ca] et OBs, et une légère diminution du contenu des UOBs causée par la compensation de charge. La diminution de la teneur en UOBs avec compensation de charge et l'augmentation de la teneur en OBs pourraient compenser l'effet de l'augmentation de la teneur en Al-O-n[Ca] et Si-O-n[Ca], ce qui conduit à une légère diminution de la tension de surface. Avec l'augmentation de la teneur en SiO_2, les polyèdres UOBs liant [AlO_n] qui contribuent le plus à la tension superficielle sont progressivement remplacés par les tétraèdres UOBs liant [SiO_n], plus une augmentation de la teneur en OBs. Il en résulterait une diminution de la tension superficielle.
iii. L'augmentation des températures peut diminuer la teneur en BO et le degré de compensation de charge et augmenter la teneur en NBO, ce qui est bénéfique à la diminution du degré de connectivité du réseau et du degré de polymérisation. Ainsi, la viscosité du système $CaO-Al_2O_3-SiO_2$ diminue avec l'augmentation de la température. Avec l'augmentation de la teneur en SiO_2, la teneur en BO et le degré de compensation de charge augmentent et la teneur en NBO diminue, ce qui augmente le degré de connectivité du réseau et le degré de polymérisation pour améliorer la viscosité du système $CaO-Al_2O_3-SiO_2$.

Abstract of Chapter 4

In this chapter, systematic in-situ measurements of density, surface tension, and viscosity of the $CaO-Al_2O_3-SiO_2$ melts (weight ratio: $CaO/Al_2O_3=1$, SiO_2: 0-25 wt%) are carried out by aerodynamic levitation over a wide temperature range. Molecular dynamic simulations, combined with the previously reported characterization results, further verify the applicability of the combined hybrid potential in oxide melts. The results show that the combined hybrid potential is appropriate in MD simulations of the $CaO-Al_2O_3-SiO_2$ system by using a comparison method similar to that of the structural factors S(Q), total distribution functions, and coordination numbers in Chapter 3.

Likewise, structural parameters including bond length distribution (BLD), bond angle distribution (BAD), oxygen species (bridging oxygen: BO; non-bridging oxygen: NBO; tri-cluster oxygen: TCO), the degree of charge compensation, network connectivity (Q_i species, tetrahedral clusters), and unsatisfied oxygen bonds (UOBs) are calculated to explore the structural evolution of the $CaO-Al_2O_3-SiO_2$ system at different temperatures and SiO_2 content.

Increasing temperature can quicken the motion of atoms and break the partial bond connection, which decreases the peak intensity of BLD. Improving SiO_2 content can increase the content of the Si-O bond, which causes the full width at half maximum (FWHM) of the first peak of BLD gradually broaden and the location of the first peak shifts to the low r-value.

The O-Al-O BAD and the O-Si-O BAD are related to the [AlO_n] polyhedrons (Al coordination number) and [SiO_n] polyhedrons (Si coordination number), respectively. And the Al-O-Al BAD and the Al-O-Si BAD are determined by Al-BO-Al and nAl-TCO, Al-BO-Si and nAl-TCO-mSi.

Increasing temperature causes an increase in NBO and a decrease in BO, the degree of charge compensation, and network connectivity. On the contrary, increasing SiO_2 content leads to a decrease in NBO and an increase in BO, the degree of charge compensation, and network connectivity.

The correlation between thermophysical properties and structure of the $CaO-Al_2O_3-SiO_2$ melts is revealed, which also extends the applicability of the theoretical correlation obtained from Chapter 3.

4.1 Introduction

The excellent mechanical and optical properties of calcium aluminosilicate ($CaO-Al_2O_3-SiO_2$, CAS) glasses have stimulated the interest of countless researchers over the years [Wallenberger et al., 1994]. Calcium aluminosilicate glasses and melts also have been extensively applied in industries by virtue of their wide range of glass-forming regions and refractory nature, such as in the production of cement and glass, in metallurgy [Puertas et al., 2003; C. Li et al., 2010; Hennet et al., 2016a]. Industrial applications of CAS melts are closely correlated to their thermophysical properties (density, surface tension, and viscosity), while chemical composition and temperature have a great influence on thermophysical properties. Therefore, it is relevant to explore the influence of chemical composition and temperature on the thermophysical properties of CAS melts, which is beneficial for optimizing compositions and synthesis conditions for designing CAS-based glasses for special purposes.

However, in situ measurement of the thermophysical properties of melts was not a straightforward operation at ultra-high temperatures. In conventional contact methods, density and surface tension are commonly measured by the sessile-drop apparatus [McClelland et al., 1995; Duchesne et al., 2017]. The viscosity of melts is obtained by using the rotating Bob method [Chebykin et al., 2017], the capillary method [Brooks et al., 2005], and the oscillating vessel viscometer [Brooks et al., 2005]. However, there is an insurmountable disadvantage in contact methods which is chemical interactions between melts and the container at ultra-high temperatures. The conventional contact methods cause generally heterogeneous nucleations at the container wall under supercooled conditions [Langstaff et al., 2013]. On the contrary, aerodynamic levitation with laser heating and the droplet methods can avoid perfectly this problem. Although Siafakas et al [Siafakas et al., 2018] measured the viscosity of $SiO_2-CaO-Al_2O_3$ slags by ADL and Takahashi et al [Takahashi et al., 2015] measured their density, the lack of surface tension was still a pity for systematically studying CAS melts. The measurements of CAS melts in this work will fill in the blanks of surface tension and make the data of density and viscosity complete.

In addition, the thermophysical properties of CAS melts have a strong dependence on the microscopic structure [Mysen, 1990; Takahashi et al., 2015]. In calcium aluminosilicate glasses, both Al_2O_3 and SiO_2 contribute to the formation of the glass network together. Al^{3+} with different coordination numbers (CN = 4, 5, and 6) can play a dual role (network modifier and network former), which would unquestionably increase the complexity and variability of the network structure. So microscopic structure of CAS melts was studied indefatigably in our lab. For instance, Neuville et al. [Neuville et al., 2006] studied Al coordination numbers, Al species, and Al/Si tetrahedral distribution in the network structure of calcium aluminosilicate glasses along with different ratios R=CaO/Al_2O_3 by Raman spectroscopy and ^{27}Al MQ-MAS NMR. Hennet et al [Hennet et al., 2016a] respectively measured structure factors of various CAS glass compositions at both room temperature and in the liquid state by X-ray diffraction (room temperature) and Neutron diffraction with ADL (in-situ). Neuville et al. [Neuville et al., 2004] investigate the degree of polymerization (Q^n) of the (AlO_4) tetrahedra and the distribution of Al in Q^2, Q^3, and Q^4 species by utilizing X-ray absorption near-edge structure (XANES) spectroscopy at both Ca and Al K-edges. Although plenty of researchers investigated the structural evolution of CAS, the correlation between structural evolution and thermophysical properties is still blurred, due to the difficulty in in-situ measurement and characterization of thermophysical properties and microscopic structure.

The large-scale Atomic molecular dynamic (MD) simulation is an effective and promising method for deeply investigating network structure, O species, and polyhedral units in melts [Hu et al., 2020; Su et al., 2020]. Su et al. [Su et al., 2020] utilized MD simulation and electromagnetic levitation to reveal a Vogel-Fulcher-Tammann-type temperature-dependent viscosity for pure Zr in the temperature range of 1600–2700 K. Hu et al. [Hu et al., 2020] developed a compositional property database that overviews on the density and elastic properties of SiO_2-based glasses by virtue of high-throughput molecular dynamic (MD) simulations. Plenty of valuable studies describe that machine learning techniques can provide an alternative method to bridge the thermophysical properties of interest with its potential microscopic structure.

In this Chapter, aerodynamic levitation with the droplet oscillation technique is performed to measure the density of CAS melts and their surface tension and viscosity during 1450-2500 K and 1850-2650 K, respectively. Combine with the previous experimental studies in our laboratory, we continued to utilize molecular dynamic (MD) simulations to explore the correlation between structure and thermophysical properties. Furthermore, $CaO-Al_2O_3-SiO_2$ glasses synthesized from SiO_2 (0-25 wt%) and R=CaO/Al_2O_3=1 (wt%). One of the purposes is to extend the $CaO-Al_2O_3$ system to the ternary system and verify that the obtained theory is applicable to the $CaO-Al_2O_3-SiO_2$ system. Based on the structural analysis of atomic scale, how the bond length distribution (BLD), the bond angle distribution, charge compensation, bridging oxygen (BO), non-bridging oxygen(NO), and tri-cluster oxygen (TCO) affect the structural evolution of $CaO-Al_2O_3-SiO_2$ system. At the same time, the theoretical correlation between thermophysical properties and the structural evolution of the CAS system is explored, which further enriches and completes the theoretical interpretation of the correlations presented in Chapter 3. All the results and analyses presented here may facilitate scientific research on thermophysical properties and structural evolutions of melts.

4.2 Experiment and MD simulation

4.2.1 Preparation of the samples of the Al_2O_3-CaO-SiO_2 system

CaO, Al_2O_3 (ALMATIS, CT3000 SG, 99.8 %), and SiO_2 (ALFA AESAR, -325 Mesh, 99.5%) were used as raw materials to prepare samples of the CAS melts. High-purity CaO power was obtained by the same method described in Chapter 3. The samples of the CAS system are that, based on $CaO/Al_2O_3=1$ (wt/wt), SiO_2 is sequentially increased from 0 to 25 wt% with an interval of 5 wt%. The components of CAS0, CAS5, CAS10, CAS15, CAS20, and CAS25 are shown detailedly in Table 4-1. Three kinds of powder were mixed completely for 0.5 h by using an agate mortar and pressed into pellets under 9.5 MPa. The pellets were placed in a drying oven for 12 h at 373 K. Each pellet was crushed into small pieces after drying. ADL was utilized to premelt the pieces into spherical samples of 16.2 ± 1 mg and a diameter of around 2 ± 0.2 mm. Liquidus temperatures of CAS0, CAS5, CAS10, CAS15, CAS20, and CAS25 were calculated by the thermodynamic software FactSage® 8.1 [Bale et al., 2016], using FTOxid and FactPS databases (Table 4-1).

Table 4-1. Composition of prepared melts (wt.%) and liquidus temperatures (K).

Melts System	Sample No.	CaO(wt.%)	Al_2O_3(wt.%)	SiO_2(wt.%)	Liquidus temp (K)
$CaO-Al_2O_3-SiO_2$	CAS0	50	50	0	1638
	CAS5	47.5	47.5	5	1726
	CAS10	45	45	10	1769
	CAS15	42.5	42.5	15	1835
	CAS20	40	40	20	1867
	CAS25	37.5	37.5	25	1846

4.2.2 Measurements of aerodynamic levitation

The measurements, principles, and methods of data processing were detailedly described in Section 2.

4.2.3 MD simulations

In MD simulations of the CAS system, the initial configurations of CAS0, CAS5, CAS10, CAS15, CAS20, and CAS25 are created, based on the well-defined crystal structures of $Ca_{12}Al_{14}O_{33}$, $Ca_3Al_4SiO_{12}$, $CaAl_2SiO_7$ from the open-access database Materials Project [Jain et al., 2013]. This is because the atom proportions of CAS0 and CAS5, CAS10 and CAS15, CAS20 and CAS25 are close to $Ca_{12}Al_{14}O_{33}$, $Ca_3Al_4SiO_{12}$, and $CaAl_2SiO_7$, respectively. The total atom number of each configuration is around 10000. The configurations of the samples are detailedly shown in Figure 4-1 and Table 4-2.

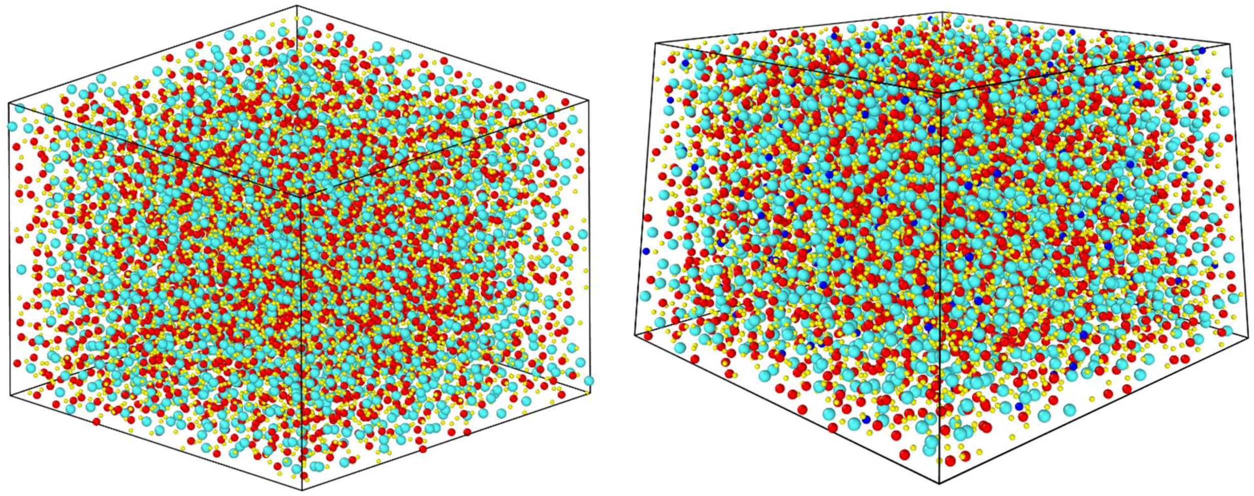

(CAS0) (CAS5)

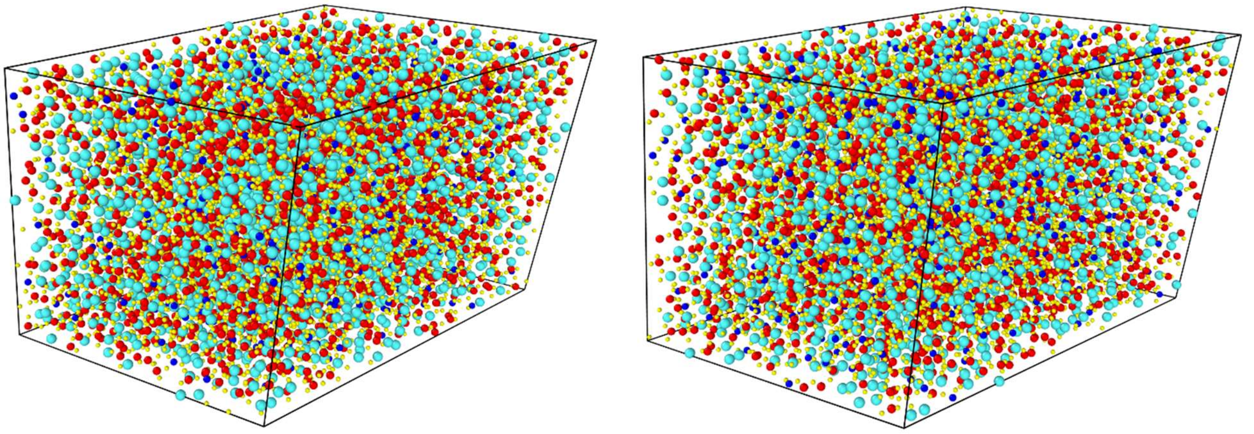

(CAS10) (CAS15)

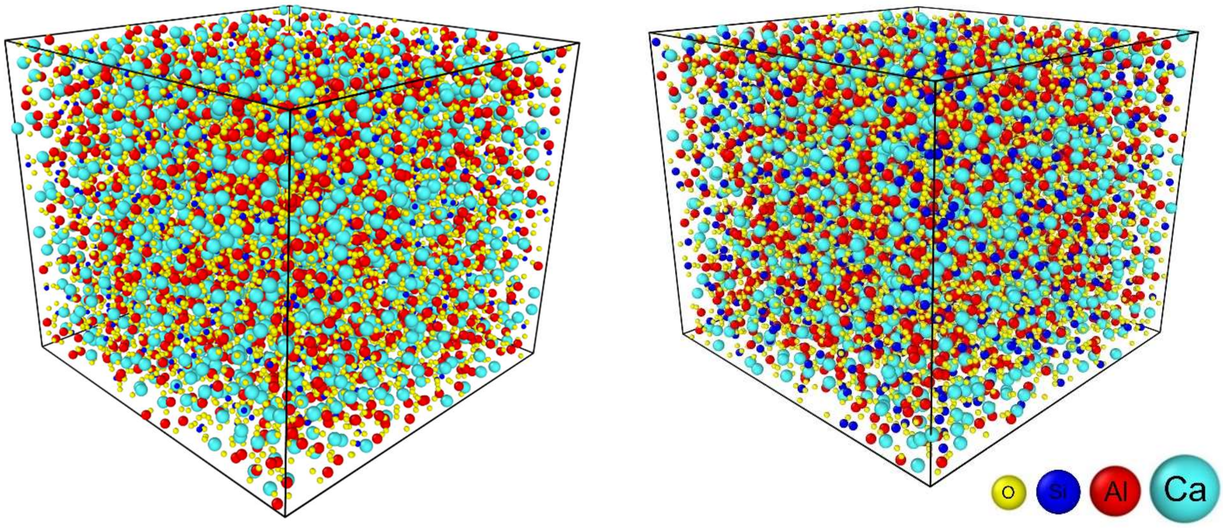

(CAS20) (CAS25)

Figure 4-1. The initial configurations of samples of the $CaO-Al_2O_3-SiO_2$ system

Table 4-2. Information of compositions, densities, atom number, and simulation box of the simulated samples

Samples	Number of atoms				Periodic boundary conditions						Density
	Ca	Al	O	Si	X(Å)	Y(Å)	Z(Å)	α(°)	β(°)	γ(°)	(1800K)
CAS0	2160	2520	5940	-	61.9142	58.2027	42.2486	109.2	109.2	110.0	2.64
CAS5	2107	2314	5992	207	60.8019	57.1571	41.4896	109.2	109.2	110.0	2.63
CAS10	1842	2028	5648	382	61.5446	44.0156	49.3157	86.6	98.9	119.6	2.61
CAS15	1723	1900	5709	568	62.6465	44.8036	50.1986	86.6	98.9	119.6	2.59
CAS20	1720	1894	6167	803	55.7125	55.7125	48.4367	89.9	90.0	90.0	2.56
CAS25	1601	1760	6229	994	55.6667	55.6667	48.3968	89.9	90.0	90.0	2.54

In addition, an appropriate potential function is a condition precedent for successful MD simulations. As described above (Section 2.2.5 and 3.2.3), the new-form hybrid potential which combines Buckingham potential and BMH potential is possibly appropriate for the glass system with ionic bonds and covalent bonds. Therefore, this combined hybrid potential is also applied in the CAS system, where Buckingham potential is utilized to define the pair interactions of Ca-O, Al-O, Si-O, and O-O; The Born-Mayer-Huggins (BMH) potential is employed to describe Ca-Ca, Ca-Al, Ca-Si, Al-Al, Al-Si, and Si-Si pair interactions. All parameters for BMH and Buckingham are indicated in Table 4-3.

Table 4-3. Parameters of the BMH potential [Bouhadja et al., 2013] and the Buckingham potential [Charpentier et al., 2018; Hu et al., 2020; Liu et al., 2020] for the CaO-Al_2O_3-SiO_2 system.

Pair	BMH Potential				
	$A=f_0(b_i+b_j)$ (eV)	$\rho=(b_i+b_j)$ (Å)	$\sigma=(a_i+a_j)$ (Å)	C (eV•Å^6)	D (eV•Å^8)
$Ca^{1.2+}$—$Ca^{1.2+}$	0.0035	0.0800	2.3440	20.9856	0
$Ca^{1.2+}$—$Al^{1.8+}$	0.0032	0.0740	1.9572	17.1710	0
$Ca^{1.2+}$—$Si^{2.4+}$	0.0027	0.0630	1.8924	22.9907	0
$Al^{1.8+}$—$Al^{1.8+}$	0.0029	0.0680	1.5704	14.0498	0
$Al^{1.8+}$—$Si^{2.4+}$	0.0025	0.0570	1.5056	18.8116	0
$Si^{2.4+}$—$Si^{2.4+}$	0.0012	0.0460	1.4408	25.1873	0

Pair	Buckingham Potential		
	A (eV)	ρ (Å)	C (eV•Å^6)
$Ca^{1.2+}$—$O^{1.2-}$	7747.0000	0.252600	93.100
$Al^{1.8+}$—$O^{1.2-}$	12 201.4170	0.195628	31.997
$Si^{2.4+}$—$O^{1.2-}$	13702.905	0.193817	54.681
$O^{1.2-}$—$O^{1.2-}$	2029.2200	0.343645	192.580

In order to adjust and optimize the initial configurations, the isothermal-isobaric (NPT) which includes a Nose–Hoover thermostat coupled to an isotropic barostat is used in the MD simulations of the CAS system. The initial configurations were relaxed at 1800 K, meanwhile, the density of each system was estimated and compared with the experimental results to determine the appropriately simulated configurations to the maximum extent possible. The time step was set to 1 fs for all the simulations. Each simulated process was similar to the MD simulations of the CaO-Al_2O_3 system, which took 2490 ps, including relaxation, heating up, cooling down, and heat preservation to reproduce the experimental process. The detailed process of MD simulation is shown in Figure 4-2, which also contains four temperature points: 3000 K, 2600 K, 2200 K, and 1800 K in sequence. Each temperature point was kept 400 ps for relaxation and calculations of structural factors, total pair distribution function (PDF), and coordination number. The simulation trajectories were analyzed by the visualization software OVITO pro [Stukowski, 2010]. In this MD simulation, on the one hand, the influence of the structural evolution of the CAS system on thermophysical properties is studied. On the other hand, whether this hybrid potential is suitable for the CAS system would be further verified.

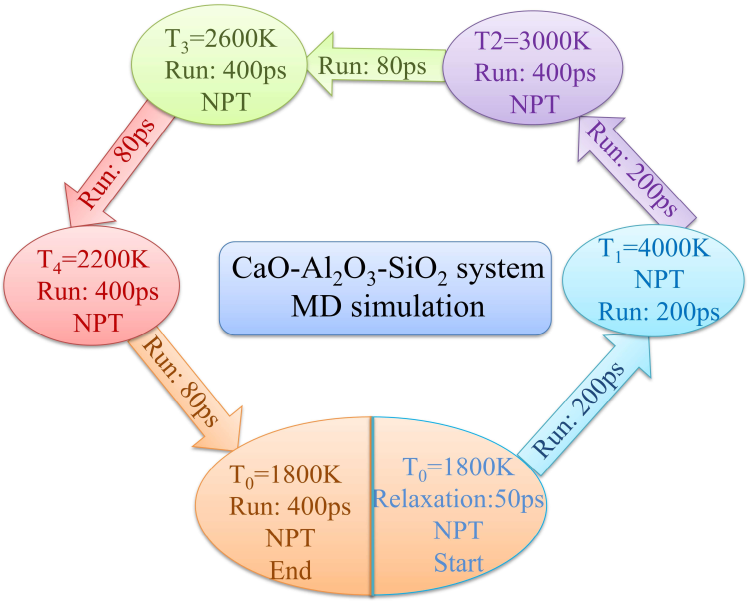

Figure 4-2 The diagrammatic drawing of the MD simulations process of the CAS system

4.2.4 Computational objects

4.2.4.1 Oxygen species and charge compensation

To deeply understand the simulated results of the CAS system, previous key definitions should be modified and indicated in advance (Figure 4-3):

- Al and Si as core atoms are surrounded by O atoms to form [AlO$_n$] and [SiO$_n$] polyhedrons;
- Non-bridging oxygens are defined as only joining one Al atom or one Si atom and one or more Ca atoms (Al-O-*n*Ca and Si-O-nCa, $n \geq 1$);
- Free oxygens are only connected by Ca atoms (O-*n*Ca);
- Tri-cluster oxygen (TCO) mean that an oxygen atom is shared with three polyhedrons, such as three [AlO$_n$], two [AlO$_n$] & one [SiO$_n$], one [AlO$_n$] & two [SiO$_n$], and three [SiO$_n$], and meanwhile connected by *n* Ca atoms ([3Al-O]-*n*Ca, [2Al-O-Si]-*n*Ca, [Al-O-2Si]-*n*Ca, [3Si-O]-*n*Ca, n ≥ 1);
- Bridging oxygens (BO) is that an oxygen atom as a bridging atom is shared by two polyhedrons, such as two [AlO$_n$], one [AlO$_n$] & one [SiOn], and two [SiO$_n$] polyhedrons;
- The degree of charge compensation in structure is defined as the ratio of total specific oxygen atoms to all oxygen atoms, where the specific oxygen atom is shared by multiple polyhedrons ([AlO$_n$] and [SiO$_n$]) and connected by *n* Ca atoms ([*x*Al-O-ySi]-*n*Ca, $x,y \geq 1$, $n \geq 1$).

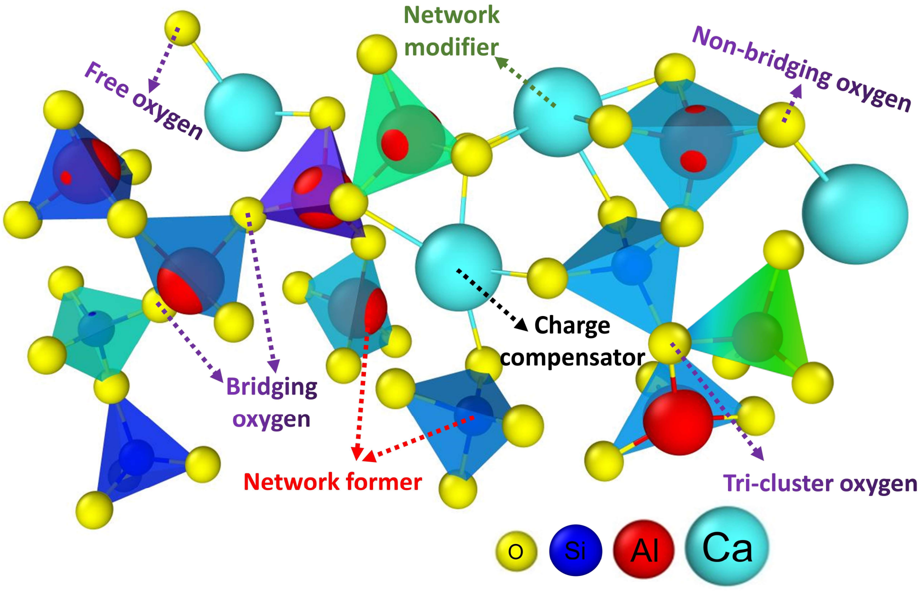

Figure 4-3. The definitions of structure parameters in the network structure of the CAS system: bridging oxygen (BO), Non-bridging oxygen (NBO), tri-cluster oxygen (TCO), free oxygen (FO), charge compensator, network modifier, and network former.

4.2.4.2 Q_n analysis and network connectivity

Q_n has been defined and analyzed as a typical method to dominate the network structure of oxide glasses. In this case, Q_n analysis is performed to explore the network connectivity of [SiO_4] and [AlO_4] tetrahedra, where n is the number of BO coordinating with a former atom of the glass network. The mean Q_n of the aluminosilicate network can be expressed as [Zhao et al., 2019]:

$$Q_n=\sum_{n=0}^{4} x_n n \qquad \text{Eq. (4-1)}$$

where x_n means the percentage of this type of Q_n. Furthermore, the network connectivity degree (NCD) is calculated by Eq. (4-2),

$$NCD=\frac{N_{si}}{N_{si}+2N_{Al}}Q_{n\_si}+\frac{2N_{Al}}{N_{Si}+2N_{Al}}Q_{n\_Al} \qquad \text{Eq. (4-2)}$$

where N_{si} and N_{Al} are the mole percentage of the Si atom and the Al atom in the CAS melt, respectively.

4.3 Results

4.3.1 Experimental results of the CaO-Al_2O_3-SiO_2 system

4.3.1.1 Density

The density for melts composed of the CaO-Al_2O_3-SiO_2 system in a wide temperature range (from 2450 to 1450 K) is shown in Figure 4-4. The density of the CAS melts increases distinctly during the whole free-cooling process. The density difference (0.175 g/cm^3) of the CAS5 is the largest from 1450 to 2450 K, compared with the other compositions. The density differences of melts (from CAS0-CAS25) gradually reduce from 1450 to 2450 K, where the density difference (0.125 g/cm^3) of CAS25 is the smallest. In Figure 4-4, the density curve of CAS0 seems to isolate and its slope is different from that of the other compositions. The composition of SiO_2 may cause structural differences that results in this phenomenon. With the addition of SiO_2 content, the density of the CAS melts successively decreases, and it is worth mentioning here that the density gap decrease from CAS0 to CAS5 is the largest. From the results, increasing temperature and the content of SiO_2 can contribute to reducing the density of the CAS melts.

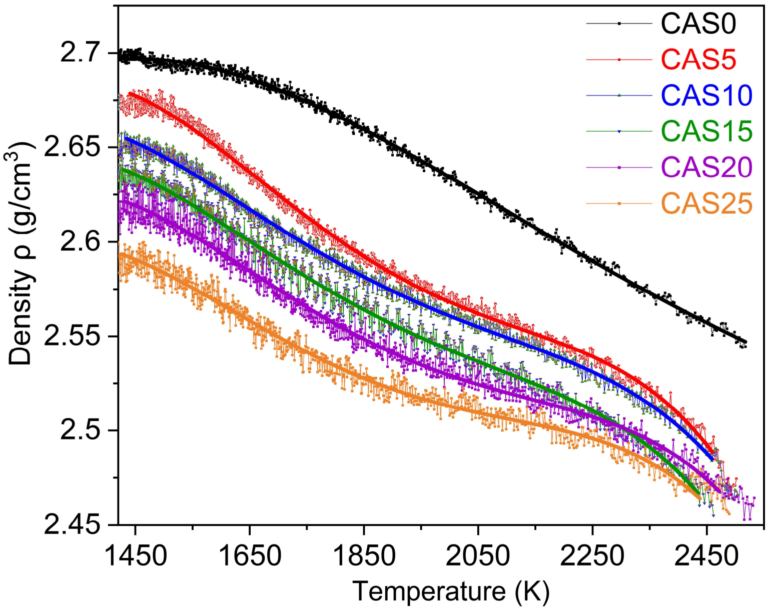

Figure 4-4. The temperature-dependent density of the CAS system.

4.3.1.2 Surface tension

The surface tension (γ) of the CAS system at a wide temperature range (from 1850 to 2650 K) is shown in Figure 4-5. With increasing temperature, the surface tension of the CAS melts slightly decreases, where the decreased interval of each composition is basically less than 0.01 N/m from 1850 to 2650 K. However, with increasing SiO_2, the surface tension of the CAS melts shows a clear decrease. The order of surface tension of the CAS melts is γ (CAS0) > γ (CAS5) > γ (CAS10) > γ

(CAS15) > γ (CAS20) > γ (CAS25), the higher the SiO_2 content, the lower the surface tension. From the results, the SiO_2 content has a greater influence on the surface tension than the temperature.

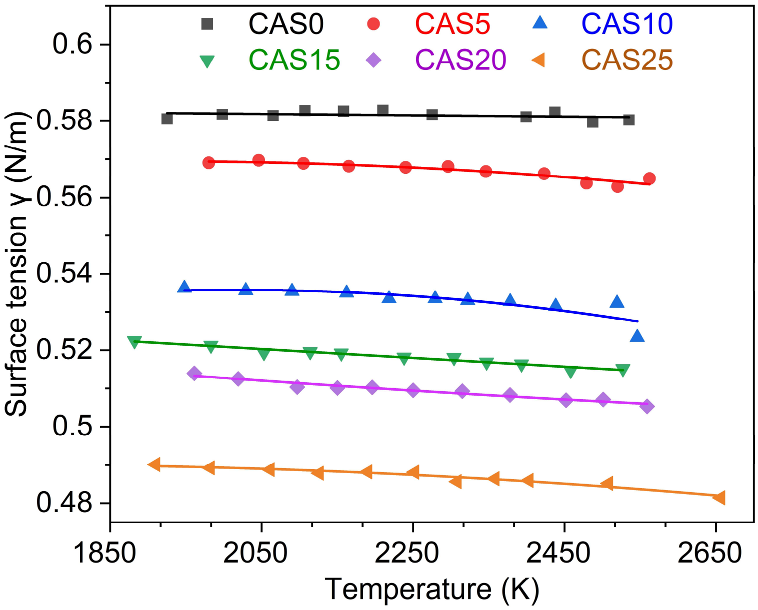

Figure 4-5. The surface tension of the CAS melts: γ versus *T*.

4.3.1.3 Viscosity

The viscosity of a similar composition (10 wt% SiO_2 + 44 wt% Al_2O_3 + 46 wt% CaO) to the CAS10 melt was measured by Rotating bob methods and ADL with DOM, which was reported by Siafakas et al [Siafakas et al., 2018]. Selecting this reported sample can be a reference for the viscosity of the CAS10 melt since the CAS melts at high temperatures measured by ADL with DOM lacks a measured benchmark. The comparison result is shown in Figure 4-6 (a). The viscosity of CAS10 during the temperature range from 1950 to 2550 K is less than the result reported previously. The differences in sample composition and the pyrometer (λ = 1.45 µm) caused the difference in corrected temperature and may cause inconsistent viscosity.

The viscosities of the CAS melts at high temperatures are in a narrow range. For the sake of observation and comparison, viscosity versus temperature is expressed in log(η) versus Tm/T. As shown in Figure 4-6 (b). The log(η) versus Tm/T is also a linear relationship, which is the same as the viscosity trend of the CaO-Al_2O_3 melts, the exponential decrease in the viscosity of the melts with the temperature rising. Meanwhile, Figure 4-6 (c) shows the viscosity of the CAS melts at a wide temperature range (1900 to 2600 K). The viscosity of the CAS melts declines with increasing temperature, and the decreasing trend of viscosity is in agreement with the exponential relation of viscosity and temperature. Increasing SiO_2 content can improve the viscosity of the CAS melts, where the viscosity order is η (CAS0) < η (CAS5) < η (CAS10) < η (CAS15) < η (CAS20) < η (CAS25).

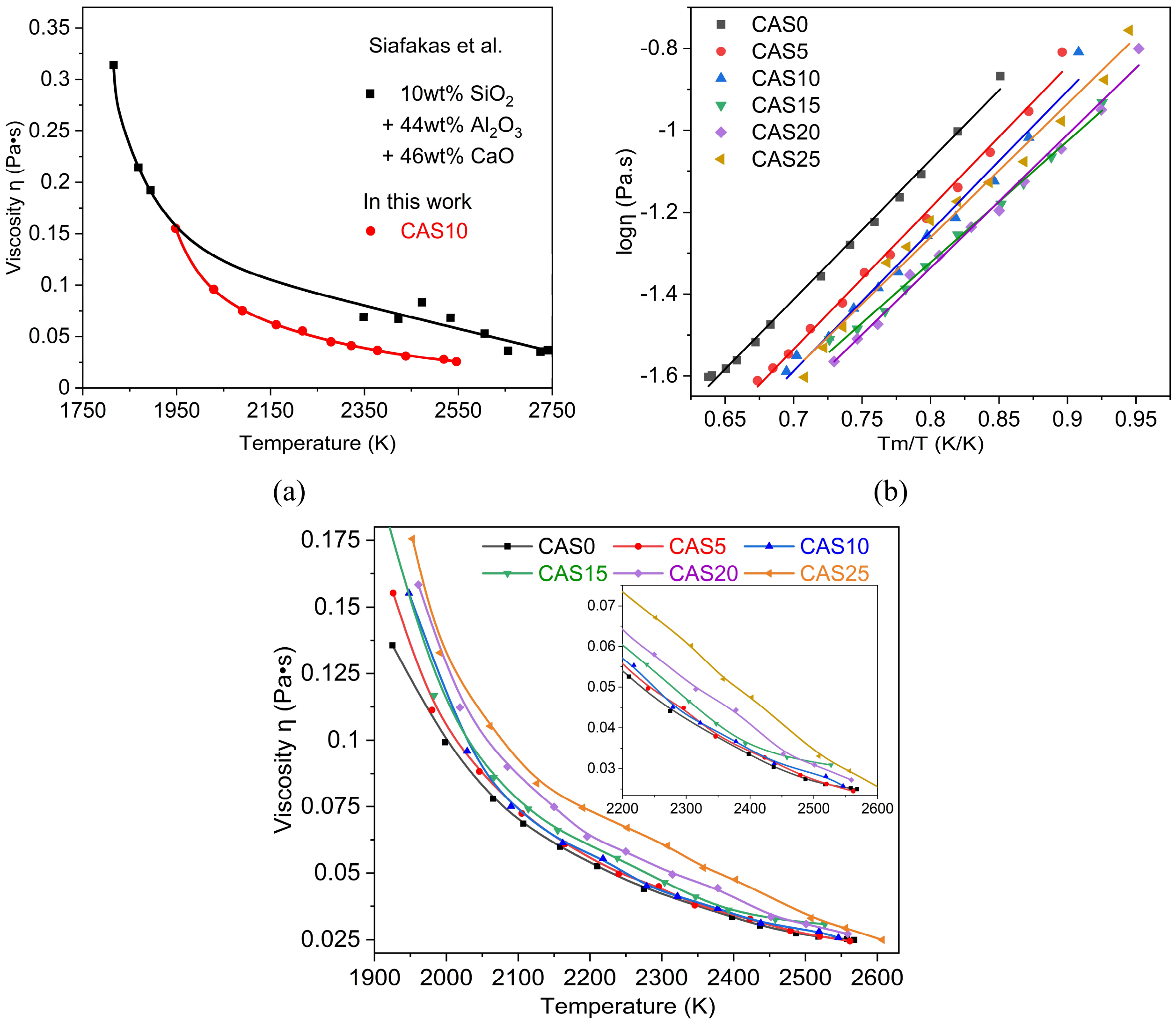

(a) (b)

(c)

Figure 4-6. The viscosity of the CAS system: (a) the comparison of viscosity; (b) log(η) versus Tm/T; (c) viscosity η versus T

4.3.2 Simulation results

4.3.2.1 Structure factors, correlation functions, and coordination number of the CaO-Al_2O_3-SiO_2 system

4.3.2.1.1 Structure factors

Figure 4-7 shows the comparison of structure factors S(Q) of Ca12.44 (composition: 12 mol.% SiO_2 + 44 mol.% Al_2O_3 + 44 mol.% CaO; Temperature: 1923 K), Ca19.40 (composition: 19 mol.% SiO_2 + 40 mol.% Al_2O_3 + 41 mol.% CaO; Temperature: 1923 K), and Ca33.33 (composition: 33 mol.% SiO_2 + 33 mol.% Al_2O_3 + 34 mol.% CaO; Temperature: 1823 K) from experimental neutron diffraction [Hennet et al., 2016] and MD simulations, where the structure factors from MD simulations were computed by three kinds of potentials: the combined hybrid potential (BMH & Buckingham), the Buckingham potential, the BMH potential. By observing comparison, three S(Q)s of MD simulations of Ca12.44 are in good agreement with experimental S(Q), except for a little discrepancy at the low-Q zone for S(Q). There is a deviation at the first peak in the S(Q)s of Ca19.40 calculated from the Buckingham potential and neutron diffraction. For Ca33.33, the S(Q) computed from the combined hybrid potential is the best agreement with the experimental S(Q) than that of the S(Q)s computed from the Buckingham potential and BMH potential, in which the comparison between the S(Q) computed from BMH potential and the S(Q) form neutron diffraction is the most unsatisfactory. Overall, the above comparisons show that the combined hybrid potential is appropriate for MD simulations of the CAS system.

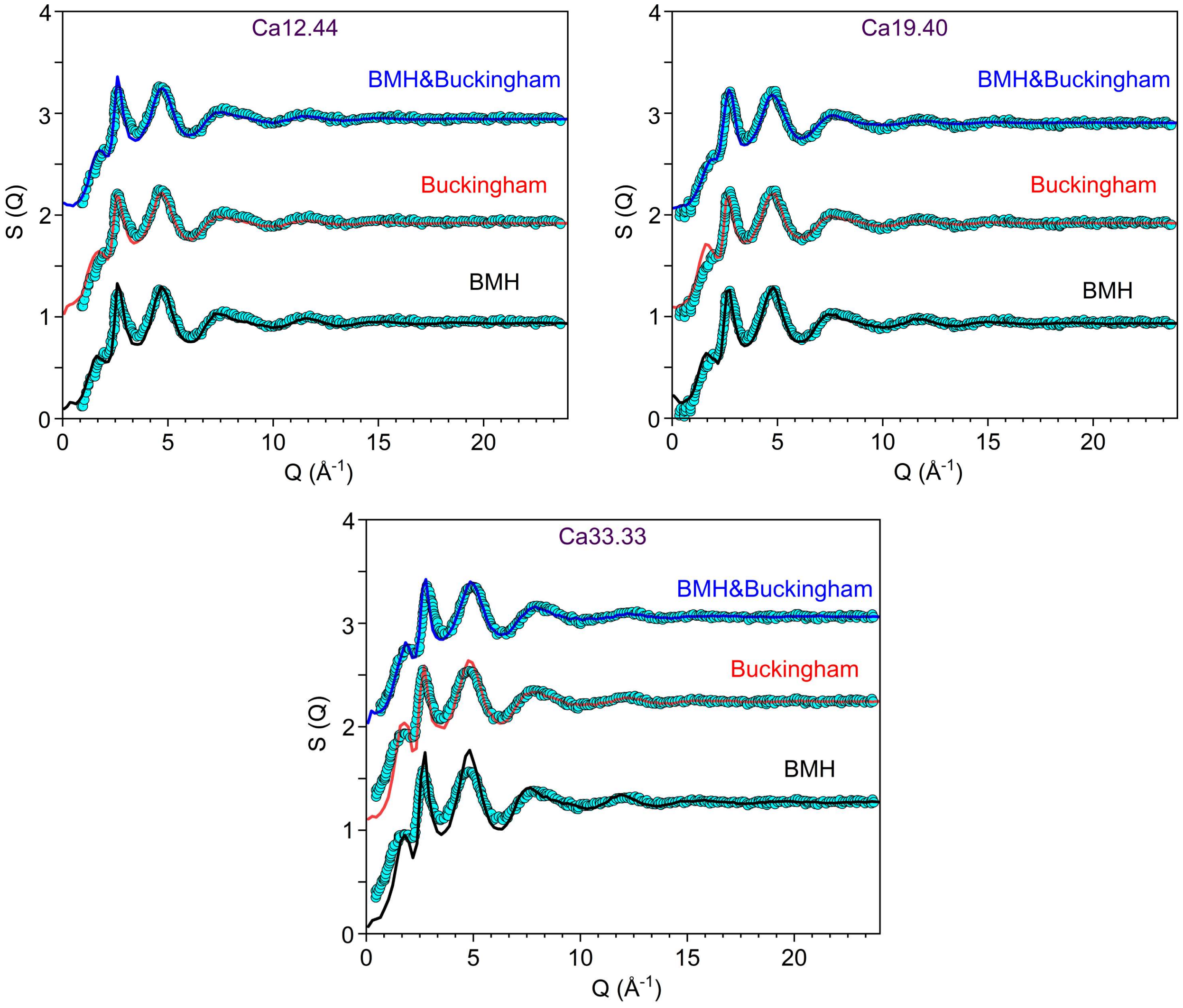

Figure 4-7. The total structure factors S(Q) of the Ca12.44 (1923 K), Ca19.40 (1923 K), and Ca33.33 (1823 K) melts from Neutron diffraction (colored circles) and MD simulation (colored solid lines). The upper curve is shifted up by 0.5 for clarity.

4.3.2.1.2 Radial distribution functions and coordination number

Meanwhile, the total pair distribution functions of Ca12.44 (1923 K), Ca19.40 (1923 K), and Ca33.33 (1823 K) melts are calculated from MD simulations, as shown in Figure 4-8, which combines with radial distribution functions (RDF) and structural parameters to compare with the experimental results.

The RDF and coordination number (CN) are shown in Figure 4-9. The first peaks of the RDFs of Si-O, Al-O, and Ca-O in the Ca12.44 melt at 1923 K are located at 1.60 ± 0.02 Å, 1.76 ± 0.02 Å, and 2.36 ± 0.05 Å, respectively. The CNs of Si-O and Al-O in Ca12.44 melt are 4.01 ± 0.1 and 4.05 ± 0.1, respectively. The first peaks of the RDFs of Si-O, Al-O, and Ca-O in Ca19.40 melt at 1923 K are respectively located at 1.60 ± 0.02 Å, 1.76 ± 0.02 Å, and 2.36 ± 0.05 Å. The CNs of Si-O and Al-O in Ca19.40 melt are 4.02 ± 0.1 and 4.06 ± 0.1, respectively. For the Ca33.33 melt, similar results about structural parameters are obtained as well: Si-O: 1.61 ± 0.02 Å and 4.00 ± 0.05, Al-O: 1.76 ± 0.02 Å and 4.05 ± 0.1, and Ca-O 2.36 ± 0.05 Å. The structural parameters from MD simulations are basically in agreement with that from experimental measurements, except the position of the first peak of Si-O from MD simulations is slightly smaller than that of experiments. But this tiny difference within the error range is neglectable. The detailed comparison of structural parameters is listed in Table 4-4.

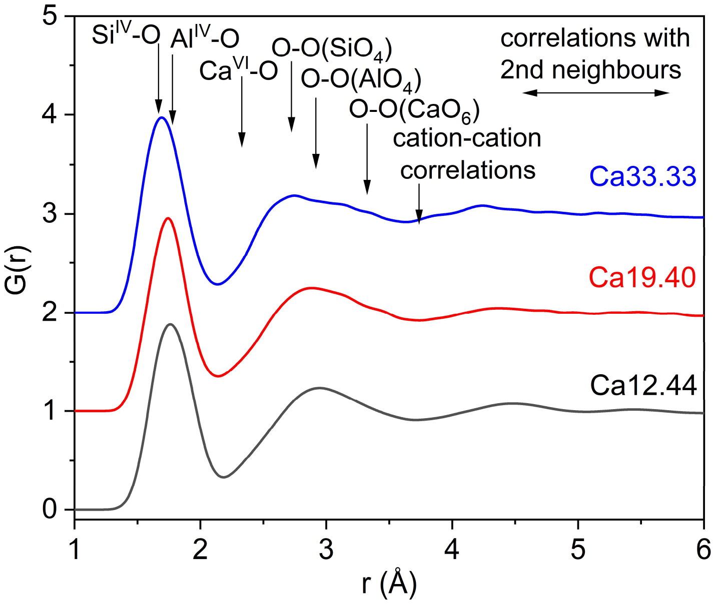

Figure 4-8. Total pair distribution functions for Ca12.44 (1923 K), Ca19.40 (1923 K), and Ca33.33 (1823 K) melts. The positions of the various O-O correlations, as calculated assuming SiO_4 and AlO_4 tetrahedra and CaO_6 octahedra, are shown as a guide. The oscillations above r = 4 Å arise from correlations between second neighbors. The upper curve is shifted up by 1 for clarity.

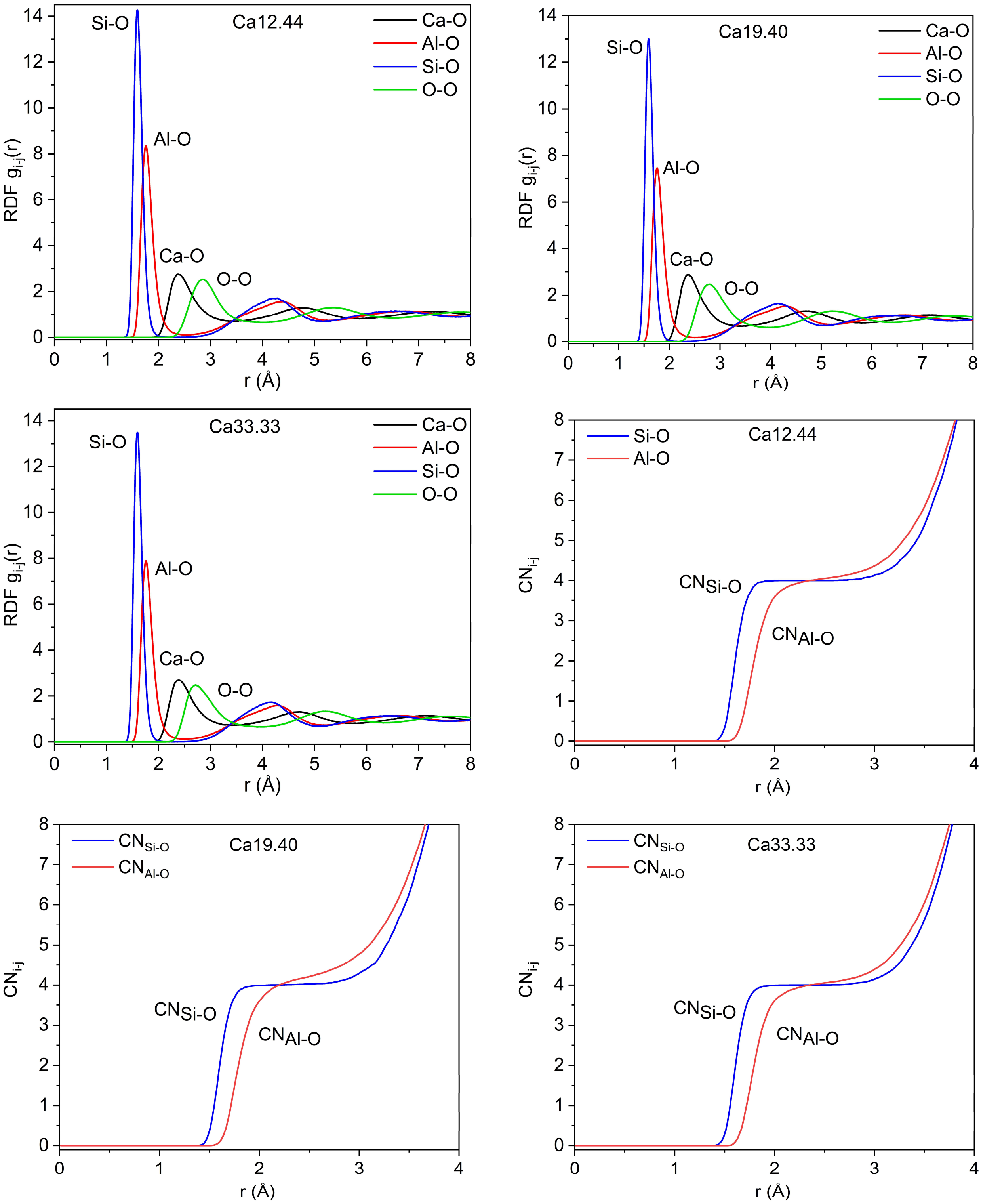

Figure 4-9. Radial distribution functions of Si-O, Al-O, Ca-O, O-O and coordination number of Si-O and Al-O in Ca12.44, Ca19.40, and Ca33.33 melts.

Table 4-4. The nearest-neighbor distance and coordination numbers of Ca12.44, Ca19.40, and Ca33.33 from neutron diffraction (ND) data [Hennet et al., 2016] and MD simulation results.

	T (K)	Method	$r_{Si\text{-}O}$ (Å) (± 0.02)	$r_{Al\text{-}O}$ (Å) (± 0.02)	$r_{Ca\text{-}O}$ (Å) (± 0.05)	$CN_{Si\text{-}O}$ (± 0.5)	$CN_{Al\text{-}O}$ (± 0.5)
Ca12.44	1923	MD	1.60	1.76	2.36	4.01	4.05
		ND	1.65	1.77	2.32	4.05	4.18
Ca19.40	1923	MD	1.60	1.76	2.36	4.02	4.06
		ND	1.65	1.77	2.34	4.05	4.10
Ca33.33	1823	MD	1.61	1.76	2.36	4.00	4.05
		ND	1.65	1.77	2.36	4.05	4.23

The above description further confirms that the combined hybrid potential (Buckingham and BMH) has a better application in the CAS system. Therefore, in the same approach, the MD simulation with the combined potential is also appropriate for the experimental samples of the CAS system.

In order to understand the structural evolution of CAS0-CAS25, the structural parameters were calculated, strictly in accordance with the RDF and CN of atoms. The RDF and CN are described as follows.

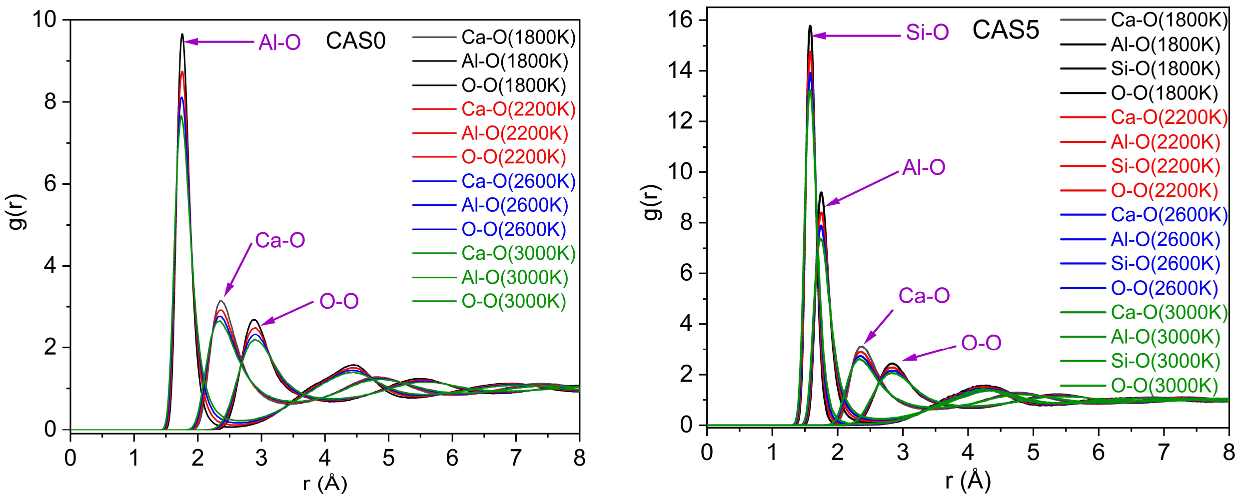

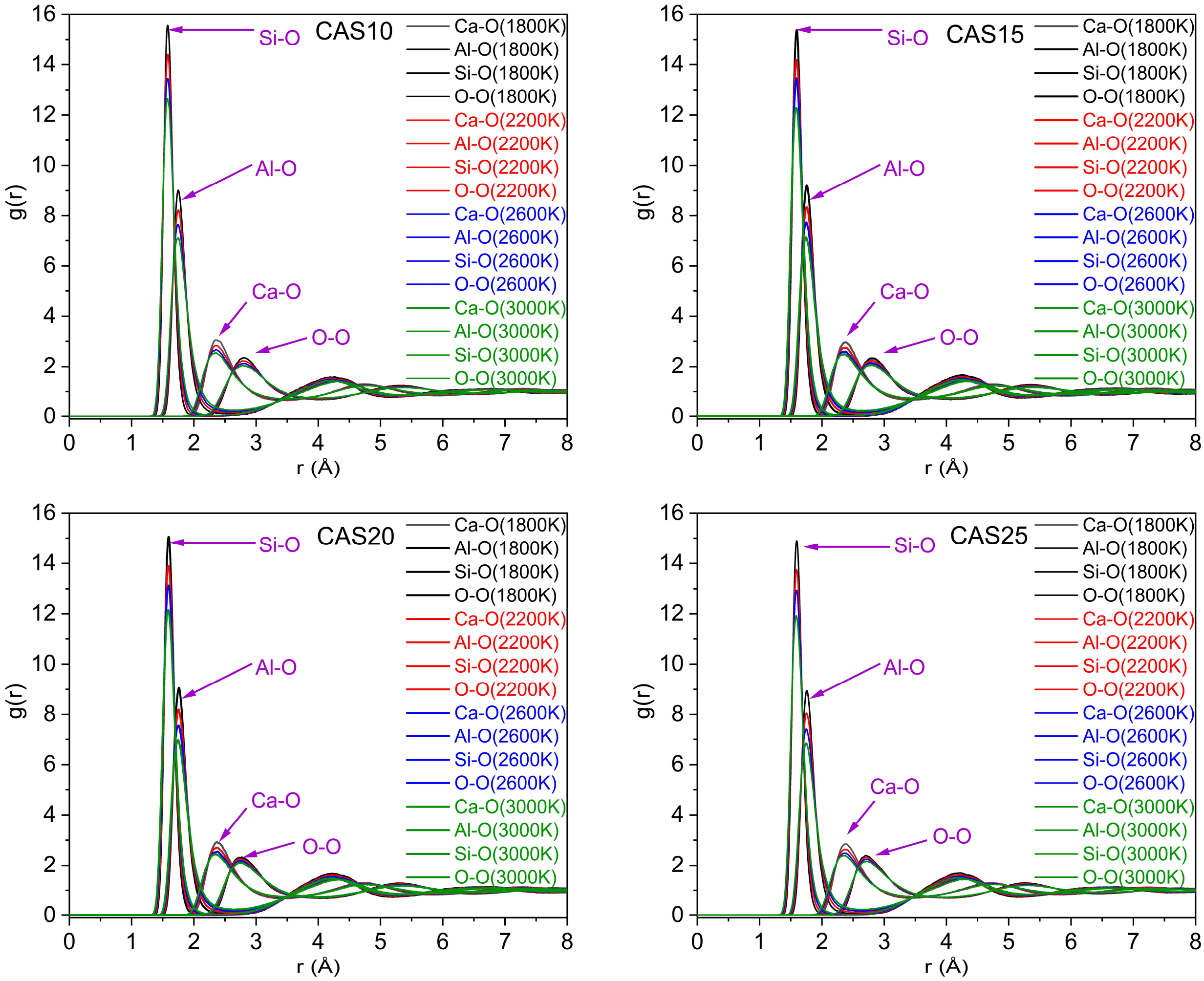

Figure 4-10. Radial distribution functions of Si-O, Al-O, Ca-O, and O-O in the CAS system at 1800, 2200, 2600, and 3000 K.

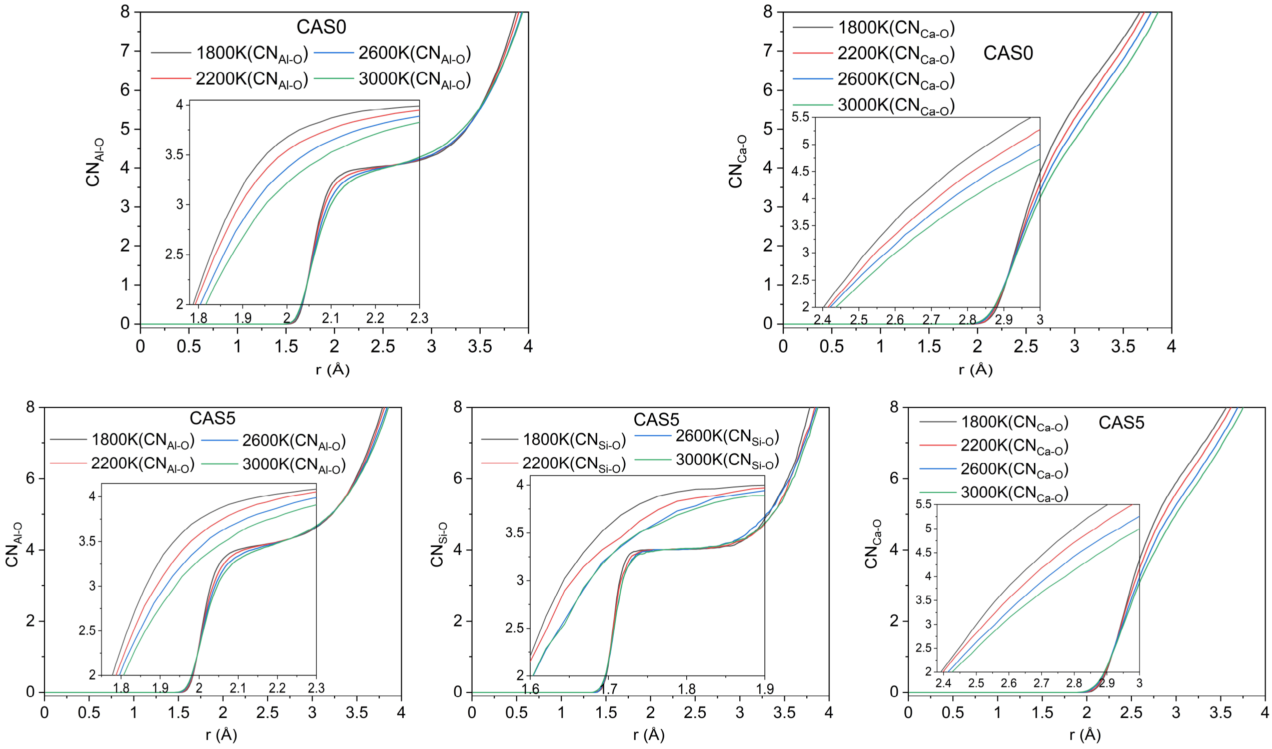

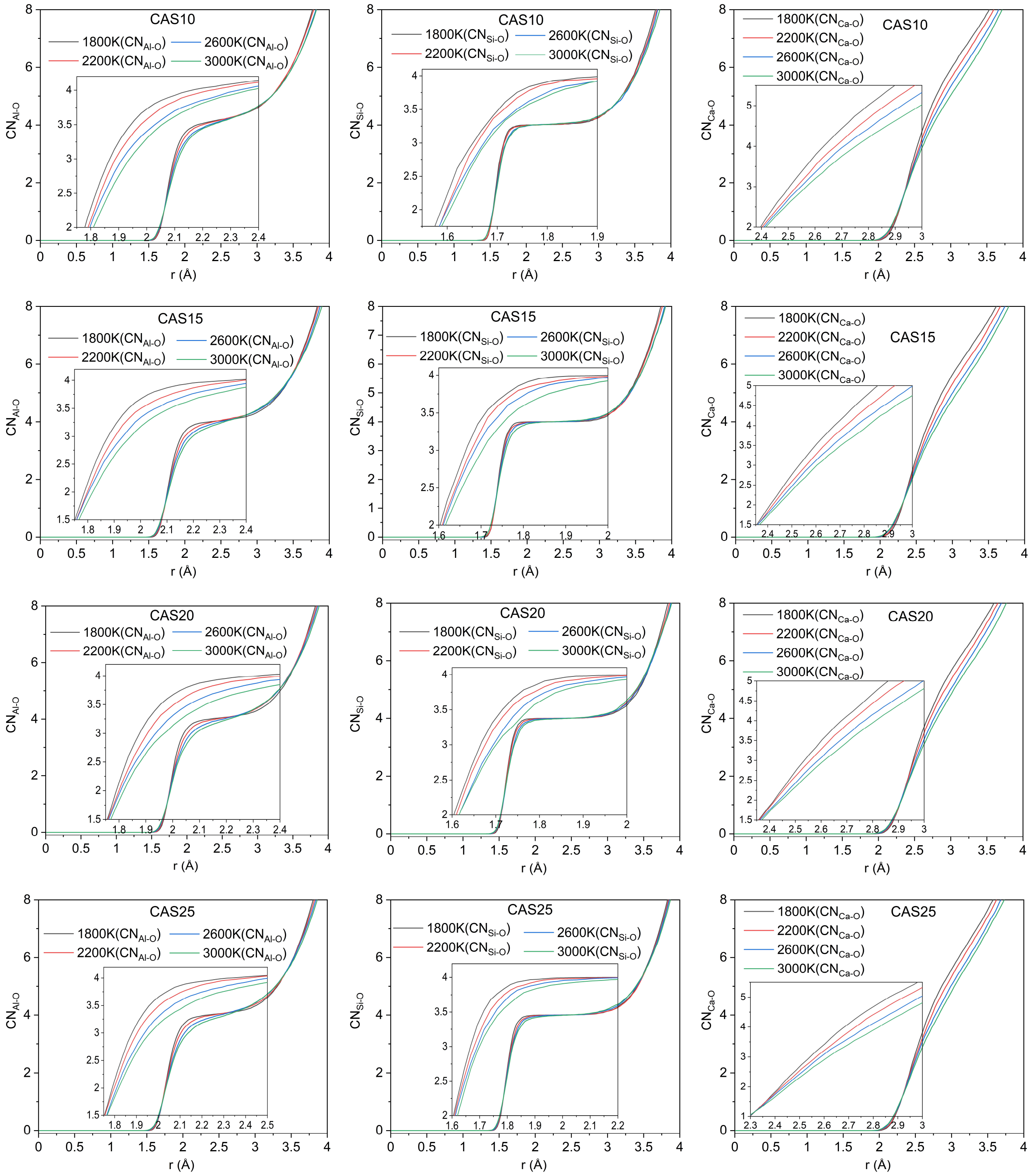

Figure 4-11. The coordination number of Al, Si, and Ca atoms in the CAS melts.

4.3.2.2 Bond length distribution and bond angle distribution of the $CaO-Al_2O_3-SiO_2$ system at 1800, 2200, 2600, and 3000 K

In this work, there are four simulating temperature points (1800 K, 2200 K, 2600 K, and 3000 K) for the MD simulation of each composition. Due to trends similarity of structural parameters, we choose a composition and a temperature as examples to be described.

4.3.2.2.1 Bond length distribution

The total bond length distribution (BLD) composed of Al-O, Si-O, and Ca-O bonds in the CAS melts at different temperatures during the *r*-value ≤ 4 Å are shown in Figure 4-12. Figure 4-12 (a1-a6) expresses the comparison of BLD of the individual melt at 1800, 2200, 2600, and 3000 K. The BLDs of the CAS melts are similar. The peaks and troughs of BLD are basically located at the same *r* value. Combined with the RDFs of Al-O and Ca-O, the first and second peaks of the total BLD mainly represent the peak of BLD of Al atoms bonding to the first neighbor O atoms and the peak of BLD of Ca atoms bonding to the first neighbor O atoms, respectively. With increasing temperatures, the peak of BLD gradually reduces. It probably expresses increasing temperature can reduce the amount of Al-O bonds and Ca-O bonds. Moreover, the full width at half maximum (FWHM) of the first peak of total BLD gradually becomes wider from CAS0 to CAS25, where the FWHM of the BLD curve of CAS25 is most visible. Combined with the RDF of Si-O, the bond length of Si-O is less than that of Al-O. Increasing SiO_2 content results in the FWHM being wide. Figure 4-12 (b1-b4) shows the comparison of BLD of the individual temperature for the CAS melts, which helps observe the influence of composition on the BLD. The FWHM of the first peak is easily observed to become wider with increasing SiO_2 content. Meanwhile, increasing SiO_2 content causes the location of the first peak to shift to a low *r*-value and the location of the second peak remains unchanged. Overall, temperature and the SiO_2 content have an effect on the BLD of the CAS melts.

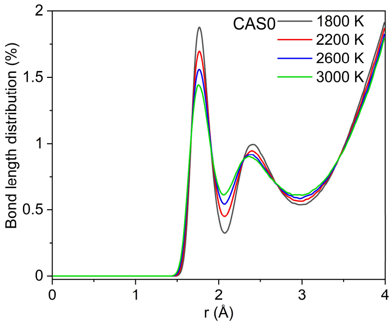

(a1)

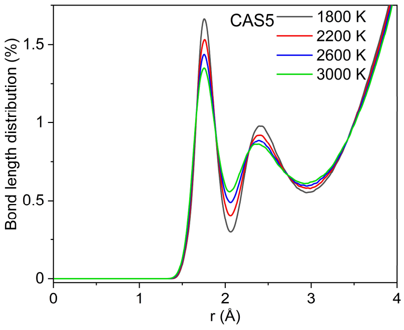

(a2)

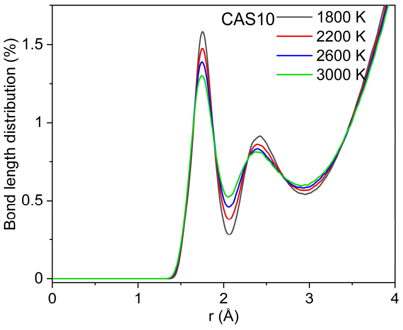

(a3)

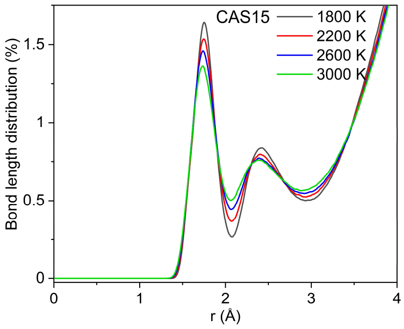

(a4)

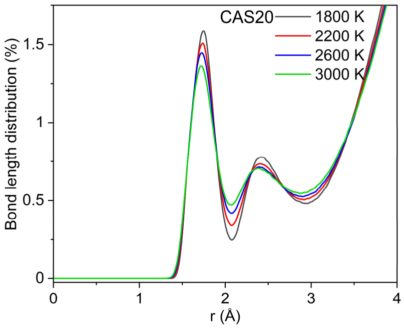

(a5)

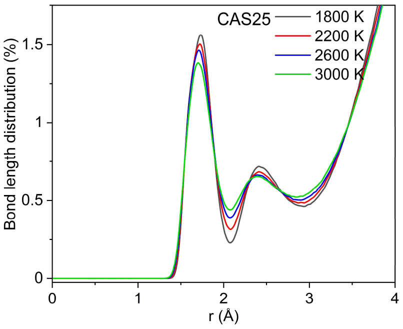

(a6)

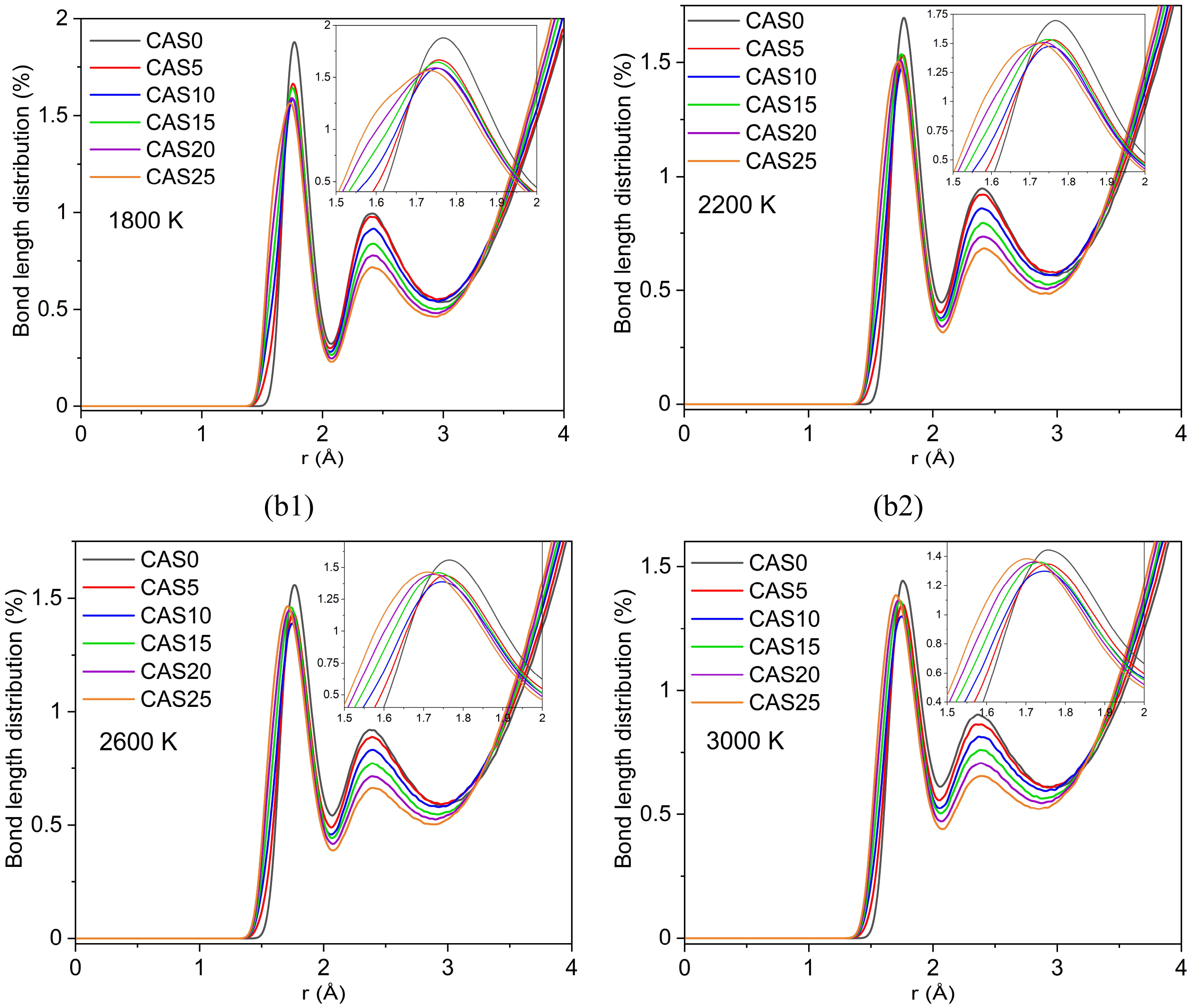

(b1) (b2)

(b3) (b4)

Figure 4-12. Total bond length distribution (normalization) of Al-O, Si-O, and Ca-O in the CAS system: (a1-a6): CAS0, CAS5, CAS10, CAS15, CAS20, and CAS25; (b1-b4): 1800, 2200, 2600, and 3000 K.

4.3.2.2.2 Bond angle distribution

Bond angle distribution (BAD) of O-Al-O, Al-O-Al, Ca-O-Ca, O-Si-O, and Al-O-Si in the CAS melts at 1800, 2200, 2600, and 3000 K were calculated, as shown in Figure 4-13. The peaks of O-Al-O BAD of the CAS melts (CAS0-CAS25) are located at 105.5 ± 1°. With increasing temperature, the intensity of the main peaks and their FWHM are gradually low and broad. With increasing SiO_2 content, a decrease in Al_2O_3 content causes the intensity of the main peaks are gradually decreasing. There are a shoulder and a peak on the Al-O-Al BAD curves, which are located at 92.5 ± 2° and 125.5 ± 2°, respectively. With increasing temperature (1800-3000 K) and SiO_2 content (CAS0-CAS25), the intensity of the peaks on the Al-O-Al BAD is gradually decreasing, while the intensity of the shoulders is gradually increasing. In Figure 4-13 (a3), there are a peak and two shoulders in the O-Ca-O BAD, where the peak is located at 67.5 ± 1°. The two shoulders are located centered around 85° and 115°, respectively. The intensity of the O-Ca-O BAD gradually decreases with rising temperature.

It is interesting to mention that the intensity of the shoulder located centered around 85° is gradually increasing with increasing SiO_2 content, where the intensity of this shoulder in CAS20 and CAS25 exceeds the intensity of the initial peak. However, the other shoulder located at 115° is gradually invisible. The peaks of the O-Si-O BAD are located at 108.3 ± 0.5° and sharper, compared to the peaks of the O-Al-O BAD. With increasing temperature, the intensity and the FWHM of the peaks gradually decrease and broaden. On the contrary, the intensity of the peaks increases with increasing SiO_2 content. For the Al-O-Si BAD, a peak and a shoulder appear in the BAD curves, which are located at 135.0 ± 2° and 94.3 ± 1°, respectively. With increasing temperature, the intensity of the peaks and the shoulders decreases and increases. Meanwhile, increasing SiO_2 content causes an increase in the intensity of Al-O-Si BAD.

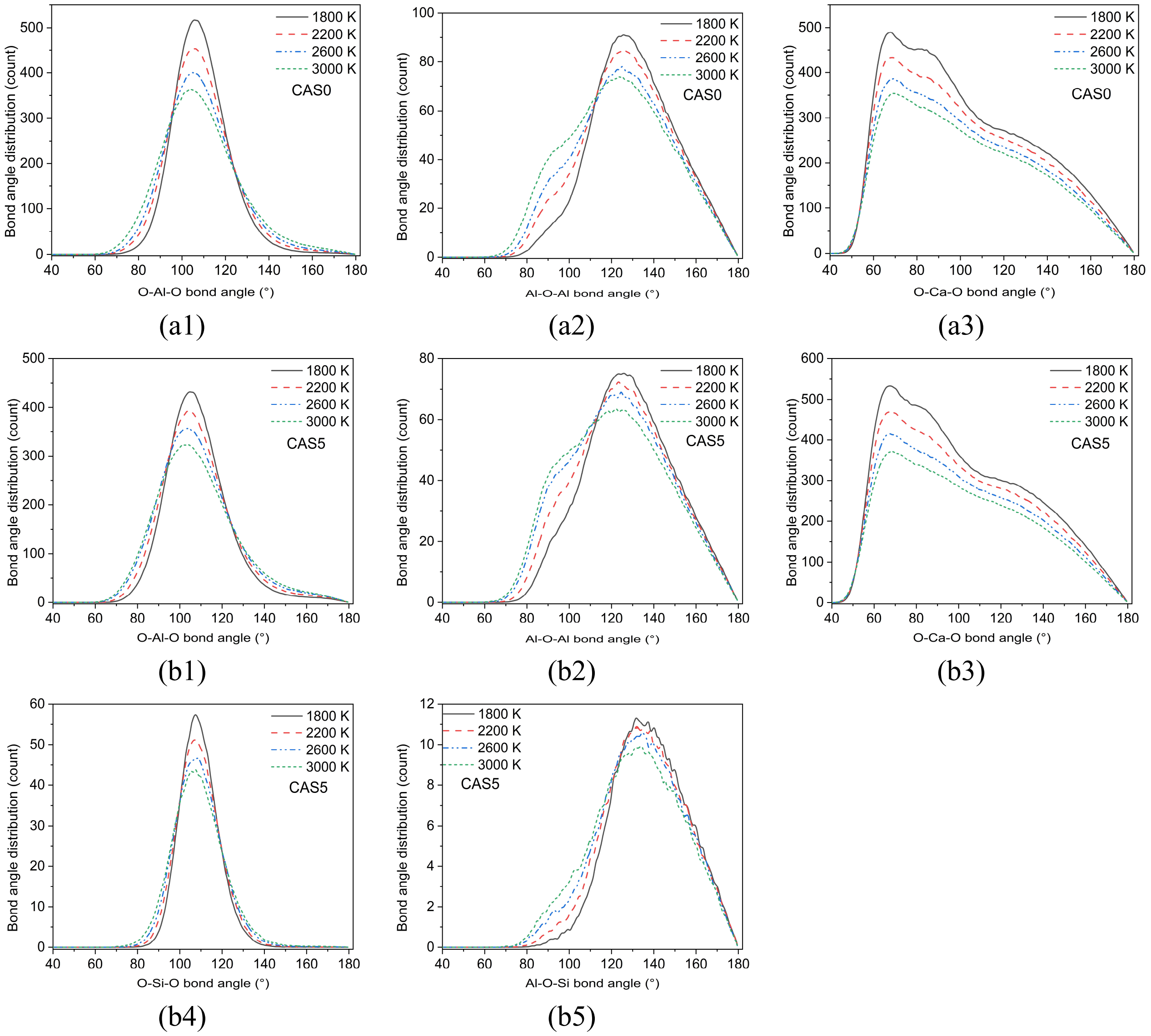

(a1) (a2) (a3)

(b1) (b2) (b3)

(b4) (b5)

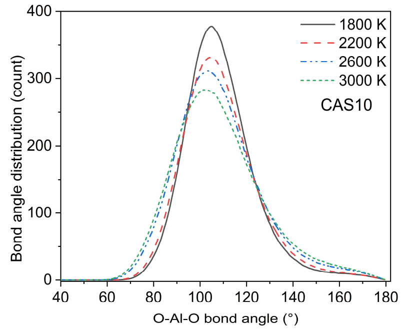

(c1)

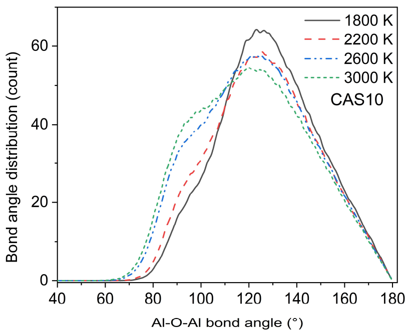

(c2)

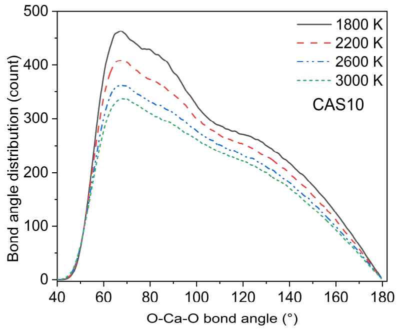

(c3)

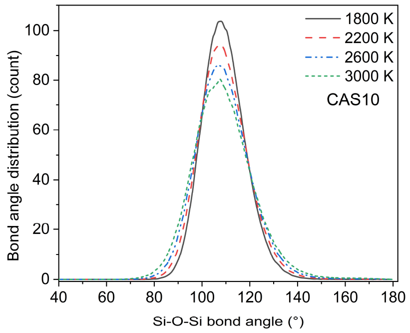

(c4)

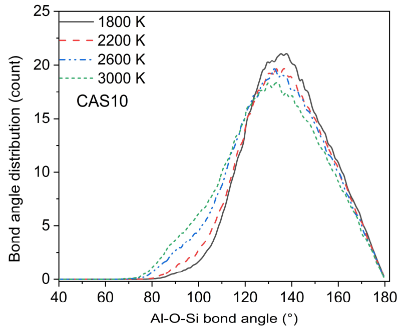

(c5)

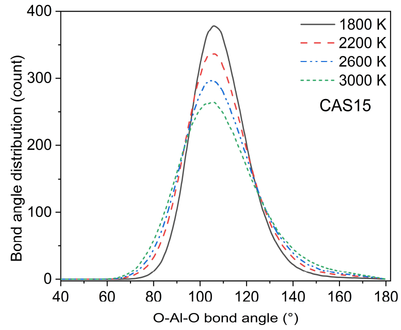

(d1)

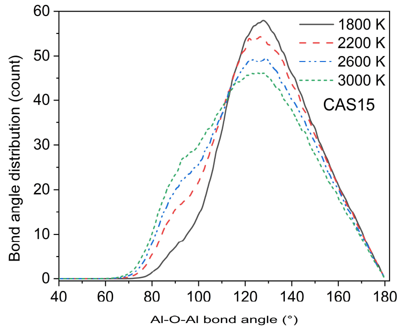

(d2)

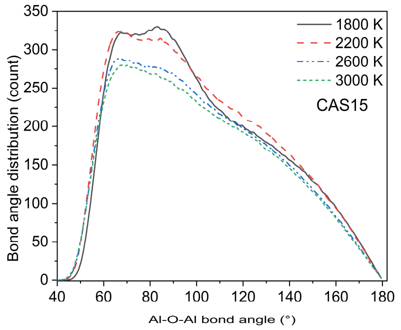

(d3)

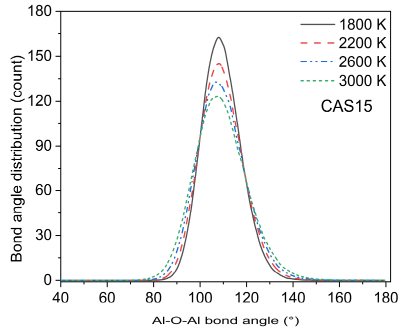

(d4)

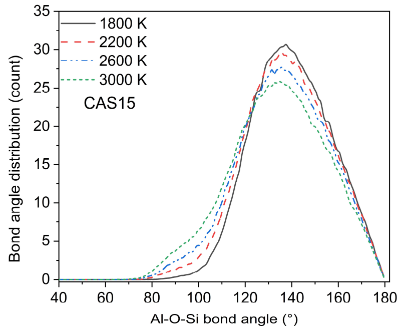

(d5)

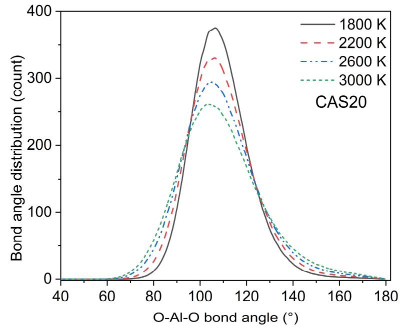

(e1)

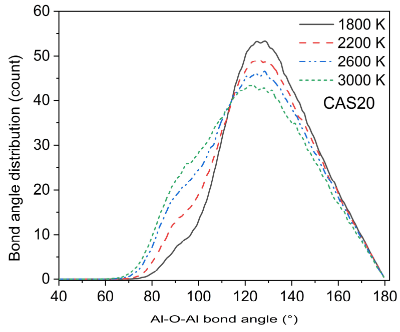

(e2)

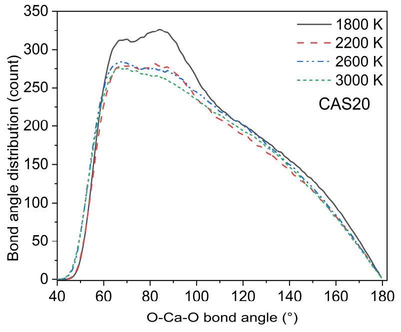

(e3)

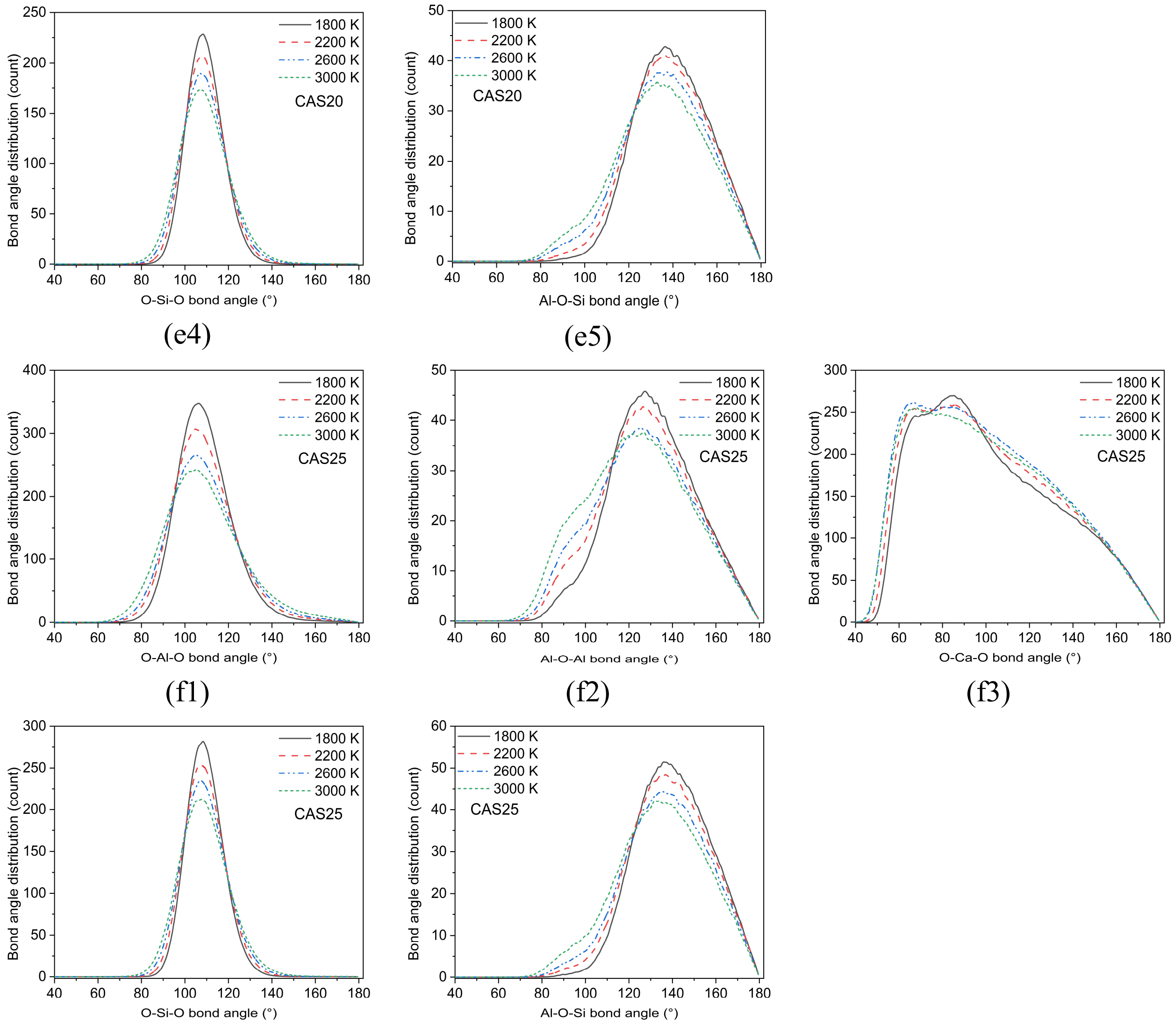

(e4) (e5)

(f1) (f2) (f3)

(f4) (f5)

Figure 4-13. Bond angle distribution of O-Al-O, Al-O-Al, Ca-O-Ca, O-Si-O, and Al-O-Si in the CAS melts: (a) CAS0; (b) CAS5; (c) CAS10; (d) CAS15; (e) CAS20; (f) CAS25.

4.3.2.3 Oxygen species, charge compensation degree, network connectivity, and unsatisfied oxygen bonds of the CaO-Al_2O_3-SiO_2 melt at 1800, 2200, 2600, and 3000 K

4.3.2.3.1 Oxygen species

To understand the network evolution of the CAS system at different temperatures, the oxygen species were calculated from MD simulations. Figure 4-14 (a1-a6) shows the fraction of BO, NBO, TCO, and FO in a single melt at 1800, 2200, 2600, and 3000 K. With increasing temperature, the fraction of BO gradually decreases while the fractions of NBO, TCO, and FO are increasing. In addition, the fractions of oxygen species in each melt have an order as follows: BO > NBO > TCO > FO, where the fractions of BO and NBO are far more than that of TCO and FO. To facilitate the observation of the effect of composition on oxygen species, the fractions of BO, NBO, TCO, and FO in the CAS system at a single temperature are shown in Figure 4-14 (b1-b4). With increasing SiO_2 content, the fraction of BO is successively increasing, while the fraction of NBO is gradually decreasing. The fractions of TCO and FO slightly decrease with an increase in SiO_2 content. Overall, the SiO_2 content has a greater influence on BO and NBO than temperature, according to the variations of BO and NBO.

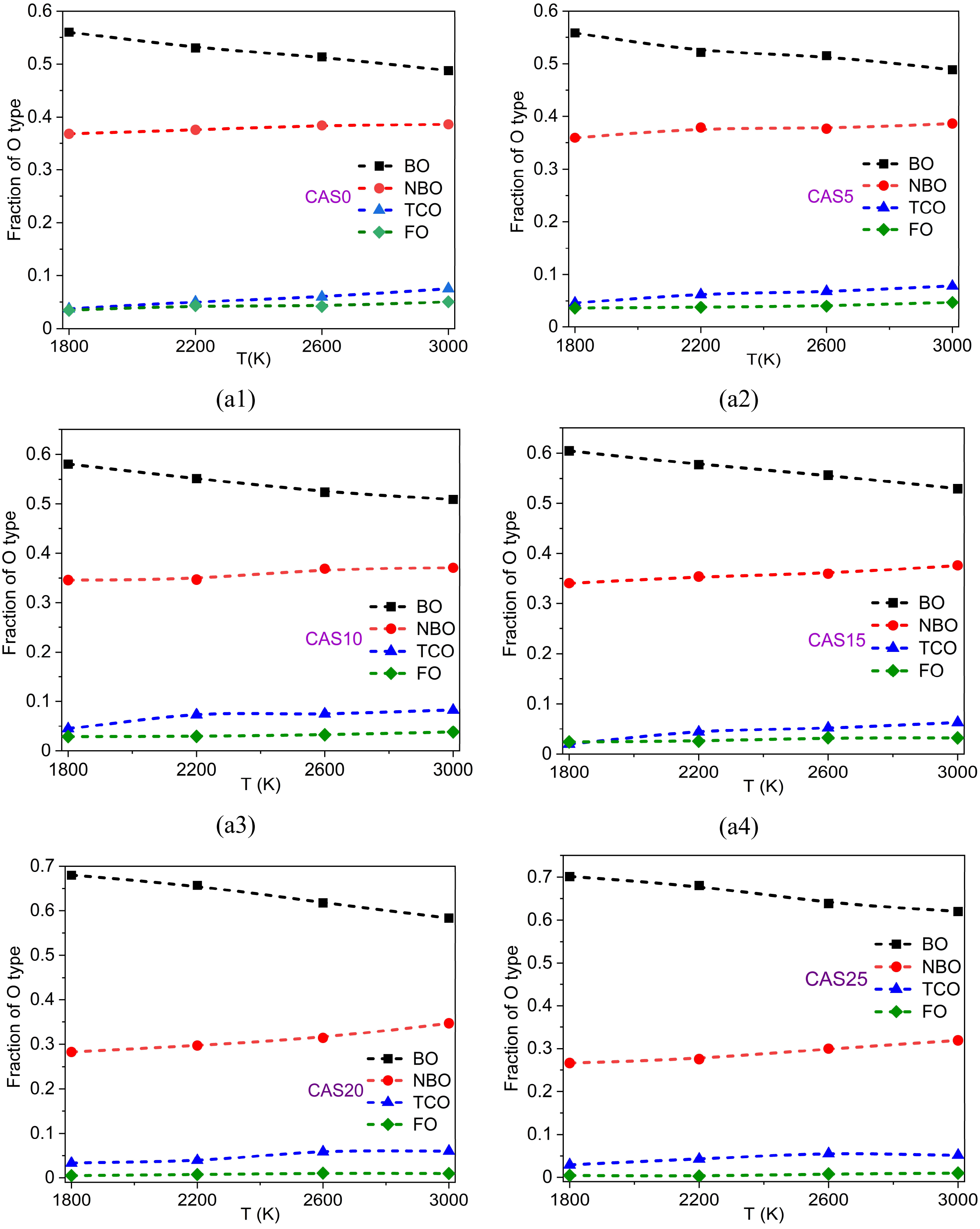

(a1) (a2)

(a3) (a4)

(a5) (a6)

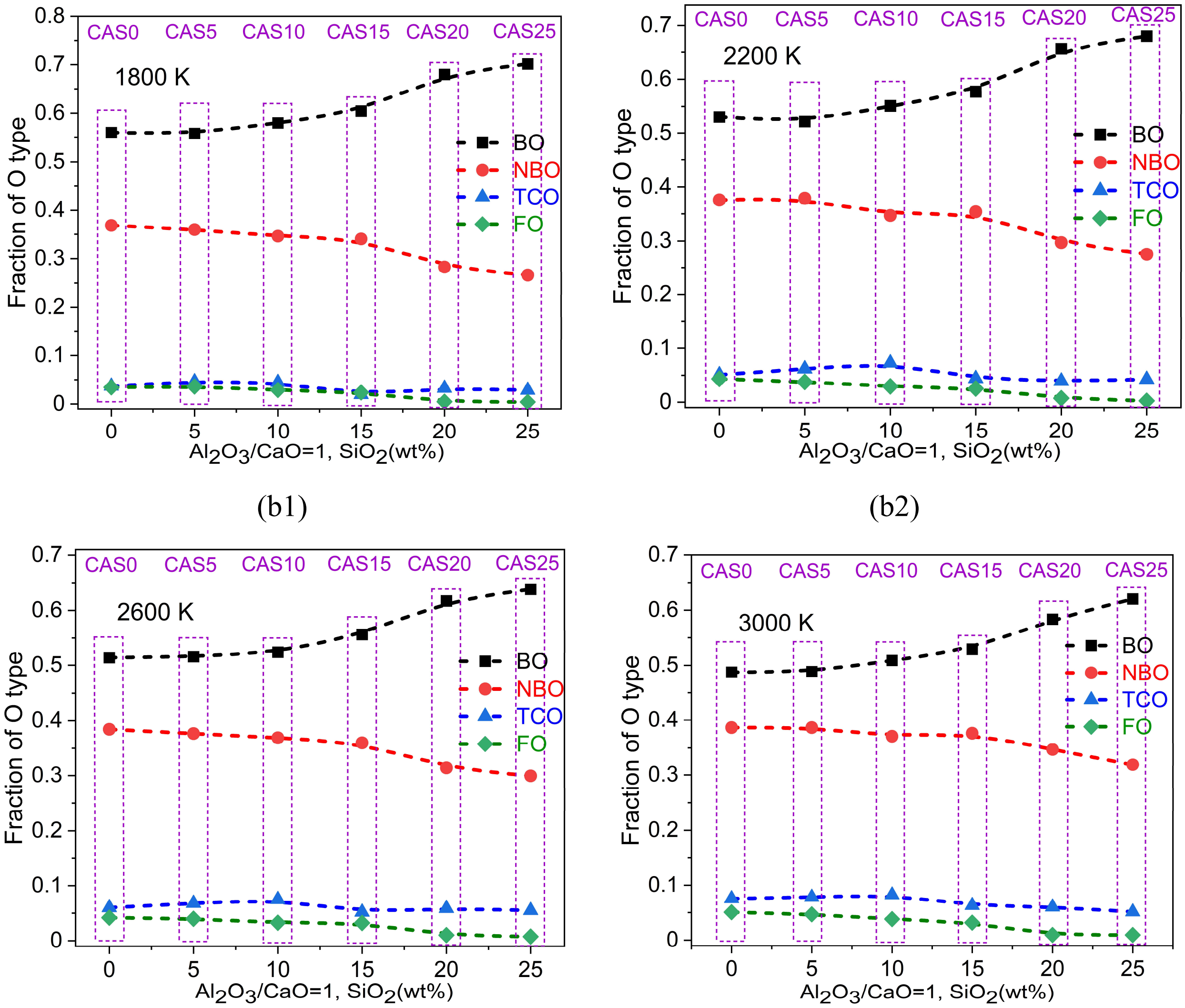

(b1)

(b2)

(b3)

(b4)

Figure 4-14. Fractions of oxygen species in the single melt at different temperatures and in the CAS system at the single temperature. (a1-a6): CAS0, CAS5, CAS10, CAS15, CAS20, and CAS25; (b1-b4): 1800, 2200, 2600, and 3000 K.

4.3.2.3.2 The degree of charge compensation

Ca^{2+} cations play a dual role in the CAS system as well, as network modifiers and charge compensators. As the charge compensator, the Ca^{2+} cation offers unbalanced charges for specific oxygen, which is connected to two or more network-forming $[AlO_n]$ or $[SiO_n]$ polyhedrons. The degree of charge compensation in the CAS system at different temperatures was calculated and is shown in Figure 4-15. With increasing temperature, the degree of charge compensation is gradually decreasing, where the difference in the degree of charge compensation at 1800 and 3000 K is around 7.5 ± 0.5 %. With increasing SiO_2 content, the degree of charge compensation is also gradually increasing.

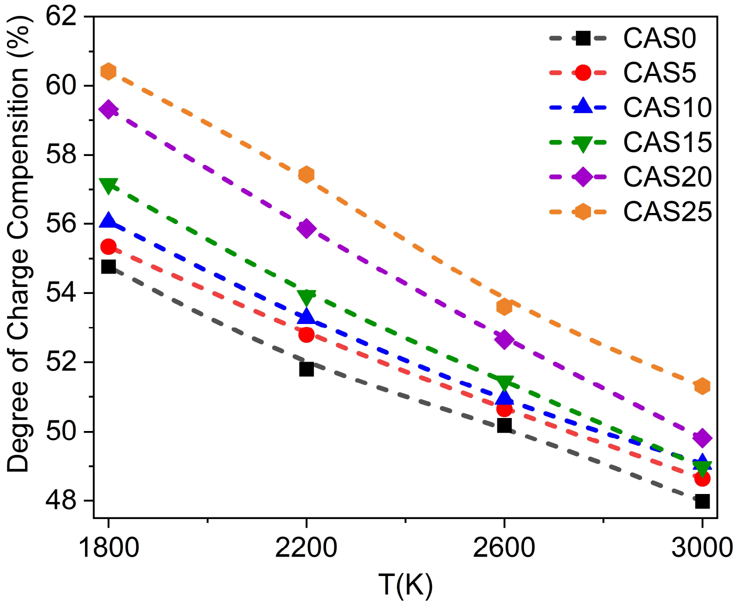

Figure 4-15. The degree of charge compensation in the CAS system at different temperatures

4.3.2.3.3 Network connectivity

Figure 4-16 shows the network connectivity of the CAS system at different temperatures. As expected, decreasing temperature and increasing SiO_2 content both would cause an increase in the network connectivity of the CAS melts. Furthermore, changes in SiO_2 content have a larger influence on network connectivity than temperature.

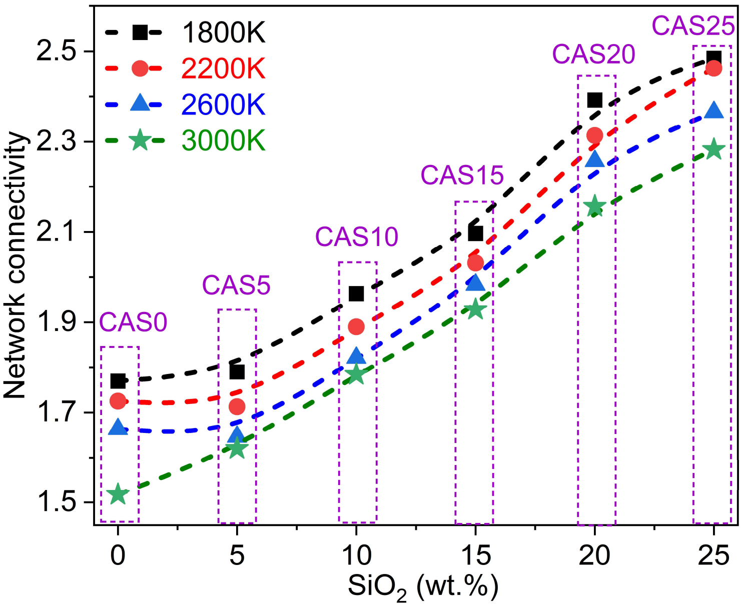

Figure 4-16. The network connectivity of the CAS system at 1800, 2200, 2600, and 3000 K.

4.3.2.3.4 Unsatisfied oxygen bonds

The unsatisfied oxygen bonds (UOBs) in the CAS system are calculated from MD simulations because it is closely related to surface tension [Zhang et al., 2021b]. The definition of UOBs in the CAS system is described as follows: partial oxygen ions forming stable bonds with network-formed cations still need network-modified cations to keep charge balance and partial NBOs are bonding with modifying cations, which forms modified unsatisfied oxygen bonds; meanwhile, charge compensation of $[AlO_4]$ is accomplished by the formation of three coordinated oxygens (namely TCO). Specific classifications are as follows:

- 2Al-O-n[Ca] (representing an O atom bonding with two Al atoms and $n \geq 1$ Ca atoms),
- Al-O-Si-n[Ca] (representing an O atom bonding with one Al atom, one Si atom, and $n \geq 1$ Ca atoms),
- 2Si-O-n[Ca] (representing an O atom bonding with two Si atoms and $n \geq 1$ Ca atoms),
- 3(Al/Si)-O-n[Ca] (representing an O atom bonding with three network-former atoms (Al or Si or both) and $n \geq 1$ Ca atoms),
- 3(Al/Si)-O (representing an O atom bonding with three Al atoms), Al-O-n[Ca] (an O atom bonding with one Al atom and $n \geq 1$ Ca atoms),
- Al/Si-O-n[Ca] (an O atom bonding with one network-former atom (Al or Si) and $n \geq 1$ Ca atoms),

where [atom] is as charge compensator.

Meanwhile, Al-O-Al, Si-O-Si, Al-O, Si-O, and O-Ca are defined as satisfied oxygen bonds (OBs). The oxygen bonds (UOBs and OBs) in the CAS system at different temperatures are shown in Figure 4-17. Figure 4-17 (a1-a6) shows the influence of temperature on the UOBs and OBs in the single melt. With increasing temperature, the contents of 2Al-O-n[Ca] and Al-O-Si-n[Ca] are gradually decreasing while the contents of Al-O-n[Ca] and OBs gradually increase, and the contents of Si-O-n[Ca], 3(Al/Si)-O-n[Ca], and 3(Al/Si)-O are slightly increasing. Figure 4-17 (b1-b4) shows the influence of SiO_2 content on the UOBs and OBs in the CAS system. With an increase in SiO_2 content, the contents of 2Al-O-n[Ca] and Al-O-n[Ca] gradually reduces while the contents of Al-O-Si-n[Ca], 2Si-O-n[Ca], Si-O-n[Ca], and OBs gradually increases. And the total content of 3(Al/Si)-O-n[Ca] and 3(Al/Si)-O is seemingly not sensitive to the change in SiO_2 content.

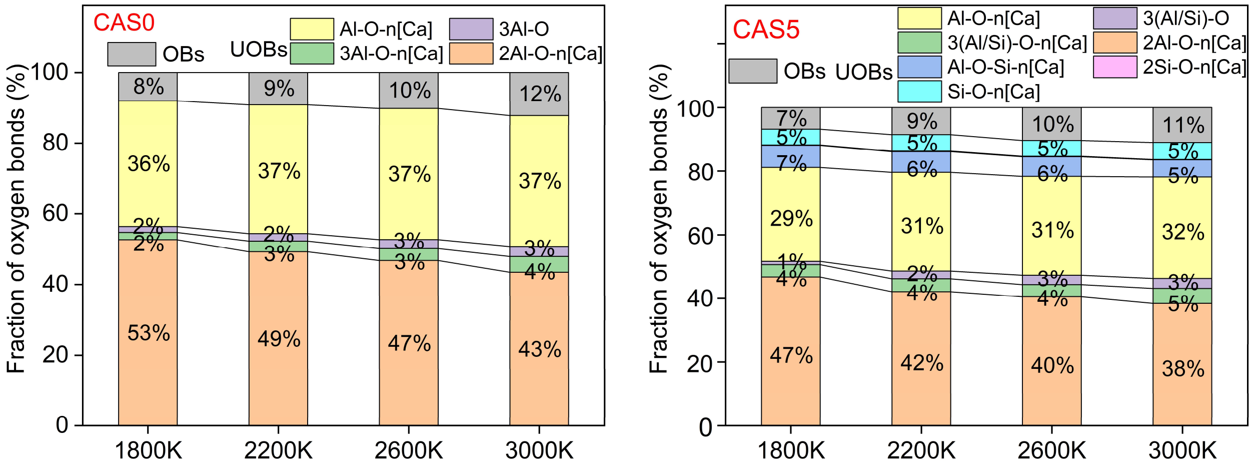

(a1)

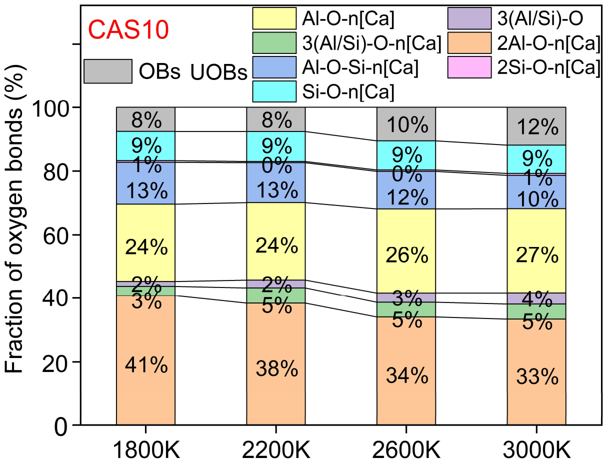

(a2)

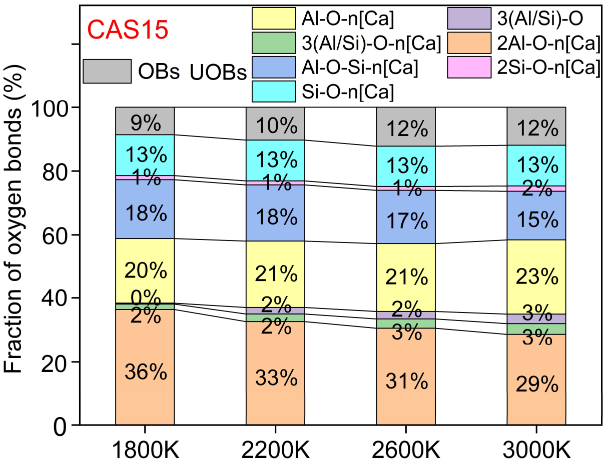

(a3)

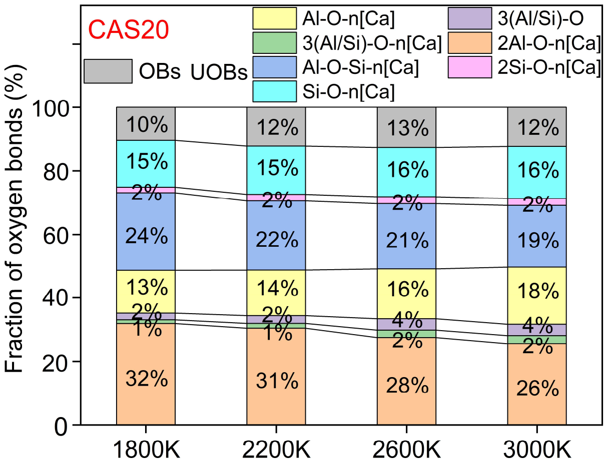

(a4)

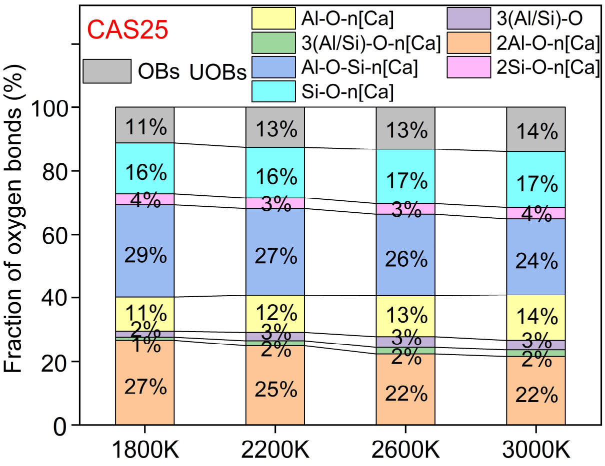

(a5)

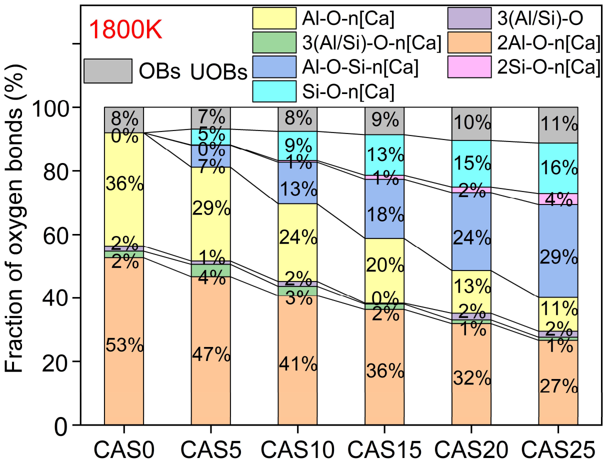

(a6)

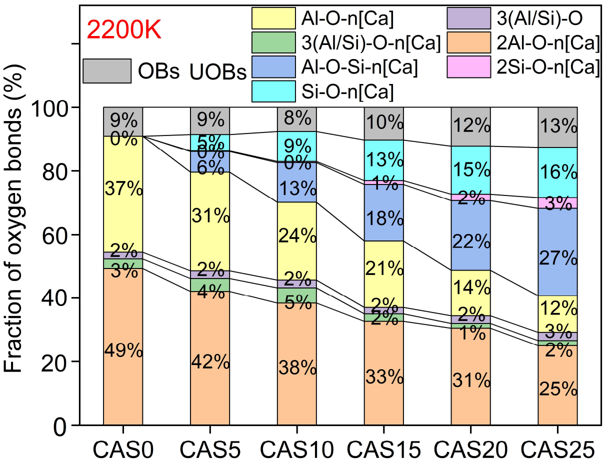

(b1)

(b2)

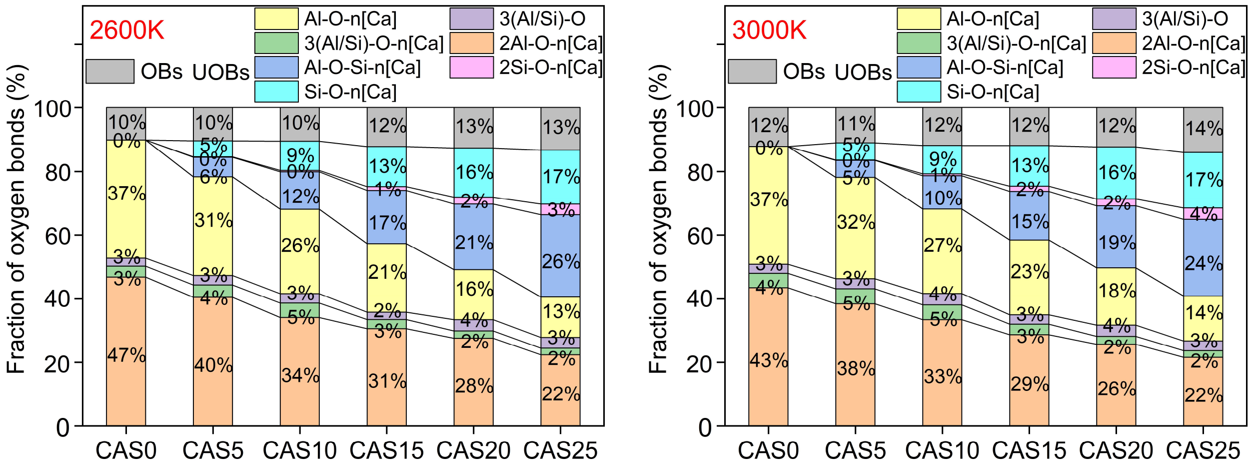

(b3) (b4)

Figure 4-17. Fraction of oxygen bonds (normalization) in the single melt at different temperatures and in the system at the single temperature. (a1-a6): CAS0, CAS5, CAS10, CAS15, CAS20, and CAS25; (b1-b4): 1800, 2200, 2600, and 3000 K.

4.4 Discussions

4.4.1 The influences of composition and temperature on structural parameters of the CaO-Al_2O_3-SiO_2 system

Based on the results of the structural parameters, the effects of different temperatures and SiO_2 content on the structural evolution of the CAS melts are observed. Increasing temperature can increase the energy and atomic motion of the CAS system, which causes some bonds to break free from the bondage of the interaction. It reflects that the peaks of BLD of the CAS melts successively decrease from 1800 to 3000 K. With increasing SiO_2 content, the Si-O bonds are gradually increasing. Due to the bond length of Si-O shorter than that of Al-O, the FWHM of the first peak of BLD gradually broadens and the location of the first peak shifts to the low r-value.

The O-Al-O BAD and O-Si-O BAD are related to the Al and Si coordination number, which can be explained by the contents of [AlO_n] and [SiO_n] species. Here the fraction of [AlO_n] and [SiO_n] species in CAS20 as an example are shown in Figure 4-18, due to the trends similarity of [AlO_n] and [SiO_n] species in different CAS melts. The bond angle of O-Al-O and O-Si-O in perfect [AlO_4] and [SiO_4] tetrahedrons is equal to $\cos^{-1}(-1/3) = 109^{\circ}$. The existence of [$AlO_3$] and [$AlO_5$] affects the peaks of O-Al-O to shift away 109°, although [AlO_4] tetrahedrons play a leading role in the CAS20 melt. For the same reason, the [SiO_3] and [SiO_5] polyhedrons exist in the CAS20 melt, which makes the peak of O-Si-O shift away109°. It is worth mentioning that the [SiO_4] tetrahedron is the leading position of [SiO_n] polyhedrons and its percentage is far more than [SiO_3] and [SiO_5] polyhedrons. The percentage of the [SiO_4] tetrahedron in [SiO_n] species is more than that of the [AlO_4] tetrahedron in [AlO_n] species, which is an answer for the sharper peak of the O-Si-O BAD, compared to the peak of the O-

Al-O BAD. Meanwhile, due to the different electronegativity of Al and Si atoms, a large number of Al-O-Si in the CAS20 melt would lead to the distortion of the [AlO4] and [SiO4], which affects the bond angles of O-Al-O and O-Si-O as well. From Figure 4-18, the percentages of [AlO4] and [SiO4] tetrahedrons are gradually decreasing with increasing temperature, which explains a decrease in the intensity of the peaks of the O-Al-O BAD and O-Si-O BAD and a broadening of FWHM.

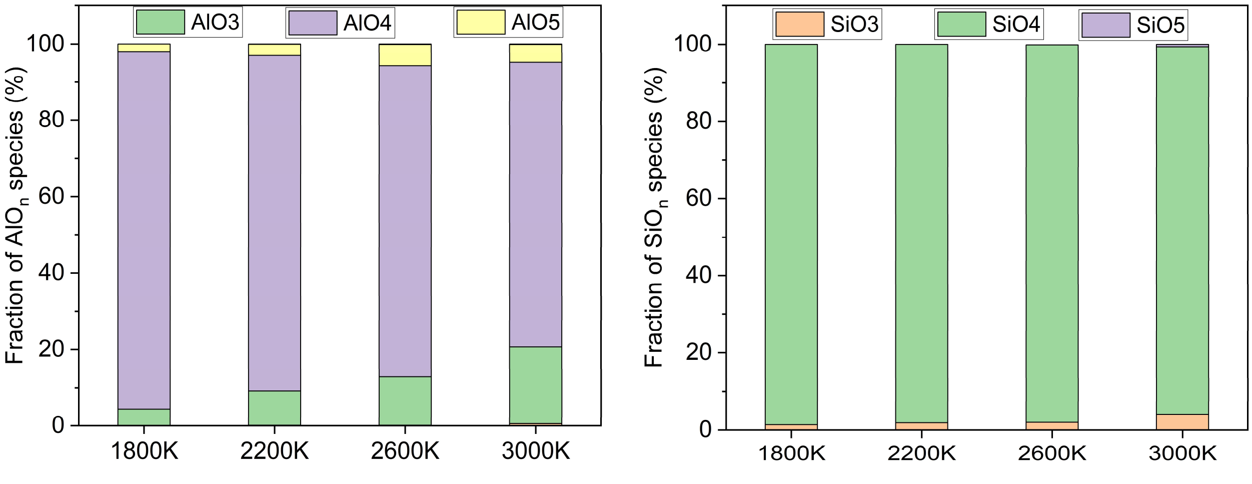

(a) (b)

Figure 4-18. Fractions of [AlO$_n$] and [SiO$_n$] species in the CAS20 melt at 1800, 2200, 2600, and 3000 K: (a) [AlO$_n$] polyhedrons; (b) [SiO$_n$] polyhedrons

The Al-O-Al BAD reflects the connectivity of [AlO$_n$] polyhedrons to each other. The peaks of Al-O-Al BAD located around 125° arise from corner shared two [AlO$_n$] polyhedrons. BO as the shared atom is bonding two [AlO$_n$] polyhedrons, which is expressed as Al-BO-Al. The shoulders of Al-O-Al BAD located around 94° are taken from a configuration that involves TCO atoms shared by three [AlO$_n$] polyhedrons [Drewitt et al., 2011]. This kind of configuration can be shown as nAl-TCO ($n = 3$). The Al-O-Si BAD reveals insight into the linked configuration of the [AlO$_n$] and [SiO$_n$] polyhedrons to each other. The Al-O-Si BAD is similar to the analysis of the Al-O-Al BAD. The peaks of Al-O-Si BAD mainly show BO as a shared atom linking one [AlO$_n$] and one [SiO$_n$], where the configuration is expressed as Al-BO-Si. The shoulder of the Al-O-Si BAD also reflects a tri-cluster configuration that is composed of three polyhedrons ([AlO$_n$] and [SiO$_n$]) shared by an oxygen atom, where the configuration can be described as nAl-TCO-mSi ($n \geq 1$, $m \geq 1$, $n+m=3$). To verify the above explanation, the fractions of Al-BO-Al, nAl-TCO, Al-BO-Si, and nAl-TCO-mSi in the CAS20 melt at different temperatures and in the CAS melts at 2200 K were calculated, as shown in Figure 4-19. From Figure 4-19 (a1 and b1), with increasing temperatures, the fractions of Al-BO-Al and Al-BO-Si are gradually decreasing, while the fractions of nAl-TCO and nAl-TCO-mSi are gradually increasing. It can explain why the intensity of the peaks of Al-O-Al BAD and Al-O-Si BAD in each sample successively decreases and the intensity of the shoulders grows with an increase in temperature. From Figure 4-19 (a2 and b2), with increasing SiO_2 content, the fractions of Al-BO-Al and nAl-TCO decrease, while the fractions of Al-BO-Si, and nAl-TCO-mSi are growing. It reveals that the intensity of Al-O-Al BAD gradually decreases and the intensity of Al-O-Si BAD increases.

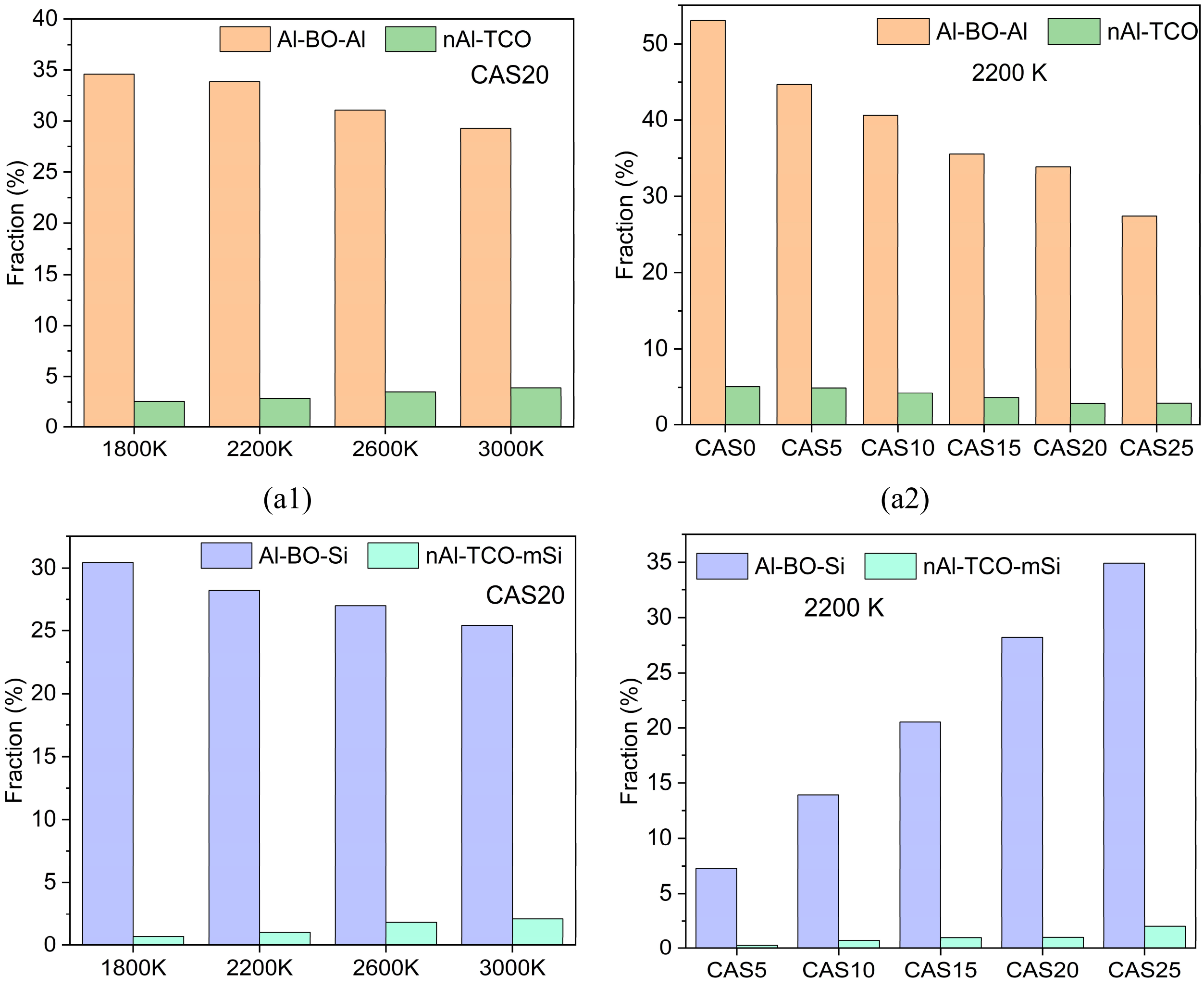

(a1) (a2)

(b1) (b2)

Figure 4-19. Fractions of Al-O-Al (BO bonding 2 Al atoms), nAl-O (TCO bonding 3 Al atoms), Al-BO-Si (BO bonding an Al atom and a Si atom), and nAl-TCO-mSi (TCO bonding 3 Al or Si atoms, $n \geq 1$, $m \geq 1$, $n+m=3$) in the CAS20 melt at different temperatures (a1 and b1) and in the CAS melts at 2200 K (a2 and b2).

The main peaks of O-Ca-O BAD around 67° originate from Ca bonded to two O atoms of the same $[AlO_4]$ tetrahedron forming distorted triangles. The shoulders located around 85° may arise from the presence of distorted sixfold octahedra [Drewitt et al., 2011] or the configurations, which is Ca atoms linked BO atoms [Cormack et al., 2001]. In addition, another broad feature in the O-Ca-O BAD may arise from Ca connected to two O atoms of two different $[AlO_n]$ polyhedrons, corresponding to a broad angle range. In order to intuitively understand the bond angle distribution, the schematic diagram of bond angles is described in Figure 4-20.

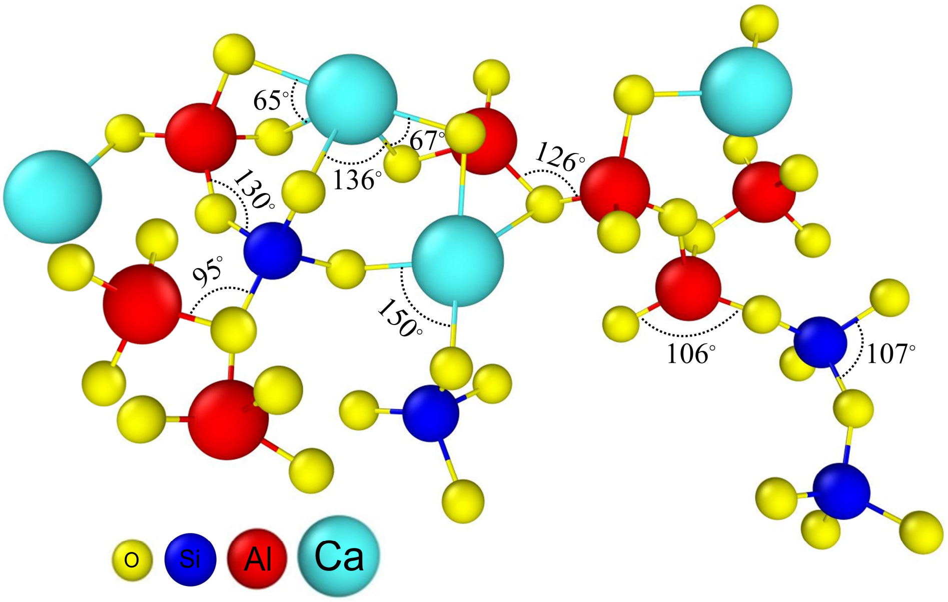

Figure 4-20. A snapshot is taken from the MD simulation of the structure of the CAS20 melt illustrating the origin of the main peaks observed in the bond angle distributions shown in Figure 4-13.

Regarding the influence of temperature on oxygen species in a single melt, a possible explanation for the variation of oxygen species with decreasing temperature is as follows: TCO which is shared by three former cations (Al^{3+} and Si^{4+}) belongs to an unstable configuration. The NBO configurations are higher-energy linking than BO configurations. The higher temperature can provide energy to generate TCO and NBO configurations. Once the temperature goes down, TCO and NBO configurations could transform into BO configurations (Al-O-Al, Al-O-Si, Si-O-Si). This causes an increase in BO and decreases in TCO and NBO. It is worth mentioning that, in amorphous aluminosilicates, when there are no charge compensators, charge compensation of [AlO_4] is accomplished by the formation of three coordinated oxygens [Du et al., 2022]. The decrease in TCO content intensifies the imbalance of charge, which enhances the role of Ca^{2+} as a charge compensator. Decreasing temperature causes more formation of BO, increasing network connectivity. Meanwhile, BO bonds with Ca^{2+}, which improves the degree of charge compensation. In addition, SiO_2 is a typical network former and increasing its content would increase the content of BO, which leads to an increase in network connectivity. The weight proportion of CaO is gradually decreasing and the role of Ca as a network modifier is gradually weakening, which results in a decrease in NBO. Al^{3+} with various coordination numbers is easy to lead to the charge imbalance of [AlO_n]-groups. Al^{3+} is one of the reasons that cause the formation of TCO configurations and decreasing the weight proportion of Al_2O_3 would decrease the content of TCO, which increases the charge imbalance of the groups containing [AlO_n]. That induces that Ca^{2+} links more groups with charge imbalance, thereby, the degree of charge compensation is gradually increasing.

4.4.2 The influences of composition and temperature on the thermophysical properties of CaO-Al_2O_3-SiO_2 system

4.4.2.1 Density

Compositional variation has a significant effect on bond lengths, bond angles, microstructural units, and oxygen network structures of CAS melts. With increasing the weight proportion of SiO_2, the bond length distribution gradually shifts to the low r-value, due to the bond length of Si-O shorter than the bond length of Al-O and Ca-O. Meanwhile, the degree of charge compensation and the content of BO both are increasing with an increase in SiO_2 content, which improves the degree of polymerization. The above results seem to be the factors contributing to the reduction of the micro-volume. However, unlike calcium-aluminate melts, [SiO_4] tetrahedrons formed by Si^{4+} need fewer charge compensators. Although the polymerization of the Si-O network and large fragments of the Si-O network in amorphous aluminosilicates are gradually increasing with increasing SiO_2 content, most of the fragments are possibly in the shape of chains or branched chains, and only a small fraction of the Si-O network forming rings [Du et al., 2006]. Thereby, the Si-O network is likely to decrease the twining degree of network structure and extend the chain structure of the CAS system, which induces an increase in micro-volume. This could explain why the microscopic volume becomes bigger and the density of the CAS system is gradually decreasing, despite the increase in the degree of polymerization and the decrease in the bond length.

Regarding the effect of temperature on the density of the CAS melts, the explanations are similar to the influence of temperature on the density of the $(CaO)_x(Al_2O_3)_{1-x}$ melts. The increase in temperature can break off some cation-O bonds to make some atoms in a free state. Moreover, the decrease in BO content can not only counterbalance the influence of the TCO formation but also generate microstructural units and reduced the degree of polymerization (the explanation in Section 3.4.2.1). Furthermore, Ca^{2+} cations as charge compensators can promote the compactness of polyhedrons ([AlO_n] and [SiO_n]) in the network structure. Improving temperature leads to a decrease in the degree of charge compensation. More structural units in a dissociated state would decrease the twining degree of each other to promote volume increase. The above may explain why the temperature rise causes the decrease in the density of the CAS melts.

4.4.2.2 Surface tension

The change in chemical composition has a greater influence on the surface tension of the CAS system than that of temperature, like the CaO-Al_2O_3 system. With increasing SiO_2 content, the surface tension of the CAS system is decreasing. The Al-O group is easier to result in the charge imbalance and link to charge compensators. When an Al atom bonds with O atoms, generally the charge is more unbalanced and Al atoms have multiple coordination numbers. Furthermore, the charge-imbalanced Al-O group may be more attractive to Ca than the Si-O group. Thereby, the UOBs bonding [AlO_n] polyhedrons could have a greater contribution to the surface tension than that of UOBs bonding [SiO_4] tetrahedrons. With increasing SiO_2 content, the content of UOBs containing Si atoms and the content of OBs increase while the total content of the UOBs containing Al atoms decreases. The UOBs bonding [SiO_4] tetrahedrons that contribute less to the surface tension replace the UOBs connecting [AlO_n] polyhedrons. That leads to a decrease in the surface tension of the CAS system with increasing SiO_2 content.

The influence of temperature on surface tension is not as sensitive as that of SiO_2 content. Increasing temperature just slightly decreases the surface tension of the CAS melt. The total content of the UOBs (3(Al/Si)-O-n[Ca], 3(Al/Si)-O, 2Al-O-n[Ca], Al-O-Si-n[Ca], and 2Si-O-n[Ca]) caused by charge compensation is also slightly decreasing while the contents of (Al/Si)-O-n[Ca] and OBs increase with increasing temperature. The O atom is shared by more [AlO_n] or [SiO_n] units, where the forming groups more require extra compensating charges to maintain the electrical neutrality of the network due to the electronegativity of the anionic units. Therefore, the UOBs caused by charge compensation could have a greater contribution to surface tension than Al-O-n[Ca] and Si-O-n[Ca]. The comprehensive functioning of the UOBs species results in a slight decrease in surface tension of the CAS system with increasing temperature.

4.4.2.3 Viscosity

It is generally believed that viscosity is closely related to the degree of polymerization of network structure. The BO, NBO, and charge compensation all affect the degree of polymerization. With increasing SiO_2 content, the content of BO and the degree of charge compensation are increasing and the content of NBO is decreasing, which results in an increase in network connectivity degree and the degree of polymerization to improve the viscosity of the CAS system. Therefore, the CAS25 with the highest SiO_2 content has maximum viscosity values. Regarding the influence of temperature, increasing temperatures can lead to a decrease in the content of BO and the degree of charge compensation and an increase in the content of NBO, which is beneficial to a decrease in the network connectivity degree and the degree of polymerization. So the viscosity of the CAS system is decreasing with increasing temperature.

4.5 Conclusions

The density (1450-2450 K), surface tension and viscosity (1850-2650 K) of the CAS system are measured by ADL with LH and DOM. Structural parameters of the CAS system at different temperatures and SiO_2 content were calculated from MD simulations to explore the structural evolution. The combined hybrid potential was verified to be more appropriate for the CAS system by the comparison of S(Q) calculated from MD simulations and S(Q) measured from neutron diffraction. Furthermore, it is revealed how the temperature and SiO_2 content influence BLD, BAD, oxygen species, the degree of charge compensation, and UOBs, as well as the relationship between BAD, $[AlO_n]$ and $[SiO_n]$ polyhedrons, bond connection, BO, TCO, and charge compensations. At the same time, it further extends and completes the description of the theoretical correlation between thermophysical properties and structural evolution in Chapter 3, where notable conclusions on structural evolution and the correlation between structural evolution and thermophysical properties of the CAS system are obtained and listed as follows:

i. Increasing temperature can quicken the motion of atoms and break the partial bond connection, which decreases the peak intensity of BLD. Improving SiO_2 content can increase the content of the Si-O bond, which causes the FWHM of the first peak of BLD gradually broaden and the location of the first peak shifts to the low r-value.

ii. The O-Al-O BAD and the O-Si-O BAD are related to the $[AlO_n]$ polyhedrons (Al coordination number) and $[SiO_n]$ polyhedrons (Si coordination number), respectively. And the Al-O-Al BAD and the Al-O-Si BAD are determined by Al-BO-Al and nAl-TCO, Al-BO-Si and nAl-TCO-mSi.

iii. Improving temperature can decrease the content of BO and the degree of charge compensation, which leads to a decrease in the degree of polymerization. That would cause an increase in micro-volume and a decrease in density. Although increasing SiO_2 content can improve the degree of polymerization, Si-O bonding could greatly extend the chain structure, it decreases the twining degree of polyhedrons to increase the micro-volume to decrease the density.

iv. Increasing temperatures cause an increase in the contents of the Al-O-n[Ca], Si-O-n[Ca], and OBs, and a slight decrease in the contents of UOBs caused by charge compensation. The decrease in the contents of UOBs with charge compensation and the increase in the content of OBs could offset the effect of the increase in the contents of the Al-O-n[Ca] and Si-O-n[Ca], which leads to a slight decrease in surface tension. With increasing SiO_2 content, the UOBs bonding $[AlO_n]$ polyhedrons that contribute more to surface tension are gradually replaced by the UOBs bonding $[SiO_n]$ tetrahedrons, plus an increase in the content of OBs. That would result in a decrease in surface tension.

v. Increasing temperatures can decrease the content of BO and the degree of charge compensation and increase the content of NBO, which is beneficial to the decrease in the network connectivity degree and the degree of polymerization. So the viscosity of the CAS system is decreasing with increasing temperature. With increasing SiO_2 content, the content of BO and the degree of charge compensation are increasing and the content of NBO is decreasing, which increases the network connectivity degree and the degree of polymerization to improve the viscosity of the CAS system.

Chapter 5

Chapter 5. Numerical calculations of melts viscosity

Résumé du Chapitre 5

Les calculs numériques de la viscosité des systèmes CaO-Al_2O_3 et CaO-Al_2O_3-SiO_2 sont effectués par le modèle Urbain, FactSage® 8.1, l'équation d'Eyring et l'équation de Green-Kubo, qui fournit une référence pour les valeurs de mesure de la viscosité, en faisant une comparaison simple. Il jettera également les bases de l'évaluation future des modèles de viscosité ci-dessus et de la création de modèles de viscosité plus précis après l'obtention de l'émissivité précise des masses fondues CaO-Al_2O_3 et CaO-Al_2O_3-SiO_2 et de la température de correction.

Abstract of Chapter 5

Viscosity numerical calculations of the CaO-Al_2O_3 and CaO-Al_2O_3-SiO_2 systems are performed by Urbain model, FactSage® 8.1, Eyring equation, and Green-Kubo equation, which provides a reference for measurement values of viscosity, making a simple comparison. It will also lay the foundation for future evaluation of the above viscosity models and the creation of more accurate viscosity models after obtaining the accurate emissivity of the CaO-Al_2O_3 and CaO-Al_2O_3-SiO_2 melts and correction temperature.

5.1 Introduction

Melt viscosity plays a significant role in determining the optimum operating conditions for slagging gasification, where a lot of processes are closely related to the viscosity, such as slag flow, slag tapping, and refractory degradation, influencing efficiency, process reliability, and safety. Based on Chapter 3 and Chapter 4, we know that melt viscosity is extremely dependent on the temperature and its compositions.

Some temperature- and composition-related models have been put forward during the past decades, including the non-structure-based models and structure-based models [Hack et al., 2019]. The Urbain model [Urbain, 1987] and its modified models [Dong et al., 2014] are the main non-structure-based models. Structure-based models are built to predict the viscosity of melts based on considering structural information, and the viscosity model in FactSage® is a typical example. The models used by Urbain and FactSage® are based on data mainly obtained at a lower temperature range, compared with ADL measurements. These models may be improved as well because they rely on thermodynamic data and optimization. Therefore, one of the purposes of viscosity measurement is to develop an accurate and reliable numerical model in the future, based on more structural parameters, which can predict viscosity over a broad range of temperatures and compositions.

However, at present, there are many difficulties on this path. There is no standard for viscosity at ultra-high temperature, due to the difficulty of measurements. Additionally, in this study, the apparent temperature measured by the pyrometers was not corrected because the emissivity of the melts is unknown at high temperature. Furthermore, most of the samples are glassy melts and their emissivity is not able to be estimated by the eutectic temperature method [Ohishi et al., 2017]. There is extreme difficulty in correcting the temperature, which results in difficulties in obtaining an accurate correspondence between viscosity and real temperature.

Given the above problem, it is necessary to observe the differences by comparing the current viscosity model with the measured viscosity. Although this comparison is approximate and crude, it being a reference for measuring values is effective. Meanwhile, it will be possible to correct the temperature when the emissivity will be known. The aim of this chapter is to provide an auxiliary reference for the measurement of viscosity, so we only list the viscosity data of melts from ADL measurements, Urbain model, Factsage®, and Molecular Dynamics (Green-Kubo equation and Eyring equation) and make a simple comparison.

5.2 Calculations of viscosity

5.2.1 Urbain model

The viscosity of melts could be calculated by the Weymann-Frenkel form:

$$\eta = AT \cdot exp(1000B/T) \qquad \text{Eq. (5-1)}$$

where η, T, A, and B are viscosity (Pa·s), the absolute temperature (K), the pre-exponential factor, and viscous activation energy (J/mol), respectively. A linear relationship between pre-exponent factor A and activation energy B could be represented by Eq. (5-2):

$$-\ln A = m \times B + n \qquad \text{Eq. (5-2)}$$

According to experimental data, for ionic melts, m and n could be deduced to equal 0.29 and 11.57, respectively. However, for the network liquid, the experiment values are m = 0.207 and n = 10.288. The viscous activation energy B is obtained from the polynomial Eq. (5-3) and Eq. (5-4):

$$B = B_0 + B_1 \cdot X + B_2 \cdot X^2 + B_3 \cdot X^3 \qquad \text{Eq. (5-3)}$$

$$B_i = a_i + b_i \cdot \alpha + c_i \cdot \alpha^2 \qquad \text{Eq. (5-4)}$$

where N is the types of oxides, X is the network former mole fraction, and α is the mole ratio of modifier oxides to the sum of modifier oxides and amphoteric oxides (α = modifier oxides/(modifier oxides + amphoteric oxides)). a_i, b_i, and c_i could be checked from the references [Urbain, 1987].

According to the above description, the viscosities of melts with various compositions at different temperatures in this research are predicted.

5.2.2 Viscosity module in FactSage® 8.1

The viscosity of samples is calculated by the thermodynamic software FactSage® 8.1 [Bale et al., 2016], where the melt database is chosen. The structure of melts in terms of concentrations of bridging, non-bridging and free oxygen as a function of composition and temperature could be calculated by thermodynamic models such as the Modified Quasichemical Model of Pelton. And then the viscosity of melts can be obtained by the thermodynamic calculation based on these structures. For the model used by FactSage® 8.1, which could be calculated by these steps: (i) Calculation of pair fractions using the quasichemical model; (ii) Characterization of the structure of the melt network (iii) Viscosity of the melts. In the first step, the parameters of model equations for the Gibbs energies of all phases in a system as a function of composition and temperature are optimized by a modified quasichemical method, which can make the data satisfy all experimental thermodynamic and phase diagram data. Next, the concept of Q^i-species is used to characterize the structural changes in the formation of the melt network, where the superscript i is the number of bridging oxygens per network-former atom. The mole fractions of O^{2-}, O^-, O^0, and Q^i are calculated by the theory put forward by Lin and Pelton [Lin et al., 1979]. Then, the bridging oxygens contents are predicted from the total number of oxygens and the fraction of network former pairs (for instance, Si-Si pairs), which are obtained from the thermodynamic calculation by a modified quasichemical method. In addition, Machacek [Machacek et al., 2006] researched the connectivity between Q^4-species to improve the calculation accuracy of the structural characterization. In the calculation of the melt viscosity, Si as the network former is taken as an example to describe the calculation method. First, the relationship between the viscosity of the unary systems and the temperature is given by Arrhenius equation [Mysen, 1990]. And the calculation factor can be optimized by the experimental data and the extrapolation from binary viscosity data. Then the viscosity of MeO_x-SiO_2 as a function of the composition could be predicted by the equation as [Grundy et al., 2008]:

$$ln(\eta) = X(MeO_x)\, ln(\eta_{MeO_x}) + X(SiO_2) ln(\eta_{SiO_2}) \qquad \text{Eq. (5-5)}$$

Finally, the viscosity data are optimized by using probability theory.

5.2.3 Eyring equation

Viscosity is closely related to the diffusion coefficient. Increasing the self-diffusion coefficient is associated with a decline in viscosity, according to the experience. MD simulations are an effective way to estimate the atomic jump mechanisms underlying diffusional processes [Du et al., 2022].

Mean square displacements (MSD) represent the average displacements of various atoms over a fixed time, which is calculated from the atomic trajectories.

The MSD ($\langle r^2(t)\rangle$) can be expressed by Eq. (5-6) [Du et al., 2022], where it is summed over all N_I species of the atom whose diffusion coefficient is being sought.

$$\mathrm{MSD}(\langle r^2(\mathrm{t})\rangle)=\langle|r(\mathrm{t})-\mathrm{r}(0)|^2\rangle=\frac{1}{N_o N_I}\sum_{j=1}^{N_O}\sum_{i=1}^{N_I}\left[r_i\left(t+t_j\right)-r_i\left(t_j\right)\right]^2 \qquad \text{Eq. (5-6)}$$

Better accuracy is obtained when summing over a large number of different time origins N_O. In principle, each time step can be used as a new time origin.

With the help of Einstein's equation, MSD was used to calculate the self-diffusion coefficient (D) for corresponding atomic specie in the system, as shown in Eq. (5-7).

$$\mathrm{D}=\frac{1}{6t}\langle r^2(t)\rangle \qquad \text{Eq. (5-7)}$$

The total diffusion coefficient D_{total} of the system can then be obtained from these individual self-diffusion coefficients as [Li et al., 2017]:

$$D_{total}=\sum_{i=1}^{i=n} D_i\bullet x_i \qquad \text{Eq. (5-8)}$$

where D_i and x_i respectively represent the self-diffusion coefficient and the mole fraction of atom species i with n being the total number of atoms in the system.

Then the viscosity η could be calculated by combing the self-diffusion coefficient with the Eyring equation, as shown below.

$$\eta=\frac{K_B T}{D\lambda} \qquad \text{Eq. (5-9)}$$

where K_B is the Boltzmann constant which equals 1.38×10^{-23} J/K, and T is the temperature of the system. λ as the hopping distance is estimated from the first neighbor distance, which can be derived from the Radial Distribution Function.

It is worth noting that the diffusion coefficient of each element is derived from its mean squared displacement. The total diffusivity is mainly determined by the diffusivity of the moving alkali metal cations from the channel structure. The partial diffusivity of different elements is converted to the partial viscosity value, corresponding to each element with “partial viscosity”. This partial viscosity can not be measured directly from experiments. However, the calculation provides insight into the different contributions of anions and cations to the total viscosity, where the main atoms come from the network. In this work, the total viscosity is a percentage-weighted average of the number of each atomic species. This is the assumption that we used to derive the total viscosity.

5.2.4 Green-Kubo equation

The Sutherland-Einstein relation [Pomeau, 1972; Cherne et al., 2002; Mouas et al., 2012] provides an excellent estimation of the viscosity of liquid metals [Iida et al., 1993]. The theoretical study of viscosity can be roughly calculated utilizing the stress autocorrelation function which corresponds to the fluctuations of the off-diagonal elements of the pressure or stress tensor $\mathcal{P}_{xz}(t)$ [Hess, 2002; Todd et al., 2017], as shown in Eq. (5-10),

$$\eta=\frac{V}{\mathrm{K}_B T}\int_0^{\infty}\langle\mathcal{P}_{xz}(t_0)\mathcal{P}_{xz}(t_0+t)\rangle\,dt \qquad \text{Eq. (5-10)}$$

where V is the volume of the system, K_B is the Boltzmann constant, and T is the temperature.

5.3 Results and discussions

The measured and calculated viscosities of the $(CaO)_x(Al_2O_3)_{1-x}$ melts (including C3A, C12A7, CA, and CA2) are illustrated in Figure 5-1. Except for CA2, the viscosity data (including C3A, C12A7, and CA) measured by ADL are lower than those calculated by Urbain model and higher than those calculated by FactSage® 8.1. For CA2 melts, the viscosity data measured by ADL are lower than those calculated by Urbain model and FactSage® in a relatively low-temperature range. With an increase in temperature, all the viscosities of melts decrease and the experiment values about the viscosity are much closer to those simulated by models. For further investigating the validity of models, the mean relative deviations (Δs) between measured and calculated viscosities of C12A7 melt by various models are calculated by Eq. (5-11).

$$\Delta=\frac{1}{n}\times\sum\frac{\left|\eta_{measured}-\eta_{calculated}\right|}{\eta_{measured}}\times 100 \qquad \text{Eq. (5-11)}$$

The Δs of Urbain models, FactSage® 8.1, Green-Kubo equation, and Eyring equation are 84%, 66%, 20%, and 9%, respectively.

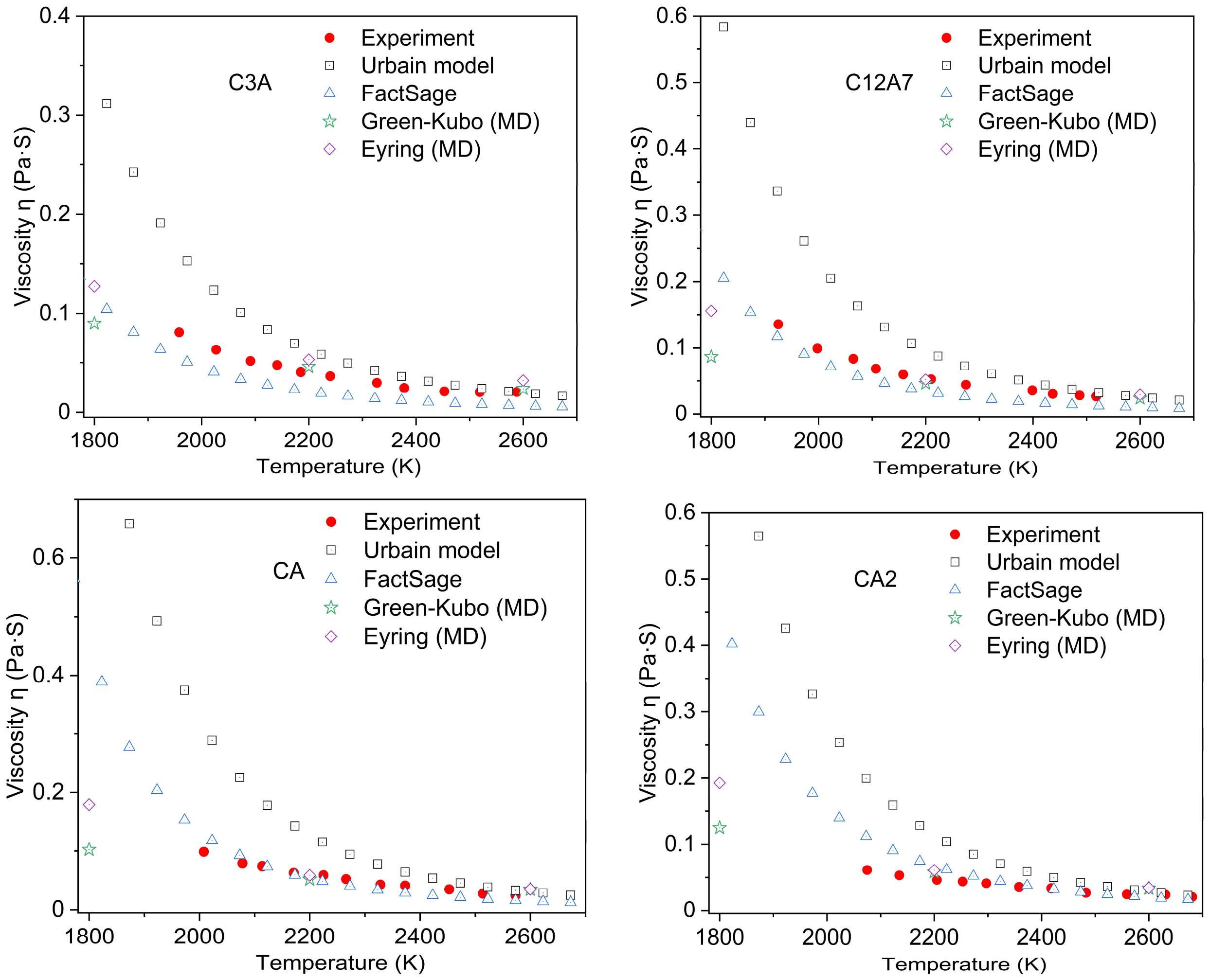

Figure 5-1. The comparison of viscosity values of the CaO-Al_2O_3 system from ADL measurements, Urbain model, FactSage® 8.1, Green-Kubo equation, and Eyring equation.

The measured and calculated viscosities of CAS melts (including CAS0, CAS5, CAS10, CAS15, CAS20, and CAS25) are illustrated in Figure 5-2. For the melts with lower silica content (CAS0, CAS5, CAS10, and CAS15), the measured viscosities are lower than those simulated with Urbain model and higher than those calculated with FactSage® 8.1. In comparison, for the melts with higher silica content (CAS20 and CAS25), the measured viscosities below 2200 K are lower than those calculated with Urbain model and FactSage® 8.1. However, when the measuring temperature is above 2200 K, the measured viscosities are between the values simulated with Urbain model and FactSage® 8.1. Similar to the $(CaO)_x(Al_2O_3)_{1-x}$ melts, with an increase in temperature, all the viscosities of the CAS melts decrease and the experiment values about the viscosity are much closer to those simulated by models. Furthermore, the mean relative deviations (Δs) between measured and calculated viscosities of the CAS10 melt by various models are calculated, as an example. The Δs of Urbain models, FactSage® 8.1, Green-Kubo equation, and Eyring equation are 88%, 31%, 16%, and 28%, respectively.

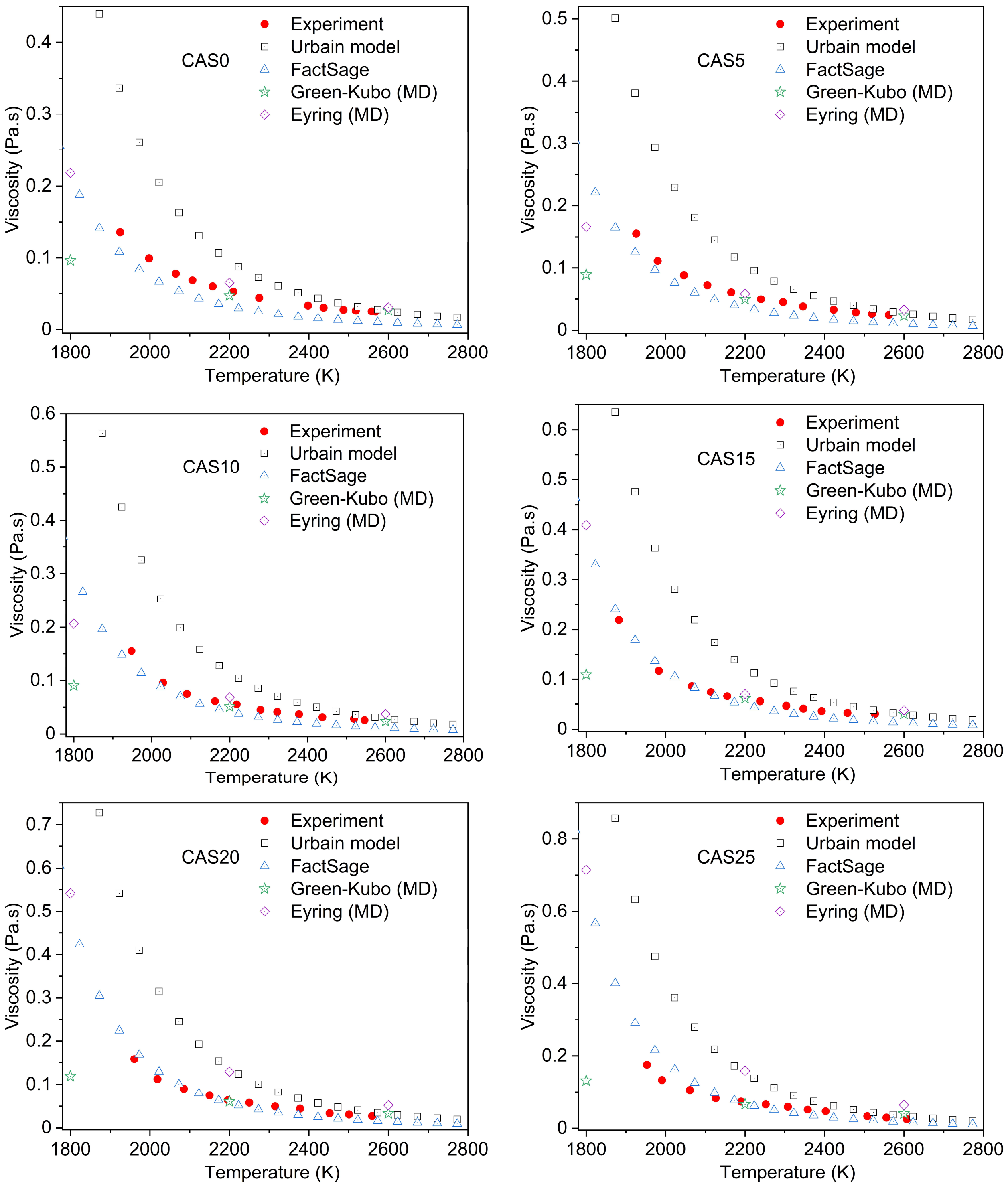

Figure 5-2. The comparison of viscosity values of the CaO-Al_2O_3-SiO_2 system from ADL measurements, Urbain model, FactSage® 8.1, Green-Kubo equation, and Eyring equation.

From the simple comparison above, the relative deviation between the measured and predicted viscosities is high, except for the differences between the models, uncorrected measured temperatures possibly exacerbate this deviation. The measured and simulated viscosities will be compared in detail when the emissivity is known.

5.4 Conclusions

Although the current viscosity comparison between various models and ADL measurements is simple and rough, this prepares for the assessment of these viscosity models after temperature correction, as well as provides a reference for studying the viscosity of the $CaO-Al_2O_3$ and $CaO-Al_2O_3-SiO_2$ systems.

Chapter 6

Chapter 6. Conclusions and future work

6.1 Conclusions

In this thesis, the thermophysical properties and structural evolution of the $CaO-Al_2O_3$ system and the $CaO-Al_2O_3-SiO_2$ system (CAS) were measured and investigated by aerodynamic levitation (ADL) and MD simulations. The correlations between density, surface tension, viscosity, and structural evolution are revealed, based on the bond length/angle distribution (BLD/BAD), the oxygen species, the degree of charge compensation, the network connectivity, and the unsatisfied oxygen bonds (UOBs). The main conclusions are listed as follows:

a) In Chapter 2, the scripts integrated with the Canny edge detector, Fourier transforms and Monte Carlo method which process the data from measurements of ADL to calculate thermophysical properties are developed. It has solved the difficult problems of determining the resonance frequency of melts and the uncertainties of measurements of density, surface tension, and viscosity, which greatly improves the accuracy of measurements, establishing a relatively complete measurement protocol. In addition, the combined hybrid potential (BMH and Buckingham) was first created and applied in MD simulations of oxide systems.

b) Chapter 3 describes the measured results of density, surface tension, and viscosity of the $(CaO)_x(Al_2O_3)_{1-x}$ melts, a series of structural parameters, and the correlation between thermophysical properties and structural evolution. With the help of previous experimental characterization (neutron diffraction and NMR), the combined hybrid potential has been verified to be more appropriate for MD simulations of the $CaO-Al_2O_3$ system than the single potential (BMH or Buckingham). In structural evolution, the influences of $R=CaO/Al_2O_3$ and temperature on BLD, BAD, oxygen species, the degree of charge compensation, and UOBs were explored, as well as the correlations between BAD and coordination number, BO, TCO, and charge compensation. The conclusions in correlations between structural evolution and thermophysical properties are listed as follows:

    i) Improving temperature and R result in a change in bond length distribution, and a decrease in the intensity of the Al-O-Al BAD and polymerization degree, which decreases the connectivity of $[AlO_n]$ each other to increase the volume to reduce the density of the $(CaO)_x(Al_2O_3)_{1-x}$ melts. The influence of $\rho_{Al2O3} \Rightarrow \rho_{CaO}$ on the density of the $(CaO)_x(Al_2O_3)_{1-x}$ melts is non-negligible as well.

    ii) surface tension is related to the UOBs, where the UOBs caused by charge compensation have a greater influence on surface tension.

    iii) Ca^{2+} as the charge compensator at the low R can lead to an unceasing rise in the degree of polymerization (CA2-CA). Ca^{2+} being network modifiers can reduce the degree of polymerization by further increasing R (CA-C3A). That is why the viscosity of the $(CaO)_x(Al_2O_3)_{1-x}$ melts climbs up and then declines from CA2 to C3A. Rising temperature can decrease BO content and the degree of charge compensation, which reduces the degree of polymerization and causes a decline in the viscosity of $(CaO)_x(Al_2O_3)_{1-x}$ melts.

c) Chapter 4 is extending the binary system to the trinary (CAS) system, obtaining test results and structural parameters. At the same time, it further verifies that the combined hybrid potential is more appropriate in MD simulations of the CAS system, as well as further improving the theoretical correlations between density, surface tension, and viscosity. For the density of the CAS melts, although increasing SiO_2 content can improve the degree of polymerization, Si-O bonding could greatly extend the chain structure, it decreases the twining degree of polyhedrons to increase the micro-volume to decrease the density. With increasing SiO_2 content, the UOBs bonding $[AlO_n]$ polyhedrons that contribute more to surface tension are gradually replaced by the UOBs bonding $[SiO_n]$ tetrahedrons, decreasing the surface tension. Furthermore, with increasing SiO_2 content, the content of BO and the degree of charge compensation are increasing and the content of NBO is decreasing, which increases the degree of polymerization to improve the viscosity of the CAS system.

6.2 Future work

The end of the PhD project marks the beginning of a new journey. This work also pointed me out new directions for future research. Aerodynamic levitation with the droplet oscillation method is a very effective approach to measuring the density, surface tension, and viscosity of melts.

- However, it is still unsolved to determine the emissivity of oxide melts and to correct measuring temperature, especially for glassy melts. It directly leads to accurate correspondences between density, surface tension, viscosity, and temperature. To date, we can not accurately assess which numerical model is closer to measured viscosity. Meanwhile, it hinders the development of a more precise numerical model of viscosity as well. Therefore, trying to find a solution to calculate and determine the emissivity of melts is one direction of future work.
- We also note that the different compositions of the levitated gas have more or less an influence on the melt density. This effect, however, is unknown. It is necessary and relevant to explore the influencing mechanism of levitated gas on thermophysical properties, since levitated gas is indispensable for measurements of aerodynamic levitation. Perhaps, it would be a good direction to explore the mechanism of this effect in conjunction with MD simulation.
- In addition, although the combined hybrid potential has been verified by comparing the structural factors calculated from MD simulations and neutron diffraction, it is necessary to

find out more theoretical supports to further confirm the science and accuracy of the thought of this combined hybrid potential. At the same time, it is also relevant to develop and extend the python script that has more computational functions such as polyhedral ring statistics, atomic migration, and connectivity of network structure.

- Surface tension is the shrink force that is derived from the particles at the close surface of melts attracted by the inner particles. It is necessary to develop a model that is the melt system surrounded by air. We will focus on the interaction between melt surface and air to calculate surface tension and further verify the influence of UOBs on surface tension. This idea may be helpful for the influencing mechanism of levitated gas on thermophysical properties.
- It is widely believed that the basicity of slag is an important parameter in studying slag corrosion on refractory. As mentioned in Chapter 1, slag corrosion on refractory is related to the density, surface tension, and viscosity of slag. Therefore, establishing an accurate definition of basicity using MD simulations and attempting to investigate the correlation between basicity and properties may contribute to revealing the corrosion mechanism of slag.
- In the end, continuously exploring the remaining melt systems that have been measured, (such as the CaO-SiO_2 system, the CaO-SiO_2-Fe_2O_3 system, the CaO-Al_2O_3-MgO, the MgO-SiO_2-Al_2O_3 system) and extending higher order system, which is indispensable to complete and improve the measurements of thermophysical properties and the correlation theory between density, surface tension, viscosity, and structural evolution.

Reference

References

[Scrivener et al. 1999] Scrivener, K. L., Cabiron, J.-L., & Letourneux, R. High-performance concretes from calcium aluminate cements *Cement and Concrete Research* 1999, *29*(8), 1215–1223. https://doi.org/10.1016/S0008-8846(99)00103-9

[Liu et al. 2020] Liu, H., Chen, W., Pan, R., Shan, Z., Qiao, A., Drewitt, J. W. E., Hennet, L., Jahn, S., Langstaff, D. P., Chass, G. A., Tao, H., Yue, Y., & Greaves, G. N. From Molten Calcium Aluminates through Phase Transitions to Cement Phases *Advanced Science* 2020, *7*(2), 1902209. https://doi.org/10.1002/advs.201902209

[Lines et al. 1989] Lines, M. E., MacChesney, J. B., Lyons, K. B., Bruce, A. J., Miller, A. E., & Nassau, K. Calcium aluminate glasses as potential ultralow-loss optical materials at 1.5–1.9 μm *Journal of Non-Crystalline Solids* 1989, *107*(2–3), 251–260. https://doi.org/10.1016/0022-3093(89)90470-5

[Chung et al. 2005] Chung, W. J., Yoo, J. R., Kim, Y. S., & Heo, J. Mechanism of the Blue Up-Conversion in Tm^{3+}/Nd^{3+}-doped Calcium Aluminate Glasses *Journal of the American Ceramic Society* 2005, *80*(6), 1485–1490. https://doi.org/10.1111/j.1151-2916.1997.tb03007.x

[Kalita et al. 2002] Kalita, S. J., Bose, S., Bandyopadhyay, A., & Hosick, H. L. Porous calcium aluminate ceramics for bone-graft applications *Journal of Materials Research* 2002, *17*(12), 3042–3049. https://doi.org/10.1557/JMR.2002.0442

[Edwards 2011] Edwards, P. P. Electrons in Cement *Science* 2011, *333*(6038), 49–50. https://doi.org/10.1126/science.1207837

[Kim et al. 2011] Kim, S. W., Shimoyama, T., & Hosono, H. Solvated Electrons in High-Temperature Melts and Glasses of the Room-Temperature Stable Electride $[Ca_{24}Al_{28}O_{64}]^{4+}\cdot 4e^{-}$ *Science* 2011, *333*(6038), 71–74. https://doi.org/10.1126/science.1204394

[Kim et al. 2012] Kim, S. W. & Hosono, H. Synthesis and properties of $12CaO\bullet 7Al_2O_3$ electride: review of single crystal and thin film growth *Philosophical Magazine* 2012, *92*(19–21), 2596–2628. https://doi.org/10.1080/14786435.2012.685770

[Miyakawa et al. 2007] Miyakawa, M., Kim, S. W., Hirano, M., Kohama, Y., Kawaji, H., Atake, T., Ikegami, H., Kono, K., & Hosono, H. Superconductivity in an Inorganic Electride $12CaO\bullet 7Al_2O_3{:}e^{-}$ *Journal of the American Chemical Society* 2007, *129*(23), 7270–7271. https://doi.org/10.1021/ja0724644

[De Bilbao et al. 2018] de Bilbao, E., Dombrowski, M., Pilliere, H., & Poirier, J. Time-resolved high-temperature X-ray diffraction for studying the kinetics of corrosion of high-alumina refractory by molten oxides *Corrosion Science* 2018, *139*, 346–354. https://doi.org/10.1016/j.corsci.2018.05.003

[Cormier et al. 2000] Cormier, L., Neuville, D. R., & Calas, G. Structure and properties of low-silica calcium aluminosilicate glasses *Journal of Non-Crystalline Solids* 2000, *274*(1–3), 110–114. https://doi.org/10.1016/S0022-3093(00)00209-X

[Jakse et al. 2012] Jakse, N., Bouhadja, M., Kozaily, J., Drewitt, J. W. E., Hennet, L., Neuville, D. R., Fischer, H. E., Cristiglio, V., & Pasturel, A. Interplay between non-bridging oxygen, triclusters, and fivefold Al coordination in low silica content calcium aluminosilicate melts *Applied Physics Letters* 2012, *101*(20), 201903. https://doi.org/10.1063/1.4766920

[Zhang et al. 2021a] Zhang, R., Wang, Z., Meng, Y., Jiao, S., Jia, J., Min, Y., & Liu, C. (a) Quantitative insight into aluminum structures in CaO–Al_2O_3–SiO_2 system via Raman and 27Al MAS-NMR spectroscopies *Journal of Non-Crystalline Solids* 2021a, *573*, 121116. https://doi.org/10.1016/j.jnoncrysol.2021.121116

[Yehorov et al. 2021] Yehorov, A., Ma, G., & Volkova, O. Interaction between MgO–C-bricks and ladle slag with a 1:1 CaO/Al_2O_3 ratio and varying SiO_2 content *Ceramics International* 2021, *47*(8), 11677–11686. https://doi.org/10.1016/j.ceramint.2021.01.007

[Xu et al. 2021] Xu, L., Zhang, D., Liu, Y., Chen, M., & Wang, N. Comparison of microstructure, thermo-mechanical property and corrosion resistance of bauxite-corundum refractory castables reinforced by two approaches *Ceramics International* 2021, *47*(10), 13660–13668. https://doi.org/10.1016/j.ceramint.2021.01.227

[Fu et al. 2019] Fu, L., Gu, H., Huang, A., Zou, Y., & Ni, H. Enhanced corrosion resistance through the introduction of fine pores: Role of nano-sized intracrystalline pores *Corrosion Science* 2019, *161*, 108182. https://doi.org/10.1016/j.corsci.2019.108182

[Cheng et al. 2013] Cheng, J., Xiao, Z., Yang, K., & Wu, H. Viscosity, fragility and structure of Na_2O–CaO–Al_2O_3–SiO_2 glasses of increasing Al/Si ratio *Ceramics International* 2013, *39*(4), 4055–4062. https://doi.org/10.1016/j.ceramint.2012.10.258

[Dimitrios Siafakas et al. 2018] Siafakas, Dimitrios, Matsushita, T., Jarfors, A. E. W., Hakamada, S., & Watanabe, M. Viscosity of SiO_2–CaO–Al_2O_3 Slag with Low Silica – Influence of CaO/Al_2O_3, SiO_2/Al_2O_3 Ratio *ISIJ International* 2018, *58*(12), 2180–2185. https://doi.org/10.2355/isijinternational.ISIJINT-2018-381

[De Bilbao et al. 2015] De Bilbao, E., Poirier, J., & Dombrowski, M. Corrosion of high alumina refractories by Al_2O_3-CaO slag: thermodynamic and kinetic approaches *Metallurgical Research & Technology* 2015, *112*(6), 607. https://doi.org/10.1051/metal/2015042

[Blond et al. 2020] Blond, E., Nguyen, A. K., Bilbao, E., Sayet, T., & Batakis, A. Thermo-chemo-mechanical modeling of refractory behavior in service: Key points and new developments *International Journal of Applied Ceramic Technology* 2020, *17*(4), 1693–1700. https://doi.org/10.1111/ijac.13499

[Wegener et al. 2015] Wegener, M., Muhmood, L., Sun, S., & Deev, A. V. Surface Tension Measurements of Calcia-Alumina Slags: A Comparison of Dynamic Methods *Metallurgical and Materials Transactions B* 2015, *46*(1), 316–327. https://doi.org/10.1007/s11663-014-0174-0

[Yan et al. 2018] Yan, Z., Lv, X., Pang, Z., Lv, X., & Bai, C. Transition of Blast Furnace Slag from Silicate Based to Aluminate Based: Density and Surface Tension *Metallurgical and Materials Transactions B* 2018, *49*(3), 1322–1330. https://doi.org/10.1007/s11663-018-1242-7

[Zhang et al. 2021b] Zhang, R., Wang, Z., Meng, Y., Jiao, S., Jia, J., Min, Y., & Liu, C. (b) Structural analysis and evaluation of surface tension of silicate melts containing CaO and FeO *Chemical Engineering Science* 2021b, *245*, 116870. https://doi.org/10.1016/j.ces.2021.116870

[Zhang et al. 2010] Zhang, G. & Chou, K. Model for evaluating density of molten slag with optical basicity *Journal of Iron and Steel Research International* 2010, *17*(4), 1–4. https://doi.org/10.1016/S1006-706X(10)60077-5

[Shu et al. 2013] Shu, Q. F. & Chou, K.-C. Calculation for density of molten slags using optical basicity *Ironmaking & Steelmaking* 2013, *40*(8), 571–577. https://doi.org/10.1179/1743281212Y.0000000083

[Zhang et al. 2015] Zhang, F., Du, Y., Liu, S., & Jie, W. Modeling of the viscosity in the Al–Cu–Mg–Si system: Database construction *Calphad* 2015, *49*, 79–86. https://doi.org/10.1016/j.calphad.2015.04.001

[Wu et al. 2016] Wu, T., Wang, Q., Yu, C., & He, S. Structural and viscosity properties of CaO-SiO_2 -Al_2O_3-FeO slags based on molecular dynamic simulation *Journal of Non-Crystalline Solids* 2016, *450*, 23–31. https://doi.org/10.1016/j.jnoncrysol.2016.07.024

[Kondo et al. 2019] Kondo, T., Muta, H., Kurosaki, K., Kargl, F., Yamaji, A., Furuya, M., & Ohishi, Y. Density and viscosity of liquid ZrO_2 measured by aerodynamic levitation technique *Heliyon* 2019, *5*(7), e02049. https://doi.org/10.1016/j.heliyon.2019.e02049

[Fu et al. 2017] Fu, L., Huang, A., Lian, P., & Gu, H. Isolation or corrosion of microporous alumina in contact with various CaO-Al_2O_3-SiO_2 slags *Corrosion Science* 2017, *120*, 211–218. https://doi.org/10.1016/j.corsci.2017.01.018

[Luz et al. 2011] Luz, A. P., Braulio, M. A. L., Martinez, A. G. T., & Pandolfelli, V. C. Thermodynamic simulation models for predicting Al_2O_3–MgO castable chemical corrosion *Ceramics International* 2011, *37*(8), 3109–3116. https://doi.org/10.1016/j.ceramint.2011.05.049

[Sasaki et al. 1994] Sasaki, H., Tokizaki, E., Terashima, K., & Kimura, S. Density Variation of Molten Silicon Measured by an Improved Archimedian Method *Japanese Journal of Applied Physics* 1994, *33*(Part 1, No. 7A), 3803–3807. https://doi.org/10.1143/JJAP.33.3803

[Arman et al. 2019] Arman & Takebe, H. Experimental Study for Measuring Density of slag melts by An Established Archimedean Double-bob Method *IOP Conference Series: Materials Science and Engineering* 2019, *619*(1), 012036. https://doi.org/10.1088/1757-899X/619/1/012036

[Fujino et al. 2004] Fujino, S., Hwang, C., & Morinaga, K. Density, Surface Tension, and Viscosity of PbO-B_2O_3-SiO_2 Glass Melts *Journal of the American Ceramic Society* 2004, *87*(1), 10–16. https://doi.org/10.1111/j.1151-2916.2004.tb19937.x

[Sukenaga et al. 2011] Sukenaga, S., Haruki, S., Nomoto, Y., Saito, N., & Nakashima, K. Density and Surface Tension of CaO–SiO_2–Al_2O_3–R_2O (R=Li, Na, K) Melts *ISIJ International* 2011, *51*(8), 1285–1289. https://doi.org/10.2355/isijinternational.51.1285

[Bachmann et al. 2000] Bachmann, J., Horton, R., van der Ploeg, R. R., & Woche, S. Modified sessile drop method for assessing initial soil-water contact angle of sandy soil *Soil Science Society of America Journal* 2000, *64*(2), 564–567. https://doi.org/10.2136/sssaj2000.642564x

[Susana et al. 2012] Susana, L., Campaci, F., & Santomaso, A. C. Wettability of mineral and metallic powders: Applicability and limitations of sessile drop method and Washburn's technique *Powder Technology* 2012, *226*, 68–77. https://doi.org/10.1016/j.powtec.2012.04.016

[Duchesne et al. 2017] Duchesne, M. A. & Hughes, R. W. Slag density and surface tension measurements by the constrained sessile drop method *Fuel* 2017, *188*, 173–181. https://doi.org/10.1016/j.fuel.2016.10.023

[Iida et al. 1993] Iida, T. & Guthrie, R. I. L. *The physical properties of liquid metals* 1993. Oxford: Clarendon press.

[Brooks et al. 2005] Brooks, R. F., Dinsdale, A. T., & Quested, P. N. The measurement of viscosity of alloys—a review of methods, data and models *Measurement Science and Technology* 2005, *16*(2), 354–362. https://doi.org/10.1088/0957-0233/16/2/005

[Riebling 1963] Riebling, E. F. Improved Counterbalanced Sphere Viscometer for Use to 1750°C *Review of Scientific Instruments* 1963, *34*(5), 568–572. https://doi.org/10.1063/1.1718505

[Hara et al. 1997] Hara, S., Inoue, K., & Tanaka, T. Viscosity of molten slags containing iron oxide Molten Slags 1997 (p. 515). Presented at the Fluxes and Salts 97 Conference, Sydney, Australia: Iron and Steel Society.

[Hennet et al. 2007] Hennet, Louis, Krishnan, S., Pozdnyakova, I., Cristiglio, V., Cuello, G. J., Fischer, H. E., Bytchkov, A., Albergamo, F., Zanghi, D., Brun, J.-F., Brassamin, S., Saboungi, M.-L., & Price, D. L. Structure and dynamics of levitated liquid materials *Pure and Applied Chemistry* 2007, *79*(10), 1643–1652. https://doi.org/10.1351/pac200779101643

[Jacobs et al. 1996] Jacobs, G., Egry, I., Maier, K., Platzek, D., Reske, J., & Frahm, R. Extended x-ray-absorption fine structure studies of levitated undercooled metallic melts *Review of Scientific Instruments* 1996, *67*(10), 3683–3687. https://doi.org/10.1063/1.1146855

[Brillo et al. 2011] Brillo, Jürgen & Egry, I. Density of Multicomponent Melts Measured by Electromagnetic Levitation *Japanese Journal of Applied Physics* 2011, *50*(11), 11RD02. https://doi.org/10.1143/JJAP.50.11RD02

[Watanabe et al. 2018] Watanabe, M., Takano, J., Adachi, M., Uchikoshi, M., & Fukuyama, H. Thermophysical properties of liquid Co measured by electromagnetic levitation technique in a static magnetic field *The Journal of Chemical Thermodynamics* 2018, *121*, 145–152. https://doi.org/10.1016/j.jct.2018.02.004

[Su et al. 2020] Su, Y., Mohr, M., Wunderlich, R. K., Wang, X., Cao, Q., Zhang, D., Yang, Y., Fecht, H.-J., & Jiang, J.-Z. The relationship between viscosity and local structure in liquid zirconium via electromagnetic levitation and molecular dynamics simulations *Journal of Molecular Liquids* 2020, *298*, 111992. https://doi.org/10.1016/j.molliq.2019.111992

[Perepezko et al. 2021] Perepezko, J. H. & Paik, J. Experimental studies of crystal nucleation: metals and colloids 2021.

[Rhim et al. 1999] Rhim, W.-K., Ohsaka, K., Paradis, P.-F., & Spjut, R. E. Noncontact technique for measuring surface tension and viscosity of molten materials using high temperature electrostatic levitation *Review of Scientific Instruments* 1999, *70*(6), 2796–2801. https://doi.org/10.1063/1.1149797

[Yoo et al. 2015] Yoo, H., Park, C., Jeon, S., Lee, S., & Lee, G. W. Uncertainty evaluation for density measurements of molten Ni, Zr, Nb and Hf by using a containerless method *Metrologia* 2015, *52*(5), 677–684. https://doi.org/10.1088/0026-1394/52/5/677

[Du et al. 2018] Du, L. Y., Wang, L., Zhai, W., Hu, L., Liu, J. M., & Wei, B. Liquid state property, structural evolution and mechanical behavior of Ti Fe alloy solidified under electrostatic levitation condition *Materials & Design* 2018, *160*, 48–57. https://doi.org/10.1016/j.matdes.2018.08.043

[Brillo et al. 2011] Brillo, J., Pommrich, A. I., & Meyer, A. Relation between Self-Diffusion and Viscosity in Dense Liquids: New Experimental Results from Electrostatic Levitation *Physical Review Letters* 2011, *107*(16), 165902. https://doi.org/10.1103/PhysRevLett.107.165902

[Winborne et al. 1976] Winborne, D. A., Nordine, P. C., Rosner, D. E., & Marley, N. F. Aerodynamic levitation technique for containerless high temperature studies on liquid and solid samples *Metallurgical Transactions B* 1976, *7*(4), 711–713. https://doi.org/10.1007/BF02698607

[Weber et al. 1995] Weber, J. K. R. & Nordine, P. C. Containerless liquid-phase processing of ceramic materials *Microgravity Sci. Technol* 1995, *7*, 279.

[Hennet et al. 2017] Hennet, Louis, Holland Moritz, D., Weber, R., & Meyer, A. High-Temperature Levitated Materials In *Experimental Methods in the Physical Sciences* 2017 (Vol. 49, pp. 583–636). Elsevier. https://doi.org/10.1016/B978-0-12-805324-9.00010-8

[Hennet et al. 2011] Hennet, L., Cristiglio, V., Kozaily, J., Pozdnyakova, I., Fischer, H. E., Bytchkov, A., Drewitt, J. W. E., Leydier, M., Thiaudière, D., Gruner, S., Brassamin, S., Zanghi, D., Cuello, G. J., Koza, M., Magazù, S., Greaves, G. N., & Price, D. L. Aerodynamic levitation and laser heating: Applications at synchrotron and neutron sources *The European Physical Journal Special Topics* 2011, *196*(1), 151–165. https://doi.org/10.1140/epjst/e2011-01425-0

[Benmore et al. 2017] Benmore, C. J. & Weber, J. K. R. Aerodynamic levitation, supercooled liquids and glass formation *Advances in Physics: X* 2017, *2*(3), 717–736. https://doi.org/10.1080/23746149.2017.1357498

[Poe et al. 1994] Poe, B. T., McMillan, P. F., Cote, B., Massiot, D., & Coutures, J.-P. Structure and Dynamics in Calcium Aluminate Liquids: High-Temperature 27Al NMR and Raman Spectroscopy *Journal of the American Ceramic Society* 1994, *77*(7), 1832–1838. https://doi.org/10.1111/j.1151-2916.1994.tb07058.x

[Rayleigh 1879] Rayleigh, Lord On the Capillary Phenomena of Jets *Proceedings of the Royal Society of London Series I* 1879, *29*, 71–97.

[Egry et al. 2005] Egry, I., Giffard, H., & Schneider, S. The oscillating drop technique revisited *Measurement Science and Technology* 2005, *16*(2), 426–431. https://doi.org/10.1088/0957-0233/16/2/013

[Langstaff et al. 2013] Langstaff, D., Gunn, M., Greaves, G. N., Marsing, A., & Kargl, F. Aerodynamic levitator furnace for measuring thermophysical properties of refractory liquids *Review of Scientific Instruments* 2013, *84*(12), 124901. https://doi.org/10.1063/1.4832115

[Kargl et al. 2015] Kargl, F., YUAN, C., & GREAVES, G. N. (, April 30) Aerodynamic Levitation: Thermophysical Property Measurements of Liquid Oxides 2015. The Japan Society of Microgravity Application. https://doi.org/10.15011/ijmsa.32.320212

[Ozawa et al. 2009] Ozawa, S., Koda, T., Adachi, M., Morohoshi, K., Watanabe, M., & Hibiya, T. The influence of temporal phase difference of m=±2 oscillations on surface frequency analysis for levitated droplets *Journal of Applied Physics* 2009, *106*(3), 034907. https://doi.org/10.1063/1.3190495

[Cummings et al. 1991] Cummings, D. L. & Blackburn, D. A. Oscillations of magnetically levitated aspherical droplets *Journal of Fluid Mechanics* 1991, *224*, 395–416. https://doi.org/10.1017/S0022112091001817

[Siafakas et al. 2018] Siafakas, D, Matsushita, T., Hakamada, S., Onodera, K., & Watanabe, M. Measurement of Viscosity of SiO_2-CaO-Al_2O_3 Slag in Wide Temperature Range by

Aerodynamic Levitation and Rotating Bob Methods and Sources of Systematic Error *International Journal of Microgravity Science and Application* 2018, *35*(2).

[Ohishi et al. 2017] Ohishi, Y., Kargl, F., Nakamori, F., Muta, H., Kurosaki, K., & Yamanaka, S. Physical properties of core-concrete systems: Al_2O_3-ZrO_2 molten materials measured by aerodynamic levitation *Journal of Nuclear Materials* 2017, *487*, 121–127. https://doi.org/10.1016/j.jnucmat.2017.02.002

[Krishnan et al. 1990] Krishnan, S., Hansen, G. P., Hauge, R. H., & Margrave, J. L. Emissivities and Optical Constants of Electromagnetically Levitated Liquid Metals as Functions of Temperature and Wavelength In J. W. Hastie (Ed.), *Materials Chemistry at High Temperatures* 1990 (pp. 143–164). Totowa, NJ: Humana Press. https://doi.org/10.1007/978-1-4612-0481-7_11

[Bale et al. 2016] Bale, C. W., Bélisle, E., Chartrand, P., Decterov, S. A., Eriksson, G., Gheribi, A. E., Hack, K., Jung, I.-H., Kang, Y.-B., Melançon, J., Pelton, A. D., Petersen, S., Robelin, C., Sangster, J., Spencer, P., & Van Ende, M.-A. FactSage thermochemical software and databases, 2010–2016 *Calphad* 2016, *54*, 35–53. https://doi.org/10.1016/j.calphad.2016.05.002

[Lamb 1881] Lamb, H. On the Oscillations of a Viscous Spheroid *Proceedings of the London Mathematical Society* 1881, *s1-13*(1), 51–70. https://doi.org/10.1112/plms/s1-13.1.51

[Canny 1986] Canny, J. A Computational Approach to Edge Detection *IEEE Transactions on Pattern Analysis and Machine Intelligence* 1986, *PAMI-8*(6), 679–698. https://doi.org/10.1109/TPAMI.1986.4767851

[Ding et al. 2001] Ding, L. & Goshtasby, A. On the Canny edge detector *Pattern Recognition* 2001, *34*(3), 721–725. https://doi.org/10.1016/S0031-3203(00)00023-6

[McIlhagga 2011] McIlhagga, W. The Canny Edge Detector Revisited *International Journal of Computer Vision* 2011, *91*(3), 251–261. https://doi.org/10.1007/s11263-010-0392-0

[Strang 1993] Strang, G. Wavelet transforms versus Fourier transforms *Bulletin of the American Mathematical Society* 1993, *28*(2), 288–305. https://doi.org/10.1090/S0273-0979-1993-00390-2

[Carothers et al. 1993] Carothers, N. L., Haydon, R., & Lin, P.-K. On the isometries of the Lorentz function spaces *Israel Journal of Mathematics* 1993, *84*(1–2), 265–287. https://doi.org/10.1007/BF02761703

[BIPM 2008] BIPM Evaluation of measurement data – Guide to the expression of uncertainty in measurement 2008. Joint Committee for Guides in Metrology. Retrieved from https://www.bipm.org/documents/20126/2071204/ JCGM_100_2008_E.pdf/cb0ef43f-baa5-11cf-3f85-4dcd86f77bd6.

[Metropolis et al. 1949] Metropolis, N. & Ulam, S. The Monte Carlo Method *Journal of the American Statistical Association* 1949, *44*(247), 335–341. https://doi.org/10.1080/01621459.1949.10483310

[Leach 1996] Leach, A. R. *Molecular modelling: principles and applications* 1996. Edinbourgh: Addison-Wesley.

[Goodman 2015] Goodman, B. J. *A Study of Vitrified Nuclear Wasteforms by Molecular Dynamics, Electron Microscopy and Raman Spectroscopy* 2015. University of Kent.

[Pedone 2009] Pedone, A. Properties Calculations of Silica-Based Glasses by Atomistic Simulations Techniques: A Review *The Journal of Physical Chemistry C* 2009, *113*(49), 20773–20784. https://doi.org/10.1021/jp9071263

[Swope et al. 1982] Swope, W. C., Andersen, H. C., Berens, P. H., & Wilson, K. R. A computer simulation method for the calculation of equilibrium constants for the formation of physical clusters of molecules: Application to small water clusters *The Journal of Chemical Physics* 1982, *76*(1), 637–649. https://doi.org/10.1063/1.442716

[Du et al. 2022] Du, J. & Cormack, A. *Atomistic simulations of glasses: fundamentals and applications* 2022.

[Charpentier et al. 2018] Charpentier, T., Okhotnikov, K., Novikov, A. N., Hennet, L., Fischer, H. E., Neuville, D. R., & Florian, P. Structure of Strontium Aluminosilicate Glasses from Molecular Dynamics Simulation, Neutron Diffraction, and Nuclear Magnetic Resonance Studies *The Journal of Physical Chemistry B* 2018, *122*(41), 9567–9583. https://doi.org/10.1021/acs.jpcb.8b05721

[Hu et al. 2020] Hu, Y.-J., Zhao, G., Zhang, M., Bin, B., Del Rose, T., Zhao, Q., Zu, Q., Chen, Y., Sun, X., de Jong, M., & Qi, L. Predicting densities and elastic moduli of SiO2-based glasses by machine learning *Npj Computational Materials* 2020, *6*(1), 25. https://doi.org/10.1038/s41524-020-0291-z

[Born et al. 1955] Born, Max, Huang, K., & Lax, M. Dynamical Theory of Crystal Lattices *American Journal of Physics* 1955, *23*(7), 474–474. https://doi.org/10.1119/1.1934059

[Born et al. 1988] Born, M. & Landé, A. Über die Berchnung der Kompressibilität regulärer Kristalle aus der Gittertheorie In A. O. Barut & A. van der Merwe (Eds.), *Selected Scientific Papers of Alfred Landé* 1988 (pp. 58–64). Dordrecht: Springer Netherlands. https://doi.org/10.1007/978-94-009-3981-3_7

[Ewald 1921] Ewald, P. P. Die Berechnung optischer und elektrostatischer Gitterpotentiale *Annalen der Physik* 1921, *369*(3), 253–287. https://doi.org/10.1002/andp.19213690304

[Ziman 1972] Ziman, J. M. *Principles of the Theory of Solids* 1972 (2nd ed.). Cambridge University Press. https://doi.org/10.1017/CBO9781139644075

[Born et al. 1932] Born & Mayer, J. E. Zur Gittertheorie der Ionenkristalle *Zeitschrift für Physik* 1932, *75*(1–2), 1–18. https://doi.org/10.1007/BF01340511

[Huggins et al. 1933] Huggins, M. L. & Mayer, J. E. Interatomic Distances in Crystals of the Alkali Halides *The Journal of Chemical Physics* 1933, *1*(9), 643–646. https://doi.org/10.1063/1.1749344

[Buckingham 1937] Buckingham, R. A. The quantum theory of atomic polarization II— The van der Waals energy of two atoms *Proceedings of the Royal Society of London. Series A - Mathematical and Physical Sciences* 1937, *160*(900), 113–126. https://doi.org/10.1098/rspa.1937.0098

[Jakse et al. 2021] Jakse, Noël, Alvares, C. M. S., & Pisch, A. Ab initio based interionic interactions in calcium aluminotitanate oxide melts: structure and diffusion *Journal of Physics: Condensed Matter* 2021, *33*(28), 285401. https://doi.org/10.1088/1361-648X/abfc0f

[Bouhadja et al. 2013] Bouhadja, M., Jakse, N., & Pasturel, A. Structural and dynamic properties of calcium aluminosilicate melts: A molecular dynamics study *The Journal of Chemical Physics* 2013, *138*(22), 224510. https://doi.org/10.1063/1.4809523

[Jabraoui et al. 2017] Jabraoui, H., Malki, M., Hasnaoui, A., Badawi, M., Ouaskit, S., Lebègue, S., & Vaills, Y. Thermodynamic and structural properties of binary calcium silicate glasses: insights from molecular dynamics *Physical Chemistry Chemical Physics* 2017, *19*(29), 19083–19093. https://doi.org/10.1039/C7CP03397D

[Kieu et al. 2011] Kieu, L.-H., Delaye, J.-M., Cormier, L., & Stolz, C. Development of empirical potentials for sodium borosilicate glass systems *Journal of Non-Crystalline Solids* 2011, *357*(18), 3313–3321. https://doi.org/10.1016/j.jnoncrysol.2011.05.024

[Fa et al. 2005] Fa, K., Nguyen, A. V., & Miller, J. D. Hydrophobic Attraction As Revealed by AFM Force Measurements and Molecular Dynamics Simulation *The Journal of Physical Chemistry B* 2005, *109*(27), 13112–13118. https://doi.org/10.1021/jp0445526

[Morris et al. 2020] Morris, J., Cowen, B. J., Teysseyre, S., & Hecht, A. A. Molecular dynamics investigation of threshold displacement energies in CaF2 *Computational Materials Science* 2020, *172*, 109293. https://doi.org/10.1016/j.commatsci.2019.109293

[Xu et al. 2010] Xu (徐海譞), H., Behera, R. K., Wang (王艳丽), Y., Ebrahimi, F., Sinnott, S. B., Wachsman, E. D., & Phillpot, S. R. A critical assessment of interatomic potentials for ceria with application to its elastic properties *Solid State Ionics* 2010, *181*(11–12), 551–556. https://doi.org/10.1016/j.ssi.2010.02.023

[Plimpton 1995] Plimpton, S. Fast Parallel Algorithms for Short-Range Molecular Dynamics *Journal of Computational Physics* 1995, *117*(1), 1–19. https://doi.org/10.1006/jcph.1995.1039

[Stukowski 2010] Stukowski, A. Visualization and analysis of atomistic simulation data with OVITO–the Open Visualization Tool *Modelling and Simulation in Materials Science and Engineering* 2010, *18*(1), 015012. https://doi.org/10.1088/0965-0393/18/1/015012

[Li et al. 2017] Li, K., Khanna, R., Bouhadja, M., Zhang, J., Liu, Z., Su, B., Yang, T., Sahajwalla, V., Singh, C. V., & Barati, M. A molecular dynamic simulation on the factors influencing the fluidity of molten coke ash during alkalization with K2O and Na2O *Chemical Engineering Journal* 2017, *313*, 1184–1193. https://doi.org/10.1016/j.cej.2016.11.011

[Hennet et al. 2016a] Hennet, Louis, Drewitt, J. W. E., Neuville, D. R., Cristiglio, V., Kozaily, J., Brassamin, S., Zanghi, D., & Fischer, H. E. (a) Neutron diffraction of calcium aluminosilicate glasses and melts *Journal of Non-Crystalline Solids* 2016a, *451*, 89–93. https://doi.org/10.1016/j.jnoncrysol.2016.05.018

[Sukhomlinov et al. 2017] Sukhomlinov, S. V. & Müser, M. H. Determination of accurate, mean bond lengths from radial distribution functions *The Journal of Chemical Physics* 2017, *146*(2), 024506. https://doi.org/10.1063/1.4973804

[Onoda et al. 1970] Onoda, G. Y. & Brown, S. D. Low-Silica Glasses Based on Calcium Aluminates *Journal of the American Ceramic Society* 1970, *53*(6), 311–316. https://doi.org/10.1111/j.1151-2916.1970.tb12114.x

[Hafner et al. 1958] Hafner, H. C., Kreidl, N. J., & Weidel, R. A. Optical and Physical Properties of Some Calcium Aluminate Glasses *Journal of the American Ceramic Society* 1958, *41*(8), 315–323. https://doi.org/10.1111/j.1151-2916.1958.tb12923.x

[De Bilbao et al. 2014] de Bilbao, E., Dombrowski, M., Traon, N., Tonnesen, T., Poirier, J., & Blond, E. Study of Reactive Impregnation and Phase Transformations during the Corrosion of High Alumina Refractories by Al_2O_3-CaO Slag 2014 (pp. 264–271). Presented at the 13th International Ceramics Congress, part of CIMTEC 2014. https://doi.org/10.4028/www.scientific.net/AST.92.264

[Akola et al. 2013] Akola, J., Kohara, S., Ohara, K., Fujiwara, A., Watanabe, Y., Masuno, A., Usuki, T., Kubo, T., Nakahira, A., Nitta, K., Uruga, T., Weber, J. K. R., & Benmore, C. J. Network topology for the formation of solvated electrons in binary CaO–Al_2O_3 composition glasses *Proceedings of the National Academy of Sciences* 2013, *110*(25), 10129–10134. https://doi.org/10.1073/pnas.1300908110

[Iuga et al. 2005] Iuga, D., Morais, C., Gan, Z., Neuville, D. R., Cormier, L., & Massiot, D. NMR Heteronuclear Correlation between Quadrupolar Nuclei in Solids *Journal of the American Chemical Society* 2005, *127*(33), 11540–11541. https://doi.org/10.1021/ja052452n

[Massiot et al. 1995] Massiot, D., Trumeau, D., TOUZOIa, B., Douy, A., & Coutures, J.-P. Structure and Dynamics of $CaA1_20_4$ from Liquid to Glass: A High-Temperature 27Al NMR Time-Resolved Study 1995, 5. https://doi.org/10.1021/j100044a038

[Du 2015] Du, J. Challenges in Molecular Dynamics Simulations of Multicomponent Oxide Glasses In C. Massobrio, J. Du, M. Bernasconi, & P. S. Salmon (Eds.), *Molecular Dynamics Simulations of Disordered Materials* 2015 (Vol. 215, pp. 157–180). Cham: Springer International Publishing. https://doi.org/10.1007/978-3-319-15675-0_7

[Drewitt et al. 2012] Drewitt, J. W. E., Hennet, L., Zeidler, A., Jahn, S., Salmon, P. S., Neuville, D. R., & Fischer, H. E. Structural Transformations on Vitrification in the Fragile Glass-Forming System $CaAl_2O_4$ *Physical Review Letters* 2012, *109*(23), 235501. https://doi.org/10.1103/PhysRevLett.109.235501

[Cristiglio et al. 2010] Cristiglio, V., Cuello, G. J., Hennet, L., Pozdnyakova, I., Leydier, M., Kozaily, J., Fischer, H. E., Johnson, M. R., & Price, D. L. Neutron diffraction study of molten calcium aluminates *Journal of Non-Crystalline Solids* 2010, *356*(44–49), 2492–2496. https://doi.org/10.1016/j.jnoncrysol.2010.03.027

[Jain et al. 2013] Jain, A., Ong, S. P., Hautier, G., Chen, W., Richards, W. D., Dacek, S., Cholia, S., Gunter, D., Skinner, D., Ceder, G., & Persson, K. a. The Materials Project: A materials genome approach to accelerating materials innovation *APL Materials* 2013, *1*(1), 011002. https://doi.org/10.1063/1.4812323

[Re3data.Org 2014] Re3data.Org American Mineralogist Crystal Structure Database 2014. https://doi.org/10.17616/R32S57

[Wang et al. 2021] Wang, Z., Huang, S., Wen, G., Liu, Q., & Tang, P. Thermal conductivity prediction and structure-property relationship of CaO-SiO_2-Al_2O_3 ternary system: A combination of molecular dynamics simulations and machine learning *Journal of Molecular Liquids* 2021, *324*, 114697. https://doi.org/10.1016/j.molliq.2020.114697

[Roller 1986] Roller, M. B. Rheology of curing thermosets: A review *Polymer Engineering and Science* 1986, *26*(6), 432–440. https://doi.org/10.1002/pen.760260610

[Duchesne et al. 2013] Duchesne, M. A., Bronsch, A. M., Hughes, R. W., & Masset, P. J. Slag viscosity modeling toolbox *Fuel* 2013, *114*, 38–43. https://doi.org/10.1016/j.fuel.2012.03.010

[Wu et al. 2015] Wu, G., Yazhenskikh, E., Hack, K., Wosch, E., & Müller, M. Viscosity model for oxide melts relevant to fuel slags. Part 1: Pure oxides and binary systems in the system SiO_2–Al_2O_3–CaO–MgO–Na_2O–K_2O *Fuel Processing Technology* 2015, *137*, 93–103. https://doi.org/10.1016/j.fuproc.2015.03.025

[Wu et al. 2015] Wu, G., Yazhenskikh, E., Hack, K., & Müller, M. Viscosity model for oxide melts relevant to fuel slags. Part 2: The system SiO_2–Al_2O_3–CaO–MgO–Na_2O–K_2O *Fuel Processing Technology* 2015, *138*, 520–533. https://doi.org/10.1016/j.fuproc.2015.06.031

[Drewitt et al. 2011] Drewitt, J. W. E., Jahn, S., Cristiglio, V., Bytchkov, A., Leydier, M., Brassamin, S., Fischer, H. E., & Hennet, L. The structure of liquid calcium aluminates as investigated using neutron and high energy x-ray diffraction in combination with molecular dynamics simulation methods *Journal of Physics: Condensed Matter* 2011, *23*(15), 155101. https://doi.org/10.1088/0953-8984/23/15/155101

[Hannon et al. 2000] Hannon, A. C. & Parker, J. M. The structure of aluminate glasses by neutron diffraction *Journal of Non-Crystalline Solids* 2000, *274*(1–3), 102–109. https://doi.org/10.1016/S0022-3093(00)00208-8

[Hennet et al. 2016b] Hennet, Louis, Drewitt, J. W. E., Neuville, D. R., Cristiglio, V., Kozaily, J., Brassamin, S., Zanghi, D., & Fischer, H. E. (b) Neutron diffraction of calcium aluminosilicate glasses and melts *Journal of Non-Crystalline Solids* 2016b, *451*, 89–93. https://doi.org/10.1016/j.jnoncrysol.2016.05.018

[Wu et al. 2021] Wu, T., Yang, W., Zhang, C., Wang, H., & Lei, J. Microstructural analysis by molecular dynamics simulation of aluminate ternary slag with alkaline oxide *Journal of Non-Crystalline Solids* 2021, *570*, 121044. https://doi.org/10.1016/j.jnoncrysol.2021.121044

[Zhao et al. 2019] Zhao, J., Xu, X., Chen, X., Xu, Q., Luo, Z., Qiao, X., Du, J., Fan, X., & Qian, G. A structure model for phase separated fluoroaluminosilicate glass system by molecular dynamic simulations *Journal of the European Ceramic Society* 2019, *39*(15), 5018–5029. https://doi.org/10.1016/j.jeurceramsoc.2019.06.042

[Wallenberger et al. 1994] Wallenberger, F. T. & Brown, S. D. High-modulus glass fibers for new transportation and infrastructure composites and new infrared uses *Composites Science and Technology* 1994, *51*(2), 243–263. https://doi.org/10.1016/0266-3538(94)90194-5

[Puertas et al. 2003] Puertas, F. & Fernández-Jiménez, A. Mineralogical and microstructural characterisation of alkali-activated fly ash/slag pastes *Cement and Concrete Composites* 2003, *25*(3), 287–292. https://doi.org/10.1016/S0958-9465(02)00059-8

[Li et al. 2010] Li, C., Sun, H., & Li, L. A review: The comparison between alkali-activated slag (Si+Ca) and metakaolin (Si+Al) cements *Cement and Concrete Research* 2010, *40*(9), 1341–1349. https://doi.org/10.1016/j.cemconres.2010.03.020

[McClelland et al. 1995] McClelland, M. A. & Sze, J. S. Surface tension and density measurements for indium and uranium using a sessile-drop apparatus with glow discharge cleaning *Surface Science* 1995, *330*(3), 313–322. https://doi.org/10.1016/0039-6028(95)00358-4

[Chebykin et al. 2017] Chebykin, D., Heller, H.-P., Dubberstein, T., Korobeinikov, I., & Volkova, O. Viscosity Measurement of Slags using Rotating Bob and Vibrating Finger Viscometer *ISIJ International* 2017, *57*(8), 1319–1326. https://doi.org/10.2355/isijinternational.ISIJINT-2016-580

[Takahashi et al. 2015] Takahashi, S., Neuville, D. R., & Takebe, H. Thermal properties, density and structure of percalcic and peraluminus $CaO–Al_2O_3–SiO_2$ glasses *Journal of Non-Crystalline Solids* 2015, *411*, 5–12. https://doi.org/10.1016/j.jnoncrysol.2014.12.019

[Mysen 1990] Mysen, B. Relationships between silicate melt structure and petrologic processes *Earth-Science Reviews* 1990, *27*(4), 281–365. https://doi.org/10.1016/0012-8252(90)90055-Z

[Neuville et al. 2006] Neuville, D. R., Cormier, L., & Massiot, D. Al coordination and speciation in calcium aluminosilicate glasses: Effects of composition determined by 27Al MQ-MAS NMR and Raman spectroscopy *Chemical Geology* 2006, *229*(1–3), 173–185. https://doi.org/10.1016/j.chemgeo.2006.01.019

[Neuville et al. 2004] Neuville, D. R., Cormier, L., & Massiot, D. Al environment in tectosilicate and peraluminous glasses: A 27Al MQ-MAS NMR, Raman, and XANES investigation *Geochimica et Cosmochimica Acta* 2004, *68*(24), 5071–5079. https://doi.org/10.1016/j.gca.2004.05.048

[Cormack et al. 2001] Cormack, A. N. & Du, J. Molecular dynamics simulations of soda–lime–silicate glasses *Journal of Non-Crystalline Solids* 2001, *293–295*, 283–289. https://doi.org/10.1016/S0022-3093(01)00831-6

[Du et al. 2006] Du, J., Devanathan, R., Corrales, L. R., Weber, W. J., & Cormack, A. N. Short- and medium-range structure of amorphous zircon from molecular dynamics simulations *Physical Review B* 2006, *74*(21), 214204. https://doi.org/10.1103/PhysRevB.74.214204

[Hack et al. 2019] Hack, K., Wu, G., Yazhenskikh, E., Jantzen, T., & Müller, M. A CALPHAD approach to modelling of slag viscosities *Calphad* 2019, *65*, 101–110. https://doi.org/10.1016/j.calphad.2019.02.001

[Urbain 1987] Urbain, G. Viscosity estimation of slags *Steel Research* 1987, *58*(3), 111–116. https://doi.org/10.1002/srin.198701513

[Dong et al. 2014] Dong, X.-J., Sun, H.-Y., She, X.-F., Xue, Q.-G., & Wang, J.-S. Viscosity and viscosity estimation model of fully liquid slags in $TiO_2–Al_2O_3–CaO–SiO_2$ and TiO_2 $–Al_2O_3–CaO–SiO_2–MgO$ systems with high TiO_2 concentration and low mass ratio of CaO to SiO_2 *Ironmaking & Steelmaking* 2014, *41*(2), 99–106. https://doi.org/10.1179/1743281212Y.0000000099

[Lin et al. 1979] Lin, P. L. & Pelton, A. D. A structural model for binary silicate systems *Metallurgical Transactions B* 1979, *10*(4), 667–675. https://doi.org/10.1007/BF02662569

[Machacek et al. 2006] Machacek, J., Gedeon, O., & Liska, M. Group connectivity in binary silicate glasses *Journal of Non-Crystalline Solids* 2006, *352*(21–22), 2173–2179. https://doi.org/10.1016/j.jnoncrysol.2006.01.036

[Grundy et al. 2008] Grundy, A. N., Liu, H., Jung, I.-H., Decterov, S. A., & Pelton, A. D. A model to calculate the viscosity of silicate melts: Part I: Viscosity of binary SiO_2#x2013;MeO_x systems (Me = Na, K, Ca, Mg, Al) *International Journal of Materials Research* 2008, *99*(11), 1185–1194. https://doi.org/10.3139/146.101752

[Pomeau 1972] Pomeau, Y. Low-Frequency Behavior of Transport Coefficients in Fluids *Physical Review A* 1972, *5*(6), 2569–2587. https://doi.org/10.1103/PhysRevA.5.2569

[Cherne et al. 2002] Cherne, F. J., Baskes, M. I., & Deymier, P. A. Erratum: Properties of liquid nickel: A critical comparison of EAM and MEAM calculations [Phys. Rev. B 65, 024209 (2002)] *Physical Review B* 2002, *66*(14), 149902. https://doi.org/10.1103/PhysRevB.66.149902

[Mouas et al. 2012] Mouas, M., Gasser, J.-G., Hellal, S., Grosdidier, B., Makradi, A., & Belouettar, S. Diffusion and viscosity of liquid tin: Green-Kubo relationship-based calculations from molecular dynamics simulations *The Journal of Chemical Physics* 2012, *136*(9), 094501. https://doi.org/10.1063/1.3687243

[Hess 2002] Hess, B. Determining the shear viscosity of model liquids from molecular dynamics simulations *The Journal of Chemical Physics* 2002, *116*(1), 209. https://doi.org/10.1063/1.1421362

[Todd et al. 2017] Todd, B. D. & Daivis, P. J. *Nonequilibrium molecular dynamics: theory, algorithms and applications* 2017. Cambridge, United Kingdom New York, NY, USA Port Melbourne, Australia Delhi, India Singapore: Cambridge University Press.

Zheng ZHANG

Étude de la corrélation entre les propriétés thermophysiques et l'évolution structurelle d'oxydes fondus par lévitation aérodynamique

Résumé :

Les systèmes fondus $CaO\text{-}Al_2O_3$ (CA) et $CaO\text{-}Al_2O_3\text{-}SiO_2$ (CAS) et leurs propriétés thermophysiques ont une large application dans les industries à haute température, en particulier dans les procédés métallurgiques et la corrosion des réfractaires par les laitiers. Peu d'études ont été rapportées sur leurs propriétés thermophysiques (densité, tension superficielle et viscosité) depuis les points de fusion jusqu'aux ultra-hautes températures et sur la corrélation entre les propriétés thermophysiques et l'évolution structurelle, en raison de la difficulté de mesurer ces propriétés à haute température.

Dans cette thèse, des mesures systématiques in-situ de la densité, de la tension superficielle et de la viscosité des systèmes fondus CA et CAS ont été réalisées par lévitation aérodynamique avec la méthode d'oscillation des gouttelettes sur une large gamme de température. Le post-traitement a particulière été optimisé pour améliorer considérablement la précision des résultats et les incertitudes sur la densité, la tension superficielle et la viscosité, ont été évaluées. En même temps, des simulations de dynamique moléculaire, validées par la comparaison avec des résultats de caractérisation précédemment rapportés (diffraction des neutrons, RMN), ont permis de calculer la distribution de la longueur/angle des liaisons, les espèces d'oxygène, le degré de compensation de charge, la connectivité du réseau (espèces d'amas tétraédriques) et les liaisons d'oxygène non satisfaites, explorant ainsi l'évolution structurelle des systèmes CA et CAS fondus à différentes températures et compositions.

Enfin, les corrélations théoriques entre la densité, la tension superficielle, la viscosité et l'évolution structurelle sont révélées sur la base de l'analyse des systèmes CA et CAS.

Mots clés : l'oxyde fond, lévitation aérodynamique, oscillation des gouttelettes, incertitude de mesure, propriétés thermophysiques, évolution structurelle, dynamique moléculaire

Study of the correlation between thermophysical properties and structural evolution of oxide melts by aerodynamic levitation

Abstract :

The molten $CaO\text{-}Al_2O_3$ (CA) system, the molten $CaO\text{-}Al_2O_3\text{-}SiO_2$ (CAS) system, and their thermophysical properties have a wide application in high-temperature industries, particularly in metallurgical processes and slag corrosion of refractory materials. Due to the difficulty to measure these properties at high temperature, few studies have been reported on their thermophysical properties (density, surface tension, and viscosity) from melting points to ultra-high temperatures and the correlation between thermophysical properties and structural evolution.

In this thesis, systematic in-situ measurements of density, surface tension, and viscosity of the molten CA and CAS systems were performed by aerodynamic levitation with the droplet oscillation method over a wide temperature range. In the measurement, a new post-processing of data is present, including the determination of the resonant frequency of the harmonic oscillation and calculations of uncertainties on density, surface tension, and viscosity, which greatly improve the accuracy of measurement. At the same time, molecular dynamic simulations validated by comparing with previously reported characterization results (neutron diffraction, NMR) allowed to calculate bond length/angle distribution, oxygen species, the degree of charge compensation, network connectivity (tetrahedral cluster species), and unsatisfied oxygen bonds, exploring the structural evolution of molten CA and CAS systems at different temperatures and compositions.

Finally, the theoretical correlations between density, surface tension, viscosity and structural evolution were revealed based on the analysis of CA and CAS systems.

Keywords : oxide melts, aerodynamic levitation, droplet oscillation, measurement uncertainty, thermophysical properties, structural evolution, molecular dynamics

CEMHTI
1d Avenue de la recherche scientifique
45071 Orléans Cedex 2